UNIVERSITÀ
DEGLI STUDI
FIRENZE

DOTTORATO DI RICERCA IN

FISICA E ASTRONOMIA

CICLO XXXI

COORDINATORE Prof. D'Alessandro Raffaello

Development of detectors for the diagnostics of ELI-NP photons beams.

Settore Scientifico Disciplinare FIS/01

Dottorando
Dott. *Borgheresi Rita*

Tutori
Prof. *Adriani Oscar*

Prof. *Veltri Michele*

Coordinatore
Prof. D'Alessandro Raffaello

Anni 2015/2018

CONTENTS

INTRODUCTION

Nowadays we are able to produce typical radiation formerly used in nuclear facilities with ultra-intense laser fields, reaching up to 10^{22} W cm^{-2}, as demonstrated in laboratories across the globe. These emerging laser driven technologies are promising in terms of cost, size and their available parameter range. However, the vast majority of the experiments were performed in laboratories where the laser system operation reliability does not reach its nuclear facilities counterpart. Crossing the gap from lab-based experiments to facility-based experiments was identified, in Europe, as a major step forward. As a consequence, the construction of a state of the art laser-centred, distributed pan-European research infrastructure was initiated through the Extreme Light Infrastructure (ELI) project.

The ELI-NP (NP for nuclear physics) facility, currently under construction near Bucharest (Romania), is the pillar of the project ELI dedicated to the Nuclear Photonics, an emerging new discipline that consists in exploring the nuclei with photons. To develop an experimental program in nuclear physics at the frontiers of the present-day knowledge, two equipments will be deployed at ELI-NP: a high power laser system consisting of two 10 PW lasers and a high brilliance gamma beam system.

The ELI-NP gamma beam will be obtained by collimating the radiation emerging from inverse Compton scattering of short laser pulses on relativistic electron beam bunches. The inverse Compton process can be looked upon as the most efficient frequency amplifier or as a "photon accelerator". Using this method it will be possible to obtain a gamma beam with unique characteristics in terms of brilliance, photon flux and energy bandwidth that are necessary to cover the proposed experiments in fundamental physics, nuclear physics and astrophysics, as well as applications in material and life sciences, industrial tomography and nuclear waste management. The system will consist of two energy lines: a low-energy line (LE) delivering gamma rays with energies up to 3.5 MeV and a high-energy line (HE) where the energy of the gamma rays will reach up to 19.5 MeV.

Such a gamma beam requires peculiar devices and techniques to measure and monitor the beam parameters during the commissioning and the operational phase. To accomplish this task, a Gamma Beam Characterisation system equipped with four elements has been developed: a Compton spectrometer (CSPEC), to measure and monitor the photon energy spectrum; a nuclear resonant scattering spectrometer, for absolute beam energy calibration and inter-calibration of the other detectors; a beam profile imager to be used for alignment and diagnostics purposes and finally a sampling calorimeter (GCAL), for a fast combined measurement of the beam average energy and intensity. The system must be able to cope with the time structure of the beam made by 32 pulses of 10^5 photons each, with a duration of 1-2 ps, separated by 16 ns and delivered at 100 Hz.

The combination of the measurements performed by GCAL and CSPEC allows to fully characterize the gamma beam energy distribution and intensity with a precision of about 0.5%, enough to demonstrate the fulfillment of the required parameters. The work described in this thesis concerns the realization and the characterization of these two detectors, which are under construction at the INFN Firenze.

The first detector described is the CSPEC, used to reconstruct the energy spectrum of the γ beam with a non-destructive method. The basic idea is to measure energy and position of electrons recoiling at small angles from Compton interactions of the beam, on a thin micro-metric mylar target. A high purity germanium detector (HPGe) will be used to precisely measure the energy of the Compton scattered electron, while a double sided silicon strip detector will determine the impact point of the e^- on the detector. The recoil photon is detected by Barium Fluoride (BaF_2) crystals, whose fast response in coincidence with the HPGe signal will provide the trigger.

The characterization procedure of the HPGe and the BaF_2 detectors is presented. We evaluated the HPGe excellent energy resolution and linearity by exposing the detector to different γ radioactive sources. In addition, the accuracy of the HPGe Monte Carlo (MC) simulations has been verified using electrons of definite energy, in particular for what concern the parameters related to the dead layers preceding the HPGe crystal. For the BaF_2 detector, we investigated the possibility to use a selection method that permits to identify the signals due to γ from the signals due to the crystal radioactivity (α particles) or to the thermal noise. Using these cuts the calibration curves and the energy resolution of the scintillators composing the photon detector were obtained. Finally, we studied the chance to use the intrinsic α radioactivity of BaF_2 to monitor eventual gain variations.

The second detector subject of this thesis is the GCAL, a calorimeter providing a fast combined measurement of the beam average energy and intensity by absorbing the gamma pulses in a longitudinally segmented calorimeter. The intensity of the gamma beam is not exactly known, so the photon energy cannot be simply determined from the total energy released, as usually happens in calorimeters. The basic idea is to use properties of the gamma energy released inside the detector, that depends only on the photon energy and not on the beam intensity. This is obtained by exploiting the monotonic energy dependence of the total photon interaction cross section for low-Z materials in the energy range of interest at the ELI-NP facility. Thus, realizing a sampling calorimeter with low Z absorber, the average energy of the beam can be measured by fitting the longitudinal profile against parametrized distributions, obtained with detailed MC simulations. Once the photon energy is known, assuming a monochromatic beam, the number of impinging photons is obtained from the total energy released. The calorimeter for the LE beamline has been realized as a sampling calorimeter composed by 22 identical layers. Each element consists of a block of Polyethylene absorber (an inexpensive and easily workable low-Z material) followed by a readout board hosting 7 adjacent silicon detectors.

The silicon detectors time response has been tested using an infrared laser. Indeed the time response is a critical issue, since the calorimeter has to be able to resolve the 16 ns separated pulses of the ELI-NP beam. To verify the functionality of all the layers, the response of each sensor composing the calorimeter has been checked with a laser. We have also verify the signal dependence from the γ impact point scanning the sensors horizontally and vertically.

The optimization of the calorimeter design has been made with a simplified MC simulation assuming homogeneous silicon layers and no geometry details. To validate the results of this initial simplified approach, new MC simulations have been made considering a very detailed geometry description of the detector. In particular we have simulated the various component of the microstrip detectors, such as dead layers, the aluminum strip and the backplane metallization. Furthermore, the presence of the aluminum supporting structures and of the acquisition board was considered. We have investigated the effects of some of the main sources of systematic uncertainties in the determination of the beam energy and intensity. We have studied the variations produced by having a γ beam with a characteristic energy spectrum and spatial distribution or with a random jitter on the beam energy (or intensity) rather than a monochromatic point-like beam. Finally, we have considered the effects related to incorrect inter-calibration of the different detector layers which could distort the measured longitudinal profile.

1 ELI-NP FACILITY

1.1 ELI PROJECT

ELI, acronym for Extreme Light Infrastructure [1, 2], is a project started as a bottom-up initiative by the European scientific laser community and the network of large national laser facilities, LASERLAB-EUROPE, in the context of the preparation of the first European ESFRI Roadmap in 2005. The aim of this project was the construction of the first European Centre for high-level research on ultra-high-power laser with focusable intensity and laser-matter interaction.

The high interest of the scientific community on high-power laser physics is confirmed by the Nobel Prize on Physics 2018 [3] given to professor Gerard Mourou (France), the Initiator of the ELI Project, and Donna Strickland (Canada) "for their method of generating high-intensity, ultra-short optical pulses". In 1985 they developed an absolutely new and original method, Chirped Pulse Amplification (CPA) [4], for generating ultra-short optical pulses. That technique takes low-intensity light, stretches and amplifies it, then compresses it back into incredibly short, ultrafast pulses with extremely great power. That's a key technology driving the Extreme Light Infrastructure.

ELI is implemented as a distributed research infrastructure based on 3 specialized and complementary facilities, currently under construction: they are located in the Czech Republic, Hungary and Romania:

- *ELI - Nuclear Physics*, situated in Magurele (Romania), will be dedicated to nuclear and material science using laser driven radiation sources and is described in detail in the next section.

- *ELI - Attosecond Light Pulse Source*, located in Szeged (Hungary), was born for providing the international scientific community a broad range of ultrafast light sources to enable temporal investigations of electron dynamics in atoms, molecules, plasmas and solids on femtosecond and attosecond scale. The secondary purpose consists in the generation of pulses with power of 200 PW.

- *ELI - Beamlines*, based in Prague (Czech Republic), will mainly focus on the development of short-pulse secondary sources of radiation and particles, and on their multidisciplinary applications in molecular, biomedical and material sciences, physics of dense plasmas, warm dense matter, laboratory astrophysics.

From a technical point of view, the main scientific result of the project will be the extension of the laser-matter interaction field from relativistic to the ultra-relativistic regime, which corresponds to move from laser intensities I of

the order of 10^{20} W/cm^2 to I $> 10^{24}$ W/cm^2 [2]. This power increase will be accompanied by a compression of laser pulses, from the femtosecond to the attosecond or zeptosecond (10^{-21} s) regime. The mentioned improvement in laser field will open the possibility to study electron dynamics in atoms, molecules, plasmas and solids up to the zeptosecond time scale. Moreover, it will offer the possibility to create ultra-short energetic particle (from 10 to 100 GeV) and radiation (up to few MeV) beams produced for various applications.

1.2 ELI-NP

The Extreme Light Infrastructure - Nuclear Physics (ELI-NP) is meant as a unique research facility to investigate the impact of very intense electromagnetic radiation on matter with specific focus on nuclear phenomena and their practical applications. ELI-NP will bring together two scientific communities, the lasers and nuclear physics aiming at achieving the integration of the two disciplines and creating a new discipline named "Nuclear Photonics". At the moment, the ELI-NP building is completed, in Fig.1 is shown a photo of the facility that I took in September, 2016.

Figure 1: Photo of the status of ELI-NP infrastructure (September, 2016).

ELI-NP will provide two kinds of "extreme light" [5, 6]:

- one 'visible', generated by a high-power laser system (HPLS) with two parallel 10 PW lasers based on Optical Parametric Chirped Pulse Amplification (OPCPA) [4] and driven by a dual front-end system with two parallel amplification arms. Only one front end will run at a time, while the second one will represents a back-up solution to minimize the down-time of the facility. Each amplification arm will have three outputs, each with its own optical pulse compressor. They will provide different power levels. Besides the 10 PW output at a repetition rate of 1/60 Hz there will be two other outputs of 100 TW and 1 PW at repetition rates of 10 Hz and 1 Hz, respectively.

- one in the 'gamma' energy range, a Gamma Beam System (GBS) designed to produce brilliant and highly collimated gamma photon beams, as will be presented in detail in the next section.

Both systems are at the limits of the present-days technology. This two instruments can operate as stand-alone systems or combined together.

1.2.1 Inverse Compton Scattering source

The process in which a free electron and a photon interact is called Compton scattering. It is usually implicit that the photon releases part of its energy to the electron and then it is scattered with a lower frequency. When this energy exchange is reversed it is the case of inverse Compton scattering, occurring when the interacting electrons are in motion at a relativistic speed and the photon increases its energy in the scattering process.

The direct Compton scattering is a well-known phenomenon and the kinematics can be fully described as a relativistic elastic collision of a photon and an electron. Fig.2 shows a schematization of the collision of a photon of energy $E_\gamma = h\nu$ colliding with an electron at rest. After the collision the electron recoils at an angle ϕ with kinetic energy T and momentum p, while the photon is scattered with an energy $E'_\gamma = h\nu$ at an angle θ.

A complete solution of the kinematics of Compton interaction can be obtained considering the conservation of both energy and momentum, resulting in:

$$h\nu' = \frac{h\nu}{1 + \frac{h\nu}{m_e}(1 - \cos(\theta))} \tag{1}$$

where m_e is the electron mass at rest.

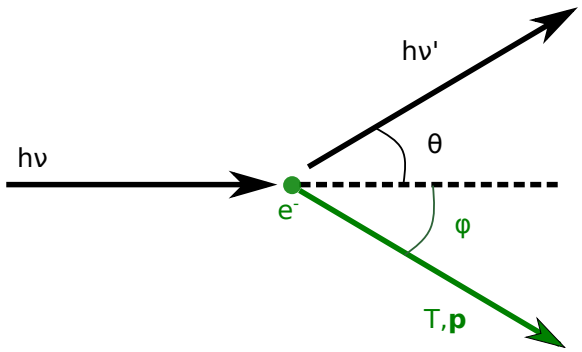

Figure 2: Representation of direct compton scattering.

Inverse Compton refers to the case in which the scatter of the photon occurs in a reference frame where the electron is not at rest but has a relativistic speed and an energy higher than the one of the interacting photon. In this process it is possible that the photon gains energy in the interaction and for this reason it is usually called inverse Compton scattering.

Consider an interaction between a moving electron and a photon with initial energy $E_\gamma = h\nu$, that propagates towards the electron at an angle θ_i, as depicted in Fig.3. After the interaction the photon is scattered at angle

θ_f with an energy $E'_\gamma = h\nu'$. The angle θ_i and θ_f are the angles between the momentum of the incident and scattered photon with respect to the direction of motion of the electron. In the rest frame of the electron the process can be described as a Compton scattering for a photon that has undergone an energy up-shift due to the relativistic Doppler effect.
Considering the electron having a Lorentz factor $\gamma = \frac{1}{\sqrt{1-\beta^2}}$, an incident angle θ_i and a velocity v$\sim$c then, the up-shifted energy $h\nu^*$ of the photon, in this reference frame will be expressed by $h\nu^* = 2\gamma h\nu_i$.

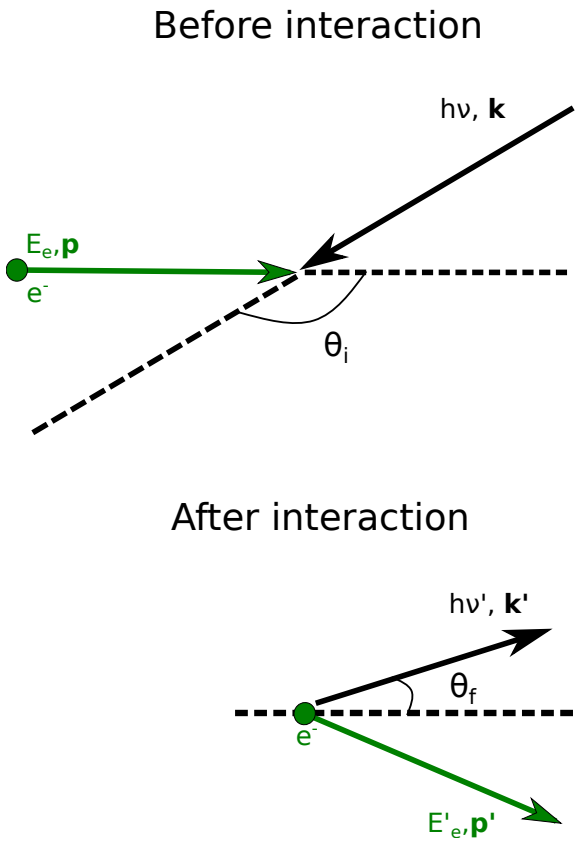

Figure 3: Representation of the inverse Compton scattering.

In the laboratory reference frame and considering an head-on collision ($\theta_i = \pi$), denoting with θ the angle of the scattered photon, the energy for the scattered photon is given by the following formula [7]:

$$E'_\gamma = E_\gamma \frac{1+\beta}{1-\beta\cos(\theta) + \frac{E_\gamma}{\gamma m_e}(1-\cos(\theta))} \tag{2}$$

In the case of a collision of a relativistic electron and a photon having an up-shifted energy negligible compared to the electron rest mass, it is possible to view the interaction in the electron reference frame as a classical Thomson scattering. This means that the electron does not recoil and the photon is re-emitted with unchanged frequency corresponding to the original one. In this case the result in the laboratory frame is a Lorentz boosted Thomson emission, where the scattered photons are peaked along the direction of

motion of the electron in a cone with aperture proportional to $1/\gamma$ and energy given by the following formula:

$$E'_\gamma \simeq E_\gamma \frac{4\gamma^2}{1+\gamma^2\theta^2}. \tag{3}$$

When the energy of the electron or of the incident photon increases so that the Thomson approximation ($2\gamma h\nu \ll m_e$) is no more valid, the electron recoil must be taken into account for the determination of the backscattered photon energy. It is possible to modify the equation 3 adding a correction parameter Δ for Compton recoil obtaining:

$$E'^{\text{Compton}}_\gamma \simeq E'^{\text{Thomson}}_\gamma (1-\Delta), \tag{4}$$

where

$$\Delta = \frac{\frac{4\gamma h\nu}{m_e}}{1+2\gamma\frac{h\nu}{m_e}}. \tag{5}$$

Considering the practical case of having a photon with an initial energy of $h\nu = 2.4$ eV, if the electron γ is 144 or 14400 ($E_e \sim 72$ or 720 MeV) the resulting Thomson scattering energy is equal to about 0.2 or 20 MeV. The ratio $2\gamma\frac{h\nu}{m_e}$, that represent the Compton correction, is equal to 1.35×10^{-2} for the highest energy case, so the Thomson approximation is already quite good. Notice that, using the inverse Compton scattering it is possible to obtain photons with a maximum energy ranging from 0.2 MeV to 20 MeV, using a visible light photon and just varying the electron beam energy. The scaling of the backscattered energy with γ^2 makes it possible to reach high values of γ energies with electron beam having energies that are easily obtainable at the state of the art of particle accelerator technology.

1.2.2 ELI-NP Gamma Beam System (GBS)

The GBS for ELI-NP was designed to provide a very intense and brilliant gamma beam with tunable energy ranging from 0.2 to 20 MeV. The experiments proposed to be performed with the gamma beam at ELI-NP, that are presented on the next section, have imposed for the beam the key parameters shown in Tab.1.

The gamma beam production is based on laser Compton backscattering off a relativistic electron beam. The results on the Compton Inverse Scattering presented in the previous section, has been made considering a simplified interaction of a single photon on a single electron. To obtain the energy of the photons after the collision between an intense laser beam and an electron beam we have to correct the formula Eq.4 as follow:

$$E'_\gamma \sim E_\gamma \cdot \frac{4\gamma^2}{1+a_0^2/2+\gamma^2\theta^2}\cdot(1-\Delta) \tag{6}$$

where a_0 is a laser parameter defined in Eq.7, which takes into account the laser pulse energy U_L, the wavelength λ_L, the beam-spot size w_0 and the FWHM pulse length σ_{tL}.

$$a_0 = 4.3\frac{\lambda_L}{w_0}\cdot\sqrt{\frac{U_L}{\sigma_{tL}}} \tag{7}$$

Parameter	Value
Photon energy	0.2-19.5 MeV
Photon energy tunability	steplessly
Bandwidth	$\leq 0.5\%$
Spectral density	(0.8-4)10^4 ph/s/eV
# photons per shot within FWHM bdw.	$\leq 2.6 \cdot 10^5$
Source rms size	10-30 μm
Source rms divergence	25-200 μrad
Peak brilliance	10^{20} - 10^{23} $\left(\frac{1}{\text{sec}\cdot\text{mm}^2\text{mrad}^2 0.1\%\text{BW}}\right)$
Linear polarization	> 99 %
Energy jitter pulse-to-pulse	< 0.2 %
# photons jitter pulse-to-pulse	≤ 3 %

Table 1: Summary of gamma-ray beam specifications [8].

The shortcoming of the inverse Compton scattering is in the reduced cross section of the process (of the order of 10^{-25} cm^2). As consequence, for the practical reason of producing high-intensity gamma beams, one needs to maximize the number of colliding photons and electrons in a small spatial volume. In the case of ELI-NP this will be achieved by using high quality interaction lasers delivering high brilliance, high repetition light pulses and a low-emittance high-intensity warm radio-frequency (RF) linear electron accelerator. The system will consist of two energy lines: a low-energy line (LE) delivering gamma with energies up to 3.5 MeV and a high-energy line (HE) where the beam energy will reach up to 19.5 MeV. A schematic layout of the GBS in the ELI-NP building is shown in Fig.4; the two energy lines and the main components of the system are marked on the figure.

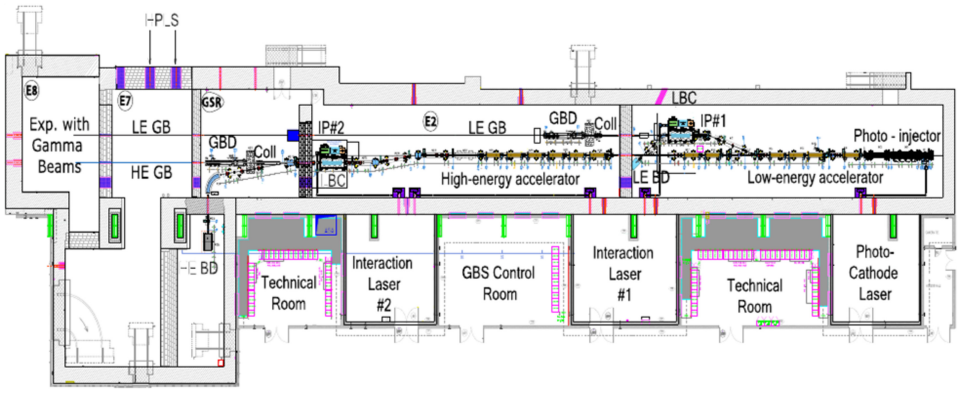

Figure 4: General layout of the ELI-NP Gamma Beam System [9]. The components of the system are marked on the figure (GB=gamma beam, GBD=gamma beam diagnostics, Coll=collimator, IP=interaction point, LBD=laser beam circulator, BD=beam dump). The experimental rooms where the gamma beams will be used are also marked on the figure (E2, GSR, E7, E8).

The main components of the GBS are[9]:

- *The RF linear electron accelerator.* The electron accelerator is a high brightness normal conducting linac consisting of two S-band and twelve C-band RF structures. The main advantage of using a linac accelerator is the excellent emittance of the provided electron beams. The accelerator will be operated at a radiofrequency repetition rate of 100 Hz. For every RF pulse 32 electron microbunches, separated 16 ns, will be accelerated. Every microbunch will have an electrical charge of 250 pC. In this way the effective repetition rate of the electron beam will become 3.2 kHz and the average current of the beam is increased. To achieve this mode of operation a new photo-injector will be designed to operate in multi-bunch mode. The accelerator is designed in two stages, a low-energy one delivering electrons with energies up to 300 MeV and a second one where electrons will reach energies higher than 720 MeV. This two different stages of acceleration are used to produce the two γ energy lines.

- *Interaction lasers.* The interaction lasers are of cryo-cooled Yb:YAG type, operating at 100 Hz and delivering green light pulses (515 nm) with 200 mJ energy. There are two of such interaction lasers. One is used for the low-energy interaction point, while at the high-energy interaction point, to ensure the high spectral density of the gamma beam, both lasers will be used.

- *Laser beam recirculator.* Since electrons are produced every 10 ms in trains of 32 micro-pulses separated at 16 ns one from the other and the interaction lasers will provide pulses every 10 ms there is the need to recirculate the laser pulses 32 times such to bring them to the interaction point for every electron micro-pulse. The very low cross section of the Inverse Compton process ensures that the number of photons in the laser pulses after every interaction will be practically unaltered. This system produces a γ beam consisting of a series of 10 ms spaced macro-pulses each of which contains a train of 32 pulses, 1-2 ps long, separated by 16 ns, as shown in Fig.5.

  To produce a quasi-monochromatic gamma beam the system has to ensure that the collision between the laser light and the electron occurs always at the same incident angle. The recirculator consists of two confocal parabolic mirrors that focus the laser beam at the interaction point and recirculate it parallel to the electron beam axis. To maintain the same crossing angle between the laser beam and the electrons, one has to consider the possibility to switch between interaction planes. This is done with a system of pairs of mirrors. Fig.6 shows a schematic design of the recirculator with the two parabolic mirrors at the extremities of the device and the system of pairs of mirrors in between the parabolic mirrors. The pairs of mirrors are also used for the fine matching of the RF frequency with the round-trip circulation of the laser inside the recirculator. The two parabolic mirrors have holes in the center to allow for the passage of the electron beam.

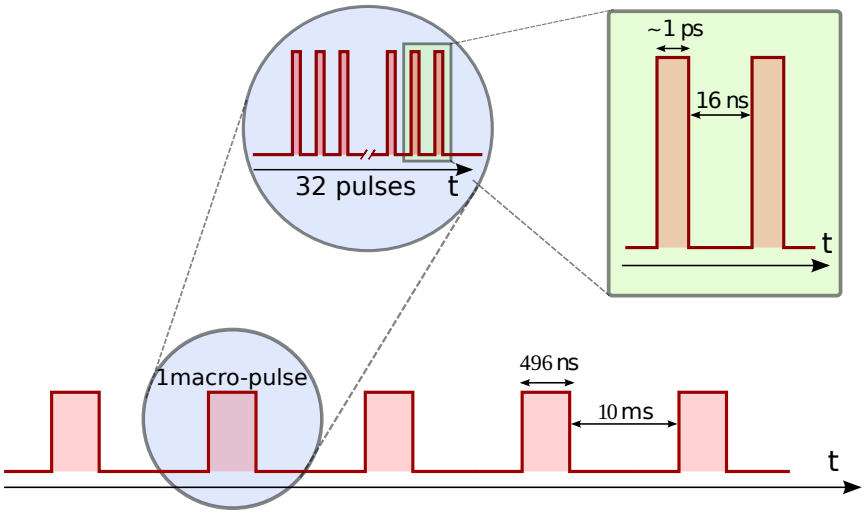

Figure 5: Time structure of ELI-NP gamma beam.

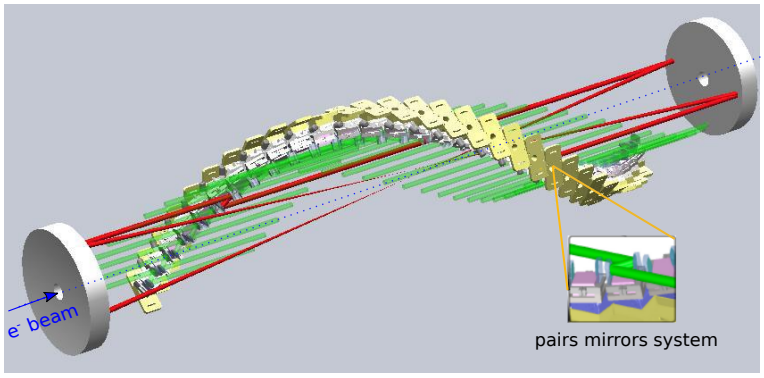

Figure 6: The recirculator geometry for the interaction points of the Gamma Beam System at ELI-NP [8]. At the extremities of the recirculator are placed two confocal parabolic mirrors. The collision angle at the interaction point is maintained with a system of pairs of mirrors as shown in the inset.

- *Gamma beam collimator [10].* The radiation obtained after the inverse Compton scattering process is not intrinsically monochromatic, but the energy is related to the emission angle (see Eq.6): it is maximum along the laser backscattering direction and decreases as the emission angle increases. Therefore the required energy bandwidth can be obtained only by using specific collimation of the gamma beam, i.e. filtering out the radiation emitted at larger angles. A versatile collimation systems was designed for the project with a continuously adjustable circular aperture, from a few hundreds of μrad, down to about 40 μrad to provide the same bandwidth and intensity of the beam for all the gamma beam energies. In addition, the collimation system has to guarantee an effective attenuation of the gamma radiation That requires high atomic number and high density materials and minimum contamination of the downstream experimental area with scattered radiation produced in the interaction of the beam with the collimators.

The final collimator, that has been designed and realized at INFN Ferrara, is shown in Fig.7. As can be seen from the figure, the resulting device is provided by a stack of 14 adjustable linear slits, arranged with a relative rotation around the beam axis, so that the overlap results in a continuously adjustable aperture. Each slit is composed of two $40 \times 40 \times 20$ mm^3 blocks made of a 97% tungsten alloy. The slits are mounted on a high precision stainless steel frame.

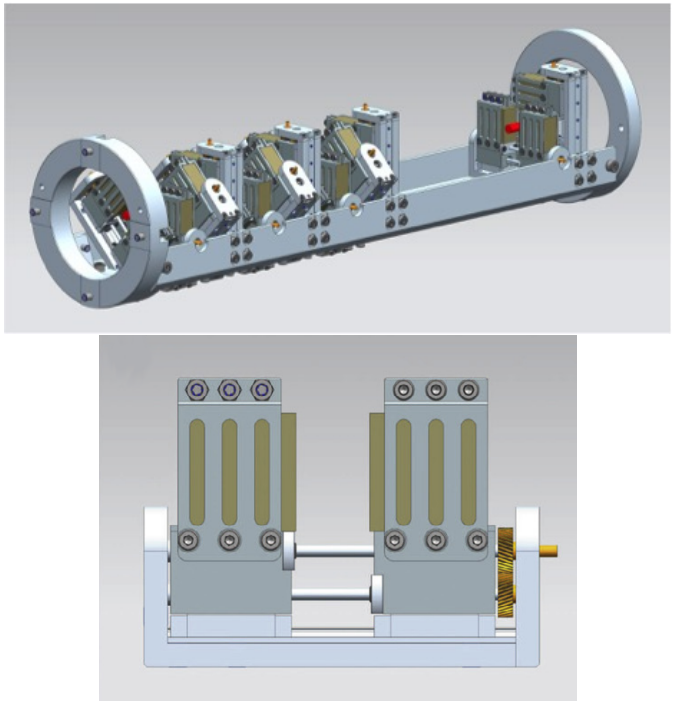

Figure 7: Sketch of the collimation system [11]: the top figure shows the frame housing the 14 slits composing the collimator and the bottom one presents a front view of a single slit.

1.2.3 The physics with ELI-NP γ beam

The scientific program of ELI-NP defined in the White Book [12] is based on the unique features of the high-power laser and gamma beams as discussed in the previous sections. In this section, we will present in particular some of the new research areas at reach and/or that can be revisited using the unique features of the brilliant and monochromatic GBS [9].

Nuclear Resonance Fluorescence (NRF) experiments

Photonuclear reactions below 20 MeV will allow for the study of various nuclear decay modes. Photoinduced nuclear excitations with energies below the particle separation energies will decay exclusively by subsequent re-emission of γ-radiation (see Fig.8). This reaction type is denoted as Nuclear Resonance Fluorescence (NRF). Primary observables of NRF processes are

the energies, intensities, polarizations, and angular intensity distributions of the fluorescent γ-radiation.

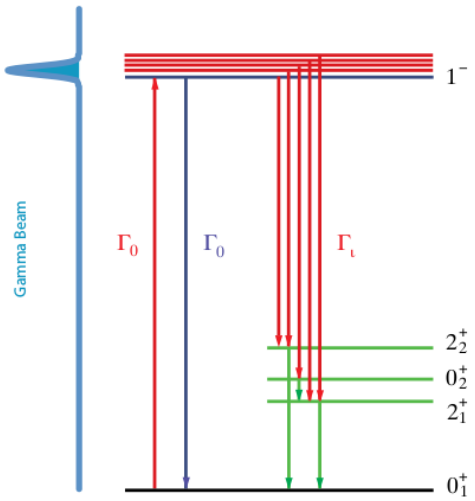

Figure 8: Schematic illustration of the NRF process starting from a $J^\phi = 0^+$ ground state of nucleus with an incoming γ beam of small bandwidth. Figure taken from [13].

The advantage of using electromagnetic probes to study nuclear structure is that the interaction is well-known and one can determine in a model independent way the observables relevant for understanding the nuclear structure. Accurate measurements of the photon scattering cross-sections allow for a model independent determination of radiative widths, and hence reduced transition probabilities and lifetimes.

The superior features of the gamma-ray beams such as tunability over a wide range of energies, narrow bandwidth, high spectral density, and high degree of linear polarization, make ELI-NP a unique facility to investigate challenging problems in nuclear physics and NRF is one of the main tools proposed to be used (see [13] for a detailed description).

Features of the GBS such as high brilliance and small transversal diameter will provide an increase in sensitivity of the measurements leading to a drastic reduction of the material quantities required for the construction of the targets. This opens the possibility to study rare nuclei available in nature in very limited quantities such as the p-nuclei; there are 35 known p-nuclei and at ELI-NP it will become possible to study their dipole response. Actinide nuclei due to their natural activity are difficult to use in large quantities because of radioprotection regulations and the generation of large radiation background that blinds the γ-ray detectors; their study will become possible at ELI-NP.

The NRF can be used also as an attractive non-destructive analysis method because it provides signatures for a wide variety of materials that can be used to characterize the irradiated samples. For this reason the NRF

scattering is becoming a fundamental tool in fields related to homeland security and nuclear waste management [14]. The general setup employed in the scattering NRF experiments is illustrated in Fig.9. Here the investigated object is placed in the beam and the resonant photons are detected in a backscattered geometry by a detector located off-beam. Except the resonant photons, all other scattered photons have lower energy due to the nature of Compton scattering. The high-energy resonant photons are therefore easily distinguished.

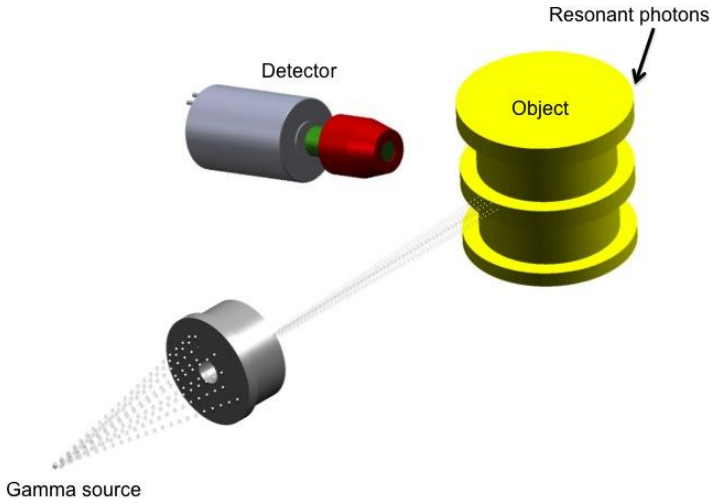

Figure 9: Schematic view of the backscattering NRF setup [14].

Photofission experiments

Photofission is a process in which a nucleus, after absorbing a gamma ray, undergoes nuclear fission. The photofission experimental program [15] at ELI-NP will address investigations of the fission potential-barrier landscape in the actinide nuclei. The experiments will address studies of angular mass and charge distributions of fission fragments and measurements of absolute photofission cross sections. Rare photofission events, such as high-asymmetric fission or ternary fission will be investigated, too [15].

Studies of neutron-rich nuclei are the main topic of recent nuclear structure research. Beams of such nuclei are produced with the isotope-separation on-line (ISOL) technique, or with the in-flight separation technique in projectile fragmentation. In both cases, the nuclei of interest are transported away from their production site, where a large background from nuclear reactions exists, to a well-shielded experimental set-ups, where different nuclear observables can be measured. The low yield of the isotopes of interest is a major shortcoming of the in-flight method, while not all elements can be extracted from an ISOL target due to the long diffusion times of many of them. Photofission provides another possibility to create exotic nuclei in the laboratory.

Nuclear collective excitation modes

The NRF method will provide important information about the nuclear structure of the irradiated nuclei allowing for the study of their dipole response. Electric dipole strength in the energy range of about 5-9 MeV is often denoted as Pygmy Dipole Resonance (PDR). A common macroscopic interpretation of this strength is as an oscillation of a neutron-skin versus a proton-neutron core. The PDR then would open a window to the determination of the neutron-skin thickness, and would potentially have impact on astrophysical scenarios, such as rapid neutron capture rates. The PDR and the complete E1 response of a nucleus can in addition constrain the symmetry energy parameter in the nuclear equation of state.

However, E1 excitation strength due to such an effect would be superimposed on the low-energy tail of the Giant Dipole Resonance (GDR), as can be seen in Fig.10; in addition, the parameterization of the GDR tail is under debate. The GDR is a dipole oscillation of the protons against the neutrons.

An important question in this respect is the amount of branching transitions from dipole excited states in the PDR region to lower-lying excited states. Such low energy γ-decay branches are difficult to observe but, thanks to the high brilliance of the GBS, selection of either individual excited states, or very narrow averaging bins can be achieved, revealing information on the fine structure of the E1 strength distribution at PDR energies [16].

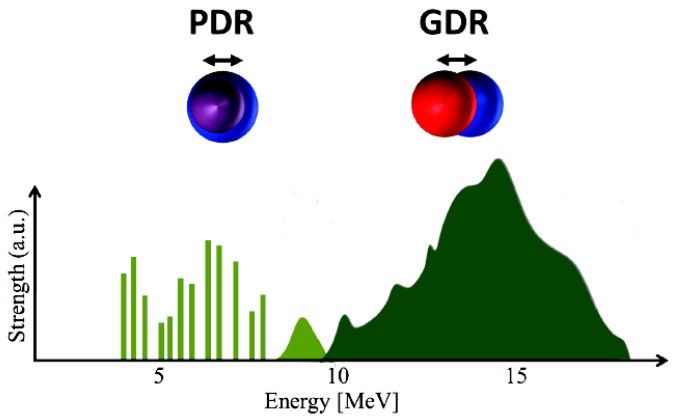

Figure 10: Schematic distribution of E1 strength in an atomic nucleus showing the splitting into a Pygmy Dipole Resonance (PDR) and a Giant Dipole Resonance (GDR) [13]. Octupole-coupled modes which can generate E1 strength at even lower energies are not included.

Nuclear astrophysics studies

Astrophysics is one of the main research topics at ELI-NP, many of its subtopics being tackled in several research programs for the experimental areas for laser-based, gamma-based, and combined laser-gamma based experiments [9]. Using the characteristics of the gamma radiation beam, it will be possible

to perform accurate measurements of cross sections of nuclear reactions relevant for stellar burning processes [17]. Indeed the γ-induced nuclear reactions were extensively studied in the past, but still they are a challenge for the experimental and theoretical physicists. The difficulty arises due to the very small cross-sections; therefore, only a very intense γ beam can be used for such investigations. The idea is to use the principle of detailed balance which stated that the cross-section of an (p,γ) process can be obtained from the measurement of the time inverse (γ,p) reaction with γ-ray beams. Indeed, measuring capture reactions by means of the inverse photodisintegration reactions, has the advantage of having different systematic uncertainties than those of characteristic charged particle induced reactions measured at low energies of astrophysical interest, thus allowing to resolve conflicting data. In particular, nuclear astrophysics, needs highly accurate measurements of cross sections for nuclear reactions of the H and He burning processes in order to enhance the reliability of stellar evolution models and simulations.

2 GAMMA BEAM CHARACTERISATION SYSTEM

The ELI-NP gamma beam system (GBS) will provide photon beams with continuously adjustable energy ranging from 0.2 to 19.5 MeV and a relative energy bandwidth of 0.5%, obtained by collimating the photons emerging from the Compton interaction region as previously described in Sec.1.2.2. A precise energy calibration of the gamma beam and the monitoring of the stability of its parameters, as well as a fast feedback on the energy distribution, intensity and shape profile of the beam, are essential for the commissioning and development of the source. Furthermore, during standard operation, the ELI-NP-GBS will need a monitoring system of these parameters for routine diagnostic of the delivered beam. Given the unprecedented characteristics of the beam, these tasks are extremely challenging. For these reasons a dedicated detectors system, named Gamma Beam Characterization System [8, 18], has been designed. This apparatus is a result of the collaboration of the INFN units of Ferrara, Firenze and Catania.

As previously described in Sec.1.2.2, the GBS will consist of two parallel beamlines, with γ of different energies and separated interaction points (IPs). For each IP a complete collimation and gamma beam characterization systems will be realized as displayed in Fig.11. The two systems are almost identical except for few differences solutions optimized to cover the two different energy ranges.

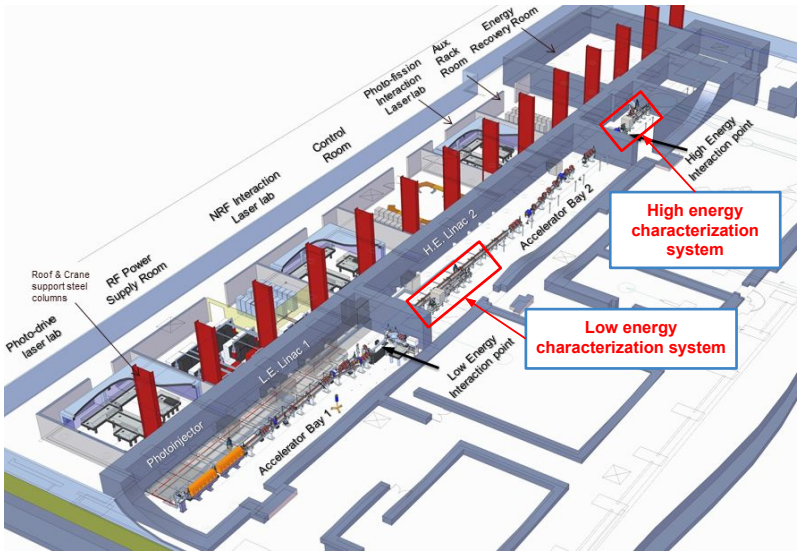

Figure 11: Isometric 3D view of building layout shown the relative position of the two characterization systems with respect to the Accelerator Hall & Experimental Areas.

In the next sections we will describe the design and the tests carried out on the detectors which are being realized for the characterization of the low energy beamline. In fact, the low energy line is the first that will be realized.

2.1 CHARACTERISATION SYSTEM OVERVIEW

In order to verify the performance of the gamma beam system, the required energy resolution on the energy measurement has to be compatible with the expected bandwidth of 0.5% within an energy range between 0.2 and 20 MeV. The system must be able to cope with pulses of 2.6×10^5 photons with a duration of 1-2 ps, separated by 16 ns.

While in the commissioning and calibration phases destructive measurements can be performed, during the routine operation of the source the performance monitoring should have a negligible impact on the beam to avoid affecting downstream applications.

Considering the measurement of the energy distribution, the ultra-short duration of a gamma pulse and the high intensity makes impossible to easily resolve the response of a single photon by using any traditional gamma spectroscopy detector directly exposed to the beam line.

A possible solution for the performance monitoring is to use Compton scattered radiation from a single photon interaction in a thin target to evaluate the energy of incident photons. In fact, by measuring precisely the energy and position of the scattered electrons with respect to the primary beam direction it is possible to retrieve the energy of a single interacting photon for each macro-pulse. The need to use detectors with high energy resolution prevents to perform this measurement on a time scale smaller than the macro-pulse length. The advantage of such technique is the negligible interference with the primary beam: the system can be optimized in order to have in average only one photon at maximum interacting in the target, making it an ideal tool for the beam energy monitoring. The beam energy distribution can then be determined, performing a suitably large amount of such measurements.

The complementary approach consists in performing a measurement of the total beam energy by absorbing the gamma pulses in a longitudinally segmented calorimeter. The advantage of this approach is that the full photon statistics can be exploited and, since fast detectors can be used, a measurement can be performed for every single pulse although with reduce significance. Though, being a destructive measurement, this technique is not compatible with any downstream application. It will be fundamental during the gamma beam system commissioning and tuning to provide an immediate feedback on the beam energy, its relative intensity and their variations within a macro-pulse.

The proposed solution is to use the combination of the measurements performed by a Compton Spectrometer (CSPEC) and by an absorption calorimeter (GCAL) to fully characterize the gamma beam energy dis-

tribution and intensity with the precision necessary to demonstrate the achievement of the required parameters.

The characterization system includes also an absolute energy calibration apparatus (NRSS). Using appropriate targets, the detection of resonant scattering condition during a fine beam energy scan attests the beam energy very precisely, providing accurate reference energies for calibrating the other subsystems.

Finally, to evaluate the spatial distribution of the beam a profile imager (GPI) is implemented. For this purpose, a detector based on a scintillator target optically coupled to a CCD camera is employed.

Fig.12 shows the four detectors of the Gamma Beam Characterisation system.

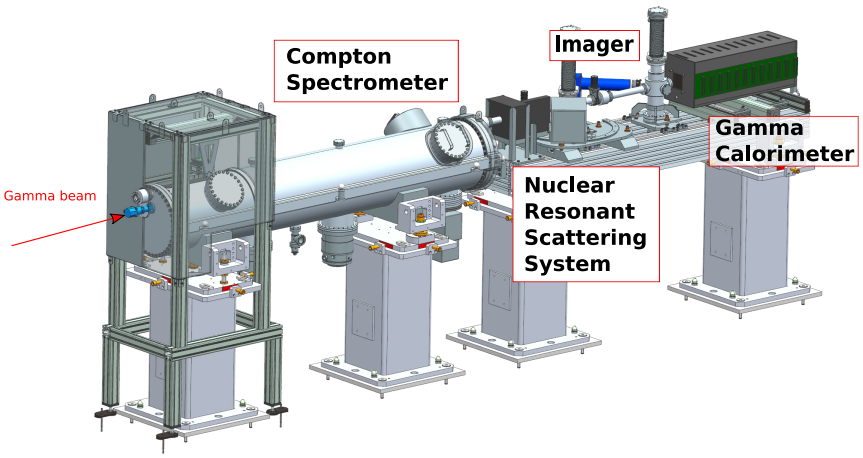

Figure 12: Overview of the Gamma Beam Characterization system and of its four detectors.

An overview of the NRSS and GPI subsystem will be given in the next sections. The Compton Spectrometer and the Gamma calorimeter, which are under construction at the INFN Firenze and are the subject of my PhD thesis, will be presented in detail in Chap.3 and Chap.5.

2.2 MONTE CARLO SIMULATIONS OF ELI-NP-GBS

To study the effects related to the beam energy and spatial distributions on the detectors of the characterization system a dedicated Geant4 [19, 20] simulation has been developed [10, 11]. It provides a realistic representation of the γ beams as well as the background reaching the detectors. The transport of the gamma beam has been simulated from the IP to the experimental area downstream the collimation system, including vacuum pipes and chambers, walls, floor, ceiling and additional shielding. The gamma beam is obtained by accelerating and transporting a realistic electron beam to the IP where its interaction with the laser beam occurs. In addition very accurate models of the collimation system has been implemented, as shown in Fig.13.

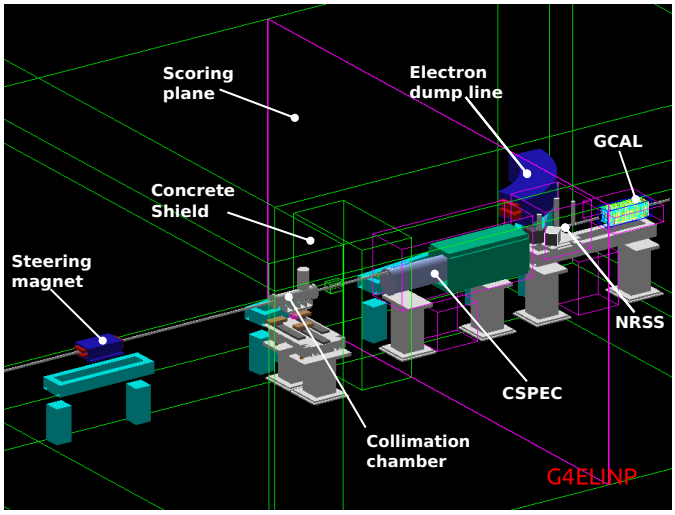

Figure 13: Sketch of the high energy (HE) beam-line of ELI-NP-GBS [11].

The electron transport is simulated by using the codes TSTEP, as described in detail in [21]. The simulation of the interaction between the electron beam and the laser pulse at the interaction point is performed by means of the Monte Carlo (MC) code CAIN [22]. This code generates a complete phase space of the gamma emission that is used as the source file for the simulation of the gamma beamline.
The used physics lists are: G4EmStandardPhysics_option4, G4HadronPhysicsQGSP_BIC_HP and G4HadronElasticPhysicsHP, with cuts set to 1 μm for all the volumes. Starting from the output provided by CAIN, the phase-space of the particles entering the envelope box of each detector (plotted in pink in the Fig.13) system has been produced with the statistics of 1 macro-pulse.

2.2.1 Simulation of the background radiation

In order to study the expected background on the characterization system detectors, the radiation in the proximity of the collimator has been evaluated. In fact, the characterisation system will be placed downstream the collimation system and before the experimental area. It was found that in order to avoid the contamination of the area with secondary radiation a block of concrete is necessary. The block will be located right after the collimation system before the gamma diagnostic area (as shown on Fig.13) and will have a hole to allow the crossing of the primary beam.

According to the simulations the radiation reaching the area behind the concrete wall is mainly composed of gammas with little particles component such as $e^{\pm}$ or n (see Sec.6.2.5). The energy and spatial distribution of this remaining background component is shown on Fig.14 for a 5 MeV gamma beam. The embedded surface plot shows the spatial distribution of the background radiation. This plot represent an upper limits for the expected one at the LE γ beam.

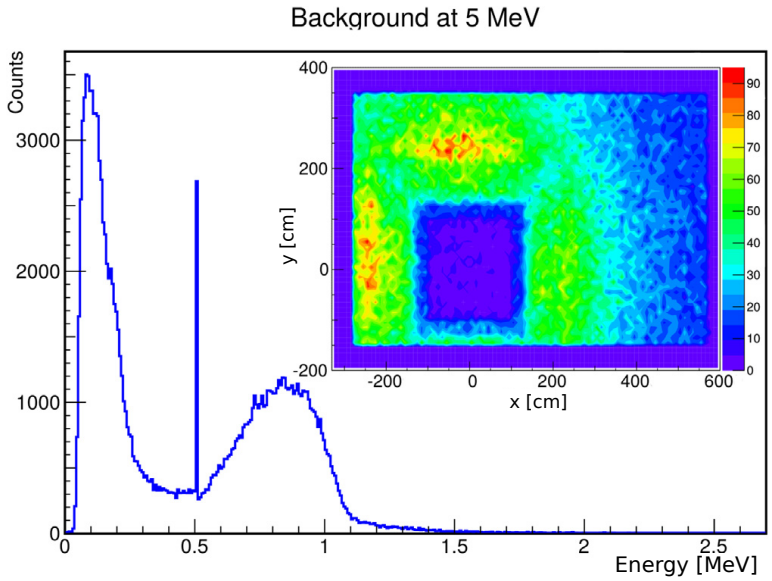

Figure 14: Background radiation. The scoring surface area correspond to the entire room cross-section on the xy plane downstream the concrete-block shielding[10].

This residual background radiation can be distinguished mainly in two different types:

1. The first component is due to photon not absorbed by the collimator. They have random directions, due to multiple scatterings on the concrete walls of the room and low energy. They mainly enter in the detector from the lateral directions and arrives delayed with respect to the beam particles.

2. The second component is directly related to the γ beam. In fact these "beam-like" γ are due to beam scattering on the edges of the collimators, so they have the same direction of the beam and a similar energy. They arrive in time with the γ beam.

2.3 NUCLEAR RESONANT SCATTERING SYSTEM (NRSS)

The nuclear resonant scattering system [23, 24] will be used to perform an absolute energy calibration of both CSPEC and GCAL, with an accuracy better than 0.1%, as well as to perform a redundant beam energy measurement.
The basic idea of this device is to detect the gamma decays, of properly selected nuclear excited levels when resonant conditions with the beam energy are achieved. Nuclear resonant scattering is a process consisting in the absorption of a gamma photon (γ) by a nucleus (X), followed by its

de-excitation with the emission of one or more photons (γ_r), according to the decay sequence of the nuclear level:

$$\gamma + X \rightarrow X^* \rightarrow \gamma_r + X \tag{8}$$

The energy positions E_r of the selected levels have been previously reported with high precision in the literature. By varying the γ-beam energy, a re-emission of gamma particles will be generated at the resonant condition. The calibration correspondence is then achieved at γ-beam energy $E = E_r$, with an uncertainty mainly determined by the step-size in the beam energy scan. The nuclear levels candidates for the calibration procedure can be searched in light stable isotopes, where usually low lying levels are highly spaced. Table 2 reports a list of levels that will be used for the low and high energy lines calibration.

^{A}X	E_r(MeV)	ΔE_r(MeV)	Γ(MeV)
^{6}Li	3.56288	$1.0 \cdot 10^{-4}$	$8.2 \cdot 10^{-6}$
^{11}B	2.124693	$2.7 \cdot 10^{-5}$	$1.17 \cdot 10^{-7}$
^{11}B	4.44498	$7 \cdot 10^{-5}$	$5.5 \cdot 10^{-7}$
^{11}B	8.92047	$1.1 \cdot 10^{-4}$	$4.374 \cdot 10^{-6}$
^{12}C	4.43891	$3.1 \cdot 10^{-4}$	$1.08 \cdot 10^{-8}$
^{12}C	15.110	$3 \cdot 10^{-3}$	$4.36 \cdot 10^{-5}$
^{27}Al	2.21201	$10 \cdot 10^{-5}$	$1.71 \cdot 10^{-8}$
^{27}Al	2.98200	$5 \cdot 10^{-5}$	$1.15 \cdot 10^{-7}$

Table 2: Examples of nuclear levels that will be used during the NRS calibration procedure [25].

A γ counter will be used to check, during an energy scan, whenever the beam overlaps the resonance level of the target material. The counting rate can be calculated by using the integrated cross-section:

$$\sigma_{int} = \int \sigma(E)dE = \sigma^0_{max}\Gamma\pi/2$$

where σ^0_{max} is the resonant cross section at E=E_r.

The detection setup has been designed in order to measure nuclear resonance scattering from γ-beam photons at backward angles (around θ=135°) with respect to the beam direction, as shown on Fig.15. This angular condition is important in order to reduce the background contribution coming from the photon Compton scattered on the target.

The mechanical design, presented on Fig.15, is mainly composed by three parts: the scattering chamber, the target holder and the γ-detector, which is placed outside the vacuum line.

The γ detector has been designed to work in two different modes:

- Fast Counter Mode (FC): allows a fast beam energy scan, giving prompt information about the establishment of a resonance condition.
- Energy Spectrum Mode (ES): permits the precise identification of the resonant level through the measurement of the energy of the emitted de-excitation photon.

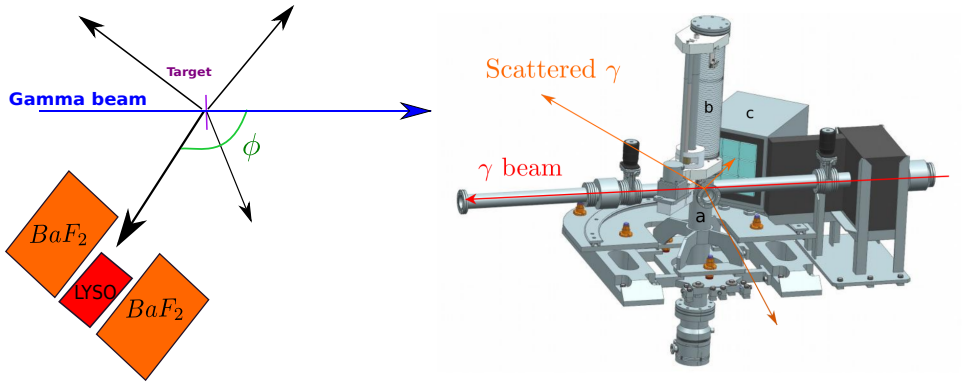

Figure 15: Left figure shows a schematic representation of the NRSS. The right one presents the layout of the NRSS: a) the scattering chamber; b) the vertical target shifter; c) the scintillators crystal for the γ detector.

The detector consists of a Lutetium-yttrium oxyorthosilicate (LYSO) crystal, coupled with a photomultiplier with a super Bialkaly Photocathode, surrounded by an ensemble of BaF_2 scintillators. These act both as fast counters for the FC mode and as Compton shield for the ES mode; while the LYSO provides the energy of the γ. Fig.16 shows the assembled γ detector for the low-energy line. In this configuration a LYSO crystal of $3{\times}3{\times}6$ cm^3 is surrounded by four BaF_2 counters ($5{\times}5{\times}8$ cm^3). The detector for the high energy line will have the same conceptual design with some differences consisting in a larger number of BaF_2 counters (from 4 to 8) with increased length (from 8 to 11 cm) and in a bigger LYSO crystal (from 3 to 5 cm).

BaF_2 crystals have been chosen for their fast scintillating component ($\tau \sim$ 0.6-0.8 ns peaked at 220 nm) extremely suitable for fast counting and timing purposes. They have also a much slower component signal at 310 nm. In order to select the BaF_2 fast scintillation component, a Cs-Te photo-cathode coupled with a Quarts window will be used.

The LYSO scintillator offers high density and light yield, which is important to have a high photo-peak counting to total counting ratio (PtT) and a good energy resolution. In addition it has a quite short decay time ($\tau \sim 45$ ns).

Detailed background studies, have been performed using the dedicated Geant4 simulation presented on Sec.2.2. From these studies emerges that two are the background sources which interfere with the NRSS operations: gamma beam environmental background and target processes competing with the resonant scattering (like the Compton scattering). In Fig.17 is shown the time distribution of the different background sources arriving at the detector as obtained from the MC simulation. In green is plotted the background environmental, in black the beam-like photons, due to the beam scattering on collimators and in red the photons back-scattered from the target. Most of the environmental background will hit a lead shielding surrounding the scintillators. The beam-like photons (with the same energy of signal gammas at resonance conditions) reach the NRSS system out of time with respect to the resonant ones and can then be rejected thanks to the excellent time resolution of the system. The most challenging background

Figure 16: A photo of the NRSS γ detector for the LE line. The central LYSO crystal, surrounded by the four BaF_2 scintillators, is embedded in a lead shielding box.

source is hence generated by the photons back-scattered from the target, that arrive in time with the resonant scattered gamma (about 50 ns after the γ beam crossing). This due to the fact that both the scattered and the signal photons travel the same path from the target to the detector.

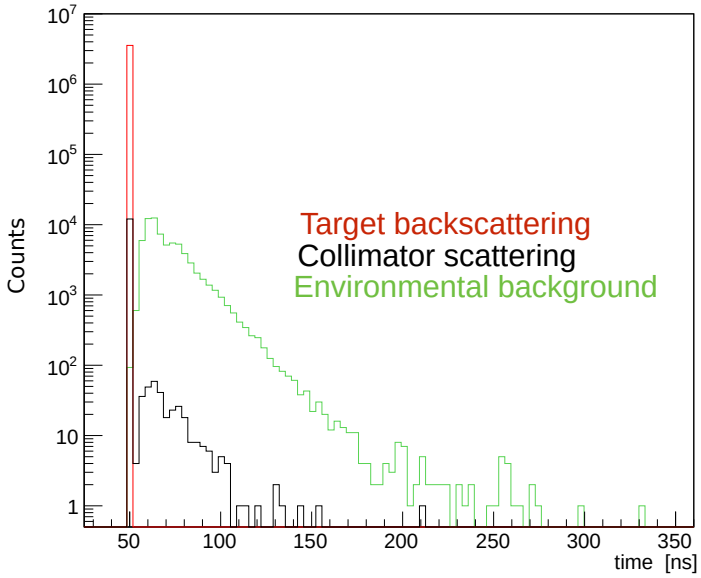

Figure 17: Distribution of the time of arrive of the background particle on the BaF_2 crystals. The NRSS signal (not shown in the figure) will be detected about 50 ns after the γ beam crossing, at the same time of the Compton scattered γ.

The energy spectra of the described background components that are detected by the BaF_2 crystals in time with the resonant γ is shown on Fig.18. The main in time background contribution, that cannot be shielded nor rejected using scintillation information only, is due to the target Compton

back-scattered γs. As can be seen from the figure, this background source at the detector angle of 135° populates the energy region below 500 keV.

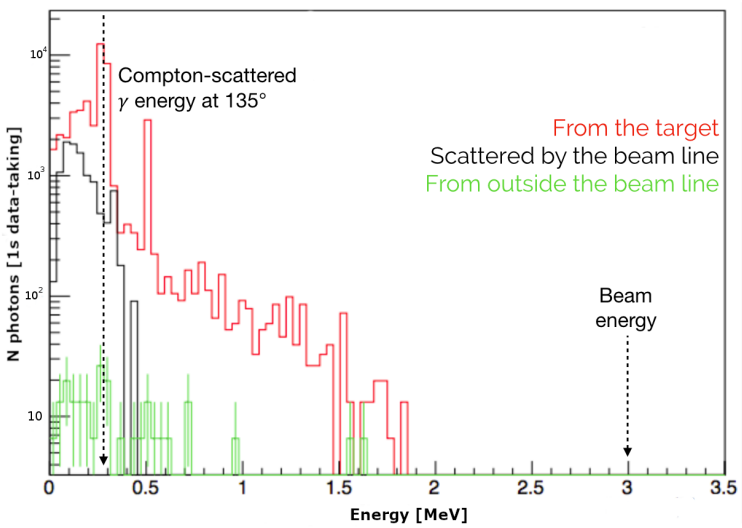

Figure 18: In time background for a 3 MeV beam on a 0.25 mm thick Al target

The pile-up rising from the big amount of Compton back-scattered photons makes impossible to rely on an energy-only rejection. For this reason a peculiar technique based on dual readout of Cherenkov and scintillation light has been developed. It consists in discrimination between the low Cherenkov emission of pile-up background from the larger one generated by the resonance signals. The power of this method has been investigated with the help of MC simulations, in Fig.19 are shown the expected energy distribution relatives to only the background component (red) and to both the signal and the background components (blue). From the figure, it can be noticed that the background component is highly suppressed using a Cherenkov selection cut, without reducing the signal.

The NRSS has a fundamental role in giving an energy reference to the whole beam characterization system, through an *inter-calibration procedure*. The calibration procedure starts with the optimization of the timing setting, which is performed by using the detector in the FC Mode and by choosing an high-Z target to increase the interaction rate. In this way it will be possible to establish the correct delay time between the beam trigger and the acquisition of the detector signal. Once the timing procedure has been completed, one has to insert one of the NRS calibration targets. Then a scan in the electron beam energy is performed in order to vary the beam energy and find the resonance condition. Once the resonance condition has been established, the detector will be operated in ES Mode with the BaF_2 crystals acting as a Compton shield for the spectrometer. The electron energy is then changed by a small amount to obtain a γ slightly outside the resonant region in order to evaluate the background spectrum. Finally, once the energy resonance condition is obtained, the cross calibration of the CSPEC and of the GCAL can be done.

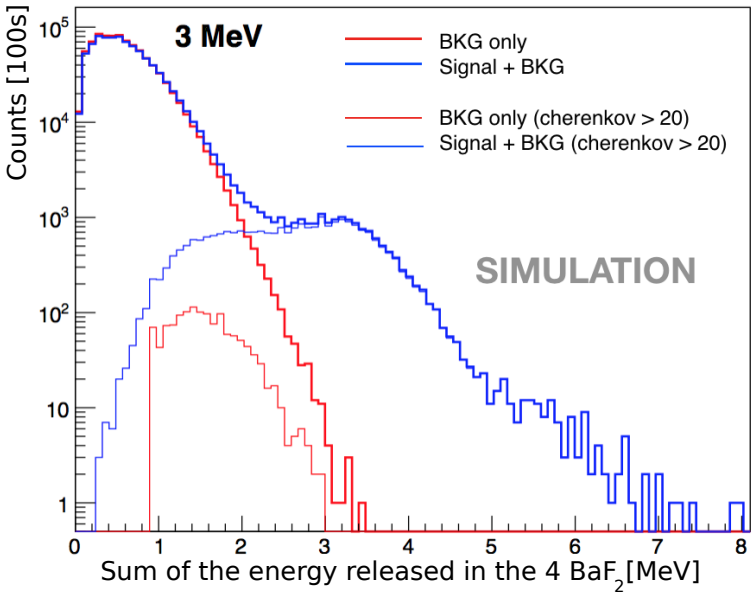

Figure 19: Energy distribution for background and signal-background distributions with and without cut on Cherenkov light.

2.4 PROFILE IMAGER (GPI)

The task of the gamma beam profile imager [26] is to provide an image of the gamma spatial distribution to display the position of the beam. This image is crucial in giving informations on the alignment of the collimation system and on the correct positioning of the other detectors, as well as to control the size and the shape of the γ beam. The designed collimation system will produce beams with an octagonal shape [11]. The GPI will be placed at a distance of 15.2 m (HE line) and 16.3 m (LE line) from the Interaction Point (IP). This implies that the typical size of the beams will vary between about 1 to 11 mm (octagon's apothem), depending on the selected energy and bandwidth. The spatial resolution of the system, will have reasonably to be at least 100 μm. The GPI must image gamma beams with variable size and brilliance, it has to provide an image of the average spatial distribution of the gamma beam in a time of the order of 1 s and to work in vacuum. The adopted solution is shown in Fig.20. The imager is made by a vacuum chamber placed in the beamline and hosting a tilted scintillator crystal, crossed by the gamma beam at an angle of 45°, and hosted in a target holder which supports interchangeable targets. Outside the chamber in air, looking at the target through a quartz viewport, is placed a CCD camera coupled with a lens system to focus the scintillator light. A mirror reflects downwards to the camera the light coming out from the vacuum window. The CCD is mounted on a remotely controlled linear stage for fine focus adjustment. The entire system is enclosed in a dark box to avoid background signals due to environmental light.

The choice of the target material and thickness is the result of a trade-off between conflicting requirements and has been carried out through a set of

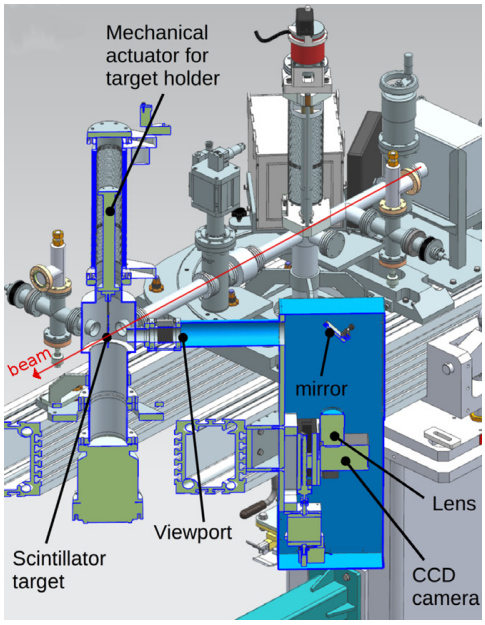

Figure 20: Layout of the GPI detector with the display of a cross-section to show the inner parts of the detector.

Monte Carlo simulations. In order to have a significant image in a reasonable time the used target should have a good conversion efficiency and therefore a high density, high-Z, and feature a good light yield. Moreover, the efficiency is strongly dependent on the target thickness, but the thickness can not be increased arbitrarily without loosing resolution. Fig.21 shows the light emission obtained with the MC from various scintillator materials of different thickness in the case of a 3 MeV beam. As can be seen, LYSO resulted the material producing more light and therefore it was chosen as the target of the GPI.

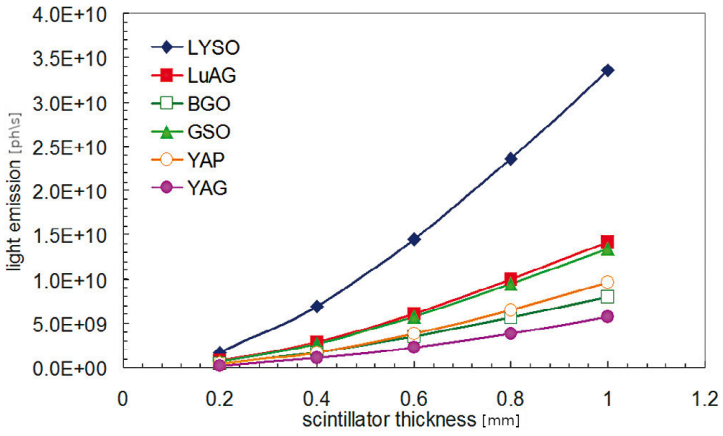

Figure 21: Light emission from various crystals as a function of thickness for a 3 MeV gamma beam obtained from MC simulation.

From thicker crystals more light can be collected; however, this leads to a degradation of the achievable image resolution. This is due to the fact that the gamma beam intersects the target at an angle of 45° and the CCD

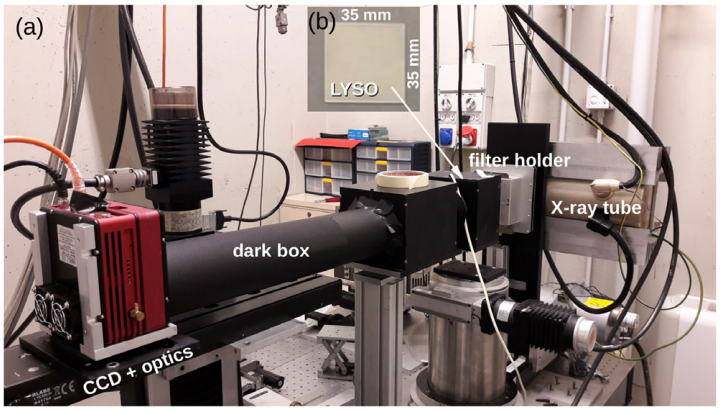

Figure 22: (a) Picture of the experimental set-up used to test the GPI prototype. (b) Picture of the LYSO scintillator crystal.

camera is placed at 90°. If the target thickness increases, its projection on the imaging plane becomes comparable with the resolution of the CCD, resulting in an horizontal blur in the image. The intrinsic resolution of the imaging system (lens + CCD) was measured by irradiating frontally the LYSO crystal with X-rays from an X-ray tube and resulted to be between 80 μm and 140 μm. Therefore, for scintillators thicker than few hundreds of microns, the blur due to the tilted irradiation is the resolution limiting factor. For this reason, the GPI target holder will host a set of crystals with thickness between 100 μm and 500 μm, allowing to suit the image requirements of higher efficiency or higher resolution depending on the ongoing experimental activity.

The radiation hardness of LYSO, compared to the average dose released by ELI-NP-GBS working at the nominal conditions, allows a continuous irradiation for several days without a significant degradation of performance. Therefore, considering the small fraction of time in which the target will be exposed to the beam during a routine use, it is possible to conclude that the degradation of performance due to radiation damage is not critical for several months of usage.

To predict the system response an analytical model has been developed with the main goal of working out an expression for the signal expected on the CCD as a function of the system configuration. This model was validated by carrying out a set of experimental tests on a prototype. This prototype was assembled and tested at INFN Ferrara laboratory using the photon beam from a Varian M-143T X-ray tube. The X-ray tube is powered by a high-frequency 50 kHz, high voltage generator, Compact Mammo-HF with an adjustable voltage from 20 to 49 kV. The used experimental set-up is shown in Fig.22. A 0.5 mm thick LYSO scintillator, shown also in Fig.22 (b), was positioned in a dark box at a distance of about 200 mm from the X-ray tube. The light emitted by the scintillator was focused through a Nikon Nikkor AF 85 mm/f1.4 D IF photographic lens onto a Diffraction Limited SBIG STT-8300M CCD camera, the scintillator-to-lens distance was set to 667 mm.

The comparison of the CCD signals with the MC has provided the tuning of the parameters of the model. Then, it has been possible to predict the expected signal with the ELI-NP-GBS beam through simulations. The energy deposition inside the LYSO crystal the γ beams of various energy was evaluated through a set of MC simulations using Geant4 and the signal on the CCD was simulated using the obtained model. The expected average signal on CCD images for the ELI-NP-GBS as a function of the gamma beam energy is reported in Table.3. The signal is expressed in average Gray Level (GL) per second of a pixel of the image, that can be written as:

$$\mathrm{GL} = \frac{E_{dep} Y \epsilon \mathrm{T} c_f \Delta_{CCD}^2}{\mathrm{Am}^2}$$

where E_{dep} is the energy deposited in the unit of time by the gamma beam in a region of the scintillator of area A, ϵ and T are the collection efficiency and the transmission factor of the optic respectively, c_f is the gray level per incident photon n, Δ_{CCD} is the length of CCD pixel side and m is the magnification ratio of the system, namely the ratio between image size and object size (in this case, the scintillation spot).

Beam energy [MeV]	**Signal (GL/s)**
0.2	305
3	2165
10	24321
19.5	51400

Table 3: Expected CCD signal for different energies of the ELI-NP gamma beam.

The expected image on the CCD was also simulated. A dedicated paraxial ray-tracing code was developed [26]. Starting from the simulated energy deposition distribution, a number of optical photons were generated randomly inside the scintillator and tracked to the optic and the CCD. The obtained image for a 3 MeV γ beam is displayed in Fig.23.

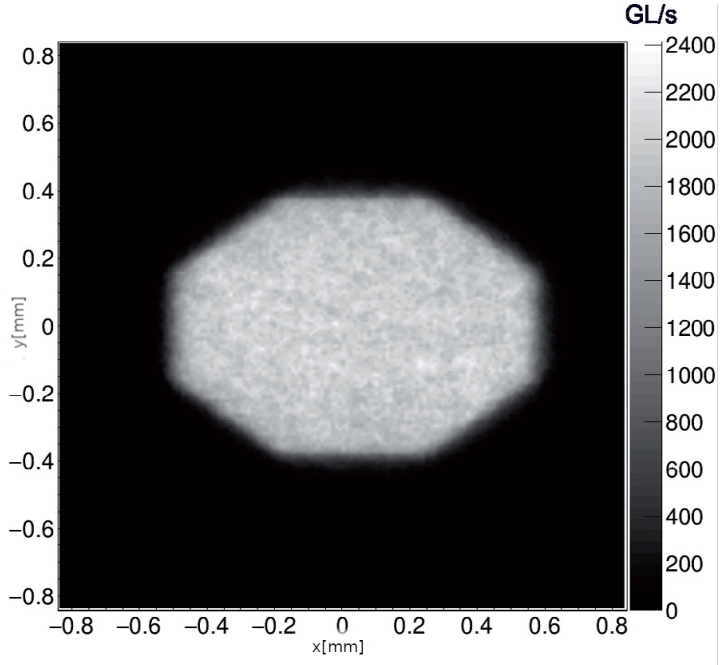

Figure 23: Simulated image on the CCD for a 3 MeV ELI-NP gamma beam.

3 COMPTON SPECTROMETER (CSPEC)

The aim of the Compton spectrometer is to reconstruct the energy spectrum of the γ beam with a non-destructive method, suitable for beam characterisation both during the commissioning phase and also for beam monitoring during routine operations of the ELI-NP facility.

3.1 WORKING PRINCIPLE

The basic idea is to measure the energy and position of electrons recoiling at small angles from Compton interactions of the γ beam on a thin target. The ELI beam energy (E_{beam}) is then obtained according to Eq.9:

$$E_{beam} = \frac{m_e \cdot T_e}{\cos(\theta)\sqrt{T_e \cdot (T_e + 2m_e)} - T_e} \tag{9}$$

where T_e, θ and m_e are the electron kinetic energy, scattering angle and mass, respectively.

A high purity germanium detector (HPGe) will be used to precisely measure T_e, while a double sided silicon strip detector will determine the impact point of the e^- on the detector, hence θ, since the spatial configuration is well known. This two detectors will be located inside a vacuum chamber, together with the target, and positioned as close as possible to the gamma beam.

The recoil photon is detected outside the vacuum by BaF_2 crystals, whose fast response in coincidence with the HPGe signal will provide the trigger of the system.

The main components and the working principle of the spectrometer are illustrated in Fig.24. The reasons and the studies that led to the choice of these detectors, their positions and dimensions will be presented in the following chapter (Sec.3.2). The Monte Carlo simulation of the detector is presented in Sec.3.3, giving highlights of the expected performances of the detector in terms of energy reconstruction and signal identification. Finally the detail of the final chosen detectors will be provided in Sec.3.4.

3.2 DETECTOR DESIGN OPTIMIZATION

A key parameter of the Compton spectrometer, to obtain the required resolution on the beam energy, is the high-resolution of the electron detector. A HPGe detector has been chosen for its well known properties of both excellent energy resolution and high efficiency. The HPGe detectors signal collection times are of the order of several hundred ns. Therefore the time

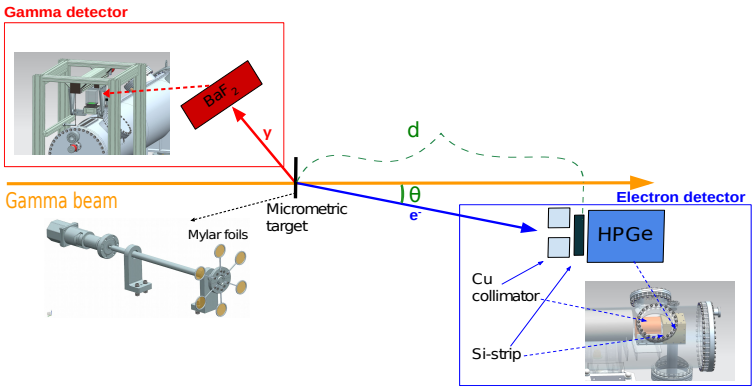

Figure 24: Schematic view of the Compton spectrometer.

needed to perform a measurement is of the same order of magnitude of a macro-pulse length (496 ns) and any pile-up occurring in this time window would spoil the measurement. This imply that the expected signal rate at detector cannot be larger than the macro-pulse repetition rate (100 Hz). This result can be obtained using a target for Compton scattering with very small thickness δ. In fact, the number of produced electrons per macro-pulse N_{eMP} is directly proportional to δ as can be seen from Eq.10:

$$N_{eMP} = N_{\gamma MP} \cdot \sigma_{Compton} \cdot \alpha \rho N_A \frac{Z}{A} \cdot \delta \sim 1 \tag{10}$$

where $N_{\gamma MP} \sim 3.2 \cdot 10^6$ is the number of impinging photons per macro-pulse, the electron density $\rho N_A \frac{Z}{A}$ is $4.4{\times}10^{23}$ cm^{-3} for a Mylar target, and the Compton electronic cross section $\sigma_{Compton}$ ($\sim$ 150 to 30 mb from 2 to 20 MeV) has to be multiplied by a realistic detector acceptance $\alpha \sim 1\%$. From this simple calculation we get $\delta \sim 3 - 16\,\mu$m. This is indeed an advantage, since such a micrometric target is almost transparent for the beam, and minimizes the multiple scattering of the emerging electron.

To enhance the full energy peak of the measured electrons, while reducing pile-up, only particles entering the inner part of the Germanium detector can be selected using a copper collimator placed in front of the detector.

The angle of the e^- detection with respect to the beam direction ideally should be the minimum allowed by the detector size, for several reasons. The sensitivity of the reconstructed gamma energy to electron polar angle, whose knowledge is limited by the beam size and the multiple scattering inside the target, is minimal. At small recoil angles, the electron carries most of the incident photon energy reducing the error on the measured angle due to multiple scattering that is inversely proportional to the electron momentum. Furthermore, the purity of signals is maximal at the lowest possible angle for any energy between 1 and 20 MeV. The purity of the signals, defined as the fraction of signals in the detector that are due to Compton electrons with respect to other radiation entering the detector (pair production photons, Compton photons and beam particle), is plotted in Fig.25 as a function of the beam energy and the polar angle of the e^- detector.

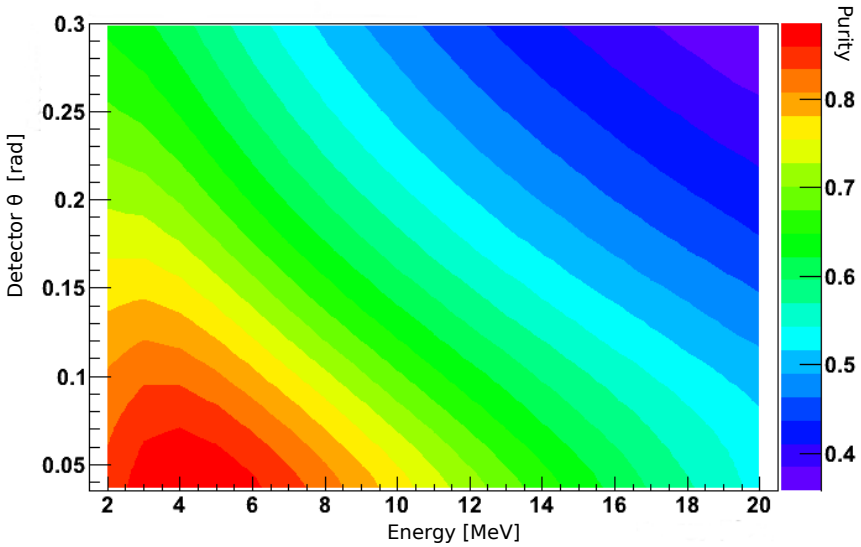

Figure 25: In this plot is reported the purity of signals, defined as fraction of signal due to Compton electrons among the particles entering the HPGe detector, plotted as a function of the beam energy and the polar angle of the detector axis.

The distance d of the detector from the target along the beam direction is chosen as a compromise between conflicting requirements:

- a larger distance allows to reduce the polar angle for a fixed detector size, and the error on its measurement due to the beam spot size;
- a smaller distance increases the acceptance, allowing to reduce the target thickness for a given rate, reducing the contribution of multiple scattering.

The detector size is dictated by the requirements on the electron energy reconstruction efficiency, so there is no possible gain on the detector cost from reducing the distance.

The distance of the Si-strip detector from the target [18] along the beam axis d was optimized computing the target thickness needed to obtain a fixed rate (20 Hz) of electron signals for 10 MeV γ, placing the detector at the minimal practically possible angle. The results for this optimization lead to the choice of d = 200 cm as a compromise between getting a reasonable rate and a good energy resolution taking into account a resolution on the electron energy as determined by the HPGe of 0.1% r.m.s., the uncertainty on the gamma position on the target (1 mm r.m.s. in the transverse directions), the effects of multiple scattering and the energy loss of the electron inside the target.

The resolution on the beam energy measurement depends, critically, on the accuracy of the electron energy determination. This depends on the HPGe detector performance, but also on the energy loss in the materials preceding the HPGe active volume:

- The energy loss inside the target, due to its tiny dimension, is $\ll 1$ keV for any electron energy.

- In the Si-strip position, the energy loss amounts to an average of about 130 keV, almost independent on the electron energy. It will be measured by the detector itself with an expected resolution of 4 keV;

- Fluctuations of the energy loss in the entrance window of the HPGe cryostat and in the surface contact of the detector are the most critical source of uncertainty. To minimize this effect, a detector with micrometric contact on the entrance side and a thin beryllium entrance window were chosen. The minimal practical thickness for the latter turned to be 100 μm for a circular aperture with radius 25 mm. The corresponding energy loss, almost independent of electron energy, has an average value of 30 keV with an r.m.s. of about 20 keV.

The γ energy resolution expected for Compton electron is shown as a function of energy in Fig.26 for a target thickness of 2 μm. Note that the calculation does not take into account the inefficiency of the electron measurements, related to electrons not fully absorbed in the detector, and also neglects the pile-up from beam background. The numbers are thus intended as best limits of the principle of the method, while a more realistic evaluation of the detector performance will be given in Sec.3.3. As it is possible to see from Fig.26, the energy resolution is expected to be dominated by the effect of the fluctuation of the energy loss in materials upstream the HPGe detector. Although the values refer to a single measurement, the peak energy of the beam and its bandwidth can be determined precisely by accumulating an adequate number of measurements, as it will be presented in Sec.3.3.

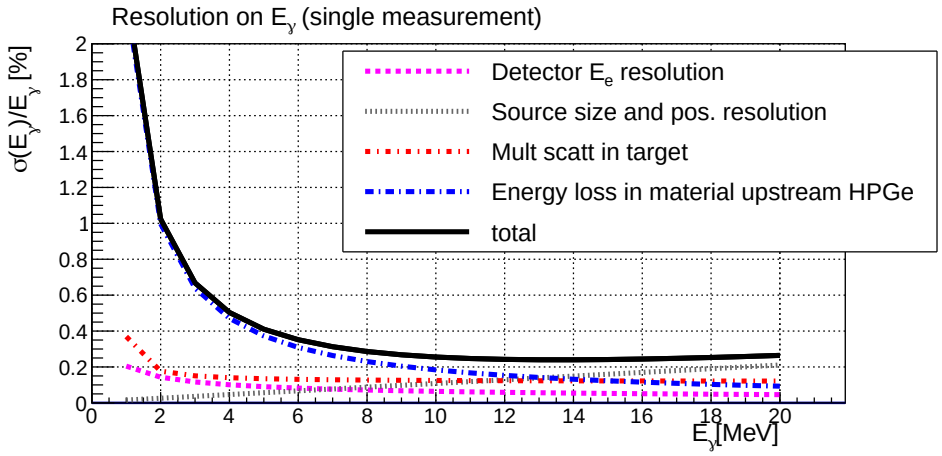

Figure 26: Achievable beam energy resolution expected from the Compton spectrometer using a target of 2 μm thickness for a macro-pulse intensity of 3.2×10^6 photons.

3.3 EXPECTED PERFORMANCES

3.3.1 Detector simulation

To evaluate the performance of the proposed Compton spectrometer a detailed simulation [18] of the detector has been developed using Geant4. The software description of the detector geometry includes, besides the detectors, a target, 2 μm thick, the up-stream/downstream beam pipe and the vacuum chamber with its flanges and the opening, to the gamma detector, hosting the carbon window. Three different beam energies were simulated (2.5, 5 and 18.5 MeV), each simulation consisting of 3.2×10^{10} events. Taking a beam intensity of $10^5\gamma$/pulse, each generated sample corresponds to a 100 s of data taking. Analytical parameterizations of the beam spectra and its spatial distribution were obtained by fitting the results of a dedicated simulation which propagates the γ beam from the interactions point through the collimator. Interactions of photons and electrons were simulated using the Penelope implementations of the Geant4 low energy electromagnetic models. The PENELOPE code [27] has been specially developed for γ and $e^{\pm}$ transport in matter with great care devoted to the description of the low energy processes.

For the transport of $e^{\pm}$ and γ a range cut of 0.1 mm was used. This cut controls the way secondary particles are created, i.e if a secondary particle would traverse in a given material a distance less than the cut, it is not created but its energy is deposited locally, Therefore the value of this parameter should be smaller than the linear dimensions of the smallest geometrical volume. To do that for the thin volumes representing the target, the beryllium window and the HPGe contact layer, we used a lower cut of 1 μm (0.25 μm for the contact). The energy resolution of the HPGe sensor was taken to be gaussian and was simulated taking the standard average energy w=2.96 eV to produce an electron-hole pair, a Fano factor of F=0.10 and adding in quadrature a constant electronic noise of $\sigma_{\mathrm{N}} = 500$ eV:

$$\sigma_{\mathrm{E}} = \sqrt{\mathrm{F}^2 \cdot \mathrm{w} \cdot \mathrm{E}} \oplus \sigma_{\mathrm{N}} \tag{11}$$

The validity of this approach has been verified by the study of the resolution performance of the HPGe detector, see Sec.4.1.5.

3.3.2 Signal identification

To identify a "signal" event it is requested a reconstructed hit in the silicon strip detector, in correspondence with the fiducial region defined by the collimator, a release of energy in the HPGe sensitive volume and a signal in the photon detector.

The expected event rates in the HPGe detector are reported in Table 4 as a function of the beam energy, using 2 μm target thickness, before and after selecting a matching signal in the Si strip and photon detectors. The rate of good signals are the ones displayed on the last column.

E_γ [MeV]	HPGeOnly [Hz]	+ SiStrips [Hz]	+ BaF_2[Hz]
2.5	11.8	4.5	3.4
5.0	19.5	11.7	9.0
18.5	77.6	46.2	12.2

Table 4: Particle rates (Hz) in the HPGe detector as a function of the beam energy before (HPGeOnly) and after selecting the coincidence with Si strip only (+SiStrip) or with Si strip and BaF_2 (+ BaF_2).

Table 5 shows the effect of the detected coincidences on the signal purity for the three simulated beam energies. The request of a hit in the Si strip strongly reduces the events due to a Compton photon, while the detection of a recoil gamma in coincidence suppresses the background due to pair production inside the target. For all the simulated energies more than 99% of the selected events contain an electron generated by a Compton interaction in the target. At higher energies photons surviving the selection are secondaries produced by electron interactions in the silicon or at the edges of the collimator which shields the electron CSPEC detectors.

E_γ [MeV]	HPGeOnly [%]			+ SiStrips [%]			+ BaF_2 [%]		
	e^-	e^+	γ	e^-	e^+	γ	e^-	e^+	γ
2.5	89	1	10	100	-	-	100	-	-
5.0	85	6	9	97	3	-	100	-	-
18.5	60	28	12	67	32	1	99	-	1

Table 5: Type of particles (in percentage) depositing energy in the HPGe volume as a function of the beam energy, before (HPGeOnly) and after selecting a matching signal in the Si strip (+ SiStrip) and requesting in addition a coincidence with photon detector (+ BaF_2) .

3.3.3 Energy reconstruction

The ELI beam energy is obtained by measuring the kinetic energy (T_e) and the scattered angle (θ) of electrons recoiling from Compton interactions of the γ beam on a thin target, as can be seen from Eq. 9. In this paragraph we present the main contributions of uncertainty expected for θ and T_e and the expected resolution on the reconstruction of beam energy spectrum.

The θ angle, measured by the Si-strip, ranges between approximately 47 and 73 mrad, given the detector location and the collimator hole dimension. A resolution on $\theta \leq 1$ mrad is obtained using a resolution of about 50 μm on the impact position. This resolution, worst than the one declared in Sec.3.4.3, is an upper limit that can be obtained simply using the position of the hit strip without any position finding algorithm. The uncertainty is dominated by the error on the collision point due to a simulated beam spot size of about 1 mm.

The electron energy T_e is measured by the HPGe detector. The energy losses in the silicon strip volume and in the passive layers preceding the detector have to be taken into account. As previously described (See 3.2)

the energy released in the silicon volume can be measured and amounts on average to about 130 keV, while the average energy lost in passive components of the HPGe detector predicted from the simulation is about 30 keV. The distribution of the energy loss in these volumes is plotted in Fig.27. The average values of this distribution can be added to the reconstructed electron energy to compensate for this effect; however a fluctuation of about 20 keV is expected.

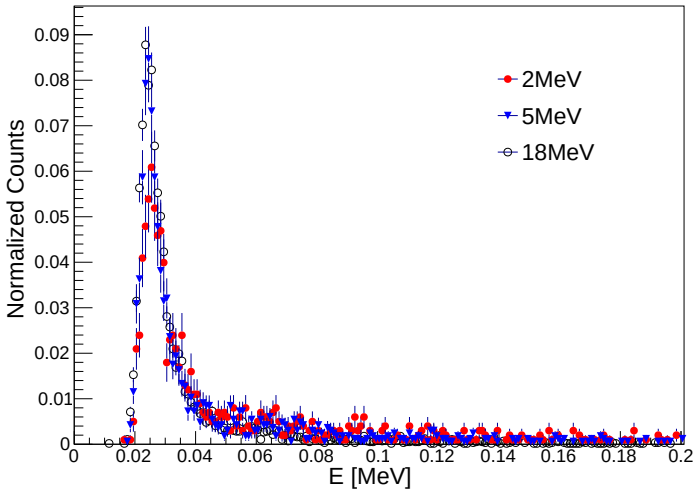

Figure 27: Distribution of energy loss in the inactive regions of the HPGE detector, namely the entrance window and the dead germanium layer, for the three simulated energies.

The MC simulated incident γ beam, obtained at the exit of the collimation system (see Sec.2.2), has an energy spectrum and a divergence.

The beam divergence is presented on Fig.28 where the distribution of φ, the angle between the momentum direction of each γ and the beam axis, is shown. As can be noticed from the figure the beam divergence is lower than 200 μrad (as reported on Tab.1) and decreases when the beam energy increases.

The simulated distribution of the beam energy is displayed on top of the figures 29, 30 and 31 [18] and is used as input energy spectrum for three different simulated energies (2.5, 5 and 18.5 MeV). The distribution of the energy reconstructed from the CSPEC according to Eq.9, obtained with a statistic corresponding to 100 s of data taking, is reported in the bottom plots of the same figures. When the beam energy, and consequently the electron energy, increases we see the increasing presence of events in which the electron is not fully contained in the HPGe volume (escapers). For comparison the distributions of events without escapers are superimposed with different colors and markers. At a γ beam energy of 2.5 MeV the two distributions coincide, indicating that all the electrons are contained. The escaper tail instead is well visible in the 18.5 MeV sample, however, as shown in the picture, the escaper do not contaminate the full energy peak which stands clear over this source of misreconstructed events. To increase the

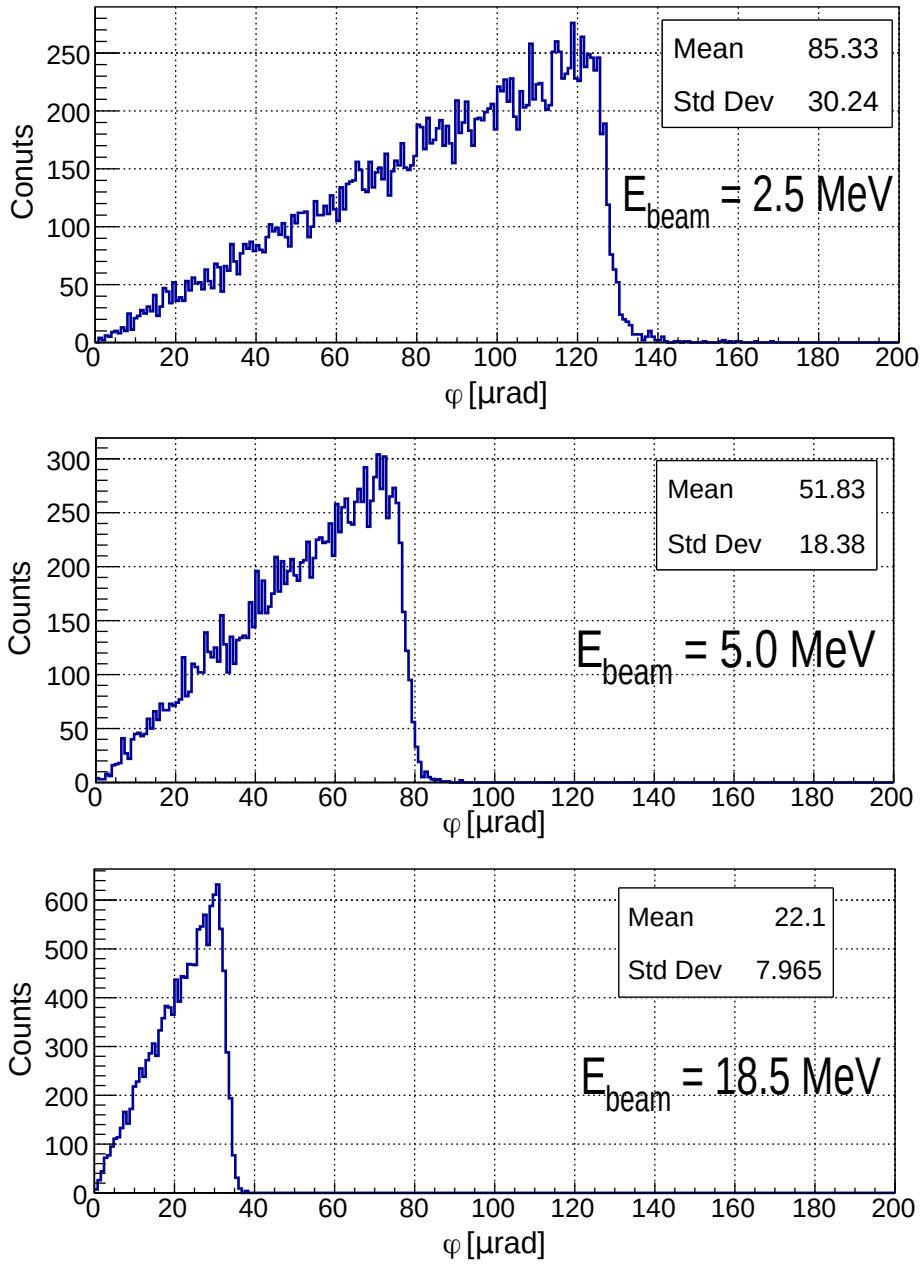

Figure 28: Distributions of the φ angle, that is the angle between the direction of the pulse of each γ and the beam axis. The plots are relative to the three different simulated energies 2.5 MeV (top), 5 MeV (center) and 18.5 MeV (bottom).

fraction of fully contained events at higher energies a much bigger volume of HPGe would be required. The chosen dimensions are a compromise between detection efficiency and detector costs. To parametrize the simulated beam spectrum a Bukin function (a gaussian core with asymmetric tail A) is used, that is displayed in the top plots. The beam production mechanism introduces an intrinsic width (σ_B), while the nominal energy value being the peak value of the energy distribution (x_B). The parameters x_B and σ_B

are the peak position and the width of the Bukin function defined in Eq.30 and ξ is an asymmetry parameter. The parameters obtained from the fit are displayed on the figures.

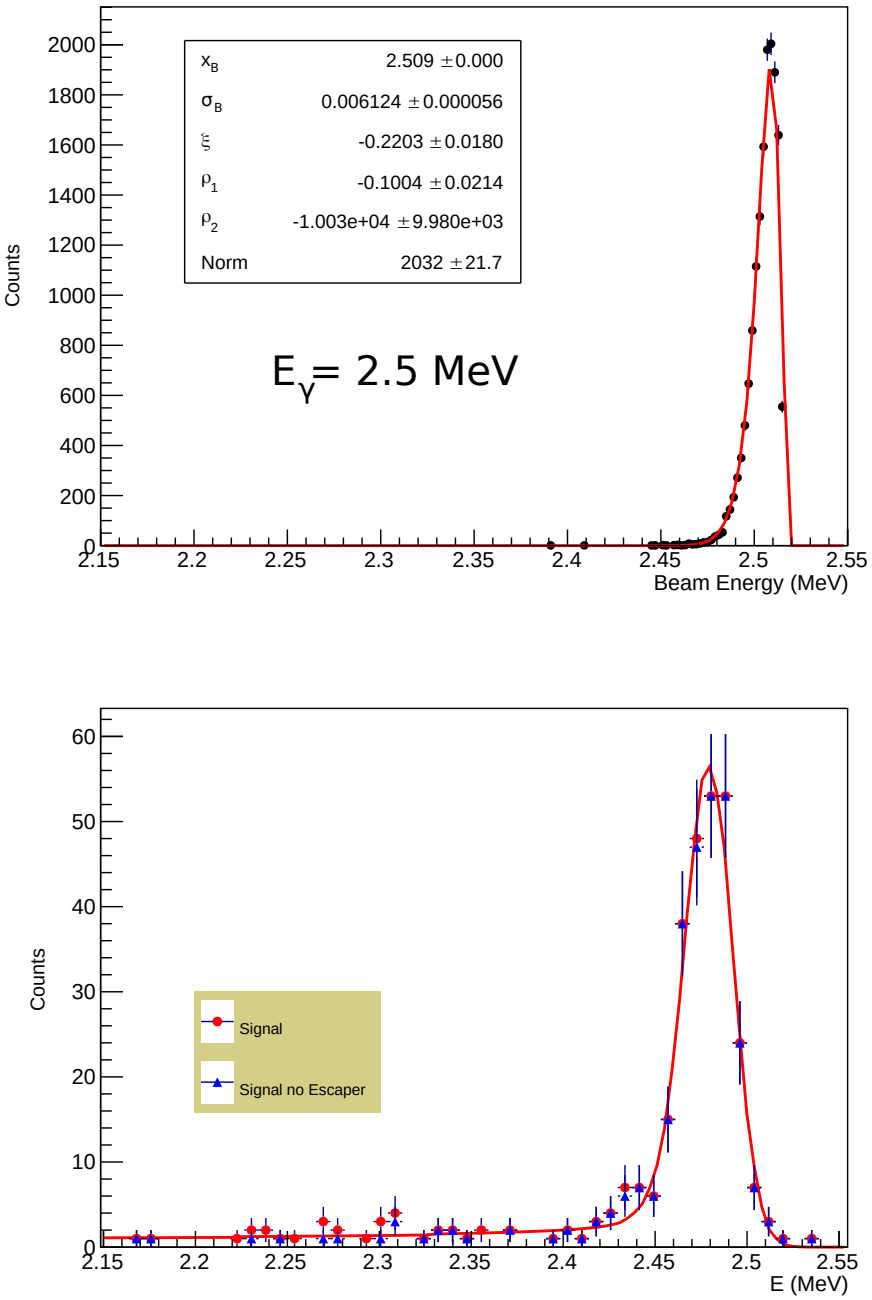

Figure 29: Top plot reports the beam energy distribution used as input to the simulation, while the bottom ones show the energy spectrum reconstructed by the measurement of energy and angle of the scattered electron. The generated γ sample had 2.5 MeV peak energy.

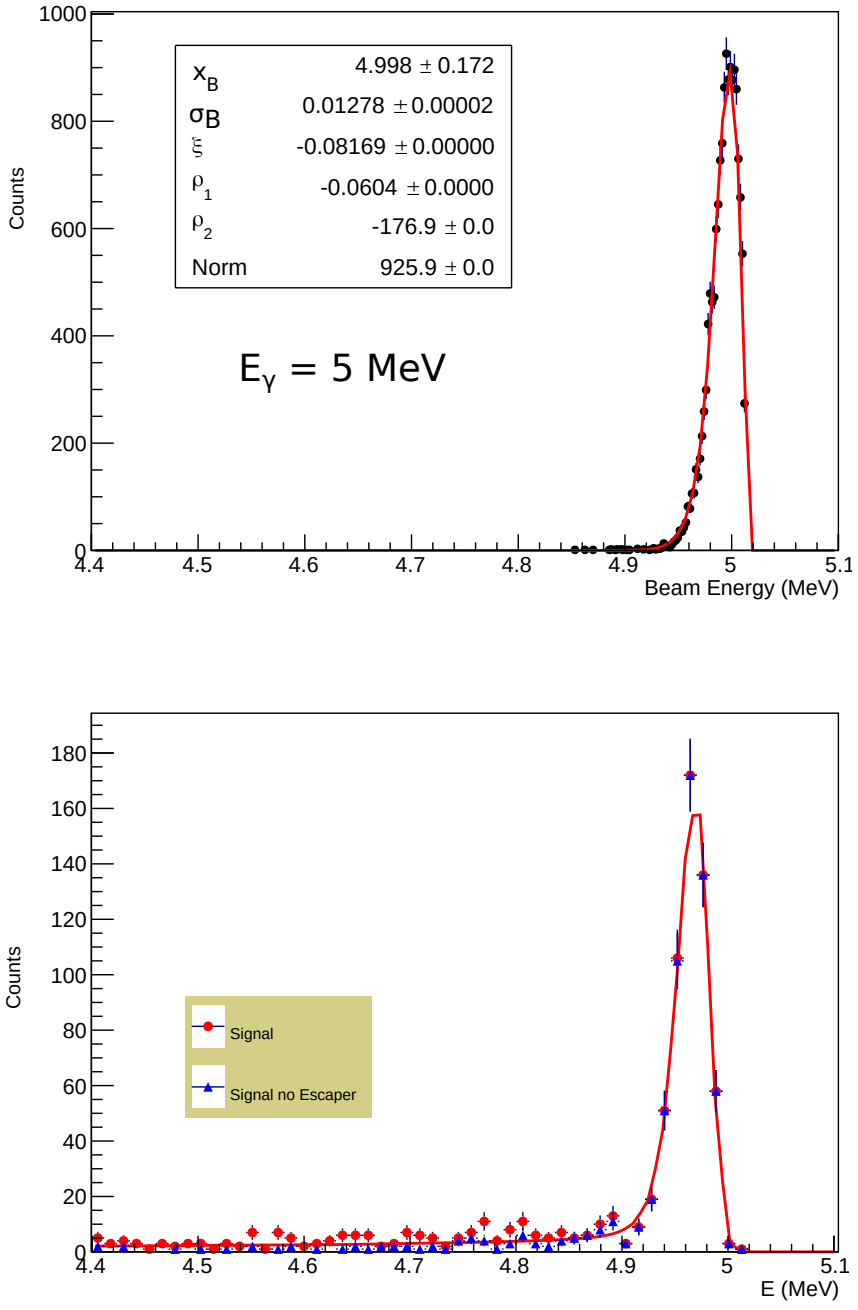

Figure 30: Top plot reports the beam energy distribution used as input to the simulation, while the bottom ones show the energy spectrum reconstructed by the measurement of energy and angle of the scattered electron. The generated γ sample had 5 MeV peak energy.

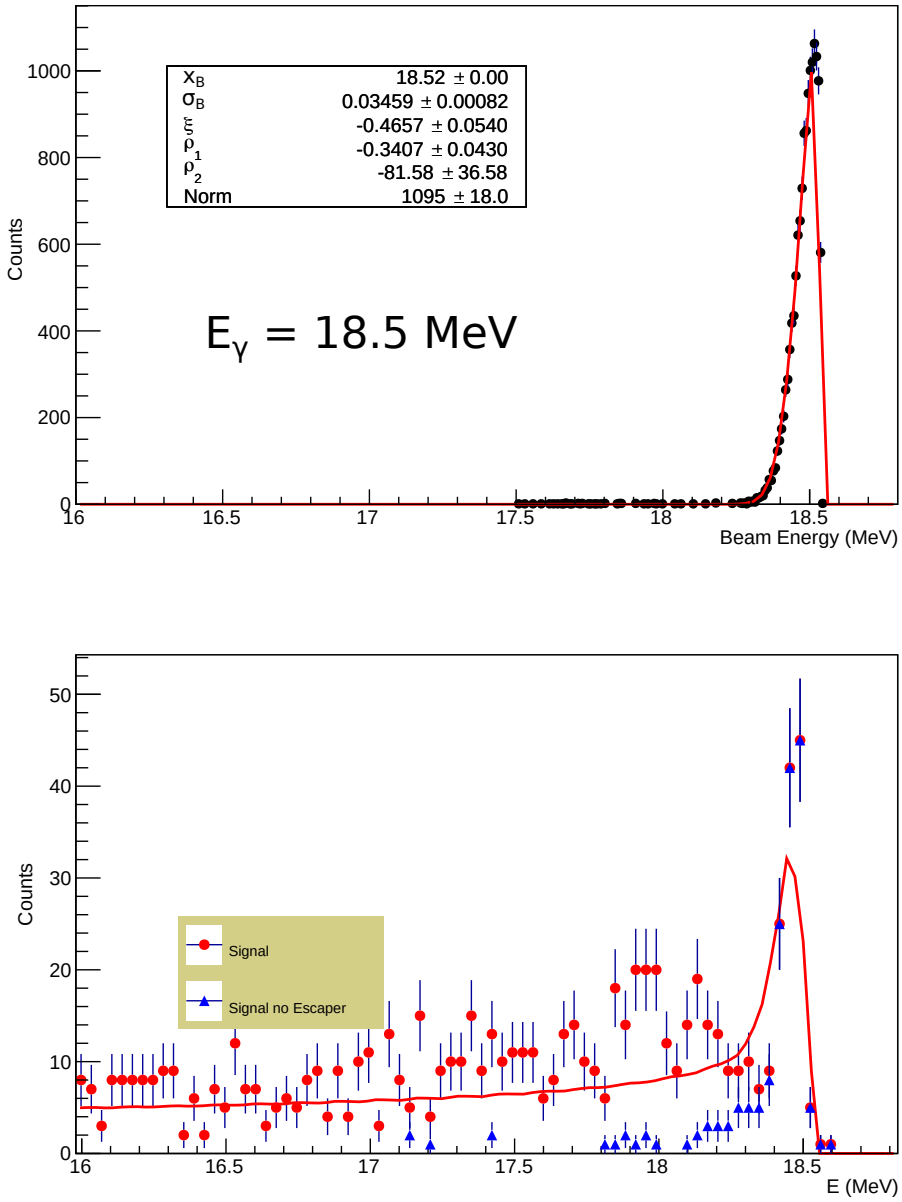

Figure 31: Top plot reports the beam energy distribution used as input to the simulation, while the bottom ones show the energy spectrum reconstructed by the measurement of energy and angle of the scattered electron. The generated γ sample had 18.5 MeV peak energy.

In order to obtain the intrinsic beam parameters the reconstructed spectrum (bottom plots) is fitted with the convolution of the Bukin function with a Crystal Ball function (a Gaussian function with a left power-law tail, presented on Eq.34) describing the detector response. The γ beam bandwidth and peak value will be determined from the width of the reconstructed energy distribution, after deconvoluting the detector response function. This fit function is plotted in red and superimposed to the reconstructed spectrum. In Tab.6 are reported the following quantities:

- ΔE = x_B - x: the shift between the γ beam (x_B) and the expected measured energy peak (x).
- σ_B: the simulated bandwith of the gamma beam (shown also on the top graphs).
- $\sigma = \sqrt{\sigma_{tot}^2 - \sigma_B^2}$: the expected experimental resolution for the CSPEC detector; σ_{tot} is the total width of the fitting function.

Notice that the shift from the true values (ΔE) is about 30 keV, as expected from the average value of energy loss in the passive materials. The detector energy resolution is $\leq 0.5\%$, then better than the γ beam bandwidth.

$\mathbf{E_\gamma}$ **[MeV]**	**2.5**	**5**	**18.5**
ΔE [keV]	27	28	30
σ_B [keV]	6	13	34
σ [keV]	12	8	26

Table 6: In this table are reported the energy shift between the measured and the true peak values (ΔE), the simulated beam bandwidth (σ_B) and the expected σ of the reconstructed energy spectrum.

The expected statistical (corresponding to 100 s of data taking) and systematic uncertainties on the peak energy and bandwidth of the photon beam estimated with this procedure have been studied. The results are reported in Tab.7 and Tab.8.

The systematic uncertainty is related to the knowledge of the corrections needed to account for the energy losses in the passive materials and for the detector resolution. We expect that both the average energy loss and the energy resolution can be readily predicted within a relative 10%. The resulting systematic error are expected to limit the accuracy of the measurements already after 100 s of data taking to a relative uncertainty below the 0.1% on the peak energy and bandwidth as can be seen from Tab.8. These systematic corrections, obtained from the Monte Carlo simulation, have been validated with tests made on the HPGe detector. Indeed we measured the energy resolution of the HPGe detector with γ sources (Sec.4.1.5), and we verified the energy loss prediction of the MC simulation exposing the detector to e^- sources (Sec.4.1.7).

In conclusion, the simulations show that a clean sample of well reconstructed Compton interactions can be selected using the Compton Spectrometer, providing an accurate reconstruction of the beam peak energy

E_γ [MeV]	2.5	5	18.5
$\sigma_{stat}(E_\gamma)/E_\gamma$ [%]	0.04	0.02	0.02
$\sigma_{syst}(E_\gamma)/E_\gamma$ [%]	0.11	0.06	0.02

Table 7: Expected relative uncertainties on the beam peak energy due to the sample size corresponding to 100 s of data taking and to the systematic uncertainty.

E_γ [MeV]	2.5	5	18.5
$\sigma_{stat}(BW)/E_\gamma$ [%]	0.08	0.02	0.014
$\sigma_{syst}(BW)/E_\gamma$ [%]	0.09	0.02	0.011

Table 8: Expected uncertainties on the determination of the beam bandwidth due to the sample size corresponding to 100 s of data taking and to the systematic uncertainty, for several values of beam energy and simulated bandwidth.

and width. The expected number of useful signals per incident photons corresponds, for the nominal beam flux, to a rate of a few Hz for the whole range of beam energy. The spectrometer will thus be able to provide a continuous monitoring of the beam energy during the routine operations of the ELI-NP facility.

3.4 DETECTOR DESIGN

The Compton spectrometer is basically composed by:

- a high purity germanium detector (HPGe), to measure the energy of the scattered electron (T_e);
- a double sided silicon strip detector, to determine the electron scattering angle (θ);
- 16 BaF_2 crystals, arranged in a small calorimeter to detect the recoil gamma.

These main components and a schematic view of their placement with respect to the gamma beam position are illustrated in Fig.24.

3.4.1 Vacuum chamber

The two electron detectors will be located inside a vacuum chamber together with the target system. The vacuum chamber is a cylindrical stainless-steel chamber with a length of 270 cm and a diameter of 40 cm. The Compton scattered photon instead can travel through the air and the detection can be done outside the vacuum chamber (see Fig.32). To reduce the absorption of this low energy photon the vacuum chamber is equipped with a carbon window only 1.5 mm-thick.

A study of the effect of the background particle on the Compton spectrometer has been done using the MC background sample described in Sec.2.2.

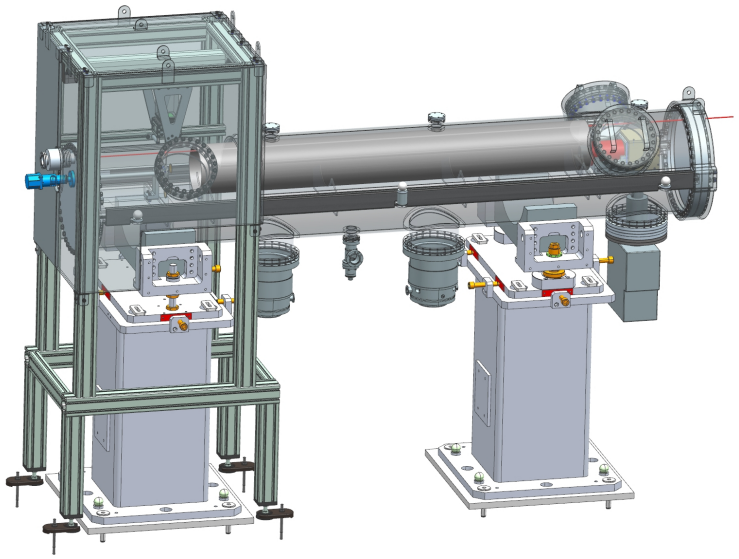

Figure 32: The CSPEC system. An overview of the vacuum chamber can be seen in transparency. The photon detector is located outside the vacuum chamber, on the top left side of the picture.

From this studies we found that the optimal shield solution is obtained with a 10 mm thick lead layer that cover completely the vacuum chamber and a further 10 mm lead surrounding the photon detector box.

A magnetic shield is necessary in order to reduce the uncertainty on the determination of the e^- polar angle due to the effects of the Earth's field and vacuum pumps along the electron path. The magnetic screen consists in a cylinder of MuMetal with diameter of 20 cm and thickness of 0.15 cm and will be positioned inside the chamber around the fiducial volume for electron propagation, as can be seen from Fig.32.

3.4.2 Target System

The target should be made of low-Z material to minimize the contribution of pair production with respect to Compton scattering. We choose to use Mylar films inserted in a Carbon fiber frame (see Fig.33). The Mylar is a thermoplastic resin, commercially used as film, with good elastic properties and with low atomic number. The target thickness should be varied according to the beam energy in order to optimize the rate of useful signals, therefore we plan to mount several targets of different thickness, ranging from 2 to 100 μm (2.5 μm, 6 μm, 13 μm, 50 μm and 100 μm), on a rotating wheel, as shown on Fig.33. The thicker target of 100 μm will be used during the start-up phase when we expect a reduced beam intensity.

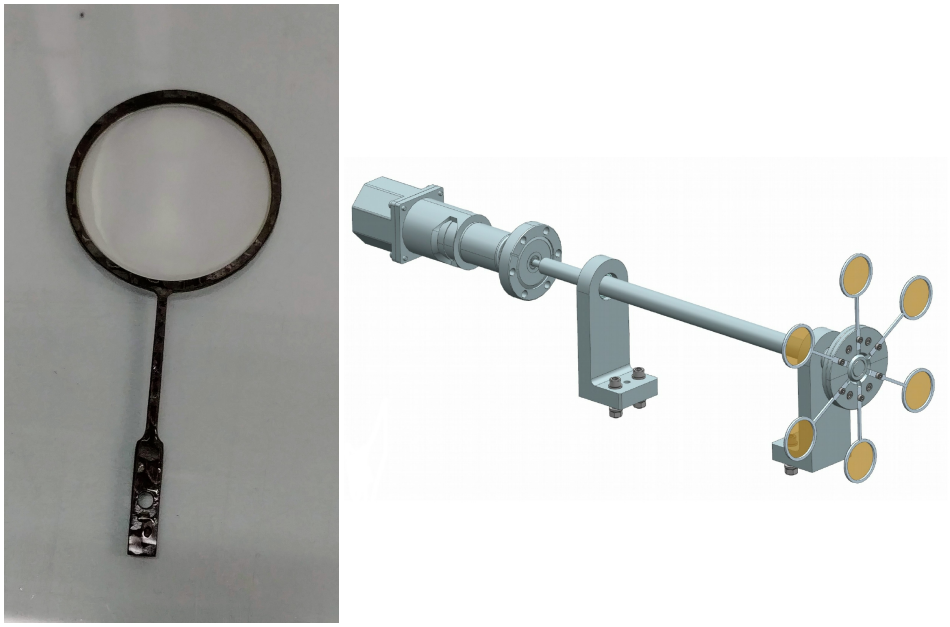

Figure 33: In the left a photo of a Mylar target of 2 μm mounted on the frame and on the right a drawing of the target holder with 6 mounted target

3.4.3 Electron detector

The position and the energy of the Compton-scattered electron will be precisely measured using a detection system made by a double-sided silicon μstrip sensor and a HPGe crystal.

Si-strip detector

The electron position has to be measured with accuracy ≤ 1 mm in order to obtain a good measurement of the beam energy. A double sided silicon strip detector originally developed for the Pamela apparatus [28] will be used. Manufactured by Hamamatsu Photonics, the sensor bulk is made by n-type silicon and segmented into micro-strips on both sides with p+ strips implanted on the junction side (x-view) and n+ strips on the ohmic side (y-view) . In the x-view, the implantation pitch is 25 μm and the read-out pitch is 50 μm; while in the y-view, the read-out pitch is 67 μm, as displayed on Fig.34. For each view 1024 strips are readout.

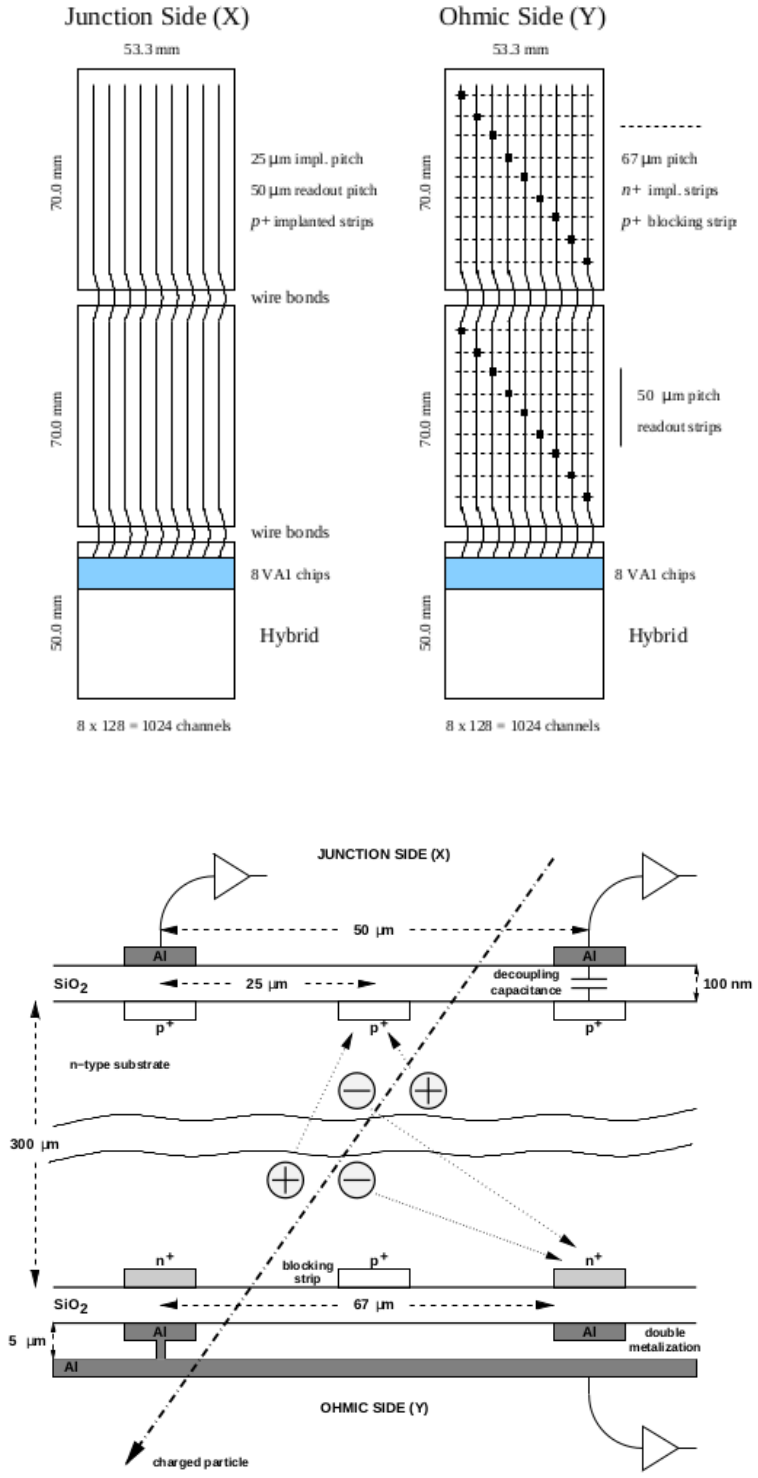

Figure 34: In top plot is shown the strip layout on both side of the original PAMELA ladder. We will use only one sensor attached to the front-end electronic board (see Fig.35) In the bottom one the cross section of a silicon sensor is presented. The upper and lower sections of the bottom figure refer to junction and ohmic sides, respectively, and they are actually rotated by 90°. Figure taken from [29].

Decoupling capacitors are integrated directly on the sensors by means of a 100 nm thick silicon dioxide (SiO_2) layer, lying between the strips and the aluminum read-out contacts. A double metalization is present on the ohmic side in order to have the read-out electronics on the same part on both views. For this purpose metallic lines, orthogonal to the first series of aluminum strips, are present. They are separated by a second thicker (5 μm) silicon dioxide layer: it provides insulation between two orthogonal series of metallic strips. The electrical contacts with the corresponding metallic strips are realized by means of small connections through the insulating layer using a chemical procedure (see figure 34). This technology gives rise on the Y side to a significant capacitive coupling between two distant strips, because ideally all the implanted aluminum strips of the external layer are coupled with the underlying orthogonal strips.

The silicon strip detector, shown on Fig.35, has dimensions of 5.33×7 cm^2 and 300 μm thickness. The front-end electronics is composed by 8 VA1 Application Specific Integrated Circuits [30] chips for each side of the detector. The VA1 chip consists of 128 charge sensitive preamplifiers, shapers and sample-and-hold circuit. The channels are multiplexed and read out serially through a front-end board. The device is glued to an aluminum frame for precise positioning inside the vacuum chamber.

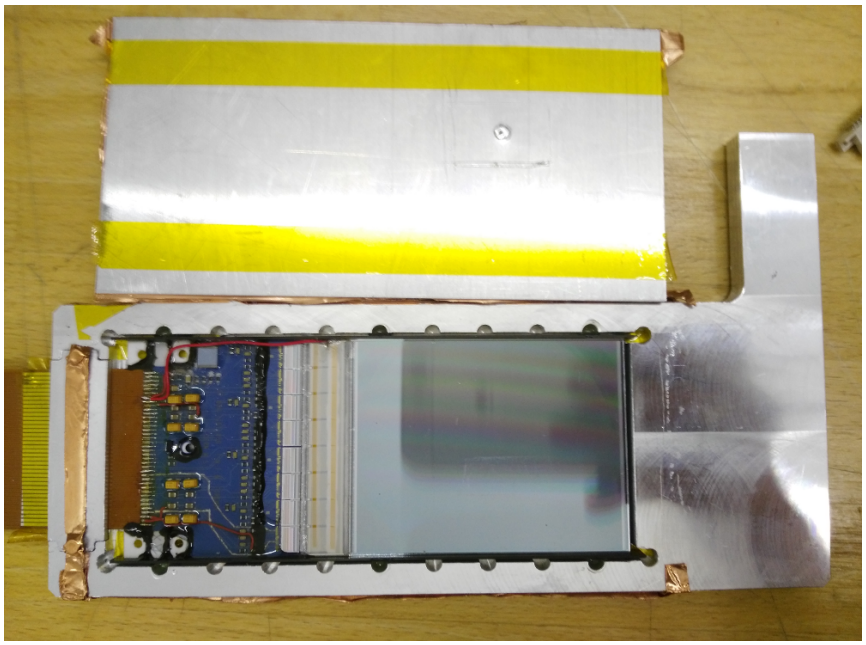

Figure 35: A photo of the silicon strip detector bonded to the front-end board.

The detector allows a 2-d reconstruction of the electron impact point with a resolution of 3/12 μm for the X/Y side. The difference in these values is related to the higher noise level of the Y side due to its greater capacitance. Indeed, for the spatial resolution, it is crucial to have little noise on the cluster tail, where the signal released on the strips is small. These spatial resolution values are obtained for orthogonal tracks with minimum ionizing particles, thanks to a signal-to-noise ratio (S/N) of about 50 for the x-view

and of 25 for the y-view [28, 31]. Actually, in the new configuration described here, from preliminary evaluation of S/N taken with cosmic rays, we obtained a mean value of about 44 and 29 for the X and Y side, respectively. Taking into account this S/N and considering that a minimum ionizing particle creates on average 27500 e^- in a 300 μm silicon layer we expect an energy resolution of about 2/4 keV for the X/Y side sufficiently to provide an accurate measurement of the energy released in the silicon sensor.

HPGe detector

To measure the electron energy the HPGe technology was chosen for its well known properties of both excellent energy resolution and high efficiency. The HPGe detectors usually are used for gamma-ray spectroscopy whose performances are not deteriorated by the presence of the detector entrance window and dead layer. Instead, for the electron energy determination the energy loss in the dead layers of the detector is really important. The HPGe crystal, built according to our custom design in a planar configuration by CANBERRA (now Mirion Technologies [32]), has a cylindrical shape with a diameter of 80 mm and a thickness of 20 mm. An important feature of the crystal is the ultra-thin ($\leq$ 1 μm) electrical contacts on its surface which minimizes the entrance dead layer. The HPGe diode, the cold head of the cooling system and the electronics are enclosed in a vacuum tight cryostat which is placed in its own vacuum and completely disconnected from the vacuum of the chamber. The detector, equipped with an electrically powered cooler[33], works at a temperature of -185° C. In Fig.36 is shown a photo of the HPGe detector connected to its cooler (bottom). The HPGe capsule is equipped with a thin beryllium window (100 μm thickness) shown in Fig.37, with a diameter of 50 mm centered on the HPGe crystal axis.

3.4.4 Photon detector

The scattered photon is detected in coincidence with the electron to provide a trigger for the Compton Spectrometer data acquisition. Monte Carlo simulations show how this coincidence will be very effective in suppressing the background from pair production, Compton photons, and beam particles (Tab.4 and Tab.5).

The data acquisition of the Si-strip detector needs a trigger ($\sim$ 1 μs) to properly reconstruct the collected integrated charge from the passage of the electron and therefore to maximize the energy and space resolution. Therefore, the photon detector should have high photon detection efficiency and a fast response.

The detected photons have an energy in the range between 200-300 keV for the low energy line and from 350 keV to 900 keV for the high energy one. The chosen material for the photon detector is the BaF_2 scintillation material which has quite good light yield and conversion efficiency and in particular is characterized by a very fast emission component ($\leq$ 1 ns decay

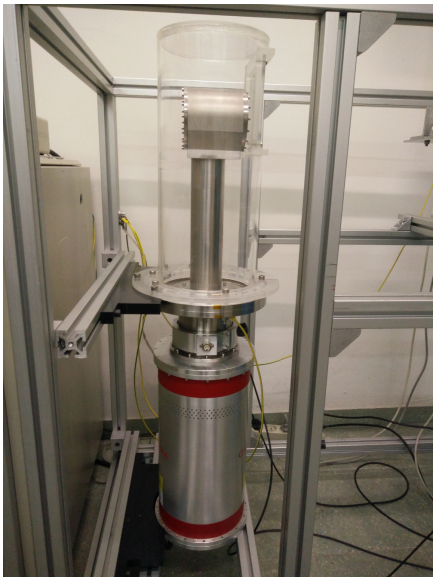

Figure 36

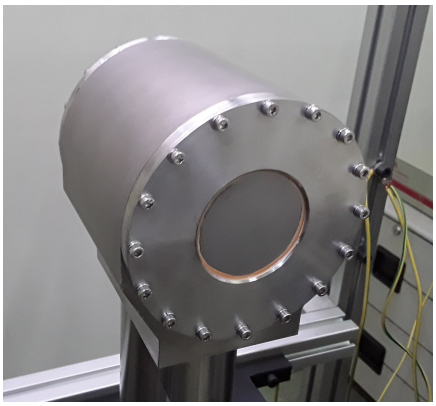

Figure 37

Figure 38: Photos of the HPGe detector. Fig.36 shows the vacuum tight cryostat which enclose the HPGe diode, while Fig.37 presents an enlarged view of the beryllium window.

time). In fact, the radioluminescence spectrum of BaF2 crystals contains two components:

- a fast component with wavelength in the deep ultraviolet range 175-250 nm and an extremely short emission time 0.6 nsec;
- a slow component in the wavelength range 250-400 nm with emission time of 620 nsec.

The BaF_2 crystals, made by Scionix [34], are arranged in a small calorimeter of 4×4 crystals, with size of 1.2×1.2×5 cm^3, displayed in Fig.39.

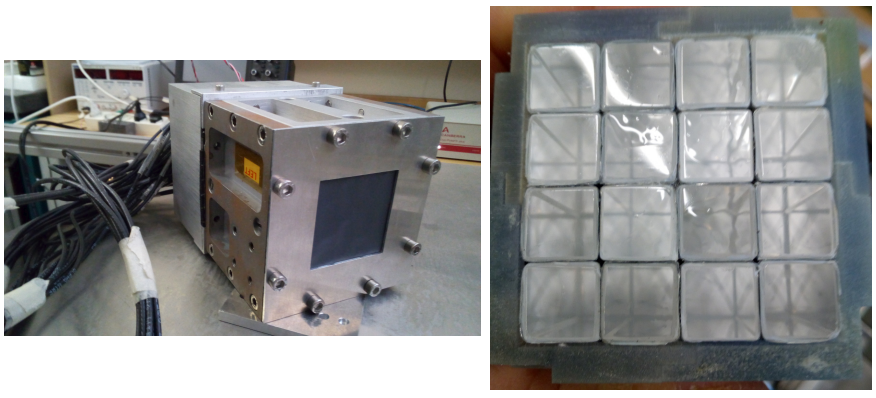

Figure 39: Photos of the gamma detector. On the left the detector inside the shielding box connected to the multianode PMT and to a custom board for the read-out electronics (on the back side). On the right it is shown the assembly of the 16 crystals.

In Fig.40 is shown the crystals disposition inside the BaF_2 detector. The number shown on the photo of the crystals correspond to the serial number reported on the scintillators data sheets. In the left of Fig.40 are indicated the channels number (CH) of the digitizer associated with the relative crystal position. This CH number will be used for identification of the crystals in this section. The figure presents also the numbers of wire reading the high (H) or the low (L) gain signal and the use of the dynode output, that is the analog sum of all the channels, and is acquired for trigger purposes.

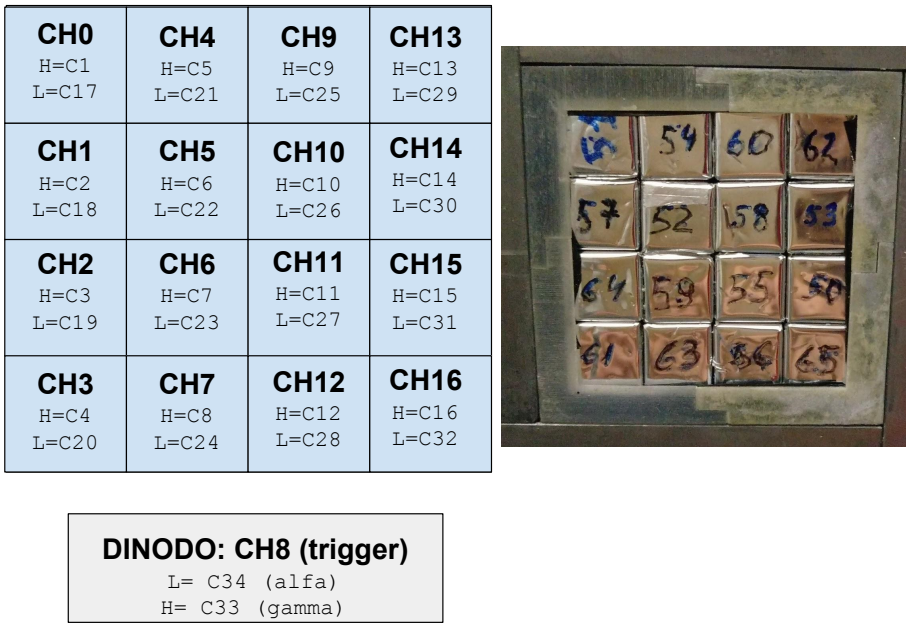

Figure 40: Photo of the crystals disposition inside the photon detector.

The crystal will be read by a multianode PMT manufactured by HAMAMATSU (H12700A-03 model [35]) which is a compact device hosting 64 photomultipliers channels of 6×6 mm^2 area each, with a 10 stages dynode structure. The chosen MaPMT is the H12700A model which is equipped with a borosilicate entrance window coupled with a bialkali photocathode with a spectral response ranging between 185 - 650 nm, and a maximum quantum efficiency of $\sim$ 33% at about 350 nm, as shown in Fig.41. In order to maximize the collection of light a silicon oil transparent to the UV light is used to guarantee an optimal contact between the crystals and the multianode.

The MaPMT channels are readout in groups of four in order to match the dimensions of the scintillator crystals.

The signals are read out by custom front-end boards developed at INFN Firenze, implementing shaping amplifiers and the drivers to send the signal to the DAQ system. The gain of the amplifiers ($\times15$) have been optimized in order to improve the resolution in the energy range of interest (200-287 keV for the low energy line). We plan to acquire also, for calibration purposes, the

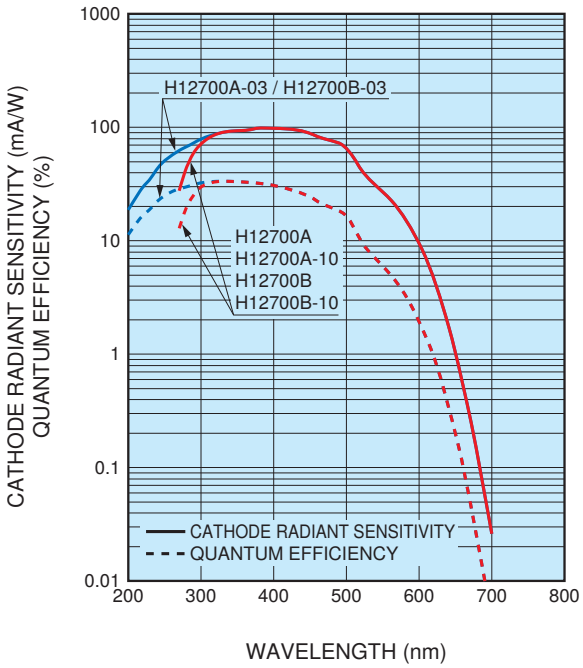

Figure 41: Typical spectral response of H12700 multianode PMT produced by HAMAMATSU. The "03" family extends the sensitivity in the UV region. Figure taken from [35].

signals produced by the intrinsic radioactivity of the crystal (see Sec.3.4.5). Given the high energies of these particles, to avoid the saturation of the signal, a second read-out line with a gain factor of 5 was implemented in the electronics.

One additional board is realized for the readout of the dynode output and is displayed in Fig.42, where is presented also one of the four readout boards of the 16 channels.

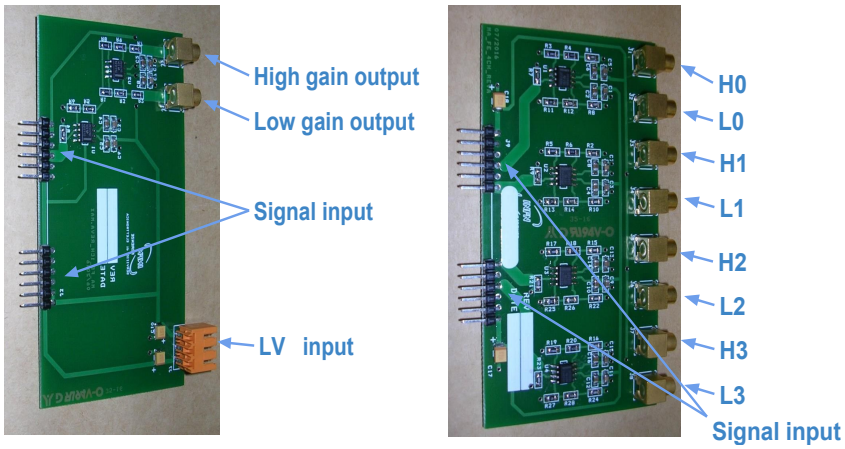

Figure 42: Photos of the custom read-out board of the BaF_2 crystals, dynode output (left) and module for 4 channels (right). Each channel is splitted in two output signals with different gains: a factor of 15, for the high gain output (labeled with letter H); and of 5 for the low one (labeled with letter L).

The detector will be positioned outside the vacuum chamber in a region close to the target. A thin carbon window will allow the scattered photon to come out of the chamber while keeping the vacuum inside.

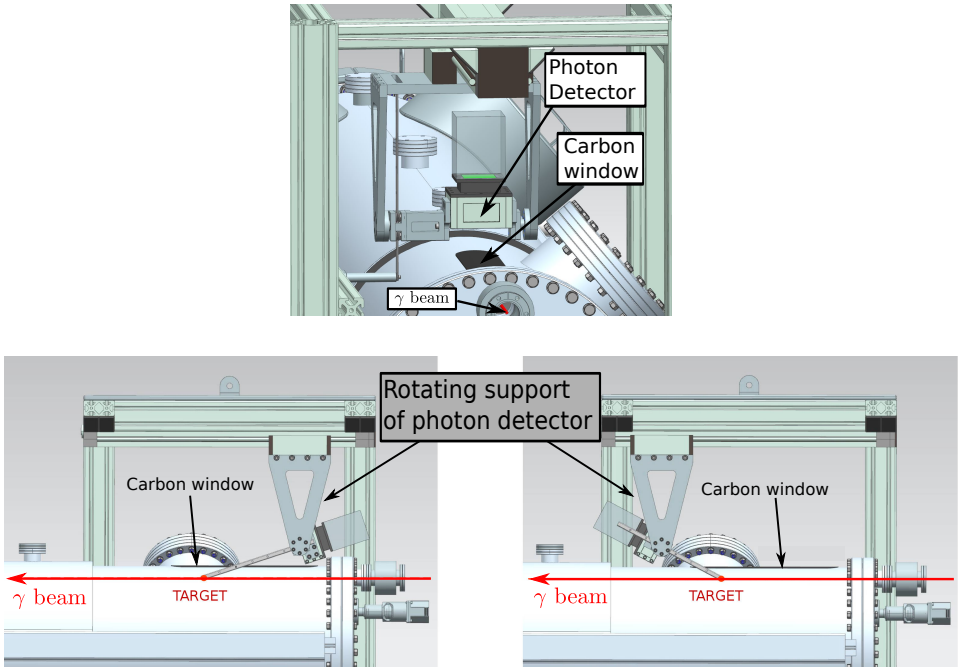

Figure 43: In this figures a rendering of the movable frame holding the gamma detector, located outside of the vacuum chamber, is depicted, as well as the thin carbon window which allows the propagation of the scattered photons from the target to the photon detector. The two extreme positions allowed for the gamma detector are displayed in the bottom figures.

The detector will be mounted on a movable system in order to match the proper detection angle as a function of the beam energy. The detector will move from -250 cm to 155 cm along the Z position around the target, this corresponds to a scattering angle from 28 degrees up to 162 degrees with respect to the incoming beam direction. As shown in Fig.43, the movement of the detector is such that its entrance window points always to the interaction point. The energy deposition of the photons produced by the beam of the low-energy line is mostly contained in a single detector crystal. The position of the crystal can be used to determine the angle of the scattered photon. Although this information does not contribute significantly to the reconstruction of the beam energy, it can be used to reduce the combinatorial background. Indeed, a requirement on the consistency between the energy T_e of the scattered electron with the photon angle can be used to reject cases where a relevant fraction of the electron energy escaped detection.

3.4.5 BaF_2 crystals intrinsic radioactivity

The BaF_2 crystals have an intrinsic radioactivity[36] that can be used to self-calibrate the detector as will be presented in detail in section 4.2.5. This

intrinsic radioactivity originates from radium impurities, which are always present as radium and barium are homologuous elements. The spectrum is dominated by the four alpha lines from the decay chain of ^{226}Ra in an energy range from about 4.8 MeV to 7.7 MeV. The decay chain of the ^{226}Ra is presented on Fig.44.

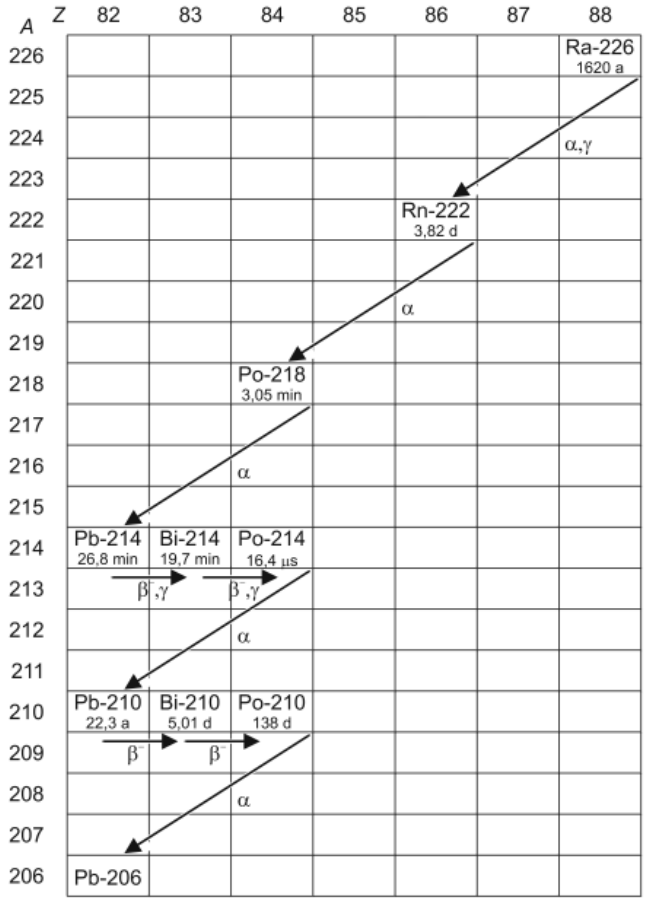

Figure 44: The decay chain of ^{226}Ra [37].

Typical activities for the ^{226}Ra decay of the BaF_2 crystals are $\sim 0.2\,\mathrm{Bq/cm^3}$, so the expected rate for the whole detector is of about 19 Hz.

3.5 DAQ AND TRIGGER

The analog signals coming out from detector devices are in general fast signals it has been chosen to acquire signals with digitizers located next to beamline.

For the data acquisition system of the CSPEC detector we used different DAQ units to readout the three different detectors.

The 1024×2 output channels of the silicon strip detector are read out serially through a front-end board. The charge collected by a given silicon strip is amplified and shaped by the corresponding channel of the VA1 chip, then stored on a capacitor, where it is "frozen" until the read-out sequence

starts. The analog signal is sent to the ADC board and there is digitized by means of a 12 bit ADC. The FE electronics is enclosed inside the vacuum chamber and directly bonded on the strips, while the ADC board is outside, on the "air" side. The digitized signal is sent to a general purpose input-output VME module (MOD.V1495 [38]). The V1495 module has two FPGA programmable units that will be used for the readout and for the VA1 chip configuration. We implemented on the FPGA a fixed delay between the arrival of the CSPEC trigger signal and the start of the Si-strip read-out. We found that a delay of about 1 μs permits to perform a correct integration of the Si-strip signal.

The HPGe device is equipped with a charge sensitive preamplifier (PSC 761-R [32]) that has a cooled input stage and an automatic voltage start off circuitry, in case of increase of the detector temperature. The preamplifier has two identical output channel. One channel is used for trigger purpose (OutT) after being differentiated in order to obtain a faster signal. The other one (OutE) is directly connected to a digital multichannel analyzer. The DT5780 Dual Digital Multi Channel Analyzer (MCA)[39], manufactured by CAEN, is a desktop system which provides a 14-bit waveform digitizer. The DT5780 is equipped with a DPP-PHA Firmware, that is a Digital Pulse Processing software which replaces a standard acquisition chain made for a spectroscopy system, providing energy (i.e. pulse height) and timing information as well as portions of the waveform and other traces for the fine tuning of the PHA settings.

The data acquisition of the BaF_2 detector is based on a CAEN Switched Capacitor Digitizer (mod. V1742 [40]) that is able to sample the analog input signals in a circular memory buffer made of 1024 cells at a selectable sampling rate of up to 5 GHz. We work at a sampling rate of 1 GHz in order to acquire 1024 ns, to fully contain the 630 ns corresponding to one decay constant of the BaF scintillation light and 150 ns before the signal start, this part is used for the baseline calculation. The CAEN model V1742 houses 32 acquisition channels, which are used to acquire the 16 + 16 signal inputs from the low/high gain lines. All the V1742 channels have a resolution of 12 bits. In addition it has also 2 trigger intput channels that are also digitized. Each trigger signal drives independently two groups of 8 channels. The channels group relative to the photon signals (the high gain lines H) are triggered from the CSPEC global trigger (Tr0 on Fig.45). Meanwhile for the trigger of the group of channels dedicated to α pulses, the low gain (L) MaPMT dynode signal is used (Tr1 on Fig.45). The signal is directly processed by an internal comparator, whit programmable threshold.

The trigger of the CSPEC detector is provided by the coincidence of the HPGe signal with the BaF_2 signal and the GBS machine clock. In order to be sensitive to the passage of the scattered photon in any of the BaF_2 crystals the dynode signal of the H output provides the BaF_2 signal. To obtain the best time resolution with this detector, we decide to use a Constant-Fraction Discriminator (CFD). In particular, the idea for the trigger of the Compton Spectrometer is to use the CFD CAEN Model V812 [41], that is a 16 channel constant fraction discriminator housed in a VME module. The use of a CFD

discriminator is useful because it reduce the amplitude-dependent time walk for slow signals [42], like the HPGe signal. Each channel of the module can be turned on or off via VME by using a mask register. A "MAJORITY" output provides a NIM signal if the number of input channels over threshold exceeds the MAJORITY programmed value. Therefore, to obtain a trigger that is given from the coincidence between the HPGe, the BaF_2 and the synchronization signal provided by the GBS machine (a NIM signal at 100 Hz frequency) the "MAJORITY" output will be used, with a programmed number of 3 channels over the thresholds.

The pulse forming stage of the discriminator produces an output pulse whit adjustable width in a range from 15 ns to 250 ns. In order to protect against multiple pulsing, it is possible to program a dead time during which the discriminator is inhibited from retriggering. A dead time of 2 μs will be used to enable a new trigger only when the signal of the HPGe detector is finished.

This obtained NIM signal (dashed lines on Fig.45) is sent as external trigger at the DAQ modules of the three detectors. A graphical schematization of the trigger and DAQ system of the CSPEC detector is shown on Fig.45.

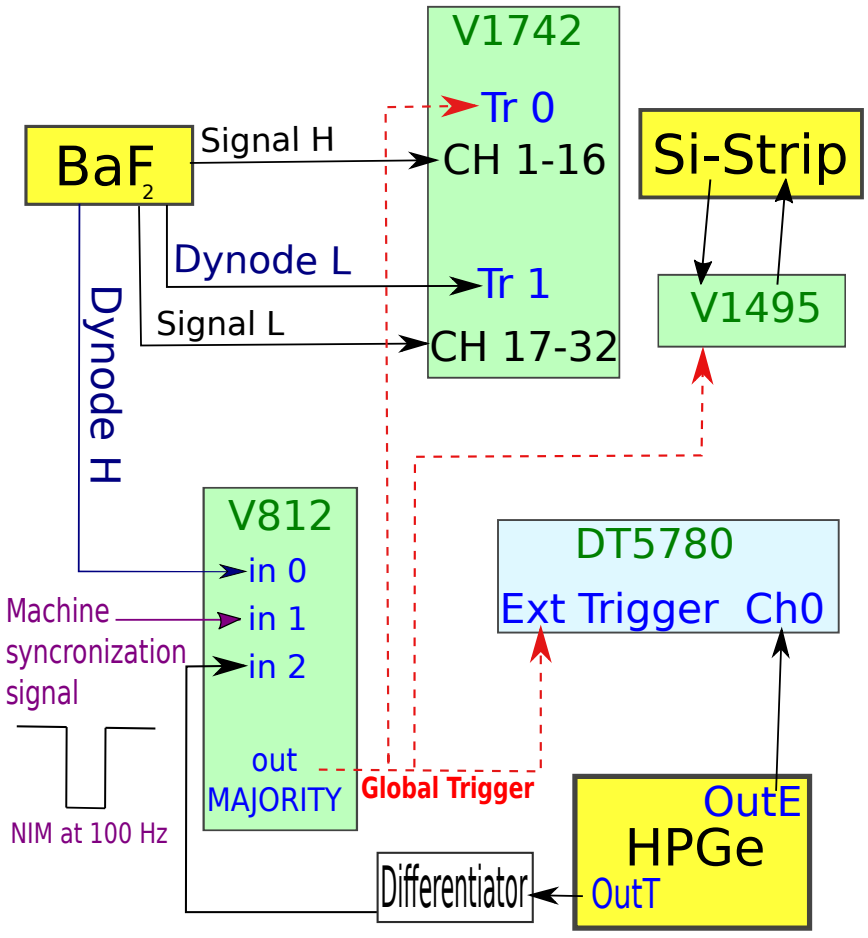

Figure 45: Graphical representation of the trigger and DAQ system of the CSPEC detector.

A dedicated DAQ software has been developed in order to readout the digitizers. The data are collected from the different digitizers with different event and data structures. The software is based on two different processes:

- Producer: reads data from the digitizers, builds the event and writes it into a circular buffer implemented in a shared memory.
- Consumer: reads data from the ring buffer in the shared memory and writes it into a binary file on the disk.

The DAQ software, made by the consumer, is complemented by an event builder program that reads the binary data file, decodes the event and produces the relative ROOT files containing the information related to the event.

4 COMPTON SPECTROMETER TESTS

4.1 HPGE DETECTOR TESTS

In this section are presented the characterization procedure of the HPGe detector and the tests of the detector linearity and energy resolution. These tests have been performed using different γ radioactive sources. In addition, the detector response was tested with electrons of definite energy in order to verify the accuracy of the MC simulations.

4.1.1 Experimental set-up

The experimental set-up used for the characterization and tests performed with radioactive sources emitting photons is displayed on Fig.46. The γ point sources are located in front of the detector at a distance such that the count rate is less than 1000 counts/s. The HPGe detector is readout by the DT5780 that has 4-step configurable input range (0.6 / 1.4 / 3.7 /9.5 V_{pp}) and works at a sampling rate of 100 MS/s. Furthermore the DT5780 provides the power supply to the detector amplifier and the high voltage of the HPGe crystal.

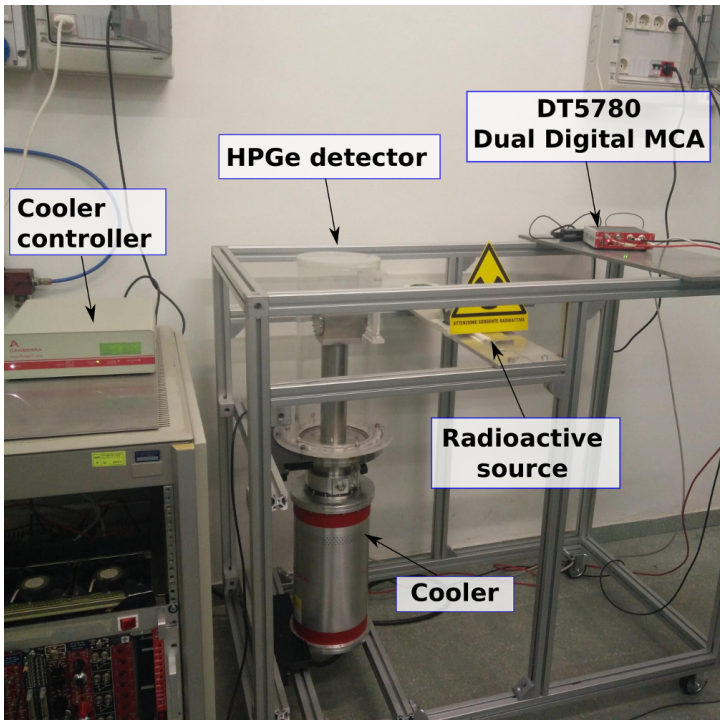

Figure 46: Photo of the set-up used to test the HPGe detector using γ ray sources.

Operational voltage:

The depletion voltage is the reverse-bias voltage at which the detector volume is maximally depleted of free charge carriers. The corresponding volume in the detector is called 'active volume', while the remaining part, in general the surface with the 'dead layer' and electrodes, remains inactive. The operational bias voltage is a conservative value above the full depletion clearing the active volume free of charge carriers. The operational HV recommended by CANBERRA is 2500 V. The detector response was tested as a function of the applied bias voltage performing an HV scans in steps of 100 V from 450 V up to 3000 V. This was done using the 1333 keV γ line of a ^{60}Co source.

The ^{60}Co acts as a volume probe. The high energy photons emitted from the ^{60}Co irradiate directly the whole active volume of the detector being able to fully penetrate into it. Indeed the linear attenuation coefficient in germanium, for a γ of 1.3 MeV is about 0.27 cm^{-1} [43].

The peak position and width remains constant once the depletion voltage has been reached, as shown in Fig.47. The peak width slightly increase for voltages greater than the operational one, due to the rise of the leakage current related to thermionic emission.

The absence of anomalies in the signal response indicates the nonexistence of regions within the HPGe crystal where the charge collection is incomplete.

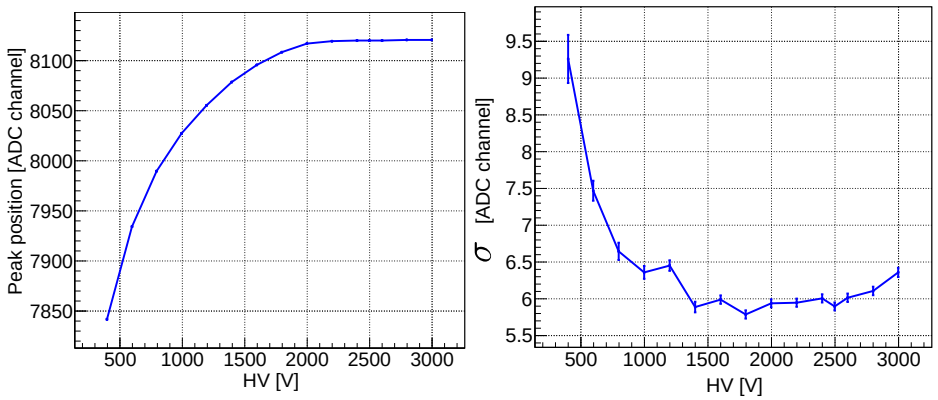

Figure 47: Peak position (left) and energy resolution (σ, on the right) as function of the applied voltage. The signal is provided by the 1333 keV line of a ^{60}Co source.

4.1.2 Optimization of the Signal Digital Pulse Processing

The DT5780 MCA (Multi Channel Analysis) implements a DPP algorithm that represents a digital replacement of shaping amplifier and peak sensing ADC. To obtain this an algorithm has been implemented inside the digitizer FPGA based on the Jordanov trapezoidal filter, [44], and called DPP-PHA (Digital Pulse Processing for Pulse Height Analysis). The trapezoidal filter transforms the typical exponential decay signal generated by a charge sensitive preamplifier into a trapezoid whose flat top height is proportional

to the amplitude of the input pulse (see Fig.48). This trapezoidal filter plays almost the same role of the shaping amplifier in a traditional analog acquisition system. There is an analogy between the two systems: both have a "shaping time" constant and must be calibrated for the pole-zero cancellation. The advantage of using the digital approach is that the user can change the readout parameters according to the detector characteristics, thus enabling the measurement of different radiations with different detectors using the same hardware.

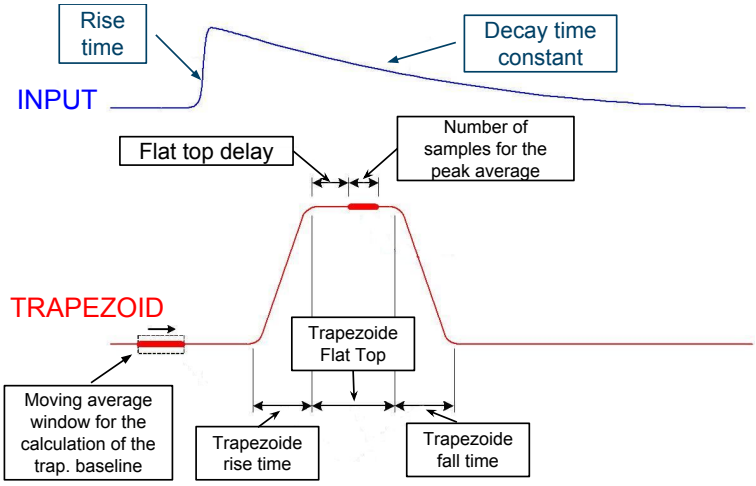

Figure 48: Graphic representation of the trapezoid filter and its main parameters (see[45]).

To achieve the expected high energy resolution with our detector we have tuned the parameters of the trapezoidal filter, the best performances are obtained with the set of parameters reported in Tab.9.

Energy filter parameter	Chosen value
Number of baseline mean samples	16384
Trapezoid flat top [μs]	2
Flat top delay [μs]	1
Number of peak mean samples	16
Decay time [μs]	52.5
Trapezoid rise time [μs]	9

Table 9: This table shows the parameters selected for the measurements

Inside the FPGA of the DT5780 digitizer, there are two parallel branches: one for for the energy, that we have just presented and the other one for timing and triggering. The aim of the Trigger and the Timing Filter (TTF) is to identify the input pulses, generate a digital signal called trigger that identifies the pulse. In Fig.49 is shown a graphic simplified representation of the signals and parameters relative to the TTF and to the trapezoidal filter. The TTF performs a digital RC-CR^2 filter onto the analog signals from the HPGe detector. The zero crossing of the RC-CR^2 signal corresponds to the trigger time stamp. In analogy with a CFD (Constant Fraction Discrimination) the RC-CR^2 signal is bipolar and its zero crossing is independent of the

pulse amplitude. The integrative component of the RC-CR^2 is a smoothing filter based on a moving average filter that reduces the high frequency noise and prevents the trigger logic to generate false triggers on spikes or fast fluctuation of the signals. The derivative component allows to subtract the baseline, so that the trigger threshold is not affected by the low frequency fluctuation. Moreover the pile up effect is significantly reduced.

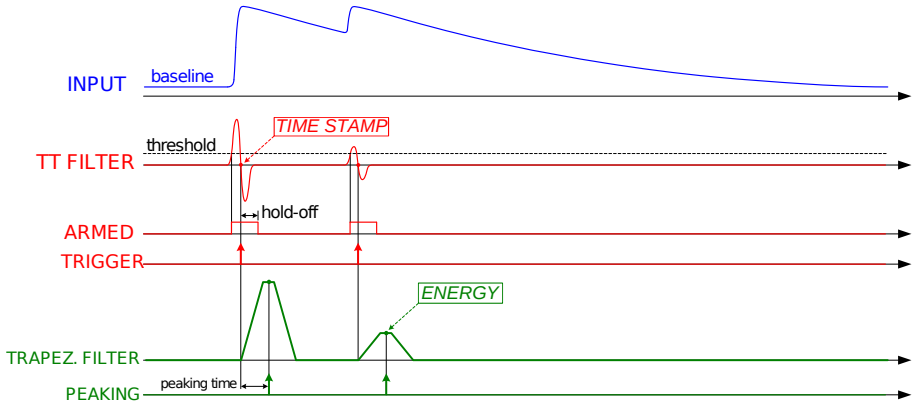

Figure 49: Simplified scheme of the Trigger and Timing filter (red) and the Trapezoidal Filter (green). In blue a graphic representation of an input pulses from a preamplifier [45].

The trigger logic gets armed at the threshold crossing, as shown on Fig.49, then it generates the trigger signal at the RC-CR^2 zero crossing. The threshold value, that corresponds to set the LLD (Lower Level Discrimination) of the energy spectrum, has to be set just below the noise level. Another important parameter for the trigger logic is the RC-CR^2 smoothing, corresponding to the number of samples used for the RC-CR^2 signal formation. In addition, a Trigger Hold-Off is set to inhibit triggers occurring during the RC-CR^2 signal. Finally the Input Rise Time is the time the RC-CR^2 reaches its maximum value. This value should correspond to the rise time of the input signal, in such a way the RC-CR^2 peak value corresponds to the height of the input signal.

The parameters that optimized the Trigger and Timing Filter applied to the HPGe detector signals are reported on Tab.10 and are used in the measurements presented in this section.

Trigger Filter parameter	Chosen value
Threshold [LSB]	300
RC-CR^2 smoothing	2
Trigger Hold-Off [μs]	1.4
Input Rise Time [μs]	0.75

Table 10: In this table are reported the parameters used for the trigger during the measurement

In Fig.50 are reported, as an example, the waveforms obtained during tests with the 511 keV line of the ^{22}Na source. In red is shown the analog signal obtained from the HPGe detector, in black the trapezoid resulting

from the energy filter, in green the peaking, i.e. the time at which the energy is calculated, time where the energy is calculated and in blue the trigger.

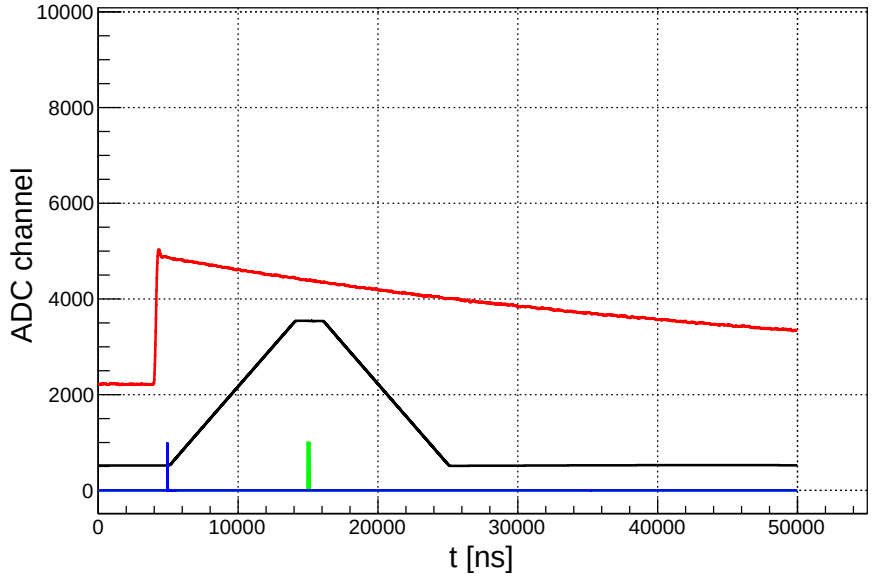

Figure 50: Analog and digital waveforms obtained with 511 keV from ^{22}Na. The reported signals are: the detector analog signal (red), the trapezoid (black), the trigger (blue) and the peaking (green).

Fig.51 shows an example of a spectrum of a ^{60}Co source acquired with the DT5780 and obtained using the optimized parameters for the MCA.

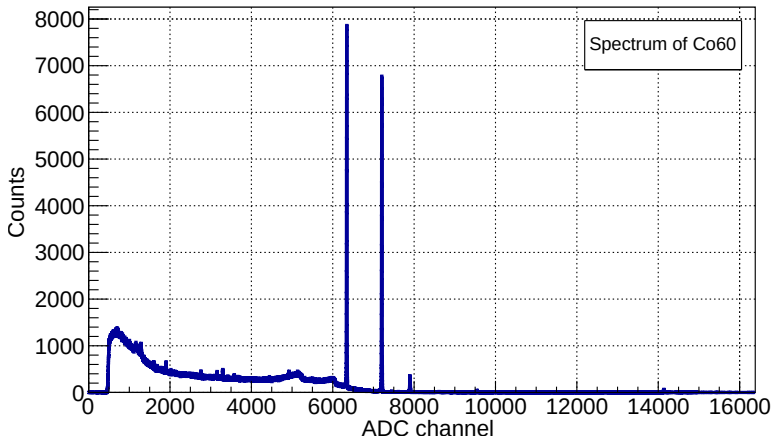

Figure 51: Acquired spectrum of ^{60}Co.

4.1.3 Acceptance test:

The detector acceptance test consisted in verifying the detector performance guaranteed and tested by CANBERRA. In particular have been tested the detector energy resolutions at two different energies: 122 and 1332 KeV. This is done by using ^{57}Co and ^{60}Co sources located in front of the detector at a distance such that the count rate is less than 1000 counts/s and applying the optimized set of signal shape parameters shown in Tab.9 and in Tab.10.

In the starting measurement we found resolutions larger by 35% with respect to what reported by the manufacturer.

To investigate possible noise effects which could produce this discrepancy we studied the baseline of the HPGe signal, i.e. the output in absence of physical signal. The evaluation of the baseline noise makes possible an estimation of the noise present on real signals.

To acquire baseline waveforms we used a random trigger generated by a pulse generator operated at a frequency of 1 kHz and directly connected to the external trigger of the environmental digitizer. Using this random trigger we acquired also few signals due to background radiation. These events were removed in the subsequent analysis by using cuts on the signal amplitude. In Fig.52 are plotted as example some of the selected waveform. As can be seen from the figure, for this baseline study we acquired a larger time interval than for default signal measurements (from 50 μs to 500 μs).

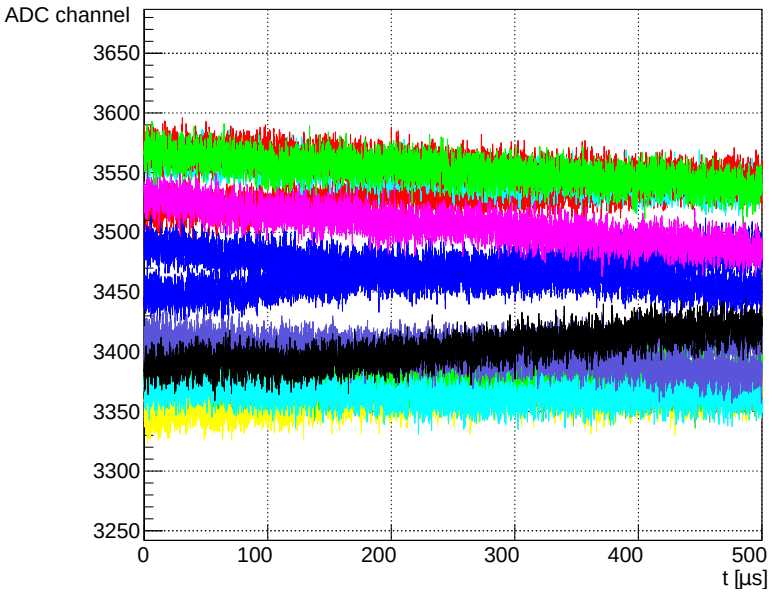

Figure 52: Example of HPGe waveforms acquired with DT5780 selected in order to study the signal baseline.

For different waveforms a linear function is fitted to the baseline to obtain the slope of the waveform. The slope should yield information on noise present on the signal. A negative or a positive slope implies the presence of a noise component with a period compatible with the time window in which the slope is evaluated. We evaluate the slope in different time windows (Δt) observing that the waveform can be considered almost flat, if we evaluate the slope in a small part of the waveform ($\Delta t \sim 25$ μs) or considering the entire waveform ($\Delta t \sim 500$ μs). Calculating the slope in a time interval $\Delta t \sim 150$ μs we obtained a distribution of the calculated slope with a double peak, as reported on Fig.53. This double peak distribution indicates the presence of a noise component.

To have a faster recognition of the problem and a different time scale we decided to study the waveform directly on the oscilloscope and we observed

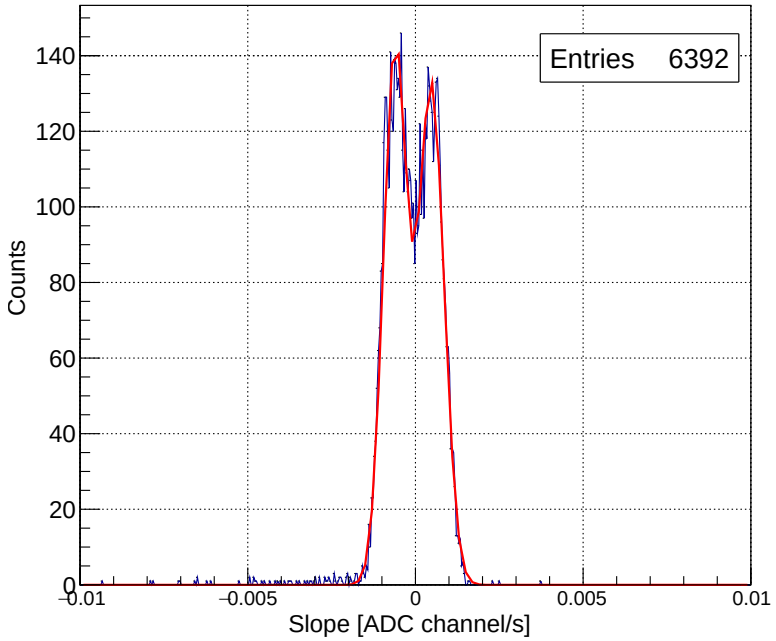

Figure 53: Histogram of the slopes calculated on 6392 waveforms in a range of 15000 points. The histogram presents two peaks that are fitted with two gaussian superimposed with a red line in the graph.

the presence of two different noise components: one at 90 Hz and the other at 15 kHz. The 90 Hz component does not affect the measurement, due to the fact that the oscillation occur on a much longer time scale with respect to the HPGe signals. Instead, the noise component at 15 kHz perturbs the measurement performance having a period comparable to the decay time of the signal. We realized that this noise component was related to ground loops and we removed it by connecting at the same ground all the components: the detector preamplifier, the cooler and the digitizer. In Fig.54 is shown the baseline of a waveform that has the 15 kHz noise component acquired with an oscilloscope LeCroy WaveRunner 64Xi-A.

With this adjustment the resolutions reported in Tab.11 were measured, these are in agreement with those reported by CANBERRA. The results were converted into keV scale by using the energy calibration, which will be described in Sec.4.2.4.

	122 keV FWHM[keV]	1332 keV FWHM[keV]	1332 keV FWTM/FWHM	1332 keV FWFM/FWHM
Measured	1.225 ± 0.005	2.082 ± 0.017	1.8 ± 0.1	2.8 ± 0.1
Guaranteed	1.35	2.35	2.0	3.0
CANBERRA	1.25	2.05	1.9	2.65

Table 11: Resolutions guaranteed by contract and actually measured by CANBERRA compared to our measurement.

The resolutions were obtained fitting the signal peak with a sum of a gaussian function and a straight line, used to describe the background. The fit function, relative to the 1332 keV line, is plotted in black on Fig.55

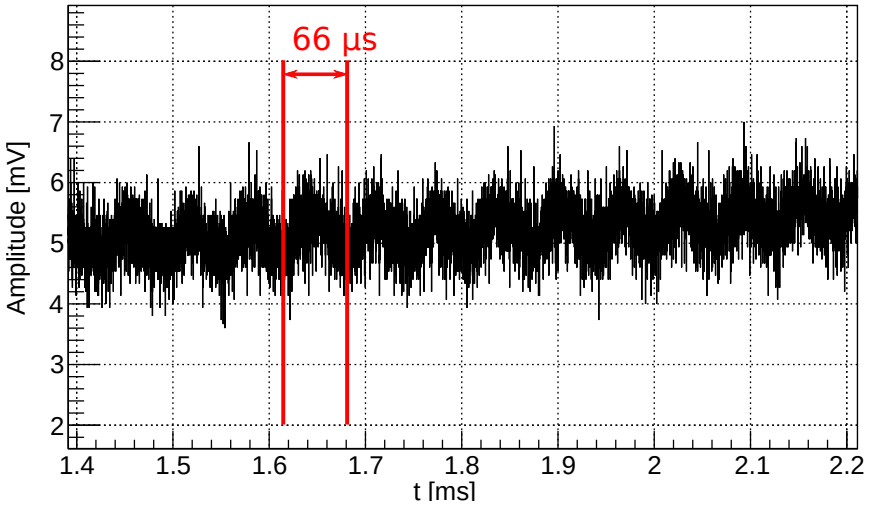

Figure 54: Waveform acquired with the oscilloscope that shows the 15 kHz noise component.

together with signal (red) and background (green). We notice that the peak shape is not exactly a Gaussian distribution, but has an asymmetric shape with a tail in the low-energy side of the distribution. The tail can arise from several physical effects [46], including imperfect charge collection in some regions of the detector, or secondary electron and bremsstrahlung escaping from the active volume. A method of specifying the severity of tailing is to quote the full width at one-tenth maximum (FWTM) of the full-energy peak, in addition to the more conventional full width at half maximum (FWHM). Another index even more sensitive to tailing is the ratio of the full width at 1/50 maximum (FWFM) to the FWHM. We have checked that this two indices, measured at 1.332 MeV, were consistent with the ones expected for good germanium detectors (2.5-3.0 [46]), as can be seen from Tab.11.

4.1.4 Energy linearity and calibration

In Fig.56 it is shown an example of a typical spectrum acquired with the HPGe detector obtained with a ^{60}Co source. This energy spectrum is expressed in ADC channels, the channel number is proportional to the gamma energy, so the channel scale can be converted to an energy scale. To calibrate the detector energy scale, the HPGe has been exposed to standard radioactive sources with known gamma-ray energies. The used sources are the following: ^{57}Co, ^{60}Co, ^{152}Eu, ^{207}Bi, ^{137}Cs and ^{22}Na (only the 1274 keV peak).

In a typically obtained spectrum, as shown in Fig.56 for the case of ^{60}Co, together with the more intense peaks corresponding to the decay radiation line, we can observe the presence of some peaks originated from the environmental background radiation. In particular around 8000 ADC ch is visible the ^{40}K line. By acquiring a spectrum when no source is present (displayed on the top right of Fig.56) the background radiation spectrum can

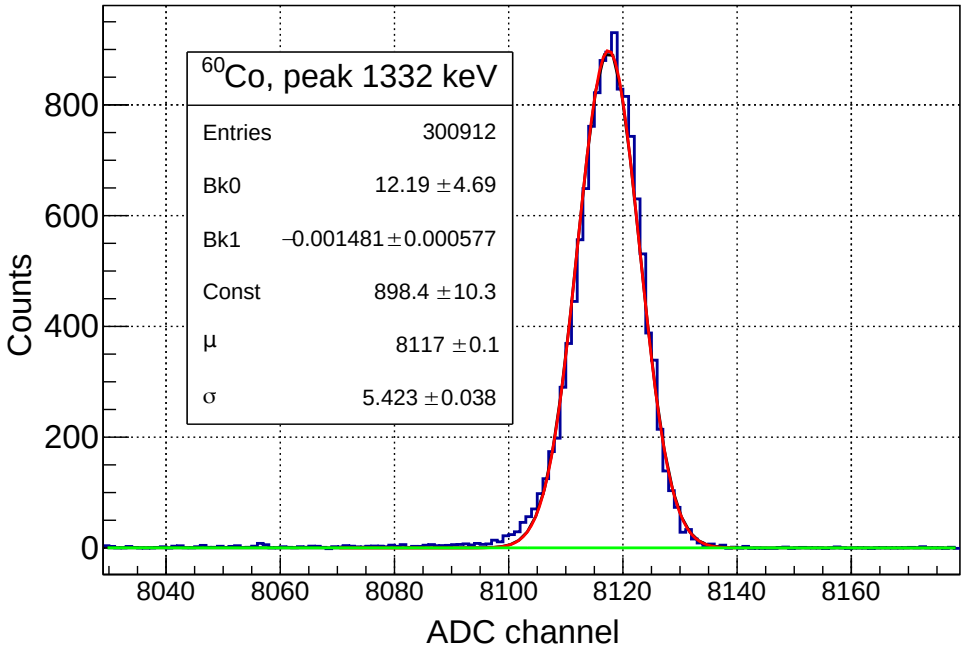

Figure 55: The fit result of the 1332 keV peak. In black is plotted the final fit function, in red a gaussian function that describes the peak and in green a line that is used to fit the background.

be obtained to be later subtracted from the signal spectrum, after proper normalization to account for different acquisition times.

To cover the energy range of the electrons produced at the low-energy line at ELI-NP ($\sim 1 - 3.5$ MeV) that will be measured by the HPGe detector, it will be necessary to use two different input ranges for the ADC of the digitizier. In particular the used input dynamics, selectable via software, are the ranges up to 0.6 V and to 1.4 V. We gathered two different calibration curves for the two dynamics ranges.

The peak positions in keV versus the peak positions in channels obtained for all the sources with the 0.6 V range are plotted in Fig.57. To obtain the energy calibration function a linear fit has been done. We also verified that a fit with a quadratic function is not necessary. The resulting calibration functions is:

$$\text{energy[keV]} = -0.0132 + 0.1642 \cdot \text{[ADC channel]} \tag{12}$$

In the bottom of Fig.57 are reported the residuals calculated as difference between the observed values and the predicted ones from the linear fit. We obtained residuals values lower than 0.7 keV verifying the excellent detector linearity in this energy range.

We evaluated the calibration function also for the higher input range of the digitizer up to 1.4 V, obtaining the following linear calibration:

$$\text{energy[keV]} = 0.085 + 0.425 \cdot \text{energy[ADC channel]} \tag{13}$$

In this case only a part of the ADC range could be tested given the limited energy available with the radioactive sources. The achieved calibration curve

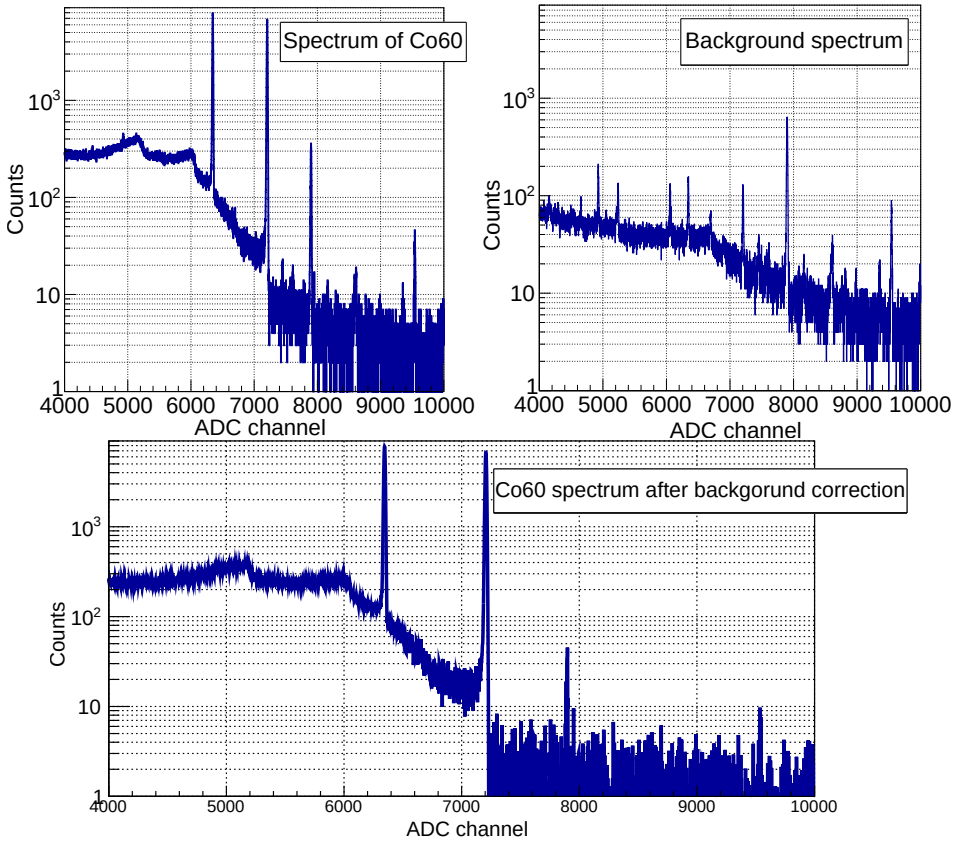

Figure 56: This figure presents a typical ^{60}Co spectrum before (top left) and after (bottom) the process of background subtraction. The background spectrum is also shown on the top right.

and residual values are reported in Fig.58. Again it was checked that a quadratic term is not necessary in the fit procedure.

To test the stability in time of the detector response this measurement has been repeated after about one month. We retrieved the same slope of the linear fit, compatibly with the error, that indicates a good detector stability. The stability of the detector will have to be tested from time to time during normal beam operations, when the detector will be installed in the vacuum chamber and not directly accessible. To do that we plan to use a ^{60}Co source placed outside the vacuum chamber. The feasibility of this procedure has been verified by placing the source behind a 5 cm lead shield at the same distance from the detector that we expect during the experiment. This lead thickness provides the same attenuation of the different layers of the vacuum chamber. We verified that the peak signal is enough populated to be well-identified with respect to the background.

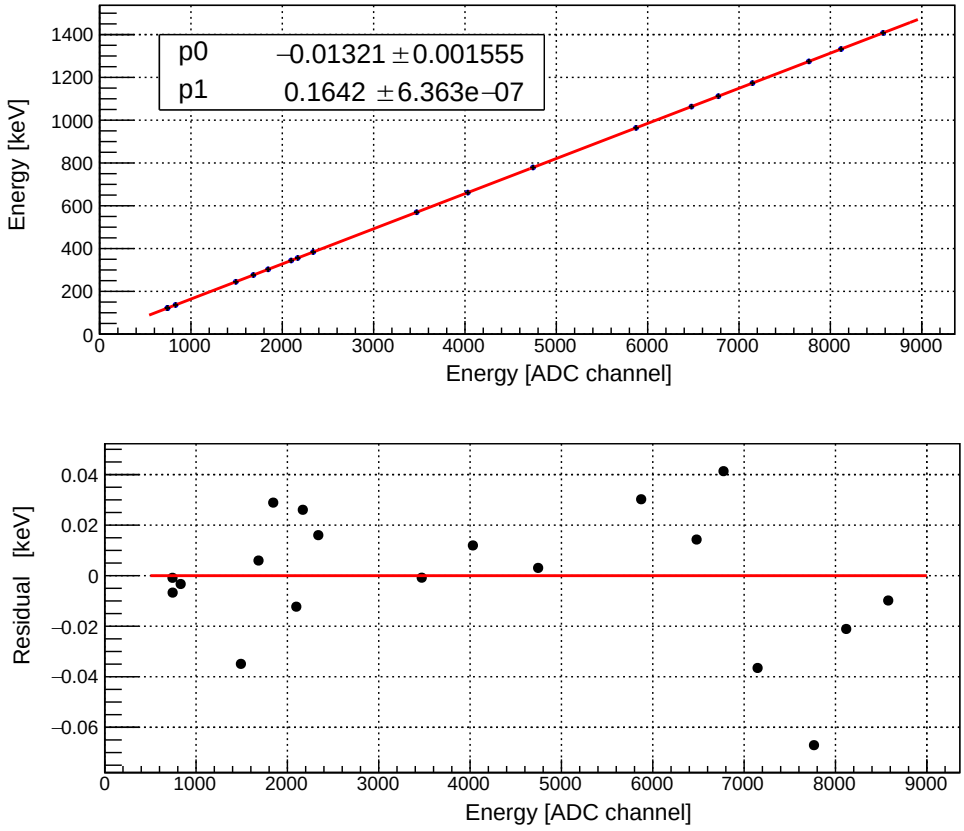

Figure 57: In the top graph is shown in red the obtained HPGe calibration curve for the 0.6 V range. In the bottom one is reported the graph of the residuals.

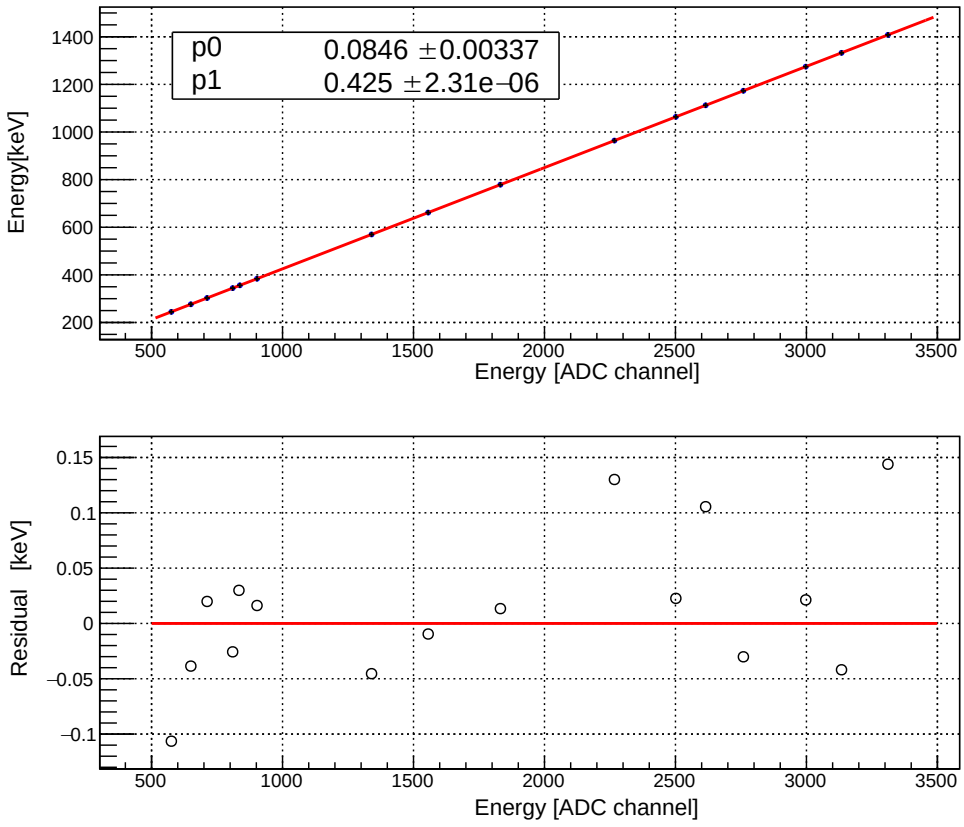

Figure 58: The HPGe calibration curve for the 1.4 V input range is presented in the top graph, while the residuals are shown in the bottom one.

4.1.5 Energy resolution

The dominant characteristic of germanium detectors is their excellent energy resolution. The overall energy resolution achieved in a germanium detector is normally determined by a combination of three factors: the inherent statistical spread in the number of charge carriers ($FWHM_D$), variations in the charge collection efficiency ($FWHM_X$), and contributions of electronic noise ($FWHM_N$). Which of these factors dominate depends on the energy of the radiation and the size and inherent quality of the detector in use. The full width at half maximum, (FWHM), of a peak can be expressed as follows[46]:

$$FWHM^2 = FWHM_D^2 + FWHM_X^2 + FWHM_N^2 \tag{14}$$

The first of these factors, $FWHM_D^2$, represents the inherent statistical fluctuation on the number of charge carriers created and is given by

$$FWHM_D^2 = (2.35)^2 F\epsilon E \tag{15}$$

where F is the Fano factor F=0.1, ϵ is the average energy necessary to create one electron-hole pair $\epsilon = 2.96$ eV and E is the gamma-ray energy. This factor set the lower limit on the energy resolution which can be achieved.

The contribution of the second term, $FWHM_X^2$, is due to incomplete charge collection and is most significant in detectors of large volume and low average electric field in the depletion region. This is not our case and this contribution is negligible.

The third factor, $FWHM_N^2$, represents the broadening effects of all electronic components following the detector. Also this contribution is minimal for HPGe detectors given the fact the preamplifier is kept at cryogenic temperature with the crystal.

The detector energy resolution was tested at different energies, using the following sources: ^{57}Co, ^{60}Co, ^{152}Eu, ^{207}Bi, ^{137}Cs and ^{22}Na (only the 1274 keV peak). The energies resolution obtained using a dynamical range of 600 mV are presented in Fig.59 as a function of the gamma ray energies. The dominant $FWHM_D^2$ term is proportional to the gamma energy, as reported on eq.15. Therefore we used the following fit curve: $FWHM = p0 + p1 \cdot \sqrt{E}$, which is displayed in red in Fig.59.

It has been tried to give an estimation of the contribution, $FWHM_N$. Usually its magnitude can be measured by supplying the output of a precision pulser to the preamplifier and recording the corresponding width of the peak in the pulse height spectrum. Trying this approach we obtained an electronic noise term greater than the total FWHM. An inspection to the acquired waveforms shows a large ringing on the test input that is due to the fact that the preamplifier output signal, obtained with the pulser connected to the test input of the preamplifier, is not correctly adapted (see Fig.60). This effect is probably related to a change made by CANBERRA to the preamplifier in order to solve a microphony problem.

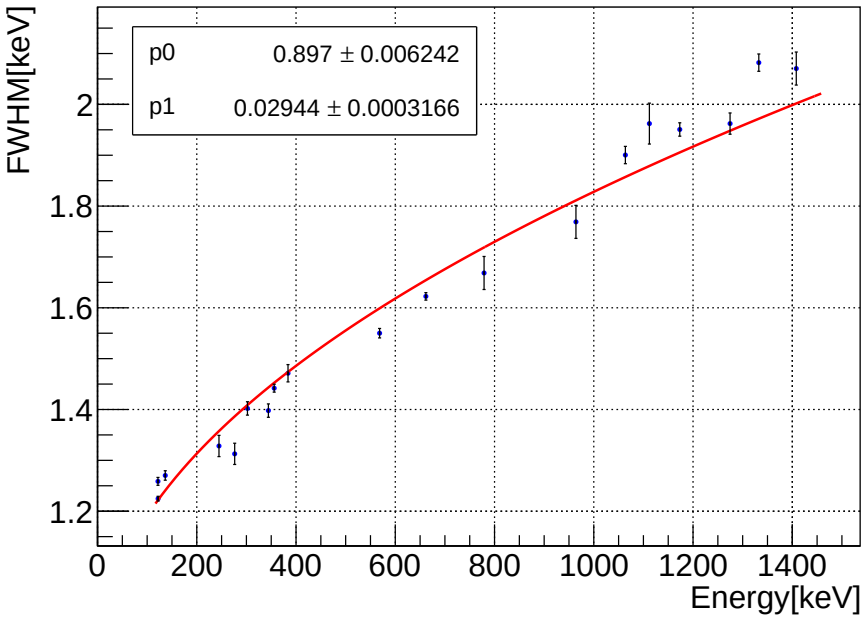

Figure 59: In this graph is represented the detector energy resolution as function of the incident gamma energy.

4.1.6 Pulser test

To have a fast feedback from the preamplifier in case of anomalies during data taking, when the experimental hall is not accessible and to provide a stability check of the electronics, we plan to connect the test input of the preamplifier PSC761 to a Tektronix AFG1062 arbitrary function generator. We therefore carried out tests on the preamplifier response to the pulser.

Due to the signal distortion operated by test channel of the preamplifier, we started by identifying the shape of the input pulse which produces the "best" preamplifier response in terms of trapezoidal signal. In particular a trapezoidal with a correct pole zero without effects of undershoot or overshoot and with a flat top region really flat. The waveforms used as test are a sine, a square, an exponential fall and a pulse. We found that the best output signal is obtained with a pulse of frequency 100 Hz, width 250 μs and amplitude in a range from 3 to 9 V. The trapezoidal filter obtained with this input waveform has the most correct pole-zero and flat top region as shown in black in Fig.60. In addition, in Fig.60, are presented in red the output signal obtain with 3 V pulse, in blue the trigger position and in green the peaking position.

The ripples present on the signal prevent to use the same optimal set of parameters used for the detector characterization (Tab.9), using those parameters we observed that the trigger fires on the oscillation of the input signal. To avoid this effect we increase the RC-CR^2 smoothing factor from 2 to 4 to average the noise samples and the trigger hold-off from 1.4 μs to 3 μs.

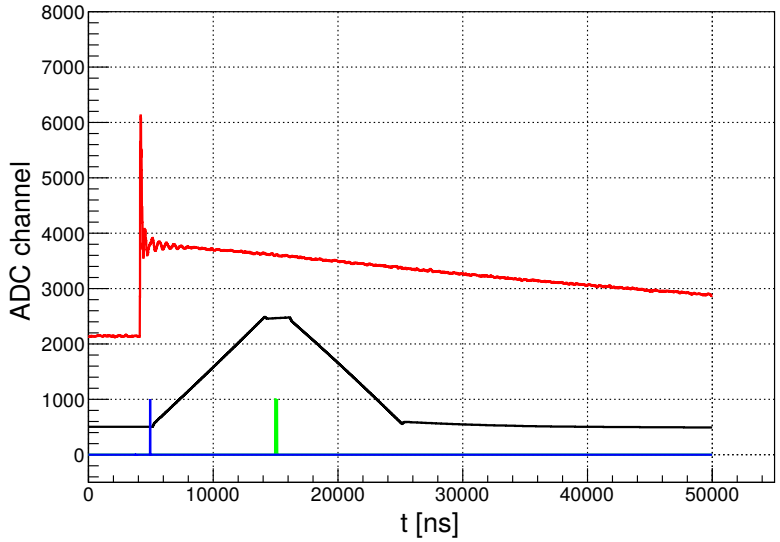

Figure 60: This plot shows the waveform provided by a 3 V step signal given in input to the test channel of the preamplifier. The ringing on the rising edge indicates a problem on the test channel. The trapezoid is shown in black while the trigger and peaking time are shown in blue and green, respectively.

We found that the peak position of the pulser signals does not depend linearly with the pulse amplitude. The result obtained using a linear fit is reported on Fig.61. The obtained residuals, plotted on the bottom, are distributed according to a non-random pattern (U-shaped), suggesting a better fit for a non-linear model. In particular we found that the best calibration curve for the pulser response is a quadratic function. Using this quadratic function we obtaining the following calibration curves:

$$\text{Peak[ch]} = -58 + 686 \cdot \text{INPUT[V]} - 3.03 \cdot (\text{INPUT[V]})^2; \qquad (16)$$

for the dynamic range of 600 mV for the DT5780, using the other dynamical range up to 1400 mV we obtained:

$$\text{Peak[ch]} = -30.3 + 267.3 \cdot \text{INPUT[V]} - 1.36 \cdot (\text{INPUT[V]})^2. \qquad (17)$$

In order to verify if the observed non linearity is due to the pulser used we studied the preamplifier response also with two other pulse generator models: the Agilent 33220A and the Hewlett-Packard 8112A. We found that also with those pulse generators we obtained the same trend, therefore we conclude that the non linearity is due to the non linearity of the input pulser signals, that have an accuracy of only about 1%.

We tested the dependency of the HPGe energy spectrum from the external temperature acquiring the pulser signal in combination with the signal due to the γ emitted by a ^{22}Na source. This temperature dependency is mainly related to the preamplifier that is at the ambient temperature. The two top graph on Fig.62 show the position of the peak relative to the lines at 511 keV and at 1274 keV of the ^{22}Na source; the bottom ones show the result for

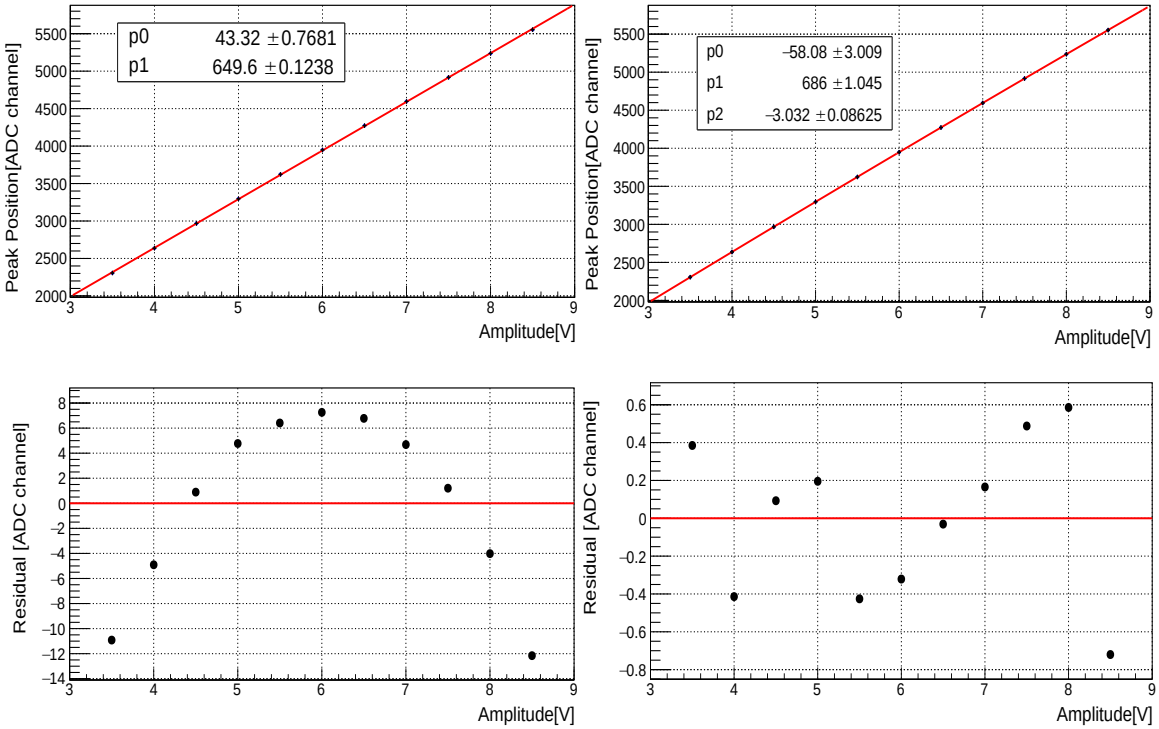

Figure 61: The peak position as a function of the amplitude of the pulse signal, superimposed in red the linear fit function (top left plot) and the corresponding residuals (bottom left plot). On the right are shown the same data fitted with a quadratic function and the relative residuals.

the pulser peak. These quantities are plotted as a function of the measured temperature.

From this measurement it is possible to observe that the signal of the HPGe detector has a very slow dependence on the temperature, indeed a change of 5 °C correspond to a shift of 1 ADC channels in the peak position. The pulser peaks have a similar temperature dependencies, therefore the monitoring of the pulser peaks position can be used to check any variations related to the temperature change.

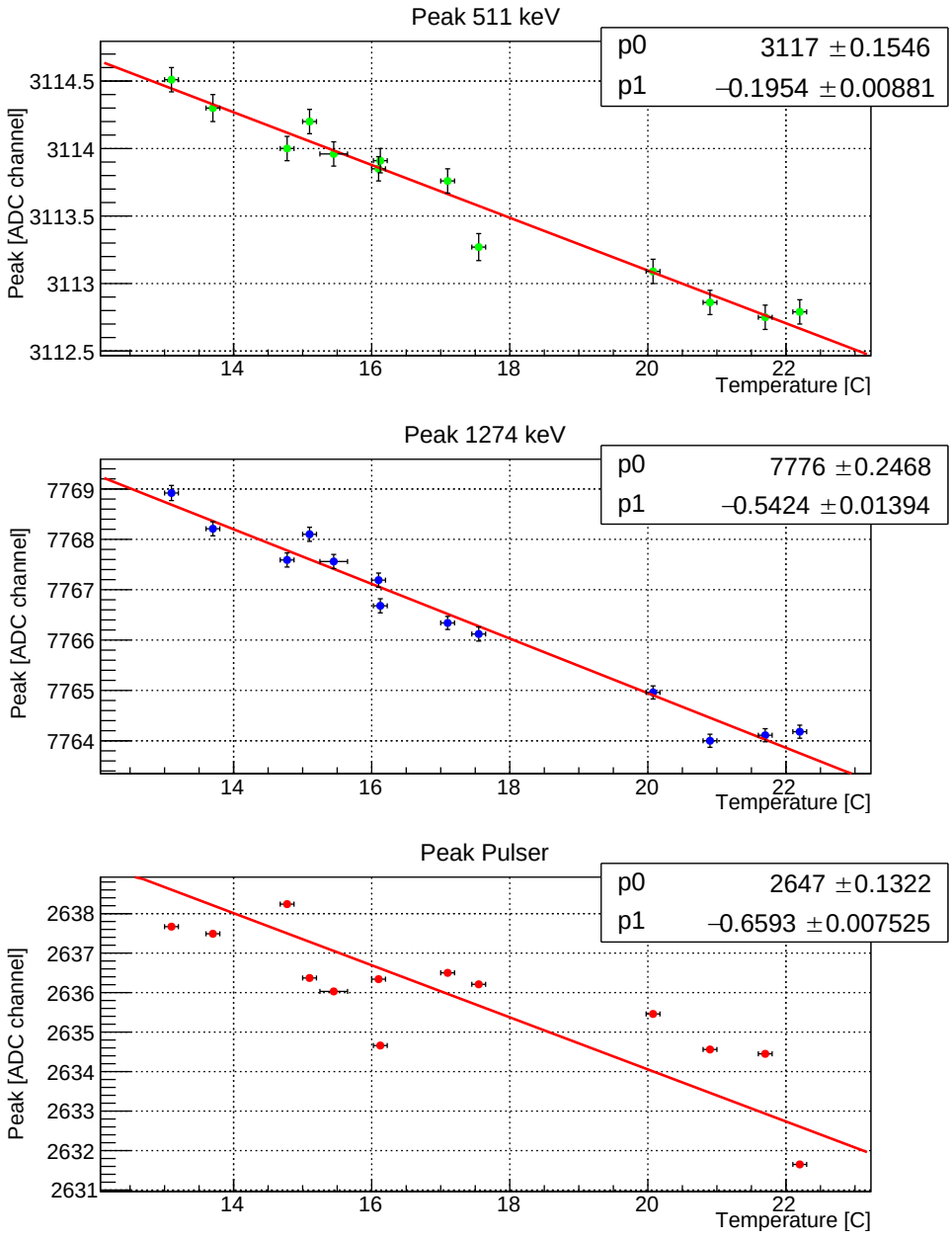

Figure 62: Peak positions of the γ lines at 511 (top) and 1274 keV (middle) of the ^{22}Na source and of the pulser (bottom) as a function of the room temperature.

4.1.7 Test with e^-

The uncertainty in the energy lost by the e^- traversing the HPGe dead layers, namely the Be window and the inactive region of the crystal contact, is one of the biggest source of systematic uncertainty (as explained in Sec.3.3.3) in the determination of the beam energy. The average values, obtained with MC simulations, will be added to the energy measured by the HPGe in order to partially compensate the loss.

To test the accuracy of the HPGe MC simulations, in particular the thickness of the dead layers used in the geometry description of the detector, we exposed the HPGe to a ^{207}Bi source whose characteristics is to emit e^- with a definite energy.

Electron tests set-up

The decay of ^{207}Bi produces X-rays, conversion electrons and γ rays over a wide energy range. The conversion electrons emitted by ^{207}Bi source permit to test the HPGe detector response with electrons of definite energy. In Fig.63 the conversion electron spectrum of ^{207}Bi is shown [47]. In the figure is also presented the decay scheme of ^{207}Bi, reporting the energies of the main emitted γ. The ^{207}Bi source is sandwiched between two 6.4 μm thick Mylar foils, in which the conversion electrons loose only about 1.6 keV energy.

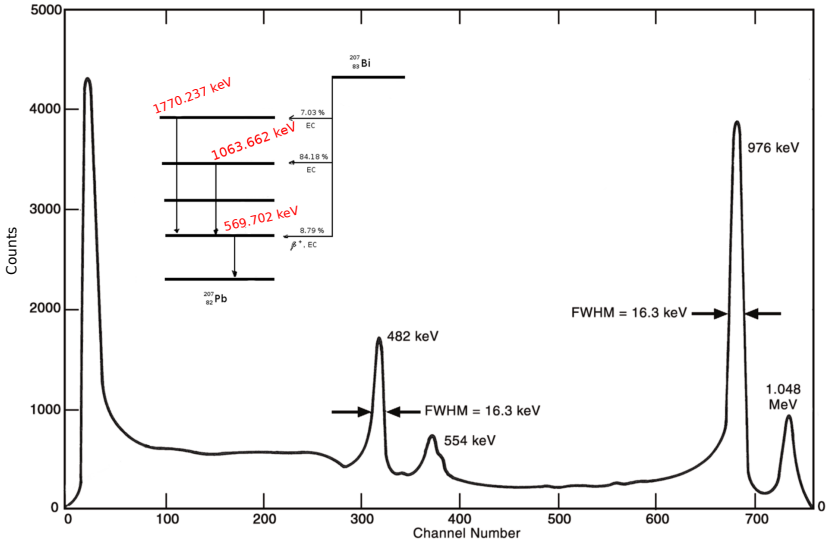

Figure 63: The conversion electron spectrum for ^{207}Bi.

To optimize the performance of the tests with electron, the measurement has been done in vacuum. A custom vacuum capsule to host the detector has been realized. In Fig.64 are shown two photos of the small vacuum chamber used for the detector tests. The chamber has a movable source holder that permits to put the ^{207}Bi in front of the detector at a distance of about 17 cm from the entrance window and exactly in the center. Using the movable target holder it is also possible to scan the entrance window with step of

about 2.5 cm. The vacuum obtained inside the chamber is a rough vacuum with a measured pressure of 30 mbar.

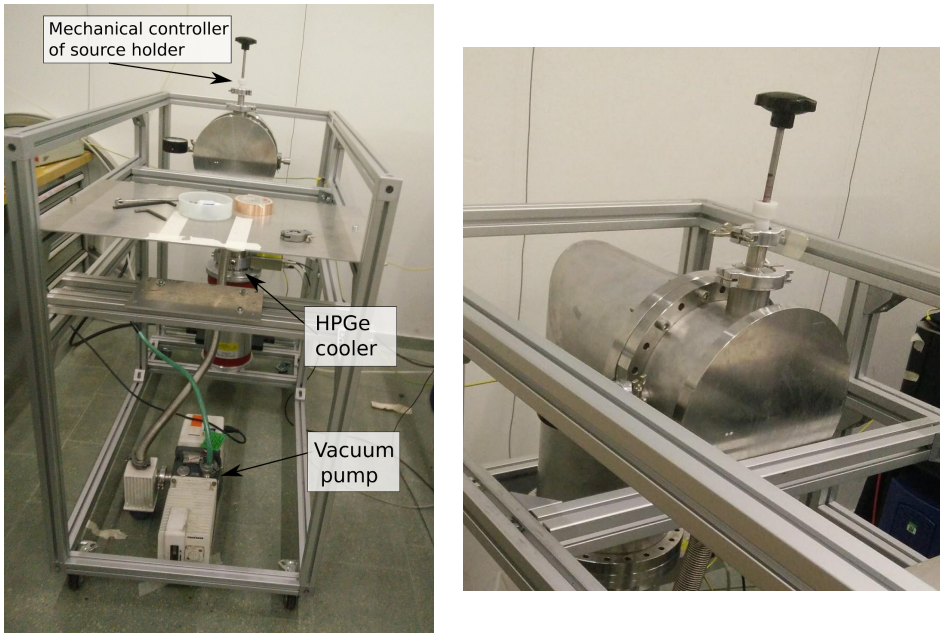

Figure 64: On the left is shown the HPGe detector enclosed in the vacuum capsule. In the right is shown a zoom on the vacuum chamber that permit to clearly see the mechanical controller of the source holder.

Test results

Comparison between the acquired energy spectrum and the simulated one obtained with ^{207}Bi directly put in front of the detector, is shown on Fig.65. The spectra were normalized using the amplitude of the electron peak at 976 keV. The two main γ lines, at 569.7 keV and 1063.6 keV, are clearly visible in the spectrum and are the highest energetic peaks of the group around 500 keV and 1000 keV. The K,L and M conversion electron lines relative to the 1063.6 keV γ lines can be identified in the spectrum, while the electron peaks relative to the 569.7 keV are not so clear due to the overlap with the Compton spectrum.

We obtained a good agreement between the overall features of the simulated and measured spectrum, although some differences are observed in some parts of the spectrum, especially in the Compton shoulder region. These differences between simulation and experiment might be due to inaccuracies in the geometry description.

We are interested in particular in the study of the position of the peaks related to the electrons. To verify the agreement between the measurement and the simulation, a fit procedure has been implemented. The fit function used for the peak expected at 976 keV, plotted in black on Fig.66, is the sum of a Crystall ball function with an exponential one. The Crystall ball, with its asymmetric left tail, is used to fit the peak while the exponential is used for the background (green line). In Tab.12 are shown the results.

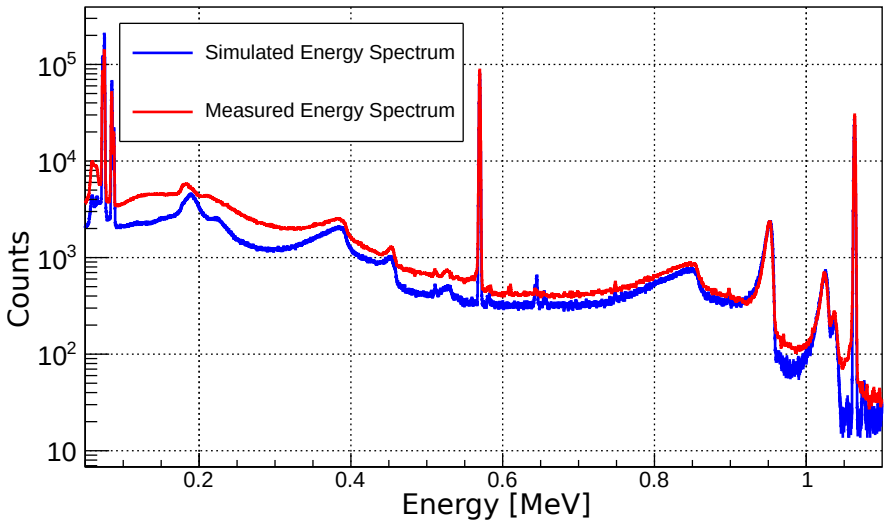

Figure 65: Comparison between experimental and simulated spectra of ^{207}Bi, for the HPGe detector. The measured spectrum is plotted in red while the simulated one, is shown in blue.

The measured peak position that is about 952 keV, as reported on Fig.66 and table Tab.12, is lower than the expected energy of the conversion electron (976 keV) due to the energy loss in the inactive layers of the HPGe detector and in excellent agreement with the simulated one.

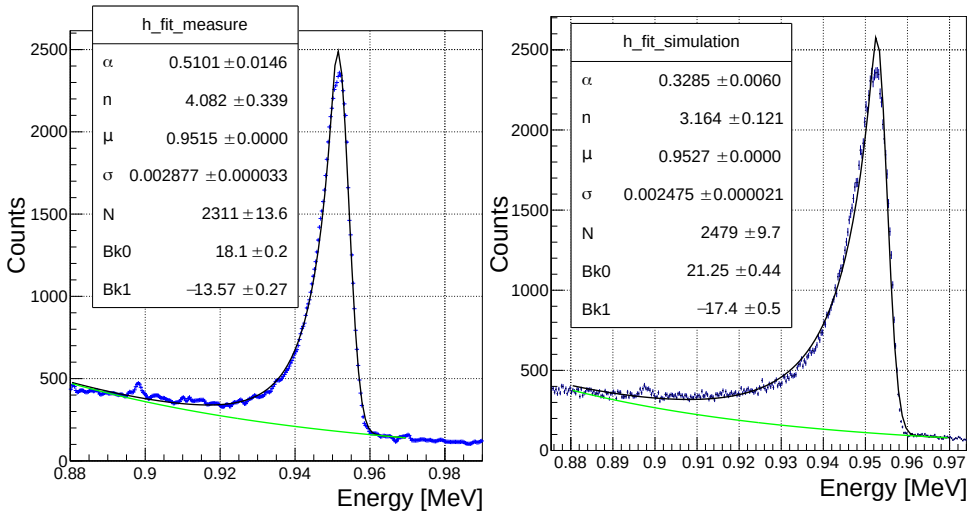

Figure 66: In the figure are shown the results of the fit performed on the acquired spectrum (left) and on the spectrum predicted by the MC simulation (right). The black line represent the fit function, that is a sum of a CB for the signal and an exponential (green) for the background.

We verified this agreement for all the electrons peaks. The only lines that we are not able to distinguish from the background are the L and M conversion lines around 554 keV. In Fig.67 are presented the fit results of the measured e^- peaks: on the left the ones relative to the K line at 482 keV and on the right those associated to the L and M lines at 1048 and 1060

keV, respectively. To correctly describe the measured spectrum, we used a gaussian fit function for the peak at 1060 keV, and a Crystall ball function for the 482 and 1048 keV.

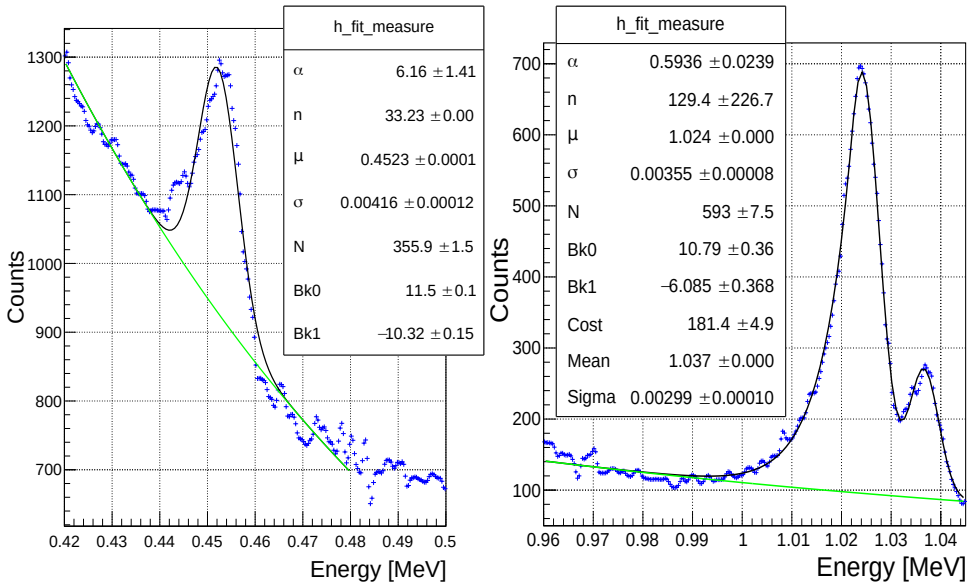

Figure 67: In the figure are shown the results of the fit performed on the acquired spectrum of 482 keV, on the left; of 1048 and 1060 keV, on the right. The black line represent the fit function, that is a sum of a Crystal Ball or of a Gauss function with an exponential one for the background (green line).

In table 12 are reported the fit results for both the measured and the simulated spectrum. The measured peak positions are in agreement with the simulated ones with a precision better than 1 keV confirming the correctness of the thicknesses implemented in the simulation geometry. The MC simulation describe well also the width of the peaks (σ), for which we measured values that differ less than 0.4 keV from the expected ones.

e^- peak	DATA		MC	
[keV]	μ [keV]	σ [keV]	μ [keV]	σ [keV]
482	452.3 ± 0.1	4.16 ± 0.12	452.5 ± 0.2	4.46 ± 0.19
976	951.46 ± 0.04	2.88 ± 0.03	952.67 ± 0.03	2.48 ± 0.02
1048	1024.1 ± 0.1	3.55 ± 0.08	1025.05 ± 0.07	3.38 ± 0.07
1060	1036.6 ± 0.1	3.0 ± 0.1	1037.11 ± 0.07	3.12 ± 0.08

Table 12: In this table are reported the peak positions (μ) and widths (σ) relative to the conversion electron peaks of a ^{207}Bi source measured (left column) and expected from the MC simulation (right column).

Furthermore we verified that moving the source vertically of 20 mm from the detector centre close to the border regions of the entrance window the peak position and width do not change, according to what is foreseen by the MC simulation.

We also acquired an energy spectrum with the silicon strip detector placed between the ^{207}Bi source and the HPGe detector. This will be the operating

configuration of CSPEC, although in that case the energy lost in the silicon layer will be estimated from the recorded signal. In Fig.68 are shown for comparison the spectra (in the region around 1 MeV) obtained when the source is placed directly in front of the HPGe (left plot) and when the Si-Strip detector is inserted (right plot). The simulated spectra relative to the electrons (green) and to the gamma particles (black) are also shown. The energy loss inside the silicon strip by the electrons of 976 and 1048 keV shifts the position of their peaks under the more intense Compton edge of the 1063 keV γ spectrum as can be seen clearly looking the graph reported on the right of Fig.68.

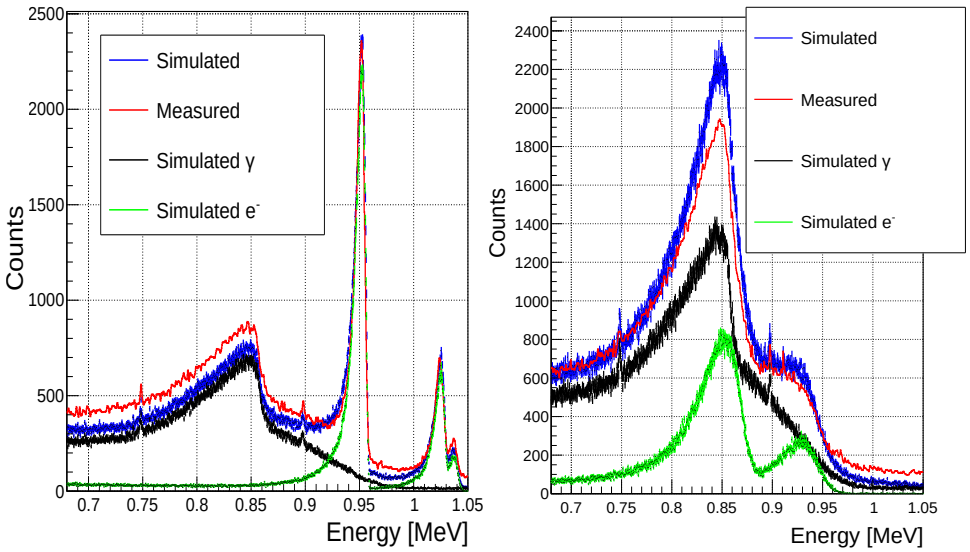

Figure 68: On the left are shown the spectra relative to HPGe detector directly exposed to ^{207}Bi source, on the right is presented the case where the Si-strip detector is inserted between the source and the HPGe. The red line represents the measured spectrum, the blue the simulated ones and in black and green are reported the contribution due to γ and to electron obtained from simulation.

To reconstruct the electron peaks from the measured energy spectrum (red lines on Fig.68) we subtract the simulated gamma spectrum (black lines on Fig.68) from the acquired one. We firstly tested this procedure with the spectrum obtained without the insertion of the Si-strip detector, in this case the e^- peaks are clearly visible over the background. The obtained spectrum is reported on Fig.69. Notice that the peak of the reconstructed e^- spectrum overlaps both the simulated and the measured electron peaks confirming the goodness of the procedure.

The same method has then been applied to the case with the silicon detector inserted, the results are shown in Fig.70 for real data (left plot) and simulated events (right plot). The peaks appear shifted by about 130 keV, the amount of energy loss inside the 300 μm thickness of the silicon. Again we observe an agreement at the keV level between data and simulation, confirming the accuracy of our MC simulation.

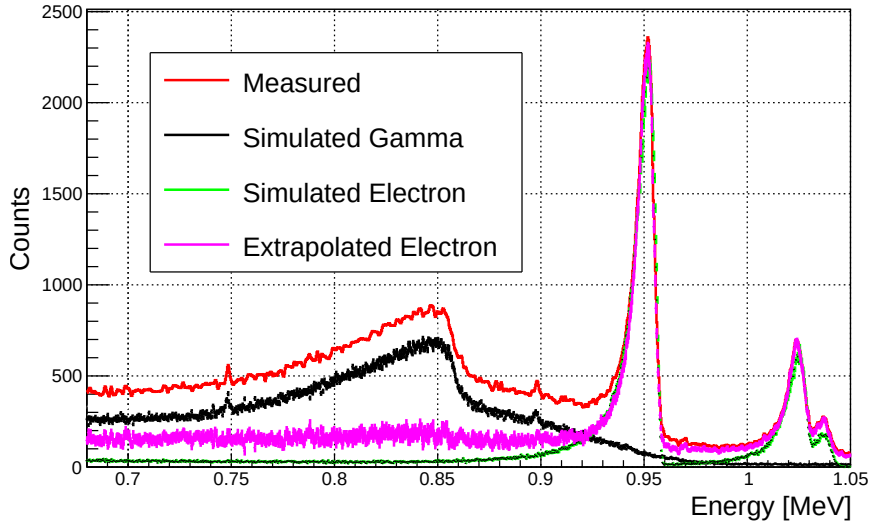

Figure 69: This figure is the same graph reported in the left of Fig.68 with the addition of the extrapoled electron spectrum plotted in grey. This spectrum is obtain from the subtraction of the gamma simulated spectrum (black) from the measured ones (red).

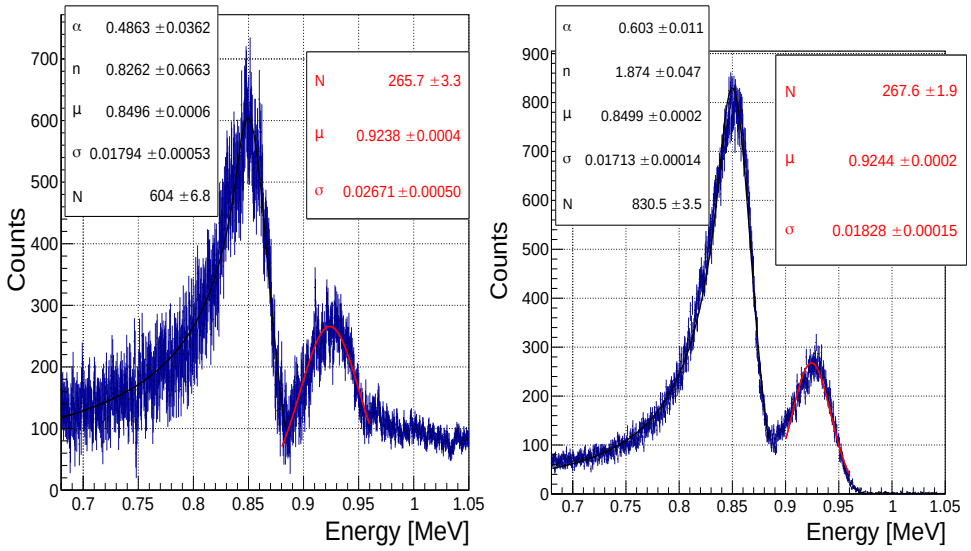

Figure 70: In this graphs are reported the fit results of the e^- peaks obtained by subtracting the γ spectrum from the measured (left) and simulated (right), when the Si-stip detector is inserted between the source and the HPGe. The peak at 850 keV is fitted with a Crystall ball (black), while the one at 924 keV is fitted with a gaussian function (red). The shift of about 130 keV with respect to the original position is due the the energy loss by the e^- traversing the 300 μm of silicon.

4.2 PHOTON DETECTOR TESTS

In this section the results of the characterization tests performed on the photon detector of the CSPEC are illustrated. We present a selection method that permits to identify the signals due to photons from those due to alpha particle and noise background (Sec.4.2.2). As already explained

in Sec.3.5, in the real experiment the coincidence between the MaPMT dynode signal and the HPGe output will be used to create the global DAQ trigger. This coincidence has been studied and the threshold to be applied to the CF discriminator has been optimized (Sec.4.2.3). Using these cuts and the trigger threshold, the calibration curves and the energy resolution of the scintillators composing the photon detector were obtained (Sec.4.2.4). Finally, the possibility of use the intrinsic α radioactivity of BaF_2 to monitor eventual gain variations of the electronics chain is explained in Sec.4.2.5.

4.2.1 Experimental set-up

The detector response has been tested using γ emitted from radioactive sources positioned on a movable slit, as shown on Fig.71. The slits are used to perform tests on the 16 detector's crystals, positioning the radioactive source in front of each crystal.

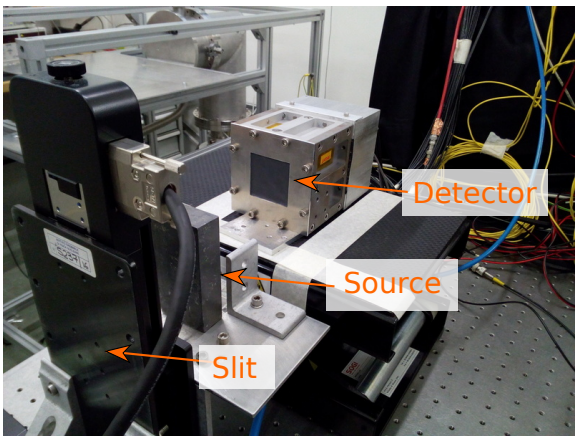

Figure 71: Set-up used to perform the characterization of the BaF_2 crystals

The BaF_2 detector is powered at -1000 V using the CAEN HV board A1536DN [48] with a measured current of about 500 μA. The read-out electronics is powered with $\pm$ 5 V using two floating channels of the CAEN A2518 boards [49].

In this section are presented the characterizations of each single crystal; hence we could have used the single channel output to trigger the data acquisition. However we used the dynode output in order to work in the same conditions that will be used in the experiment.

The data acquisition is based on CAEN V1742 switched capacitor digitizer (see Sec.3.5 for detail) working at a sampling rate of 1 GHz in order to acquire 1024 ns to fully contain the 630 ns corresponding to one decay constant of the BaF_2 scintillation light and 150 ns before the signal start, this part is used for the baseline calculation. Then the particle energy is computed doing the sum of the signal in an interval of 1 μs.

4.2.2 Event selection

The ratio between the fast and slow decay components of BaF_2 depends upon the incident particle type and, generally, decreases for heavier particles [50, 51]. In particular, the fast component of the scintillation light is absent in the light induced by the alpha particles [36]. Therefore, we investigated the possibility to use the signal shape to discriminate between signals produced by γ and those due to α particles (the intrinsic radioactivity of the crystal) or those due to thermal noise.

The thermal noise results from thermionic electrons that are spontaneously emitted by the photocathode. Therefore, no emission of scintillation light is related to this kind of signal which is like an isolated spike without the two decay components.

For the pulse shape discrimination we use the radio (R) between the maximum value of the fast component (f) and the average of the slow component (<s>) calculated between 20 ns after the occurrence of f and the end of the signal. The quantity R is defined as:

$$R = \frac{f}{< s >};$$

The meaning of this values is explained in Fig.72, where a typical signal obtained with γ from ^{22}Na is displayed.

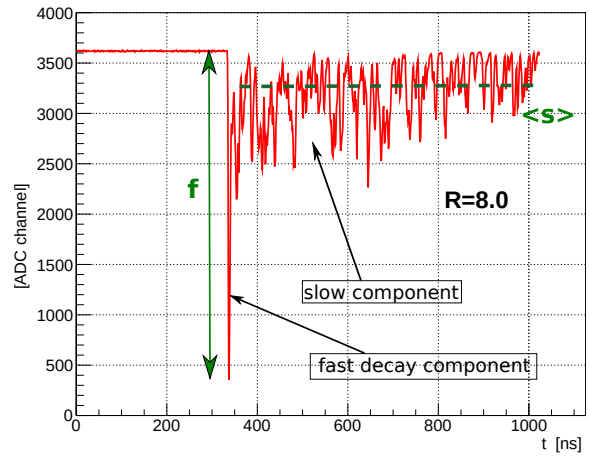

Figure 72: Typical detector signal obtained with photons. In the plot is shown the meaning of the quantities f and <s> used to calculate the variable R.

Fig.73 presents single pulses obtained with alpha-particle on the top and with thermionic electron noise on the bottom. In the alpha signal, it can be notice the absence of the prominent peak related to the fast component in the scintillation light. We expect therefore smaller values of R with respect to the case of γ signals. In the noise waveform, the scintillation light is completely absent, therefore the average of the slow component is almost zero, providing very large values of R up to >1000.

The distribution of the R values obtained with a ^{57}Co source is shown on Fig.74. The small peak corresponding to R values between 1 and 4 is

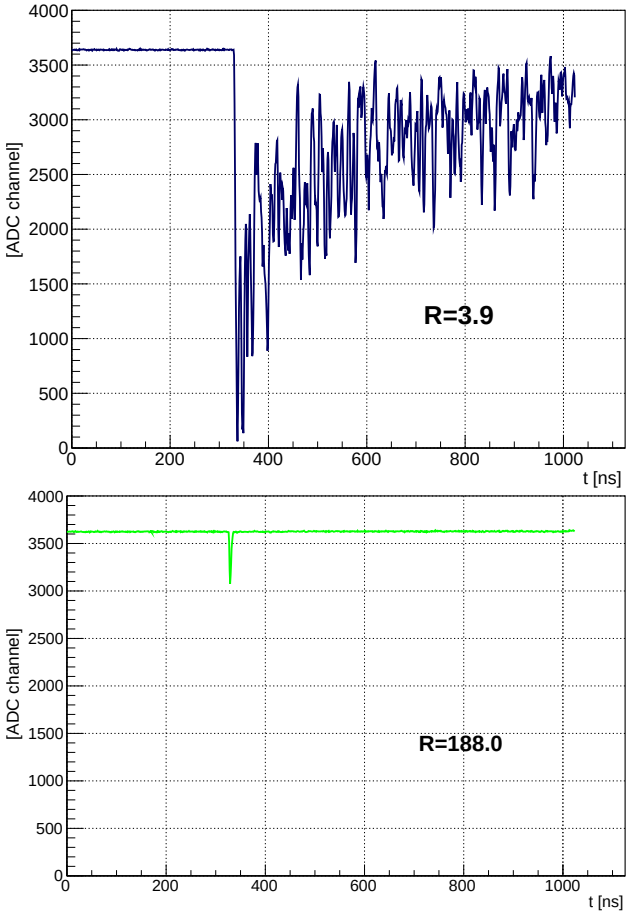

Figure 73: In these graphs are shown the typical signals obtained with α-particle (top plot) and thermal noise (bottom plot). On the plot are superimposed the corresponding values of the calculated ratio R.

related to α particles. The main peak ($4 \lesssim R \lesssim 25$) is given by γ signals and the tail at higher R values is due to noise.

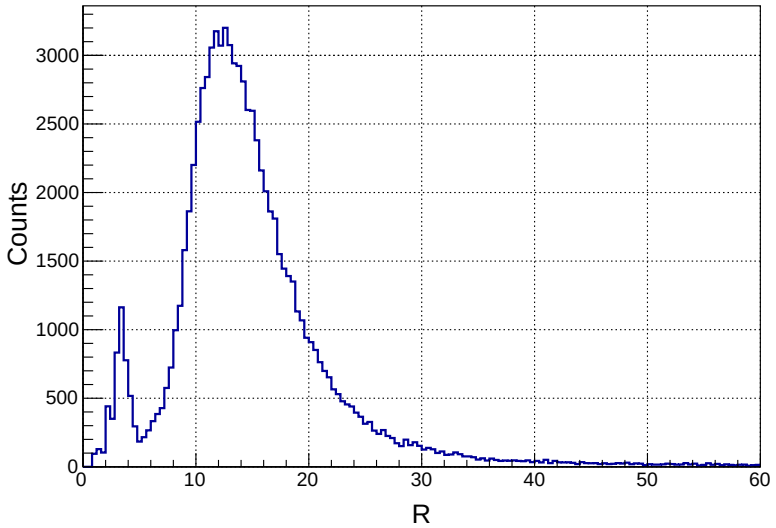

Figure 74: Histogram of the R values obtained from CH6 with a ^{57}Co source.

To find the best range of R values that identify a γ signal, the scatter plot of the deposited energy versus R has been examined for the 16 crystals. In Fig.75 is reported the plot obtained in one crystal from data taken with a ^{22}Na source. In the figure it is possible to clearly identify the structures due to the three types of signals and a range for the acceptance of γ signals can be defined, as displayed on Fig.75.

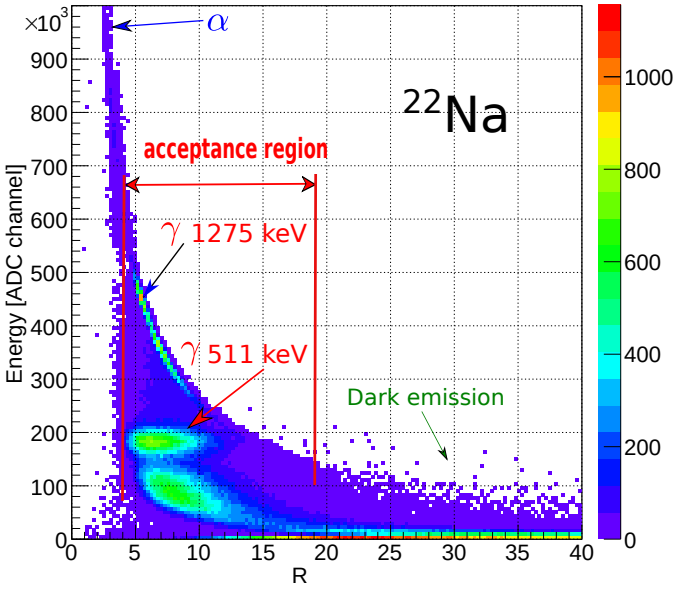

Figure 75: Scatter plot of deposited energy versus R, obtained exposing the BaF_2 crystal to a ^{22}Na source.

In the measurements presented in the next paragraphs this selection method is used. The sources used in those measurements are: ^{22}Na, ^{152}Eu and ^{57}Co. In Fig.76 are shown the scatter plot obtained with ^{152}Eu and ^{57}Co, reported on the top and on the bottom figure respectively. The ^{152}Eu photo-peaks around 1 MeV can not be clearly separated, so they are labeled all together in the plot. The range of R values used to select the signals related to γ particles is quite the same for this three sources, and is roughly between 4 and 19 as can be seen from Fig.75 and Fig.76.

The effectiveness of this method can be seen clearly on Fig.77, obtained with the ^{22}Na source. In this figure is shown in red the acquired energy spectrum and in blue the one obtained with signals that passed the shape cuts. In the selected spectrum is present only the part due to the γ particles. The components due to alpha and to thermal electrons, that are respectively the high and the low energy parts, are correctly removed from it.

This signal shape identification method is really useful in the measurements presented in this section, where the trigger used for the data acquisition is produced only by the BaF_2 signals. When the CSPEC will be used at the real experiment, the contamination due to α particles and noise will be heavily suppressed due to the coincidence with the HPGe signal, however the use of this signal selection may help in suppressing random fake coincidences.

In addiction to this shape selection, we applied cuts on the area and on the peak time of the signals. Only the waveforms with an area greater than 2000

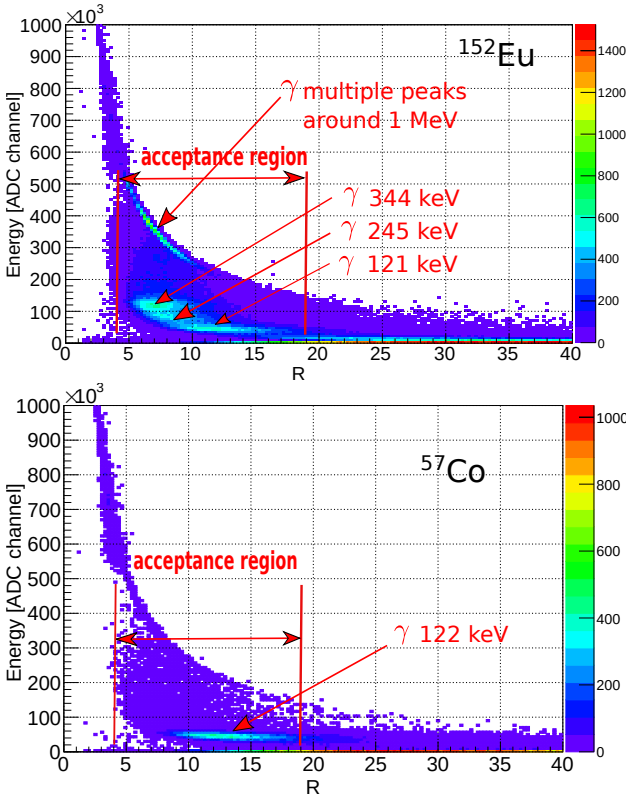

Figure 76: In the top plot is reported the two-dimensional graph of the released energy versus R obtained with ^{152}Eu source, while in the bottom the ones taken with ^{57}Co.

ADC channels are accepted, this was done to further remove the component of very little signals related to noise.

In Fig.78 is plotted the distribution of the time of the occurrence of the maximum value of the signal obtained without cuts on signal shape. As can be seen from the figure, the majority of the acquired waveforms have the maximum in time with the trigger (trigger time $\sim$ 365 ns). The accepted signals are the ones contained between the two red lines plotted in Fig.78, therefore with a peaking time 358 ns $< t_{max} <$ 375 ns. The anticipated/delayed signals are due either to random noise spikes or to good signals "out of time", i.e. not correctly positioned within the sampling window. They have been rejected in order to obtain a valid estimation of the energy released by the particle.

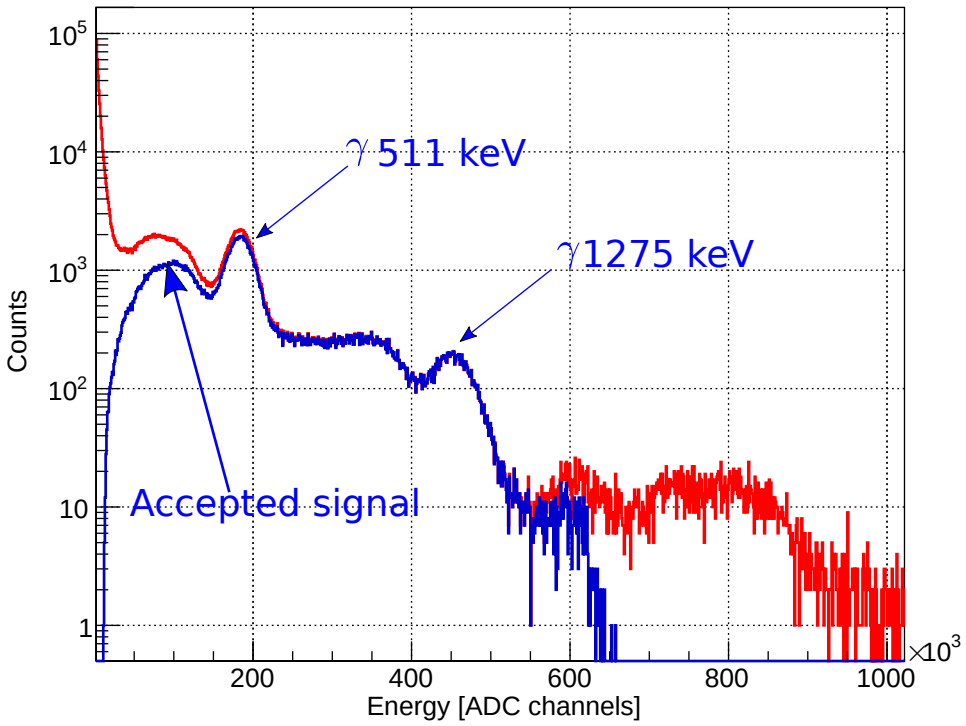

Figure 77: This plot presents: in blue, the energy spectrum obtained with the ^{22}Na source using the cuts on signal shape, and in red the full spectrum without cuts.

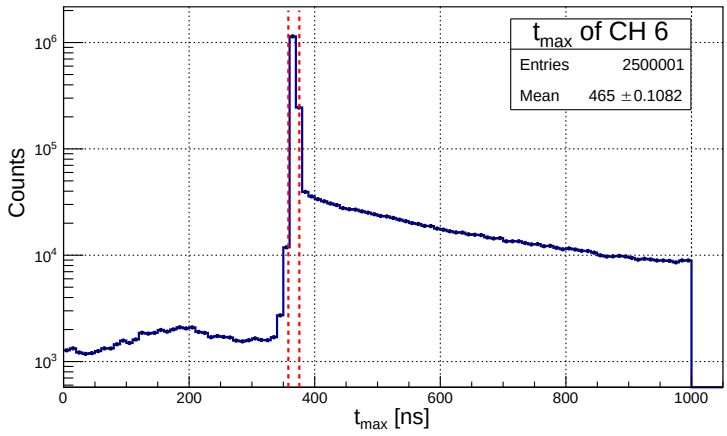

Figure 78: Distribution of the peaking time (t_{max}) of the acquired signals relative to CH6. The accepted waveforms are the ones with t_{max} contained between the two red lines. In this plot the cuts on R where not applied.

4.2.3 Trigger threshold optimization

To discriminate the output dynode signal we used a CFD (CAEN V812 model), as described on Sec.3.5. Using this discriminator, the signal is triggered at a fixed time after the leading edge of the input pulse reaches a 20 % constant fraction of its final amplitude. This is obtaining summing a delayed, full height input signal to an inverted and attenuated signal. The resulting signal is fed into a zero-crossing comparator, thus obtaining a precise timing information that eliminates any walk errors. However, to prevent the sensitive zero-crossing comparator firing on electronic noise, is necessary to sets the energy threshold of the CFD just above the noise level. In fact it does not correspond to the actual level that triggers the discriminator outputs, the latter being the constant fraction of the input signals. This energy threshold values can be programmed in a range from -1 to 255 mV.

An optimization of the threshold values to be applied to the CFD have been done. The threshold values were scan in order to find the better ones that reject the noise without compromising the signals. The expected range for the energy deposition inside the photon detector is between 200 keV and 287 keV. To optimize the trigger threshold the 122 keV lines of ^{57}Co was used to obtain a conservative lower limit. A preliminary study of the threshold using a fast oscilloscope have been done. Then the peak position, the energy resolution (RE) and the number of peak counts were studied. In Fig.79 are shown as example the energy spectra obtained in one crystal with different threshold values without using any selection criteria.

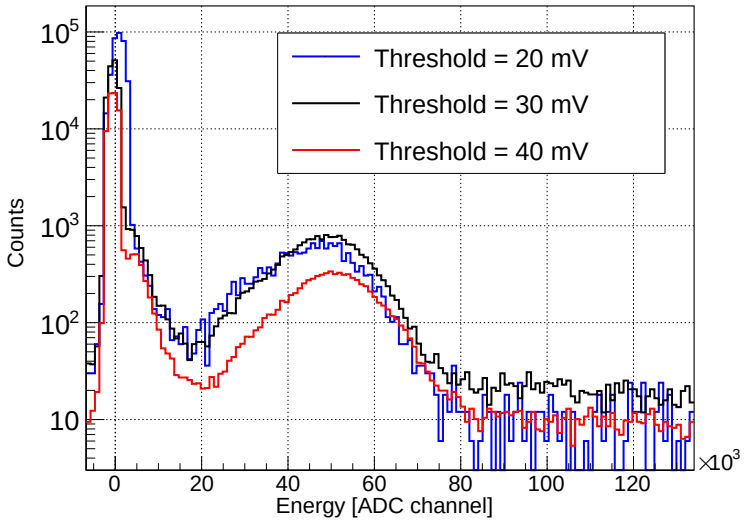

Figure 79: Comparison of the energy spectra obtained with ^{57}Co using different threshold values and no selection criteria.

The 122 keV peak of these spectra is fit with a gaussian function and an exponential one, used to fit the background, as is shown on Fig.80. The results obtained for three different crystals are reported on Tab.13

for different threshold values. The crystals are identified with the channel number using the convention illustrated on Fig.40.

Crystal	Peak position [ADC counts]	Counts	RE [%]
	Threshold= 20 mV		
1	36864 ± 147	$(1.3559 \pm 0.0012)\cdot 10^6$	20.8 ± 0.9
2	45920 ± 170	$(1.6941 \pm 0.0013)\cdot 10^6$	23.3 ± 0.9
5	34108 ± 137	$(1.1691 \pm 0.0011)\cdot 10^6$	20.1 ± 0.9
	Threshold=30 mV		
1	41772 ± 58	$(7.756 \pm 0.003)\cdot 10^6$	17.0 ± 0.3
2	49453 ± 55	$(1.497 \pm 0.004)\cdot 10^7$	17.9 ± 0.3
5	38893 ± 65	$(4.388 \pm 0.002)\cdot 10^6$	17.5 ± 0.4
	Threshold=40 mV		
1	44757 ± 72	$(4.571 \pm 0.002)\cdot 10^6$	16.0 ± 0.4
2	52290 ± 58	$(1.370 \pm 0.004)\cdot 10^7$	16.7 ± 0.3
5	41772 ± 91	$(1.6896 \pm 0.0013)\cdot 10^6$	17.5 ± 0.5

Table 13: This table reports the peak position, the counts under the peaks and the energy resolution (RE) of the 122 keV gamma rays from a ^{57}Co source for three different values of the threshold applied to the CFD. The results refer to three different crystals.

Considering the result reported on Tab.13 and plotted on Fig.79 we choose a threshold of 30 mV. As can be seen from the figure, this value reduces the noise component without affecting the signal peak whose number of counts is maximum (see Tab.13).

Note that, at this low energy values, the amplitude of the signal obtained from few (2-3) photoelectrons randomly emitted from photocathode is compatible with a physical signal. Therefore it is not possible to find a threshold values that is above the noise level and does not remove the signals due to source photons. This phenomenon leads to a dependence of the peak position from the threshold value, as can be seen on Tab.13.

4.2.4 Energy calibration and resolution

In order to calibrate the detector and to study the energy resolution, the crystals have been tested with a ^{57}Co, a ^{22}Na, and a ^{152}Eu sources which provide 121, 122, 244, 511, 1274 keV γ-rays. The pulse height spectrum obtained in one crystal for each of these sources is shown in Fig.80. In order to extract the signal, the spectrum has been fitted with a sum of gaussian and an exponential one for ^{22}Na and ^{57}Co. These are superimposed on the plot in red and green respectively. In the figure there are also shown in black the used fit functions. Instead, for the spectrum of ^{152}Eu (bottom plot) we used a sum of three gaussian function.

The energy calibration of all crystals was determined fitting a straight line to the peaks obtained from the spectrum of these three sources. The calibration curves obtained for the 16 crystals are displayed on Fig.81. As

it is possible to see from the figure the number of used peaks to obtain the energy calibration function is not the same for all the crystals. This is due to a low gain factor of CH3 and CH16 from which not all the peaks were distinguishable.

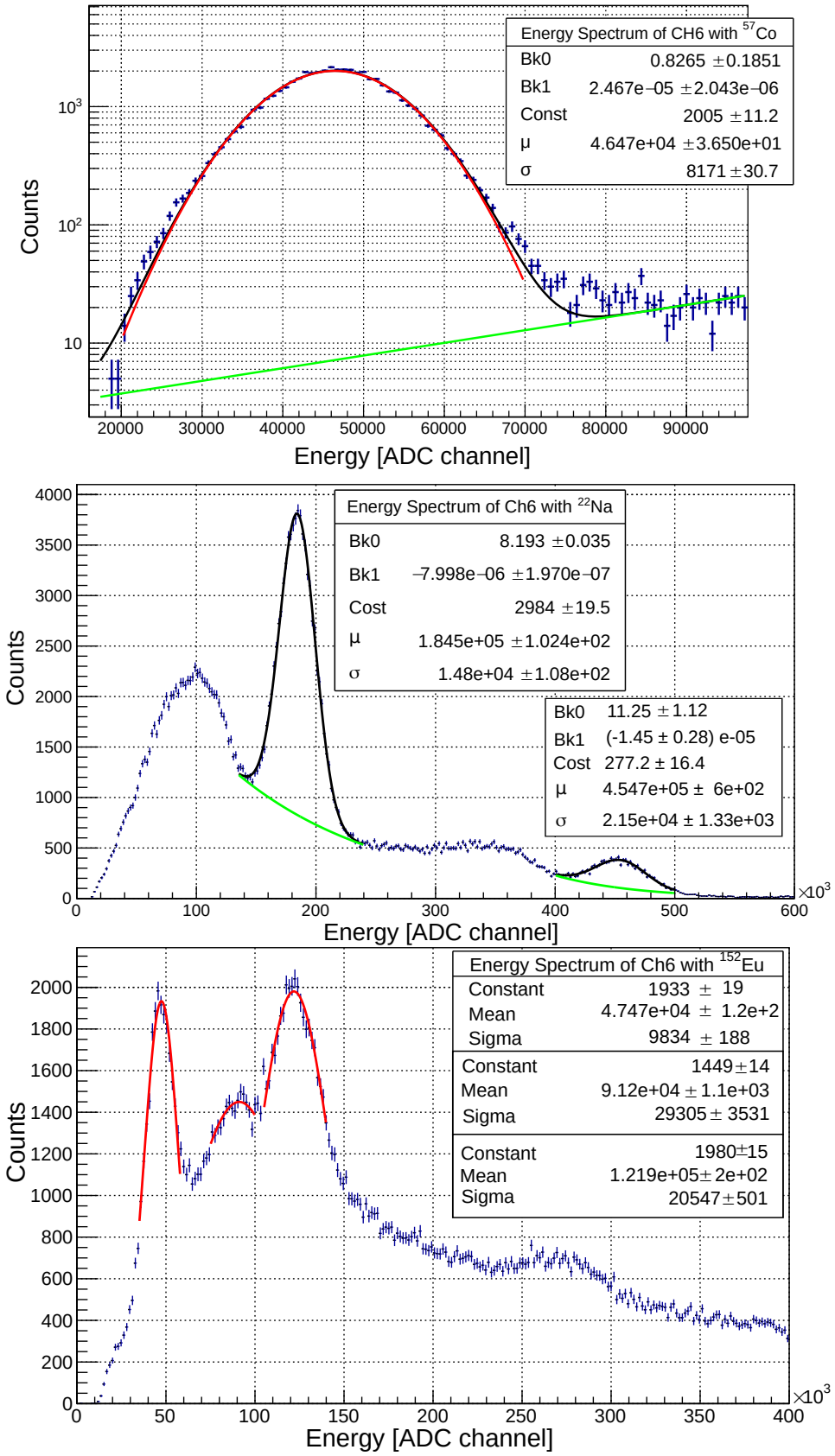

Figure 80: In the plot is shown the spectrum obtained from the crystal relative to CH 6 with a ^{57}Co source (top), ^{22}Na (center) and ^{152}Eu (bottom).

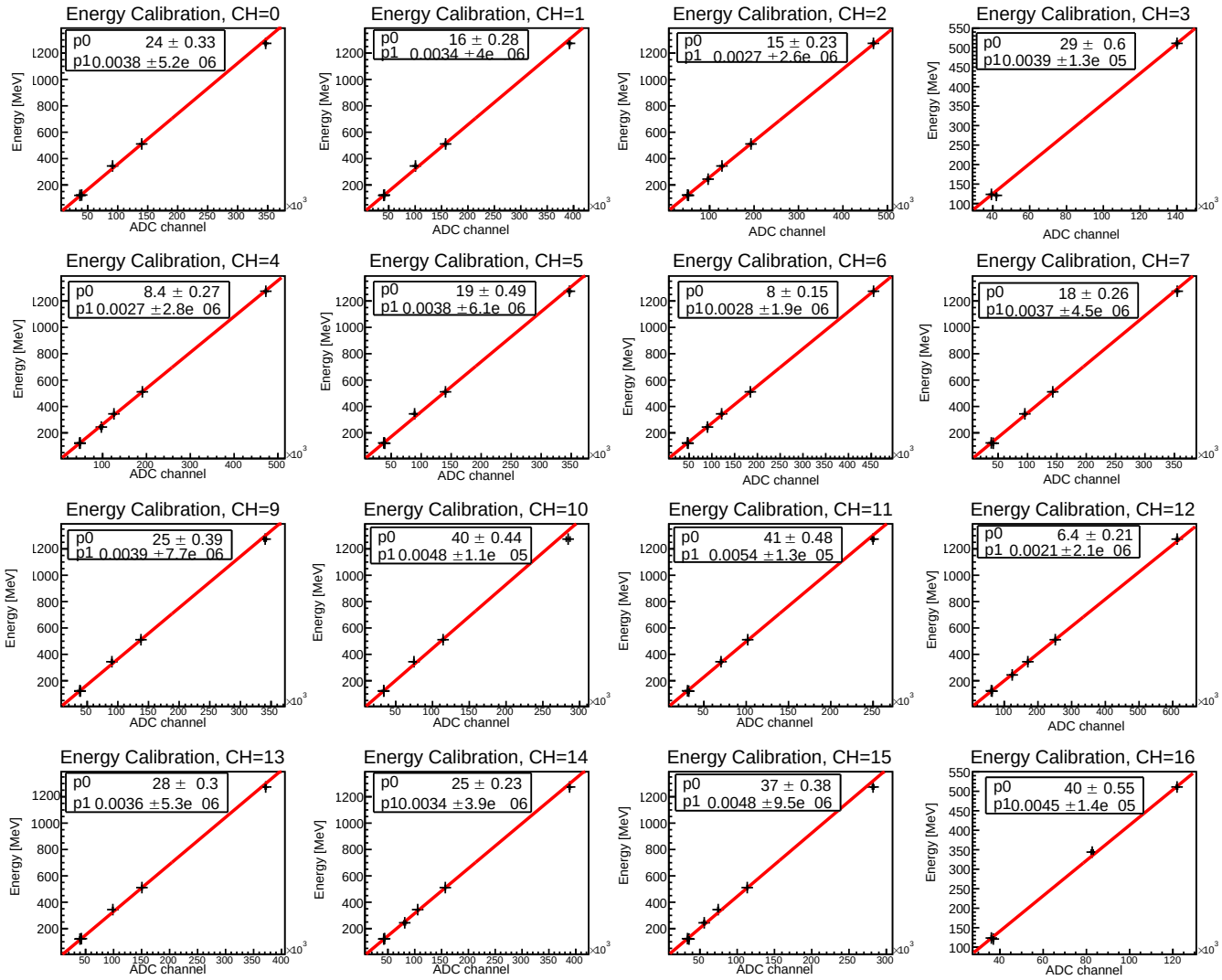

Figure 81: In these graphs are presented the energy calibration curves obtained for the 16 crystals of the photon detector.

The energy resolution of BaF_2 crystals has been studied at 122, 511 and 1274 keV. The peaks obtained with ^{152}Eu source can not be clearly separated, therefore they have not been taken into account for this evaluation. As example, the energy resolutions obtained for each of the 16 crystals at 122 keV is shown in Fig.82.

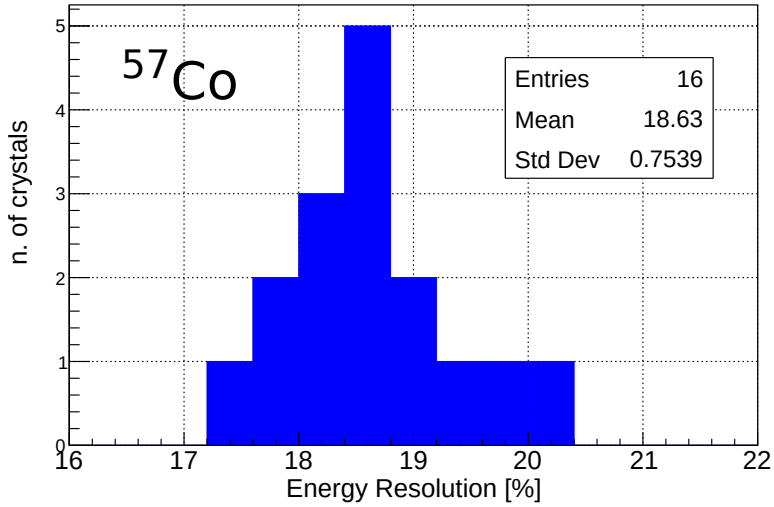

Figure 82: Distribution of energy resolution values for the 16 BaF_2 crystals of the photon detector.

The average energy resolution as a function of gamma-ray energy is shown in Fig.83. The average energy resolution is obtained as the mean calculated for the 16 crystals. The error bars are the σ of the distribution of measured values. The energy resolution decreases with increasing photon energy following with good approximation the $1/\sqrt{E}$ law used for the fit.

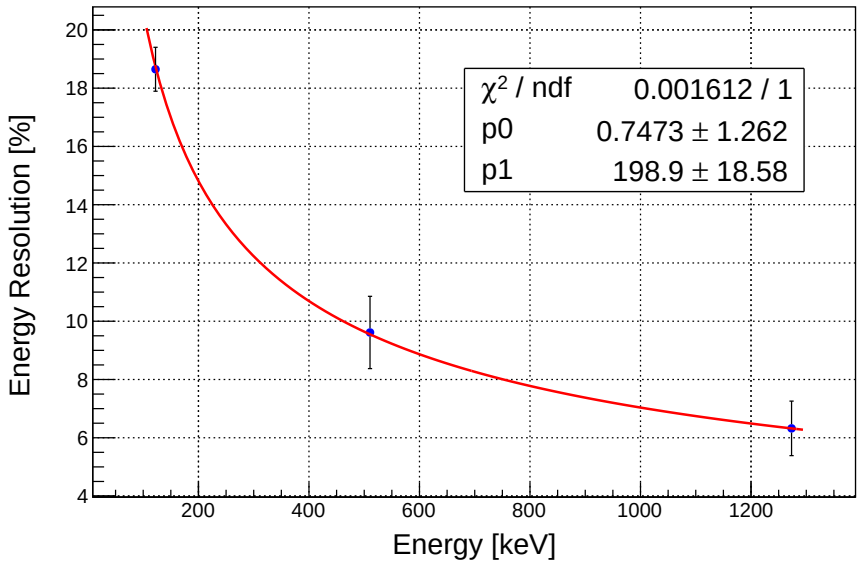

Figure 83: Average energy resolution of the 16 BaF_2 crystals in the energy range from 122 keV to 1274 keV.

The response uniformity of the crystals that compose the detector can be evaluated looking at Fig.84. In Fig.84 the distribution of the slope of the fit line (p1) obtained for each crystal has been plotted. From the gaussian fit of the distribution (superimposed with a red line) we obtained that the response uniformity of the crystals that compose the detector is at level of 23%. Using this energy calibration we can correct the effect due to different gains factor. Indeed, in a calibrated energy spectrum, the peak position will be the same for all the crystals.

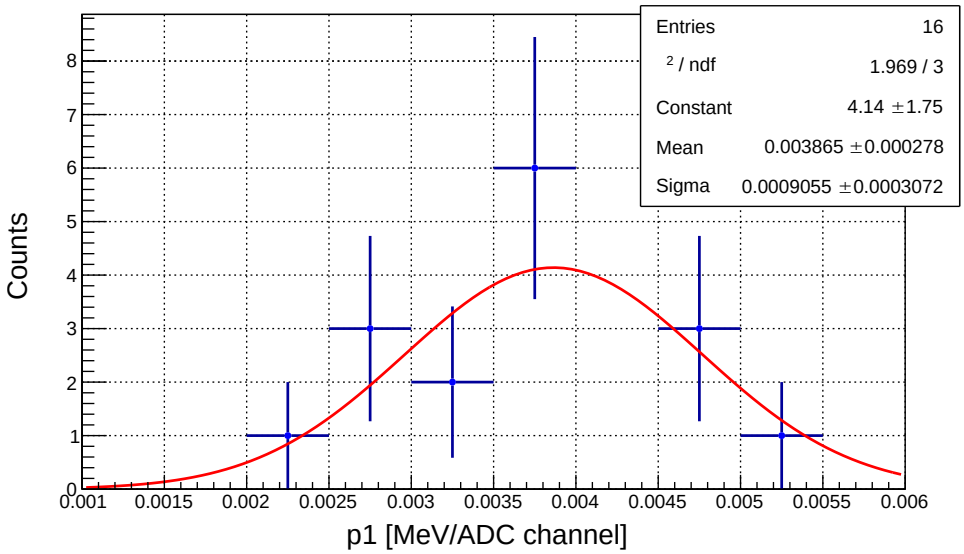

Figure 84: Calibration coefficients distribution relative to the 16 crystals of the photon detector.

4.2.5 α Measurement

The BaF_2 crystals intrinsic radioactivity, can be used to infer changes in the energy calibration of the scintillators composing the photon detector. This intrinsic radioactivity of BaF_2 crystals is originated from radium impurities, as presented on Sec.3.4.5.

The fact that signals from alpha-particles do not show a fast component can be used for separating them by pulse shape discrimination as illustrated on Sec.4.2.2.

To optimize the α signals to the input range of the digitizer two separated read-out lines with a different gain factor are used for the α and the γ signals, as presented on sec.3.4.4. In Fig.85 is reported, as example, the obtained energy spectrum from the α signals. Four gaussians functions, shown with red lines on the figure, are used to fit the main five alpha lines from the decay chain of ^{226}Ra.

The light output of scintillator detectors usually depends on the atomic number, energy and mass of the impinging particle. This is due to the fact that an important fraction of the kinetic energy lost by the charged particle is dissipated nonradiatively. This imply that the energy calibration of the detector depends on the particle type. Therefore, the information obtained

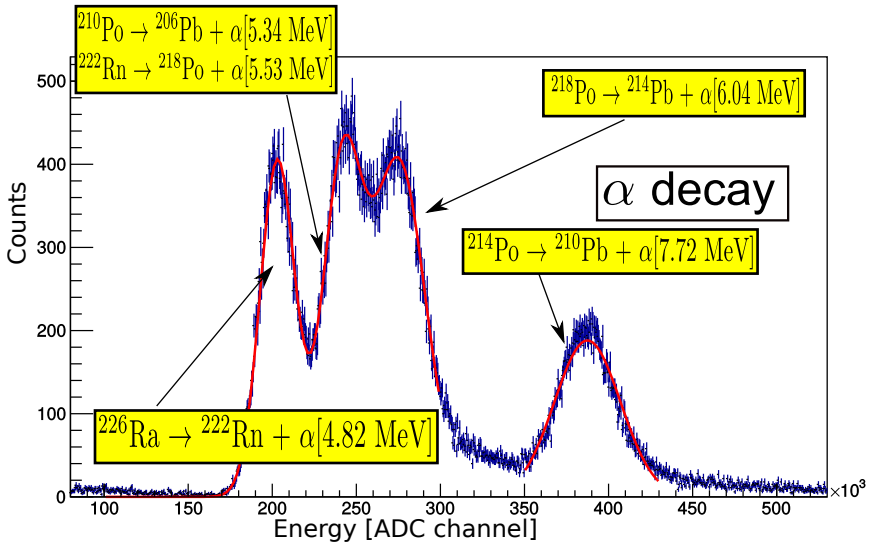

Figure 85: Energy spectrum of alpha-particles for one channel. The events were selected using the shape cut R (see Sec.4.2.2.

from the acquisition of the alpha lines of the radium impurities can not be used directly to calibrate the BaF_2 energy spectrum, as needed for gamma measurement. However, using the alpha peak position as internal standard, a change in the detector gain can be inferred and used, and a correction can be implemented. This eventual time variation could be due to many different effects, for example to a change of the photomultiplier gain or of the coupling between the detectors and the MaPMT. We plan to use the position of the well-isolated 7.7 MeV line from the decay of ^{214}Po for this purpose. During CSPEC measurements of the ELI-NP γ beam, the alpha spectra of the 16 detector modules will be continuously monitored to check if the position of the 7.7 MeV alpha line deviates from the reference one and in this case the appropriate action will be taken.

The measured rate for the whole detector relative to the α particles is 18.6 Hz. This rate is sufficiently low compared to the beam rate and therefore is expected to not affect the detector measurement. We will acquire photon from Compton scattering during the ELI-NP micro-pulse and α particles randomly when they are emitted. In order to save disk space we plan to reduce the number of the digitized alpha signals using a proper scale factor in the DAQ system.

5 GAMMA CALORIMETER (GCAL)

The gamma calorimeter is designed to measure the average energy and intensity of the gamma beam by absorbing a relevant fraction of its energy in a longitudinally segmented device. The detector makes a destructive measurement, so it can not be used during normal data taking. It will has a key role during the commissioning phase providing a fast feedback, including the ability to detect instability of the beam energy and intensity within a macro-pulse. The GCAL will be mounted on a movable support platform, remotely controlled, that will allow to put the detector centered in and out of the beam.

5.1 WORKING PRINCIPLE

In a classic nuclear or sub-nuclear experiment the particles are detected one by one. Indeed, the calorimeter here described, must be able to measure the energy of a γ beam that is supposed to be approximately monochromatic (within 0.5% as we have seen in Sec.1.2.2) but whose intensity is not known. The calorimeter has to be able to record the release of energy due to the simultaneous arrival (within $\sim$ 1 ps) of a large number of γ, about 10^5 at nominal intensity, all with the same energy. But the photon energy can not be simply determined from the total energy released, as usually happens in calorimeters, due to the fact that the intensity is not exactly known. Therefore, the basic idea adopted in GCAL, is to use properties of the gamma energy release inside the detector that depend only on the photon energy and not on the beam intensity.

This is obtained using the monotonic energy dependence of the γ cross-section for low-Z materials in the energy range of interest at the ELI-NP facility. This dependence is related to the predominance of Compton scattering interactions with respect to pair production. In fact, above 1 MeV, for high Z material the Compton cross-section decreases rapidly with energy, resulting in a much less energy dependent cross-section. As an example, figure 86 reports the total attenuation coefficient for the low-Z polyethylene (PE) and the high-Z lead, a material commonly used in calorimeter detectors.

Due to this characteristic energy dependence, the average depth of a photon interaction inside a light absorber is expected to increase with energy. Moreover, the average depth of the resulting electromagnetic shower in the detector also increases. Therefore, in the case of a monochromatic photon beam impinging on a low-Z calorimeter, the longitudinal profile of the energy deposition can be uniquely related to the photon energy.

Since the analytic expression of this energy dependence is not known, it is necessary to parametrize the longitudinal profile of the energy release as

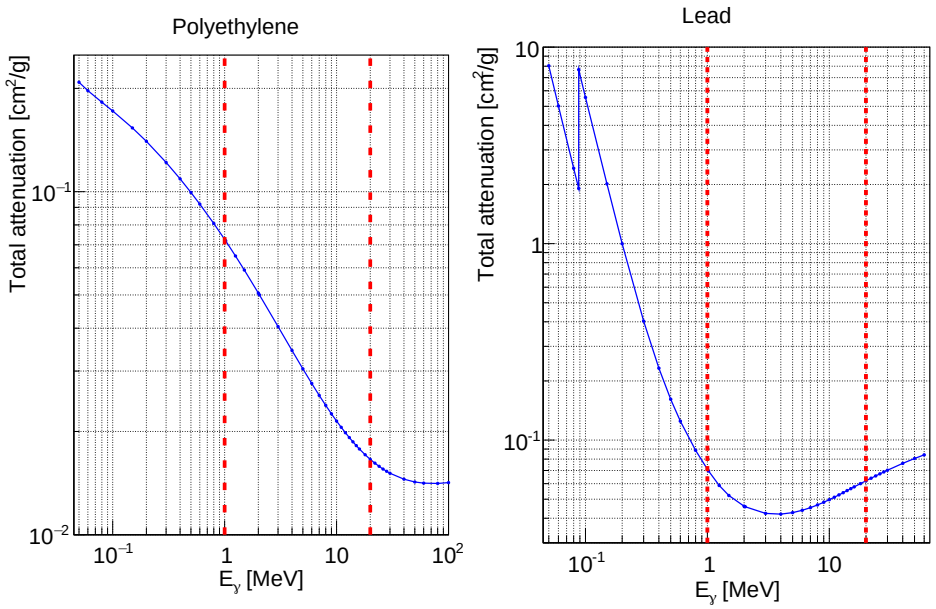

Figure 86: Total photon attenuation in polyethylene and lead as a function of the photon energy. The dashed red lines indicate the range of energies of the ELI-NP γ beam. The plotted values are obtained using the data available at [43].

a function of the γ beam energy. This has been done with a Monte Carlo simulation and will be explained in detail in Sec.6.2.

Once the photon energy is determined, the beam intensity or, more precisely, the number of incident photons per pulse, can be inferred from the total measured energy, under the assumption of a monochromatic beam.

5.2 DETECTOR GEOMETRY OPTIMIZATION

As already explained in the previous section, it is necessary that the absorber material has a low atomic number Z. The organic scintillators could be natural candidates being low-Z absorber and active detector at the same time, also having the advantage of fast response time allowing to resolve pulses within a macro-pulse. However, the absorption of the very intense and collimated gamma pulses requires the detectors to be radiation hard, condition not fulfilled by organic scintillators. Indeed, from our simulation, doses up to 10^{-4} Gy are expected along the beam direction for every micro-pulse (10^5 photons). After about 1 hour of operation at nominal intensity the performances of any plastic scintillator would be quickly degraded.

A sampling calorimeter device was chosen in order to disentangle the requirements for the absorption material and the detection technology. Due to the large energy release expected for each single beam pulse, sampling fluctuations are expected to have a limited impact on the detector performance.

The absorber will be made of blocks of Polyethylene (PE), an inexpensive and easily workable low Z material, interleaved with layers of silicon detectors.

An absorber thickness of 3 cm was chosen, which leads to a good compromise between energy resolution and numbers of layers. It can be seen in Fig.87 where the energy resolution (obtained by simulating 10^5 monoenergetic photons of 11 MeV) is reported as a function of the distance between the active layer of the calorimeter. The value "0 cm" refers to a homogeneous detector. The energy resolution was estimated with the method described on section 6.2.

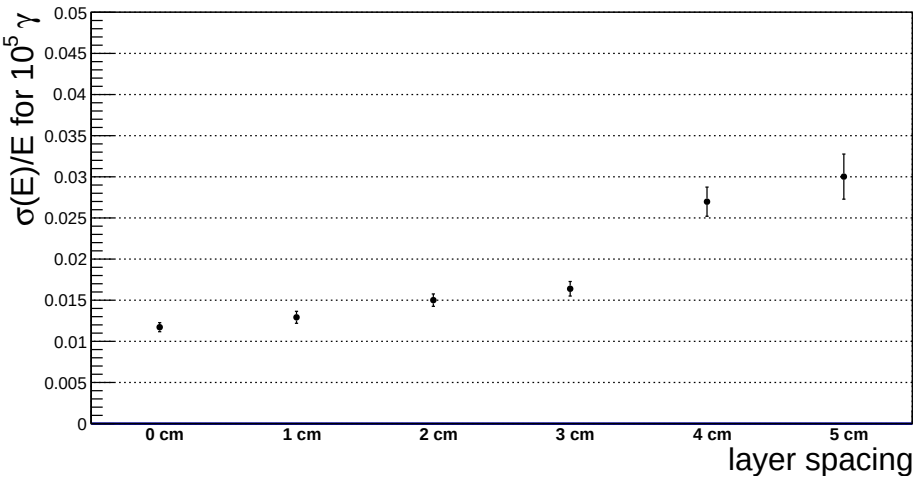

Figure 87: Expected energy resolution as a function of the spacing between active layers, for a fixed total PE absorber length and a monoenergetic beam of 11 MeV photons. Figure taken from [18]

The detector lateral and longitudinal dimensions were chosen after studying the fluctuations of the sampled signals inside a given absorption volume. In Fig.88 are displayed the energy resolution released in the active layers from a γ micro-pulse of different energies. For each size the energy is sampled every 3 cm of absorber. The plotted arrows indicate the chosen detector dimensions for the low energy line. As can be seen from the Fig.88 such fluctuations tend to saturate for absorber dimensions larger than the chosen size for the low energy photons ($E_\gamma \leq 3.5$ MeV). At higher energies a longer calorimeter would be required.

The GCAL layers were chosen to be identical in order to reduce systematic effects. In particular the inaccuracy on the sampling fraction predicted by the simulation, are expected to affect the calibration constants of all layers by a similar factor, so that their effect on the determination of the longitudinal energy profile is suppressed.

5.3 DETECTOR DESIGN

Taking into account the requirement described in the previous section, the calorimeter layout for the low energy line, which optimizes the performance and minimizes the cost, is made by 22 identical elements as shown in Fig.94. Each element will be composed of a block of PE absorber, with a thickness of

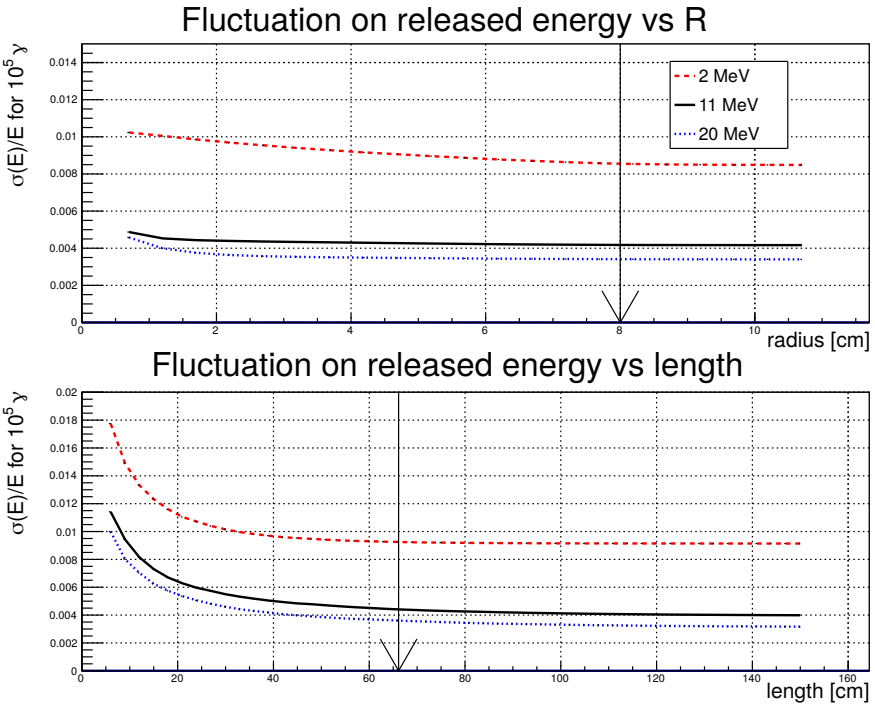

Figure 88: Fluctuation of the energy released in the active layers from a pulse of 10^5 photons of different energies, as a function of the detector size: (top plot) radius around the beam axis and (bottom plot) detector length. The arrows indicate the chosen detector dimensions for the low energy line. Figure taken from [18].

3 cm and 8.8×8.8 cm^2 transverse size. The PE blocks have a larger transverse size, than the predicted from Fig.88, to cover completely the Si-strip plane (8.7×8.2 cm^2). Each layer of the calorimeter will consist in a U-shaped support structure, made of aluminium, used to hold the PE absorber and a custom readout board hosting seven adjacent Si-strip modules. A layer picture is shown in Fig.89.

The GCAL subsytem will be located at the end of the characterisation line, as displayed in Fig.90, and will be operated in air. In fact, the amount of plastic material which compose the detector is not compatible with a ultra high vacuum (UHV) environment and the adaptation to a vacuum compatibility would imply a difficult design and a significant cost increase. Also, in vacuum placement would require a cooling system to avoid overheat, while the low power needed for the detector and front-end electronics can be safely dissipated in presence of air at room temperature. Moreover, the calorimeter provides a destructive measurement; for this reason it will be installed on a movable platform, shown on Fig.90, to allow switching its position on/off the beam. The vacuum-air transition of the beam will be obtained installing a beryllium window (150 μm-thick) downstream the GPI and before the calorimeter. The material and thickness of the transition window are chosen is such a way to guarantee mechanical stability, without interfering with the beam.

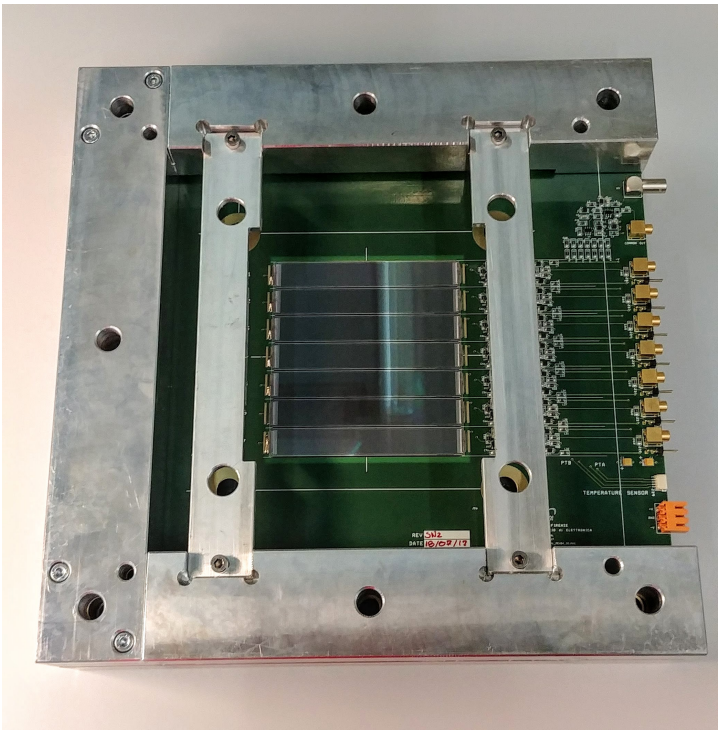

Figure 89: Picture of a GCAL layer. In this photo one can see the seven Si-strip sensors connected to the readout board and the U-shaped support structure which holds together the board and the absorber block.

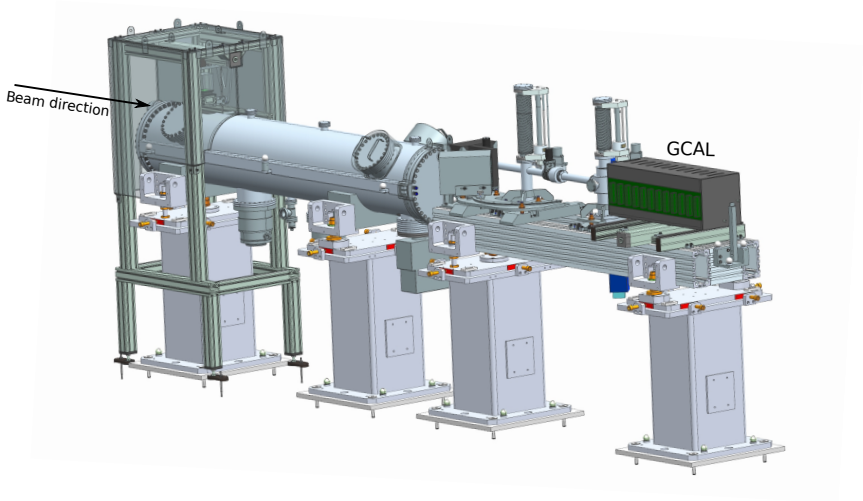

Figure 90: 3D CAD model that shows the position of GCAL inside the characterization system.

5.3.1 Si-strip detectors

The silicon technology was chosen for its ability to meet the following main characteristics:

- The active detections layers of the calorimeter have to be radiation hard to survive to the extremely high photon flux and space density expected at the ELI-NP beam.

- The detectors should be fast enough to allow clear separation between the various pulses in the macro pulse. In this way we can provide important feedbacks on the tuning of the laser recirculation system and of the interaction region.
- A good efficiency and response linearity is also necessary for a wide range of energy deposition values.

The chosen Si-strip sensors have been developed by Hamamatsu Photonics for the inner barrel tracker detector of the CMS experiments [52, 53]. In particular, they are the IB1 mini-sensors, which are part of the test structures associated with CMS sensors and shown in Fig.91. The silicon pad has been cut precisely from the structure at the FBK in Trento using a diamond cutting machine. We measured, using a micrometric slit coupled to a microscope, that the average cut margin is 24 ± 3 μm.

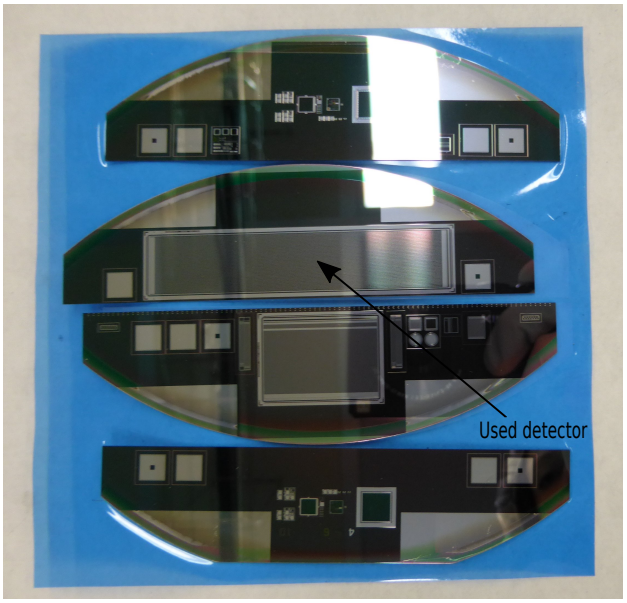

Figure 91: The photo shows the structure inside which is located the silicon pad that is used to make the calorimeter.

All the sensors are processed from n-type phosphorous doped wafers, 320 μm thick, with a low resistivity (1.5-3 kΩ cm) and are segmented in 128 p+ strips with 80 μm pitch and 20 μm width. The active area is 10.32×80.00 mm^2. These sensors are radiation hard and can safely sustain irradiation up to 100 kGy. According to the simulations the maximum expected dose on a single silicon sensor for beam energies ranging from 1 to 20 MeV varies in the interval $(1.6\text{-}8.0) \times 10^{-4}$ Gy/s. We therefore do not expect a degradation of performances due to irradiation. In addition the calorimeter will not be continuosly exposed to the beam since it will be pulled off during normal beam operations.

The I-V and C-V characterization has been done for all the silicon detectors. In Fig.92 is reported an example of the typical curves obtained. The silicon sensors will be operated at a bias voltage of 600 V in order to reduce the response time. This value is well above the full depletion voltage, as can be

seen from Fig.92, this guarantees the achievement of the saturation of the charge drift velocity.

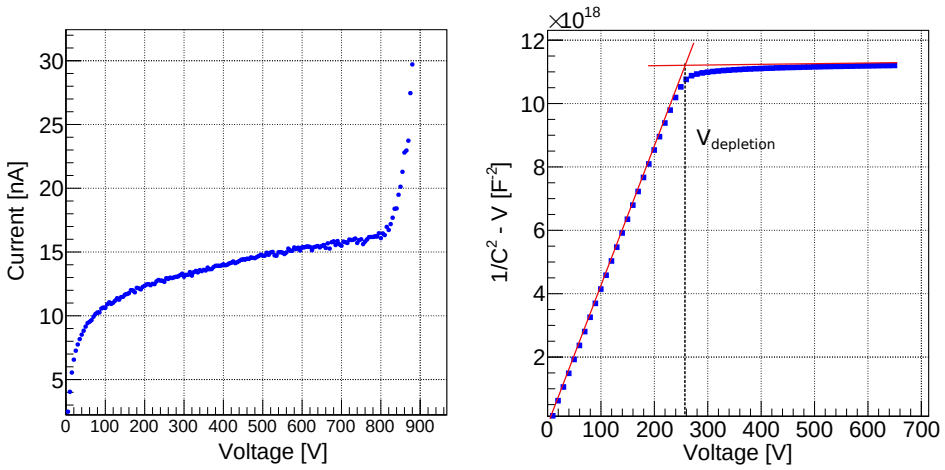

Figure 92: In this figure are shown an example of a typical obtained I-V (left) and C-V curves (right).

The measured detectors capacitances at 600 V (C_{600V}) are reported in Fig.93 and have values 294 pF $< C_{600V} <$ 300 pF. The seven adjacent sensors which made a layer have been chosen in order to have $\Delta C_{600V} < 1$ pF, this guarantees a good detectors uniformity inside each layer.

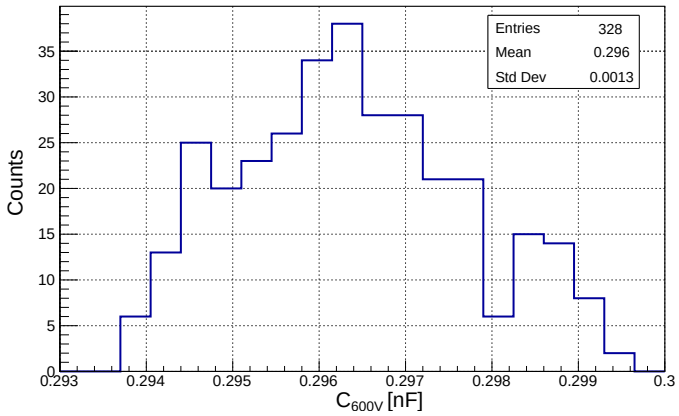

Figure 93: Distribution of the measured detectors capacitances at 600 V.

Using seven detectors whit low capacitance guarantees to cover a large active area while keeping the detector time response fast and with an efficient charge collection and reduced noise.

5.3.2 Readout Board

A custom readout board has been designed at INFN Firenze in order to comply with the demanding requirements imposed by the ELI-NP gamma beam characteristics, in particular the ability to disentangle pulses separated by 16 ns. The designed readout board provides the front-end electronics for the sensor readout and the mechanical support for the accurate positioning

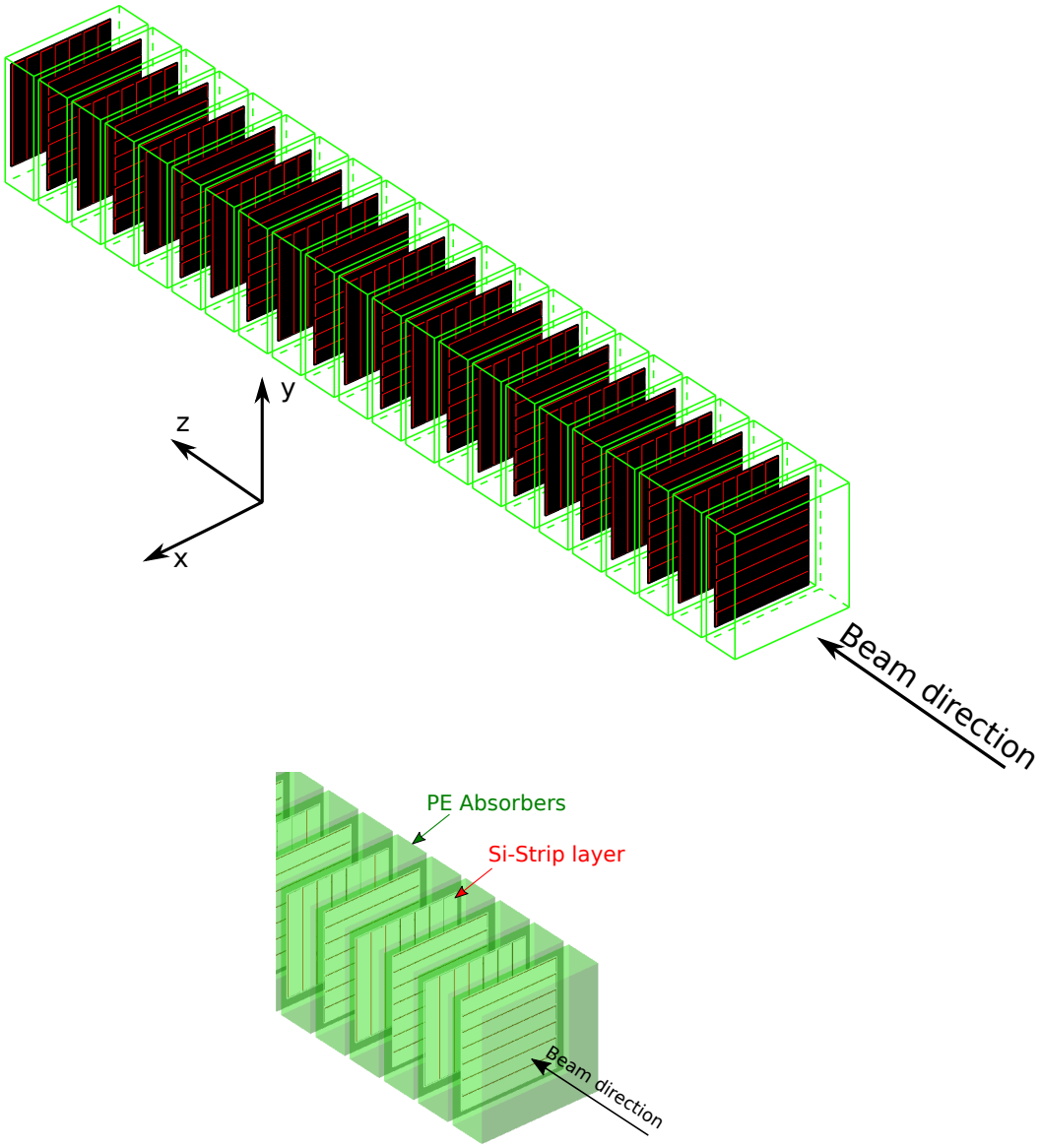

Figure 94: Layout of the absorption calorimeter obtained from Geant4 simulation. The bottom plots presented an enlargement on the first calorimeter layers.

of the sensors in each layer. Fig.89 shows an example of custom readout board equipped with the seven silicon detectors. The board transverse size is 250×250 mm^2. The silicon sensors of each layer will share a single high voltage channel.

To define the characteristics of the electronic channels (in particular noise and dynamic range), the total energy release that we will expect in every silicon layer for a single photon bunch have been evaluated. As shows in Sec.6.2.3 we notice that the maximum energy release for the LE lines, that we could expect in a single layer, is about 450 MeV for a 3.5 MeV beam energy.

Figure 95 shows the schematic diagram of the front-end circuit. Each sensor is connected both to an individual readout channel and to an analog sum circuit which will provide the signal corresponding to the total energy released in the layer.

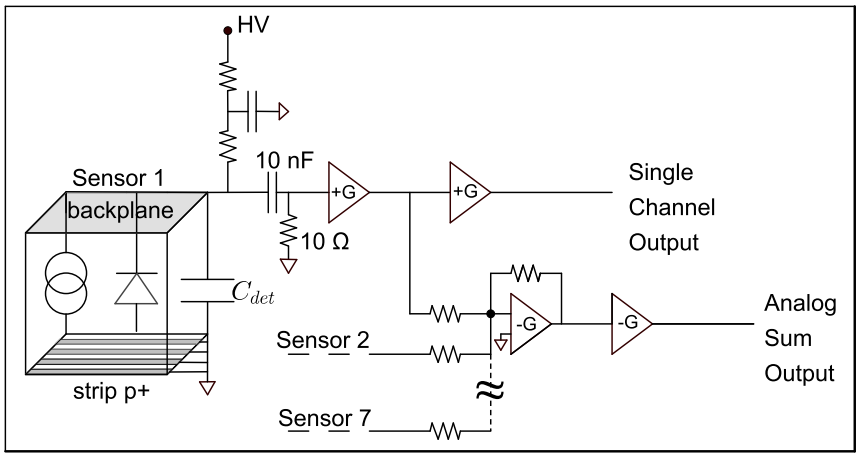

Figure 95: Schematic diagram of the front-end circuit used in the readout boards of the silicon detectors.

The shape of the signal pulse produced from a single event strongly depends on the input characteristics of the circuit to which the detector is connected, usually a charge preamplifier followed by a shaping amplifier. In order to achieve a very fast signal we decided to avoid the use of a pulse shaper and to integrate the current directly into the amplifier. The time constant of the external circuit has to be kept small compared with the charge collection time, so that the current flowing through the load resistance is essentially equal to the instantaneous value of the current flowing in the detector. For this purpose, the signal is read out from the back side of the device so that the implant strip resistance (that is of the order of 1 MΩ) does not affect the time constant of the readout. The load resistance has been chosen to be 10 Ω that is the best compromise between two conflicting needs: a low time constant and a good current injection in the charge amplifier.

In order to prevent the introduction of additional, not controlled, parasitic series resistance to the load resistance, the sensor's backplane has been wire-bonded to the readout circuit. A multiple stage cascade amplifier configuration has been chosen, both for the single sensor readout as well for the sum circuit, in order to increase the gain bandwidth up to 300 MHz. The result of the time response tests of the silicon detector coupled with the presented readout board will be described in sec.6.1.2.

The GCAL signals will be digitised by fast digitisers using a CAEN Switched Capacitor Digitizer (mod. V1742[40]). The sampling rate will be 1 GS/s in order to acquire the whole macro-pulse (496 ns) and a sufficient number of samples for the baseline calculation. The trigger of the system will be the beam crossing signal provided by the GBS machine.

The strips in each Si-strip sensors are bonded together to provide a single readout signal. They are alternatively placed along the x or y direction

in different layers (see Fig. 94) to reduce possible systematic effects. For the first two layers of the calorimeter will be readout the five central Si-strip modules independently and the 7 detector sum signal, providing a rough transverse energy profile. For the subsequent layers, signal from all seven modules will be summed in order to limit the needed number of data acquisition channels to 36. Indeed, the knowledge of the transverse distribution of the energy release is not strictly needed for the beam energy and intensity characterisation, it provides information on the beam position and on the presence of beam halo. It also allows to test the reliability of the Monte Carlo simulations.

6 GAMMA CALORIMETER SIMULATION AND TESTS

In this chapter will be described the tests carried out on the silicon si-strip devices which are the active part of the calorimeter. The functionality of the pads and their time response have been evaluated showing that it will be able to cope with the demanding time structure of the ELI-NP γ beam. Here will also be reported the results, in terms of resolutions and systematic effects, of detailed simulations of GCAL done with Geant4.

6.1 LASER TESTS

The response of the 22 front-end board equipped with the silicon detectors that compose the low-energy line calorimeter have been characterized using an infrared laser (IR). Pulsed-infrared laser can be used as a relatively simple, inexpensive, and effective means of simulating the effects caused by intense gamma ray sources on semiconductors [54]. High levels of ionization can be created in semiconductor devices by irradiating the devices with short pulses of light. If the light frequency is properly selected, sufficient and relatively uniform energy deposition is obtained which results in ionization rates orders of magnitude above those presently attainable from other sources.

6.1.1 Experimental set-up

The IR laser used to test the silicon detectors response is a neodymium laser (PicoQuant model LDH-P-1060 [55]) with variable optical power coupled to a PDL 800-B Pulsed Diode Laser Driver. The laser characteristics are reported in Tab.14.

Light Wavelength	1060 nm
Repetition Rate	from single up to 80 MHz
Pulse FWHM	< 100 ps
Max Average Power	21 mW

Table 14: Main parameters of the PicoQuant LDH-P-1060 laser used to test the silicon devices.

A laser wavelength of 1060 nm, which corresponds to a penetration depth of 900 μm in silicon, well above the sensor thickness, has been chosen in order to guarantee an uniform energy deposition along the whole depth of our devices. The board and the laser head are positioned on movable slits, as shown in Fig. 96 to perform horizontal and longitudinal scans of the 7 sensors. The front-end board and the laser were enclosed in a light tight box. The temperature and the humidity inside the box were continuously

monitored using a thermohygrometer (HD 9216 [56]). Given the high value of the voltage used to bias the sensors (see next section) we experienced occasionally HV "trips" due to the increase of the leakage current. This increase was correlated to the level of air humidity. To prevent this problem the box was continuously fluxed with dry air during the measurements.

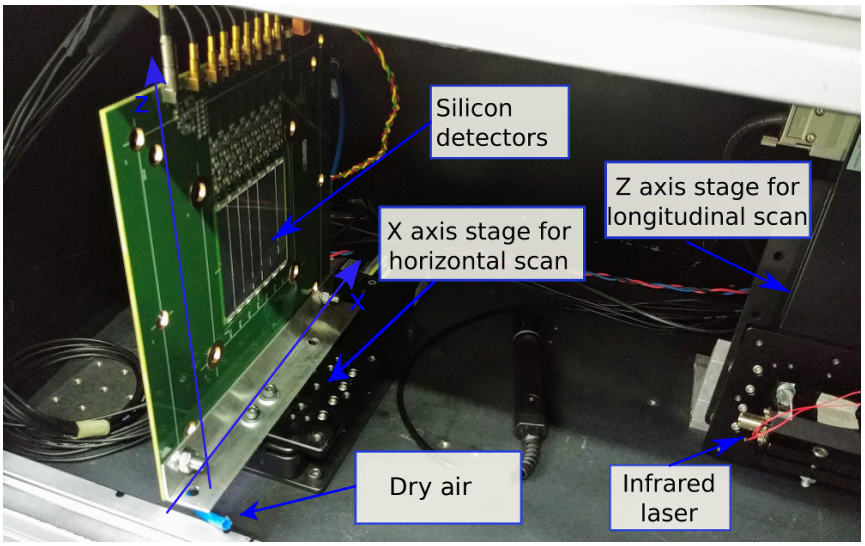

Figure 96: Experimental set-up used to characterize the silicon sensors response with IR laser.

Using this configuration the laser spot has an elliptical shape with dimension, measured with a photodiode, of about 1.5 mm ×3.5 mm. The laser pulse lasts less than 100 ps, so it is short enough compared to the charge collection times of a 300 μm thick silicon device that is of the order of a few ns. We are therefore confident that the detector signal is not distorted by the duration of the pulse. The high value of the average power allows simulating very large energy depositions as the ones expected at the ELI-NP facility.

The silicon sensors are powered at + 600 V using the CAEN multi channel HV boards A7030TP [57] with a measured layer current in the range 0.2-0.7 μA. The read-out electronics is powered with ± 5 V using two floating channels of the CAEN A2518 boards [49]. The signals are acquired with a Caen V1742 Switched Capacitor Digitizer at a selectable sampling rate from 1 to 5 GS/s. We will operate at a sampling rate of 1 GS/s, during the real data acquisition and in these tests if we want to acquire a time window (496 ns) corresponding to the whole macro-pulse. A higher sampling frequency is used for a better characterization of the signal profile during the ongoing phase of tests.

The laser is driven at 300 Hz with an external trigger generated by an arbitrary waveform generator Agilent mod.33220A. The trigger for the data acquisition is obtained using the synchronization output given by the laser driver that is always synchronized to the trigger source of the laser pulses.

The firsts 150 ns of the acquired waveforms are used to calculate the baseline. The distribution of the measured baseline is shown in Fig.97 for

the single channel output and in Fig.98 for the sum output channel. The superimposed curves are the results of a gaussian fit, the mean value provides the common mode of the signal and is subtracted from the acquired waveform. In addition, an estimation of the electronic noise is given from the standard deviation of these distributions. As can be seen from the figure, the sum channel has a higher typical noise of about 12 ADC ch, while the single channel of about 5 ADC ch. This corresponds to an energy value of about 0.7 MeV for the single channel, and of about 1.7 MeV, for the sum channel, according to the calibration done exposing the detectors to a proton beam (see Sec.6.2.6).

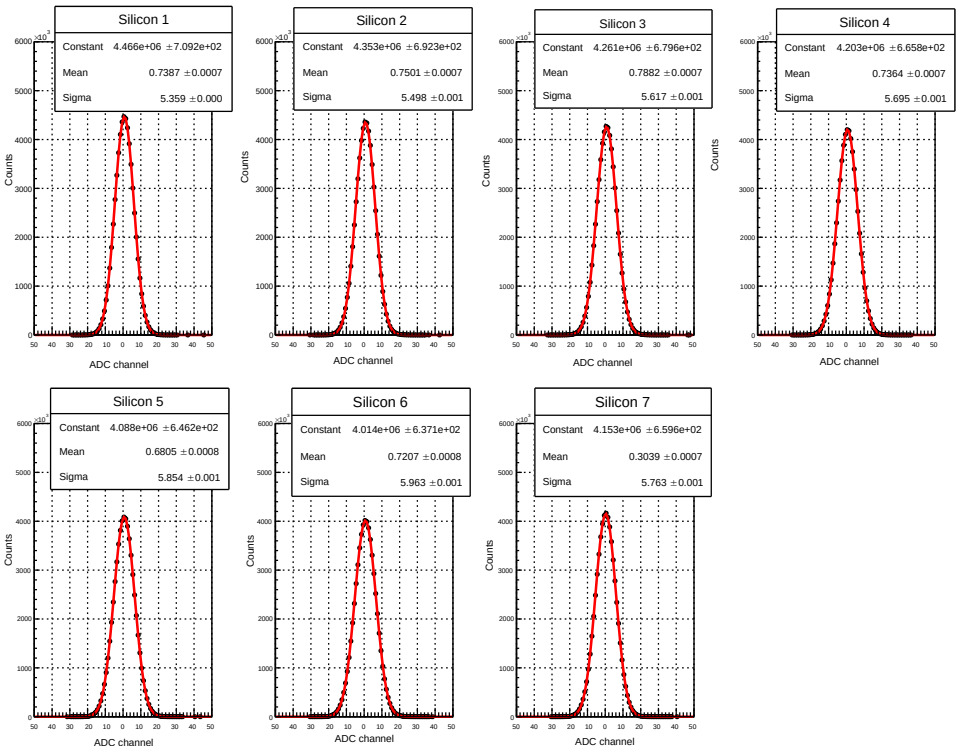

Figure 97: Baseline distribution obtained from the 7 silicon detectors. The superimposed red lines show the gaussian fit functions obtained from the fit.

6.1.2 Time response study

The calorimeter has to be able to resolve the 16 ns separated pulses of the ELI-NP beam, therefore the time response of silicon detectors is a critical issue to keep under control. It has already been explained the backplane readout strategy (see Sec.5.3.2) implemented to minimize the time constant of the electronic circuit, here is described the approach used to optimize the charge collection time.

To reduce the collection time in the silicon detector high field strengths are required. At low-to-moderate values of the electric field intensity, the

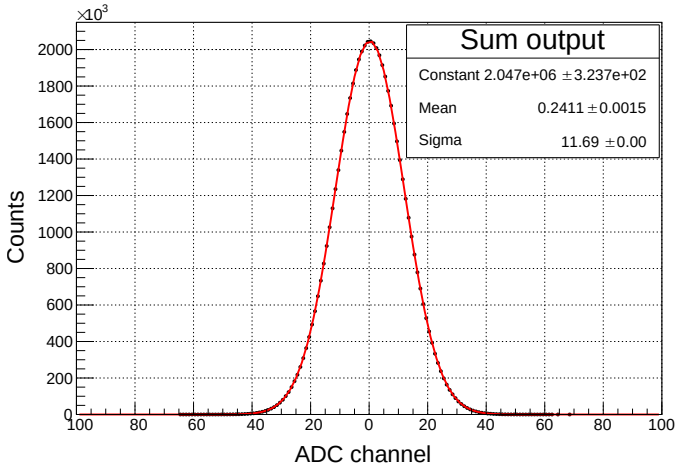

Figure 98: Baseline distribution obtained from the sum channel output of the 7 silicon detectors. The superimposed red line shows the result of the fit with a gaussian function.

drift velocities $v_{e,h}$ of the charge carriers, electrons (e) and holes (h), are proportional to the applied field E [46]:

$$v_{e,h} = \mu_{e,h} \cdot E \tag{18}$$

where $\mu_{e,h}$ are the mobilities of the charge carriers.

The carrier mobility is constant at low field $E \leq E_c$, where $E_c \sim 2.5 \cdot 10^3$ V/cm, and becomes inversely proportional to the electric field at high fields. Therefore working with electric field values sufficiently high results in a saturated drift velocity. In order to obtain high field strengths throughout its sensitive volume the detector must be over-biased. The choice of the best operational voltage has been done studying the signals obtained illuminating the silicon sensors with the IR laser as a function of the applied bias voltage. The obtained waveforms and their falling time (t_{fall}) are presented in Fig. 99 for a variation of the bias voltage in the range from 100 to 600. Notice that t_{fall} decreases strongly when the bias polarization increase until the depletion voltage ($\sim$ 250 V) is reached. With higher polarization t_{fall} decrease slowly following a quadratic law, used as fit function. This is due to the fact that the detector's capacitance decreases with increasing bias voltage as long as it remains lower than the depletion voltage, then it ranges on a constant value, as explained in detail in Sec.5.3.1

An operational voltage of 600 V is chosen. This value, well above the voltage needed for full depletion, guarantees an adequate safety margin with respect to breakdown voltage that is at about 900 V (Fig. 92).

To verify that the detectors are able to provide a signal with proper duration (i.e. less than 16 ns) even at the highest energy deposition expected for the low-energy beam line, which amounts to about 470 MeV (see Sec.6.2), we adjusted the output laser power to 35%. This corresponds to signals with maximum value of about 3200 ADC ch (Fig. 100), according to the calibration done exposing the detectors to a proton beam (see Sec.6.2.6) this value corresponds to the maximal energy release expected in the silicon sensors.

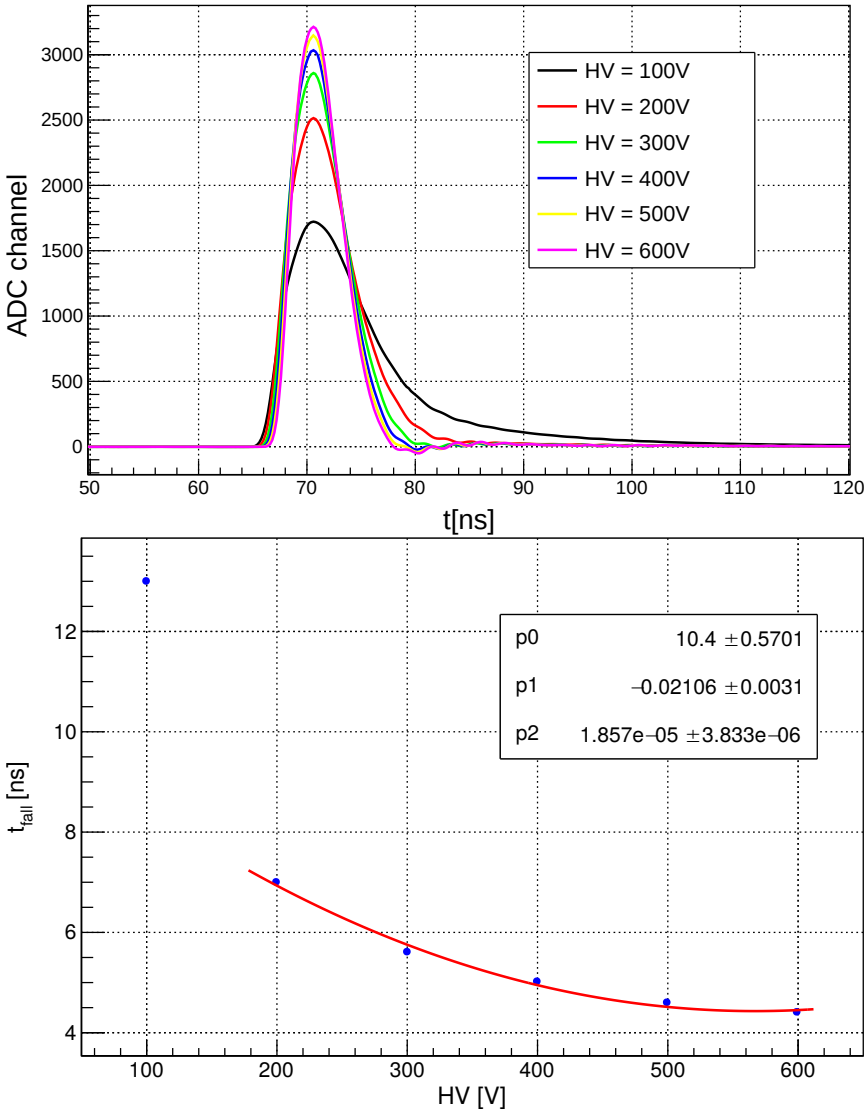

Figure 99: In the figure are shown the waveforms (top) and the signals falling time (bottom) obtained with different supplied voltage with a Si-strip detector exposed to the laser.

The response of all the seven sensors of each board was acquired, both the individual channels and the sum readout. The laser beam was directed onto the center of the silicon pad, 10000 waveforms were collected and subsequently averaged. The results are shown in Fig. 100, on the top are shown the signals of the individual channel, while on the bottom the signals from the sum output channel. The vertical dashed lines marks off the 16 ns separation time between two pulses, while the horizontal line indicates the signal baseline. As it can be seen from the figure the fast response of the detector coupled to front-end electronics keeps the signal well inside the 16 ns boundary i.e. the time spacing between pulses at ELI-NP.
Fig.101 shown an enlargement on the baseline after the pulse of the waveforms shown on Fig.100. From the figure we can observe that the sum signals (right plot) presents a small overshoot after 16 ns which has an amplitude

and an area that amounts to about 1 % contribution in correspondence of the following pulse when operated in train mode.

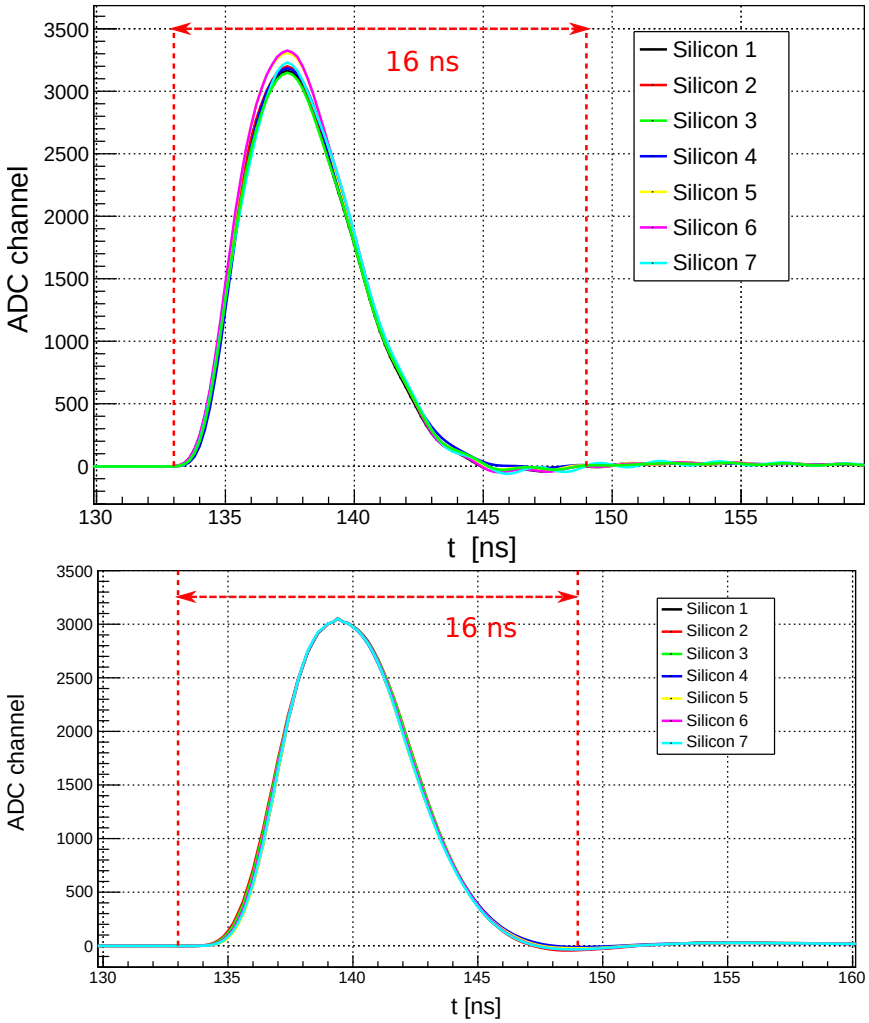

Figure 100: Detector response to a single laser pulse, individual channel (top) and 18 sum output (bottom).

To study the detector response in the most similar condition to the real detector use, the laser was driven with an external trigger in order to obtain a train of pulses with the same temporal structure of the ELI-NP gamma beam. The train signal used as external trigger, generated with Tektronix AFG3252 [58] arbitrary function generator, is shown in Fig. 102.

Fig. 103 displays the detector response to the train of 32 laser pulses. By comparing several events, we observe a reproducible structure in the series of single pulse height. The more evident effect is on the first pulse that is always a few per cent higher than the following ones. Using a calibrated fast photodiode we verified that this particular structure is a feature of the emission intensity of our laser, when operated in burst mode, and it is not ascribable neither to our sensors nor to the readout electronics. In the bottom figure is presented with red line the result of a fit algorithm based on single pulse deconvolution. The fit function F(t) is made by the sum of

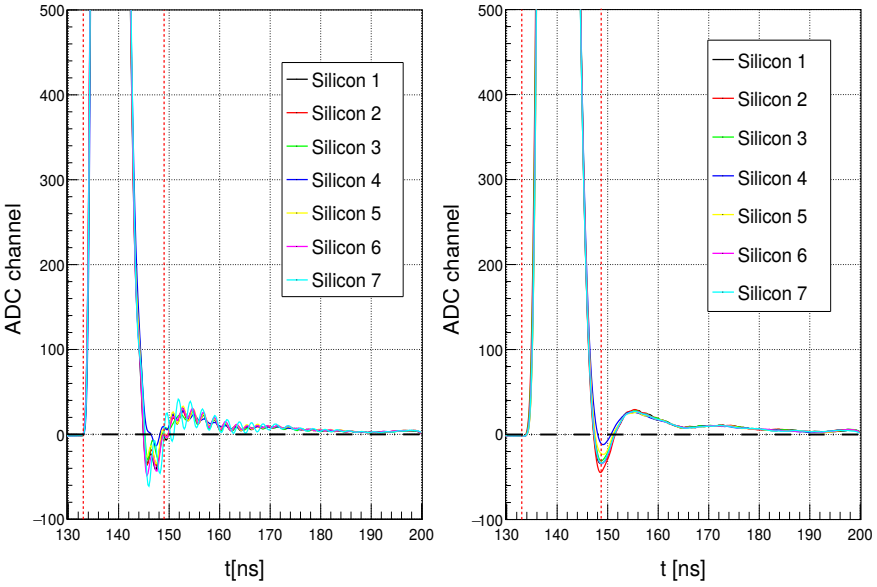

Figure 101: This graphs are an enlargement of pictures Fig. 100. On the left is shown the individual channel response and on the right the response of the sum output.

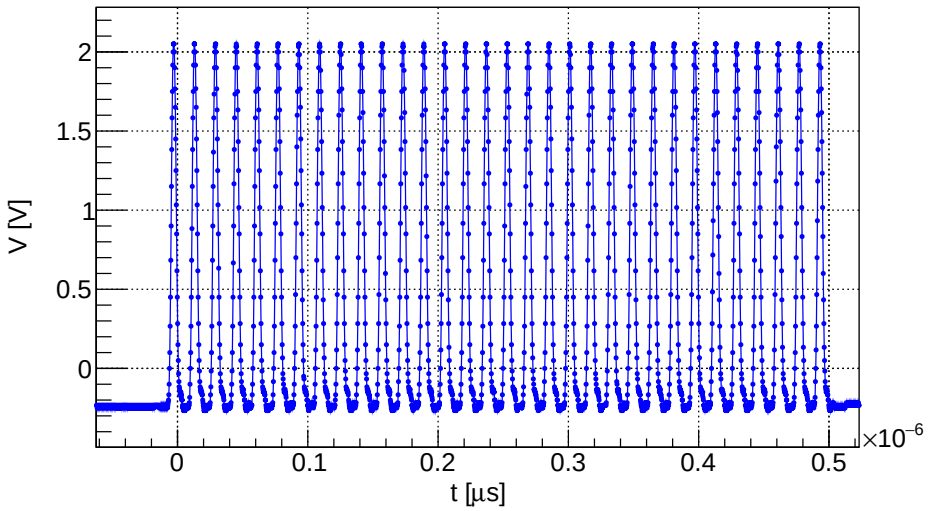

Figure 102: Signal used as external trigger to drive the laser emission.

32 single pulse template functions, properly shifted in time and weighted with a factor p_i which represents the pulse height.

$$F(t) = \sum_{i=1}^{32} f(t - 16 \cdot i - t_0) \cdot p_i \tag{19}$$

The fit results have been validated using simulated events. The procedure has proven the capabilty of detecting differences in amplitude of the order of per mil among single pulses. In addition, the good agreement between the fit function and the detector response demonstrates that the charge pile-up, due to the such high pulse rate, does not degrade the signal waveform.

This makes us confident that our silicon sensors, equipped with custom fast electronics, will be able to disentangle pulses separated by 16 ns with an accuracy at the level of per mil, allowing the calorimeter to measure the beam energy and intensity and their variation in time within a ELI macro-pulse. In addition, as can be seen from Fig.103, we observe that the tiny contributions due to the signal overshoot do not affect the detector response to this train of pulses.

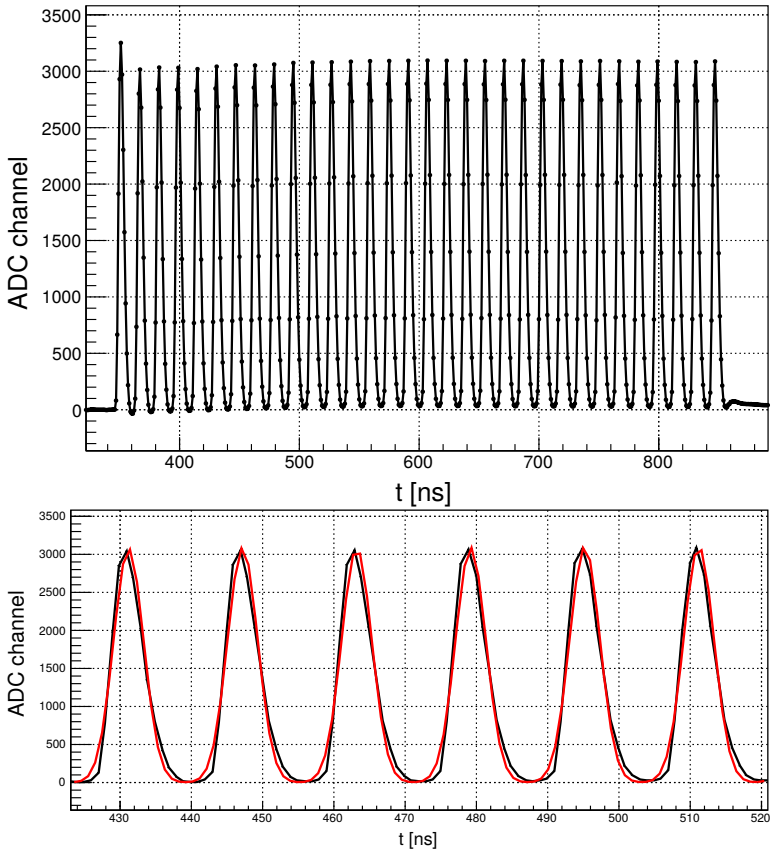

Figure 103: In these two graph is presented the train acquisition with 32 pulse. On the bottom one the fit function is superimposed in red.

6.1.3 Characterization of Si-strip with laser

To check the functionality of all the layers that compose the calorimeter and to spot eventual regions with bad/not correctly bonded strips every sensor has been exposed to the laser. The readout board were scanned horizontally in steps of 2 mm with a relative laser power of 25%.

Unfortunately these measurements (as the previous ones) cannot be used to compare the response of detectors of different GCAL layers. This is due to the fact that the penetration and interaction mechanisms of photons of laser light differ in several aspects from gamma photons. In particular the laser light is subject to reflection and refraction on surface and subsequent silicon layers (pads, passivation, protection, etc.). A change in the position of the sensors with respect to the laser beam, changes the energy deposited inside

the detector. In addition we used a laser without cooled head that has an emission power that turned out to be correlated to the ambient temperature. Indeed measurement on different board have limited reproducibility due to change in time of the temperature (we measured a temperature coefficient between about $-1\ \%/°C$ and $-2\ \%/°C$).

However, this measurement can be used to make sure that there are no anomalies on detector response and to verify gain differences between sensors belonging to the same board. For each position of the scan along the "X" direction, i.e. along the short side of the silicon pad, we acquired 3000 events and evaluate the distribution of the signal maximum. Fig. 104 shown an example of the distribution of the maximum obtained at a fixed position. The mean value is then calculated from a fit with a gaussian function.

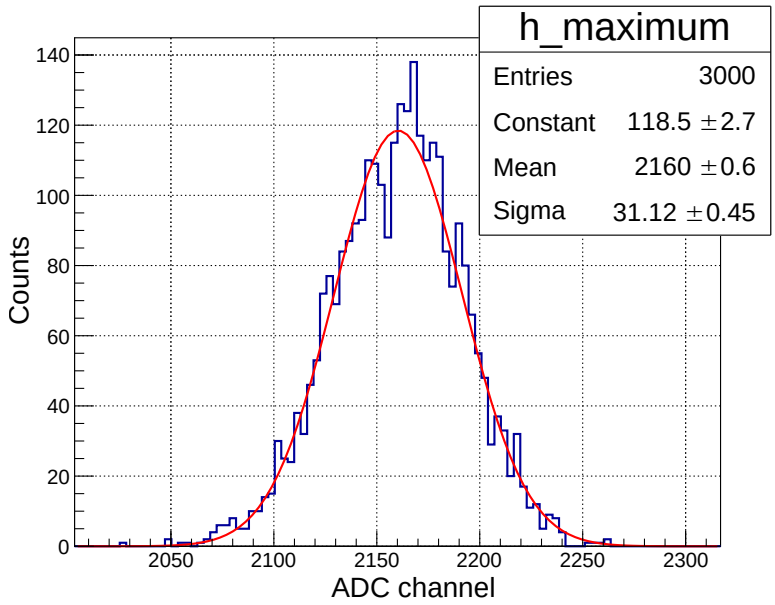

Figure 104: Example of a distribution of the obtained signal maximum.

The results of the scan for one board is shown in Fig. 105. The average value of the signal maximum is shown as a function of the laser position. The responses of the 7 detectors are displayed with different colors and the sum channel output is plotted as a dotted line. The sensor signal is almost zero when the laser illuminates the region between two detectors and then ranges on a constant value when the laser beam is inside the detector.

This scan procedure has been performed on all the 22 layers of the calorimeter. We calculate a quantity proportional to the energy released from the laser inside a pad in an entire scan as the integral of the average maximum, i.e. the integral of the histogram relative to a sensor plotted on Fig. 105. Then, to evaluate the gain uniformity of the sensors inside each layer we calculate the mean (μ_{layer}) over the 7 detector and the standard deviation (σ_{layer}). In Fig. 106 are shown in percentage the ratio $\frac{\sigma_{layer}}{\mu_{layer}}$ obtained for the 22 layer.

Looking at the Fig. 106 it is possible to notice that using the laser we obtain differences between sensors inside the same layer that are in average of about 2.1 %. This difference are mainly due to the laser intensity variations,

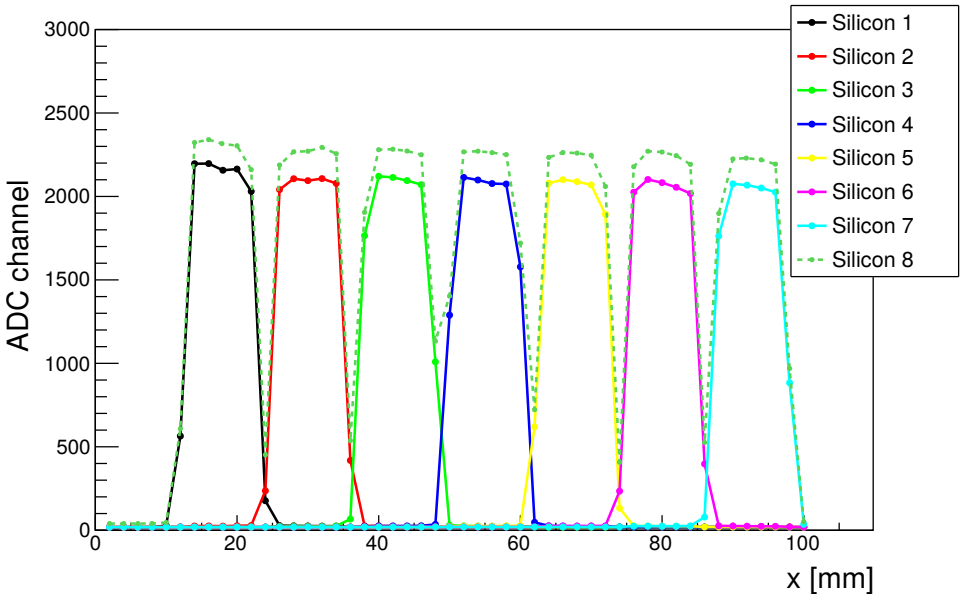

Figure 105: Average value of the signal maximum obtained during the horizontal scan of a calorimeter board with the IR laser. The channel output of different pads is plotted with different colors and the sum channel output is plotted with a dashed line. The dots represents the various laser positions.

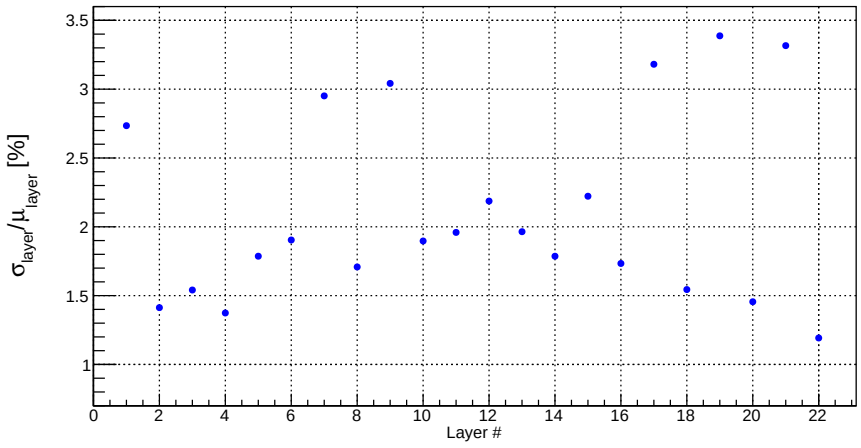

Figure 106: The plot displays the percentage ratio between the standard deviation σ_{layer} and the mean μ_{layer} of the signal maximum measured from the 7 silicon sensor in a layer. This ratio is plotted as function of the layer number.

that do not allow to calibrate the silicon pads better than a few percent. Indeed, as can be read from the laser manual [55], the stability of the laser power is 1% RMS for a cooled laser, and worst for a not cooled one, that is our case.

This hypotesis is confirmed from the results obtained during the tests of the detectors performed with protons at the DEFEL beam-line of the Tandetron accelerator at LABEC in Sesto Fiorentino, Italy. In this measurement

we observed differences between sensors belonging to the same layer or to different layers of about 1 %.

The difficulties in the evaluation of the fraction of energy reflected/refracted inside the detector bulk makes measurement done with laser not useful for absolute energy calibration. The calibration of the energy scale is obtained from the sensors test with monochromatic proton bunches at DEFEL.

6.1.4 Signal dependence from the γ impact point

We have also performed scans of the sensors along the "Z" direction, i.e. along the long side of the silicon pad. The scan has been done using steps of 1 mm and acquiring 5000 events on each point. For each point the average signal maximum is evaluated from the gaussian fit of the distribution as done previously during the "X" scan as well as the average waveform and the area of this waveform. In Fig. 107 are shown the average waveforms obtained when the laser spot is contained inside the detector active area. Notice that the Z zero position correspond to laser pointing on the opposite side of the read-out electronics. From the figure we can observe that when the laser photons hits the region close to the read-out electronics the waveform have greater rise time and lower amplitude than when the laser spot is directed onto the opposite side. The variation of the average maximum as function of

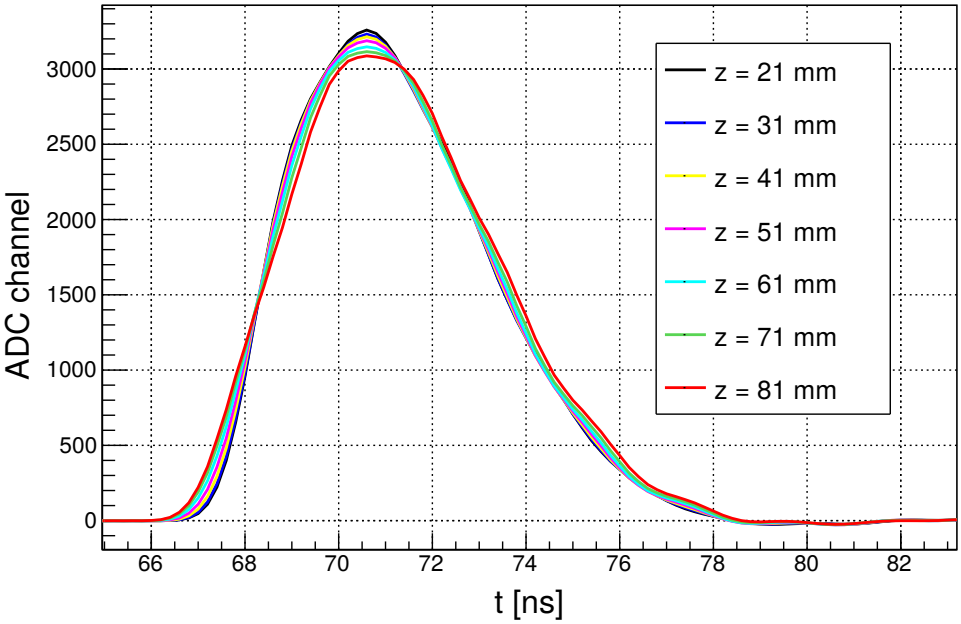

Figure 107: Average waveforms obtained for different laser position along the longitudinal detector axis.

the impact point is shown on Fig. 109, from which we can observe a decrease of about 100 ADC channels from the detector start point to the end.

The waveform area, calculated as the integral from 65 to 83 ns remains almost the same, independent from the laser position, as it can be observed from Fig. 109.

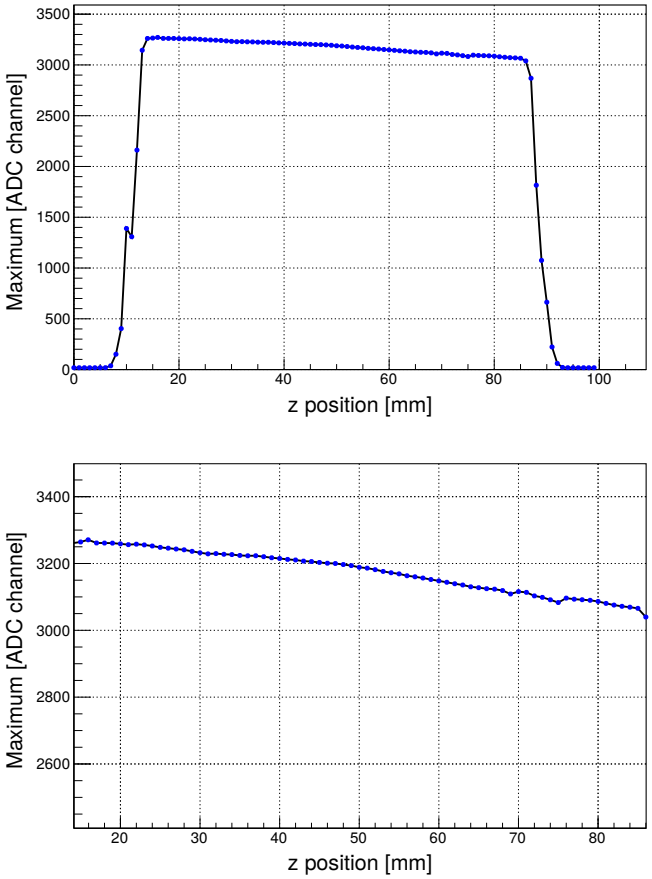

Figure 108: The graphs display the signal average maximum as function of the laser spot position on the z-axis. On the bottom plot is presented an enlargement on the detector central region.

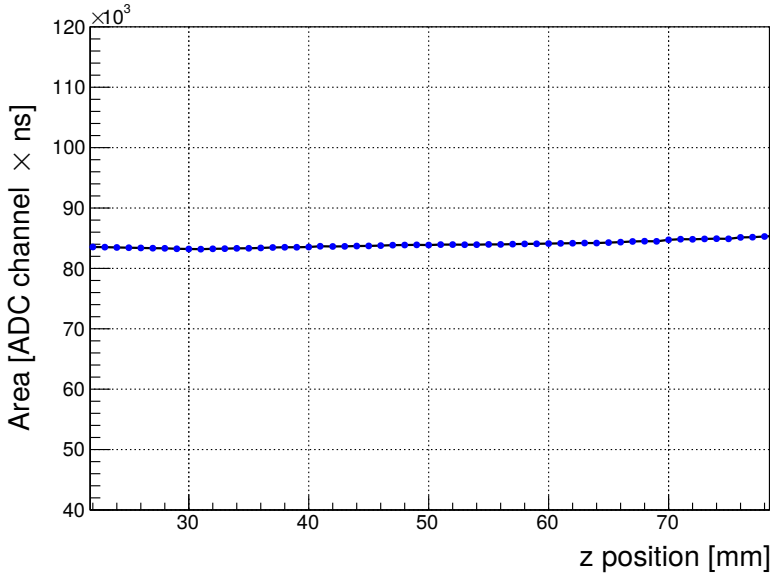

Figure 109: The graph presents the area of the average waveform plotted as function of the laser spot position on the z-axis.

We observe a similar change on the signal waveform when the load resistence is changed of about 1 Ω. In particular with greater resistence the signal has an higher maximum and shorter rise time. From this evaluation we inferred that the observed waveform modification are probably related to the presence of an additional resistence due to the longer path to be crossed by the produced charge when the photons impinge on the opposite side of the read-out electronics.

We evaluate the possible effect of this signal dependency on the particle impact point using a toy MC. Due to the symmetry of the beam and of this effect with respect to the beam axis, this impact point dependency does not affect the energy reconstructed in a calorimeter layer and then does not change the calorimeter performances.

We perform also an additional horizontal scan of the detector, using this time a smaller step of 40 μm and evaluating the average maximum as previously described. The results are shown in Fig.110. From the figure we can observe that the detector response is independent on the photon impact position, furthermore we can not observe the structures due to the single strips because the beam spot(1.5 mm× 3.5 mm) is much larger than the strip pitch, 80 μm. From this measurement we can roughly verify that the horizontal dimension of the active region is $\sim$ 10 mm, as shown in Fig. 110 where the active region is enclosed between the red dashed lines.

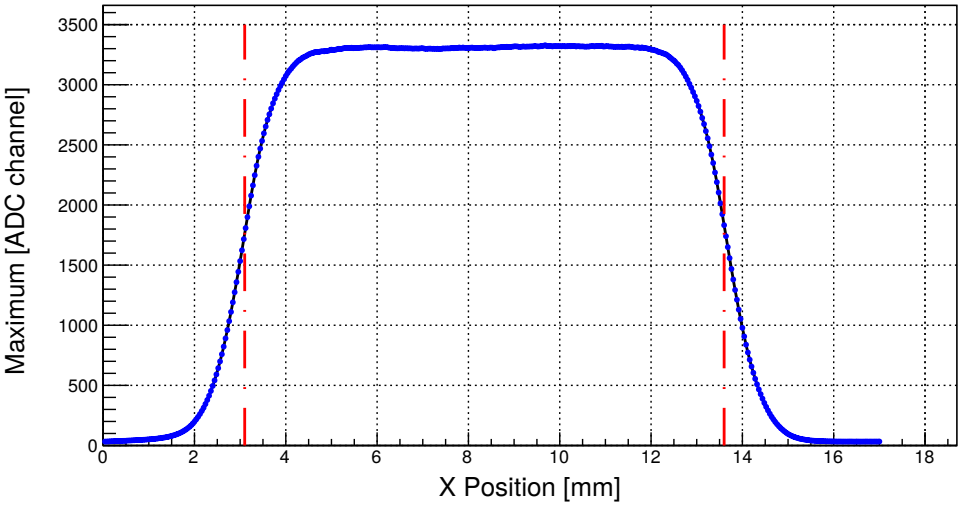

Figure 110: In the graph are shown the signal average maximum as function of the laser spot position on the x-axis. The detector active region is enclosed between red dashed lines.

6.2 DETECTOR SIMULATION

The optimized layout of the calorimeter for the low-energy ELI-NP beam described in Section 5.3, consisting of 22 elements made of 3 cm of PE absorber and 0.32 mm Si planes, has been simulated in detail using Geant4 software toolkit.

6.2.1 Geant4 Monte Carlo simulation toolkit

Simulation plays a fundamental role in various domains and phases of an experimental physics project; for example the design of the experimental set-up, the evaluation and definition of the potential physics output of the project, the assessment of the detectors performance. The Geant4 [19, 20] object oriented toolkit is a full set of libraries written in C++ allowing the user to simulate their detector system. Specifying the detector geometry, the software system automatically transports the particles shot into the detector by simulating the particle interactions based on the MC method. Such a method searches for solutions to mathematical problems using statistical sampling with random numbers.

To create a simulation, the user must define a world, and populate this with materials and geometries. Primary particles (e.g. proton, e^-, γ etc.) must then be defined, and the physics processes required for the simulation added. Geant4 will then simulate the passage of the primary particles through the world, transporting each particle via a series of steps. For each step through the simulated geometry, Geant4 calculates the mean free paths for any competing physics processes, and 'chooses' a process based upon the relative strengths of each interaction channel and a random number generator. This then determines the step length and the physics process to be simulated. The maximum value of the step length can also be defined by the user, and will be limited if the step encounters a physical boundary. Each primary particle is known as an event, and Geant4 stops tracking it when the particles kinetic energy reaches a cut-off threshold, or it exits the world volume. Information about each particle can be obtained at both the pre-step and post-step points, including the energy deposited per step, the type of particle, number of secondaries, position, trajectory etc. By combining the information across all steps, information for each event can be obtained, and therefore used to create useful outputs, such as energy spectra.

6.2.2 MC implementation

Physics

Geant4 offers a wide set of alternative and complementary electromagnetic and hadronic physics models together with several physics processes for the particles-matter interaction that cover the physics of photons, electrons, muons, ions and hadrons from 250 eV up to several PeV. For a particle

interaction it is crucial the type of process, the particular initial state and the final one with a defined cross-section and mean-life, and the model that implements the production of secondary particles. The Geant4 toolkit offers multiple models for the same process. In general the user can construct a physics list [59] choosing among the various physics models contained in the Geant4 kernel or directly using a reference physics list, already containing a set of well-tested physics components.

To describe the electromagnetic process Geant4 has two basic sets of libraries designed to be applied in different energy ranges: for the high-energy there is a package known as the Standard model, and for the low-energy one there is a set of models named "Low-Energy models" [60, 61]. These have to be used when is needed a precise treatment of the electromagnetic showers and interactions at low-energy scale (keV). Indeed, since the atomic shell structure is more important in most cases at low energies than it is at higher energies, the low energy processes make direct use of shell cross section data. The standard processes, which are optimized for high energy physics applications, often rely on parameterizations of these data. Given the energy involved at ELI-NP we need the low energy implementation of the electromagnetic process for the GCAL simulation.

In particular we decided to use the PENELOPE model [27] that accurately describe the physics process for electron, positron and gamma-rays in the 100 eV- 1 GeV energy range. The name is an acronym that stands for PENetration and Energy LOss of Positrons and Electrons (photon simulation was introduced later). The simulation algorithm is based on a scattering model that combines numerical databases [62] with analytical cross section models for the different interaction mechanisms (Compton scattering, photoelectric effect, Rayleigh scattering, gamma conversion, bremsstrahlung, ionisation and positron annihilation, see [63] for detail).

For the high-energy line the γ beam has energy larger than the binding energy of the nucleon in the nucleus, therefore are possible also photonuclear reaction with the emission of hadrons such as p, n and α. To model this processes in the MC simulation we used the QGSP-BERT reference physics lists [64].

Primary particle

Primary particles are those that are defined within the primary generator, and are then propagated throughout the simulated geometry. To define a particle, the type is specified (γ, neutron, etc.), and an initial position and momentum/direction is given. For the GCAL simulation we generate events using photons of definite energy impinging perpendicularly on the centre of the calorimeter. The systematic effects due to the expected energy and spatial distribution of the ELI-NP γ beam on the detector performances have been studied in detail and are presented in Sec.6.2.6.

Geometry and material

In the first stage of the project [18] the layout for the calorimeter provided 24 layers also for the GCAL to be operated on the low energy line. We evaluated that the percentage of energy released in the lasts two layers with respect to the total energy deposited in the calorimeter for photons of the LE line is < 2 %. Therefore, after checking that the energy resolution was not deteriorated, we decided to realize a 22 layers calorimeter. To verify this new arrangement and the results produced in the early stage of the project during the design of the calorimeter, new simulations were made considering a thorough description of the detector geometry. In particular we have simulated in detail the various components of the microstrip detectors, including dead space, the aluminium strip and the backplane metallization. Furthermore, the presence of the aluminium supporting structures, of the acquisition board and of the air recess in the PE absorber block were included in the geometry description. The layout of one calorimeter layer, as implemented in the simulation, is shown in Fig. 111, on the left the front side (the one entered by the beam), on the right the rear one.

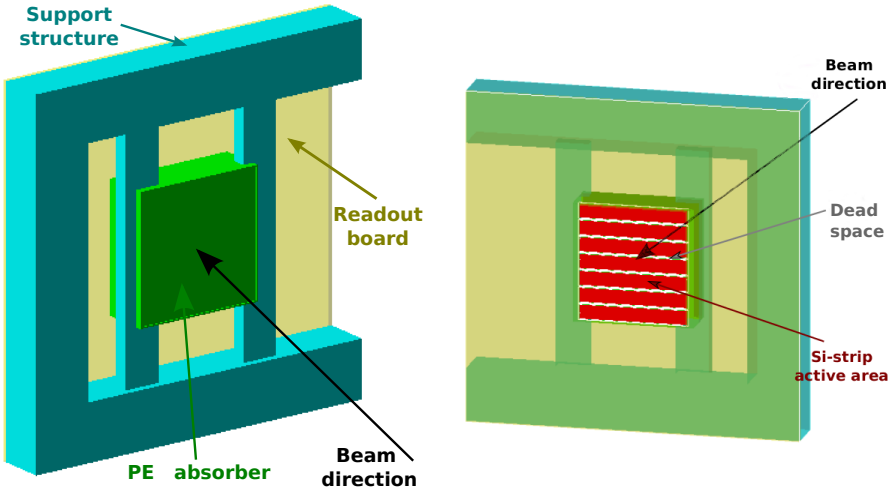

Figure 111: Overview of a calorimeter layer layout as implemented in the Geant4 simulation. On the left is shown the front side (the one entered by the beam) view and on the right the rear one.

In Fig. 112 are presented the design and dimensions, of a simulated active calorimeter layer. In yellow is shown the readout board which has an inner hole with dimensions of 88×80 mm^2 that is sufficient to not cover the silicon detector active region but also to guarantee a contact surface for gluing the sensors on the board. To simulate the readout board, we defined a fiberglass G10 material composed by $SiO_2C_3H_3$ with a density of 1.7 g/cm^3.

The area named as "Si-strip sensor region" in the plot, represents the active region and it is surrounded by two implanted rings covered by an aluminium layer (the bias and the guard rings) and by the additional region that remains after the cut of the pad from the original lunette structure (the average distance from the edge is 24 μm, as described on Sec.5.3.1). These regions, although receive contributions from energy deposition, do not

participate to the signal formation in the real detector and are considered as "dead". The total lateral dimension comprising the active area, the two rings [65] and the distance from the edge is 12.136 mm and is the dimension of the "Si-strip sensor region" used in the simulation. The distance between two adjacent sensor used in the MC simulation is about 0.36 mm and is obtained considering the pitch of 12.5 mm realized in the readout board and the simulated detector dimension.

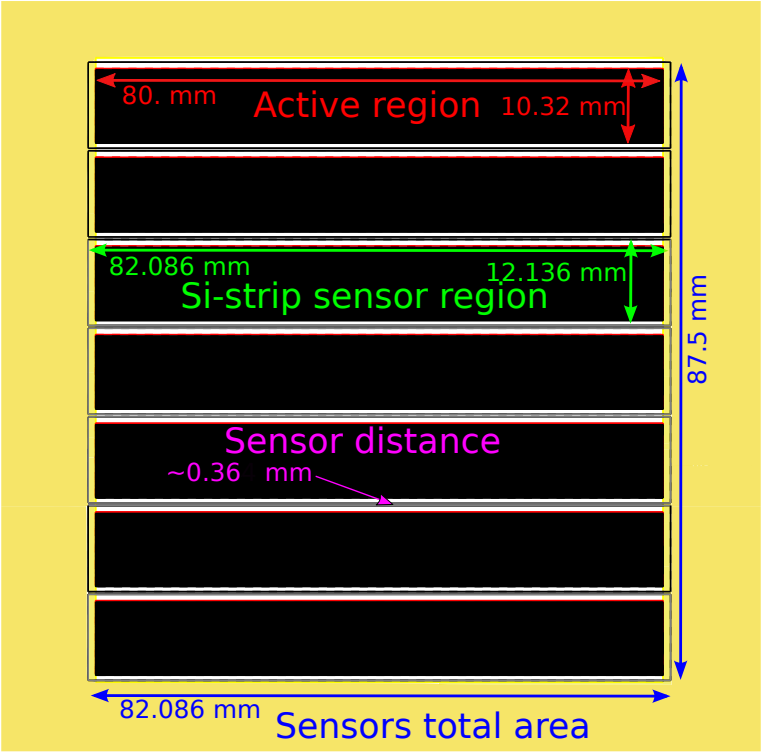

Figure 112: Zoom of the layout of a calorimeter layer as implemented in the Geant4 simulation. The dimensions of the different regions used in the MC simulation are shown in the figure.

The active region of the Si-strip detectors has been defined as "sensitive detector" in the simulation, that is a way in Geant4 used to declare a geometric volume "sensitive" to the passage of the particles. It activates the scoring functionality of Geant4 and gives the user a handle to collect quantities from these volumes.

In the GCAL detector we used a tracking cut of 0.05 mm, that is a threshold on the production of secondary particle as described in Sec.3.3.1; indeed only particle able to travel at least the range cut are produced. In the thin volumes representing the Al-strips and the Al-backplane we used lower cuts of 0.4 μm respectively.

6.2.3 Energy reconstruction

The longitudinal profile of the energy released in different layers of the GCAL is sensitive to the energy of the incident photons, so it can be used to reconstruct the γ beam energy, as explained in detail on Sec.5.1.

To obtain the longitudinal profile we calculate the average energy deposited in the calorimeter layers by tracking the γ inside the detector. In Geant4 it is possible to retrieve information about the particle at the level of a step, defined as the "delta" information between two subsequent points. To evaluate the energy released from a single photon inside the sensitive region of a layer, the sum of its energy deposition in each step performed inside the layer during a hit has been calculated. To obtain the average energy deposition of N photons first we evaluate the mean energy (μ) released by a single photon in each layer. Then, assuming that the energy deposition is linear, it is possible to calculate the total energy simply multiplying μ by N.

The distribution of the single photon energy released in the second layer of the calorimeter for different beam energies is shown as example in Fig. 113. The "Mean" values of the histograms represent exactly the desired quantities (μ). Indeed, to obtain the correct calculation of the average energy released, it is necessary to calculate the sum of all the energy deposited, taking into account also the case in which the energy deposition is zero.

Finally, the simulated longitudinal profiles of the energy released per micro-pulse can be obtained and is shown for various beam energies in Fig. 114.

We evaluated also the expected energy loss in the "dead" area of the silicon detector. In Fig. 115 is shown the ratio between the energy loss and the measured one in each layer of the GCAL. From the figure we can notice that this fraction slightly increases with the beam energy, remaining however less than 12% for all the considered energies.

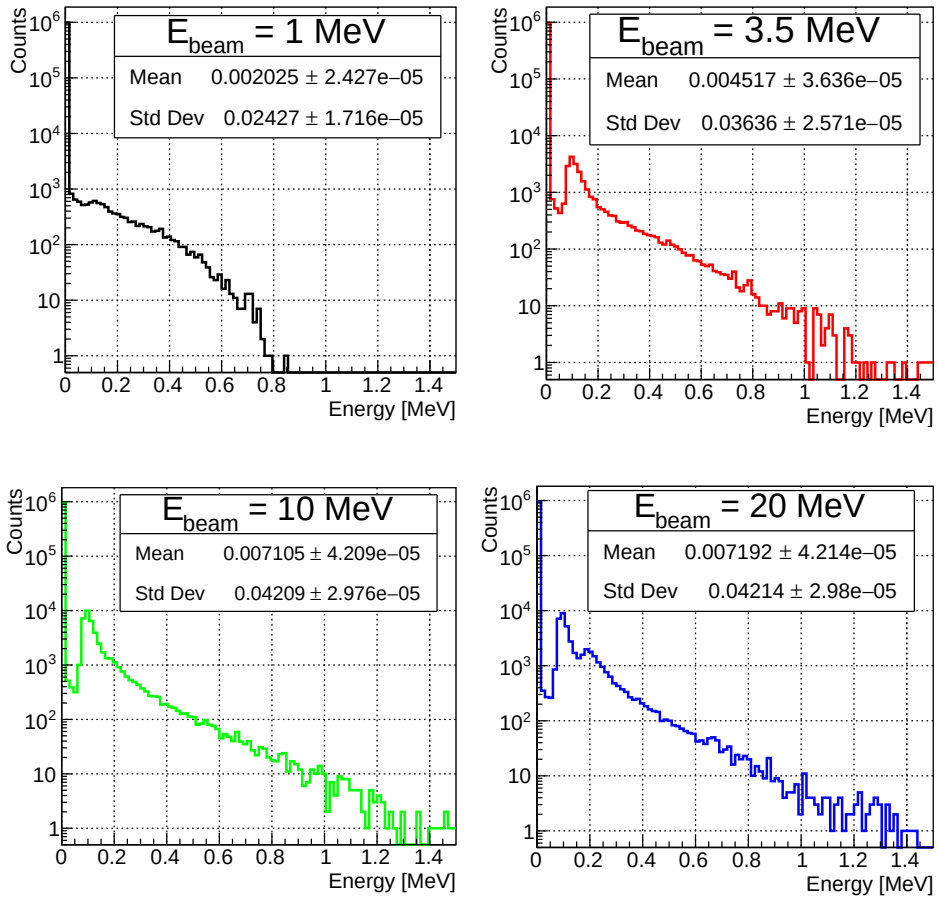

Figure 113: Distribution of the energy released in the 2nd layer of the calorimeter for different beam energies (E_{beam} = 1, 3.5, 10 and 20 MeV).

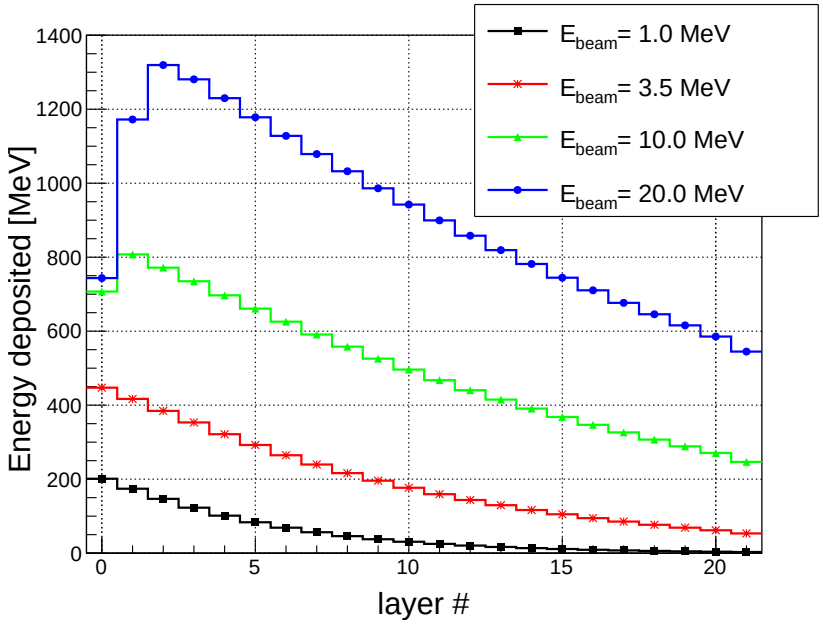

Figure 114: Longitudinal profile of the energy released in the 22 detector layers from a single pulse of a beam of nominal intensity (10^5 photons) and for different beam energies.

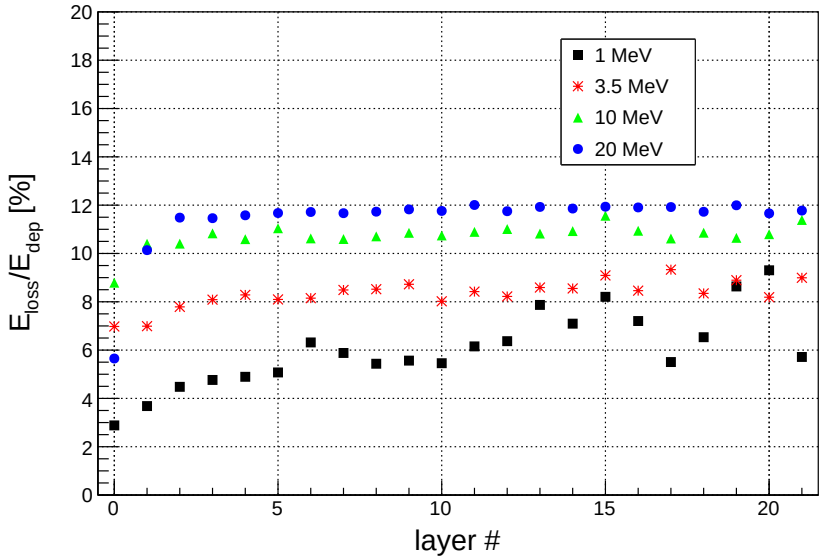

Figure 115: Ratio of the energy loss (E_{loss}) and the deposited energy (E_{dep}) in the 22 detector layers for different γ beam energies.

The analytic expression of the longitudinal profile vs. E_γ is not known and it is necessary to reconstruct the energy of the γ beam. Therefore, we use MC simulations to parametrize the profile of the energy release as a function of the γ beam energy. To obtain this parametrization, photons interacting in the calorimeter were produced with energy values ranging from 0.5 to 22 MeV, in steps of 0.1 MeV. For each energy, we have simulated 200 pulses of nominal intensity (10^5 γ per pulse), this will be referred to as MC^{thruth} sample. In Fig. 116 is shown the fraction of the energy released in each layer ($p_i(E_{beam})$), normalized to the total measured energy E_{tot}, determined as follows:

$$p_i(E_{beam}) = \frac{E_i}{E_{tot}} = \frac{E_i}{\sum_{i=1}^{22} E_i} \tag{20}$$

where E_i is the energy deposited in the i-th layer. A profile parametrization as a function of energy is then obtained by interpolation of these points. The solid red curves are the interpolated profiles of the energy profile distributions.

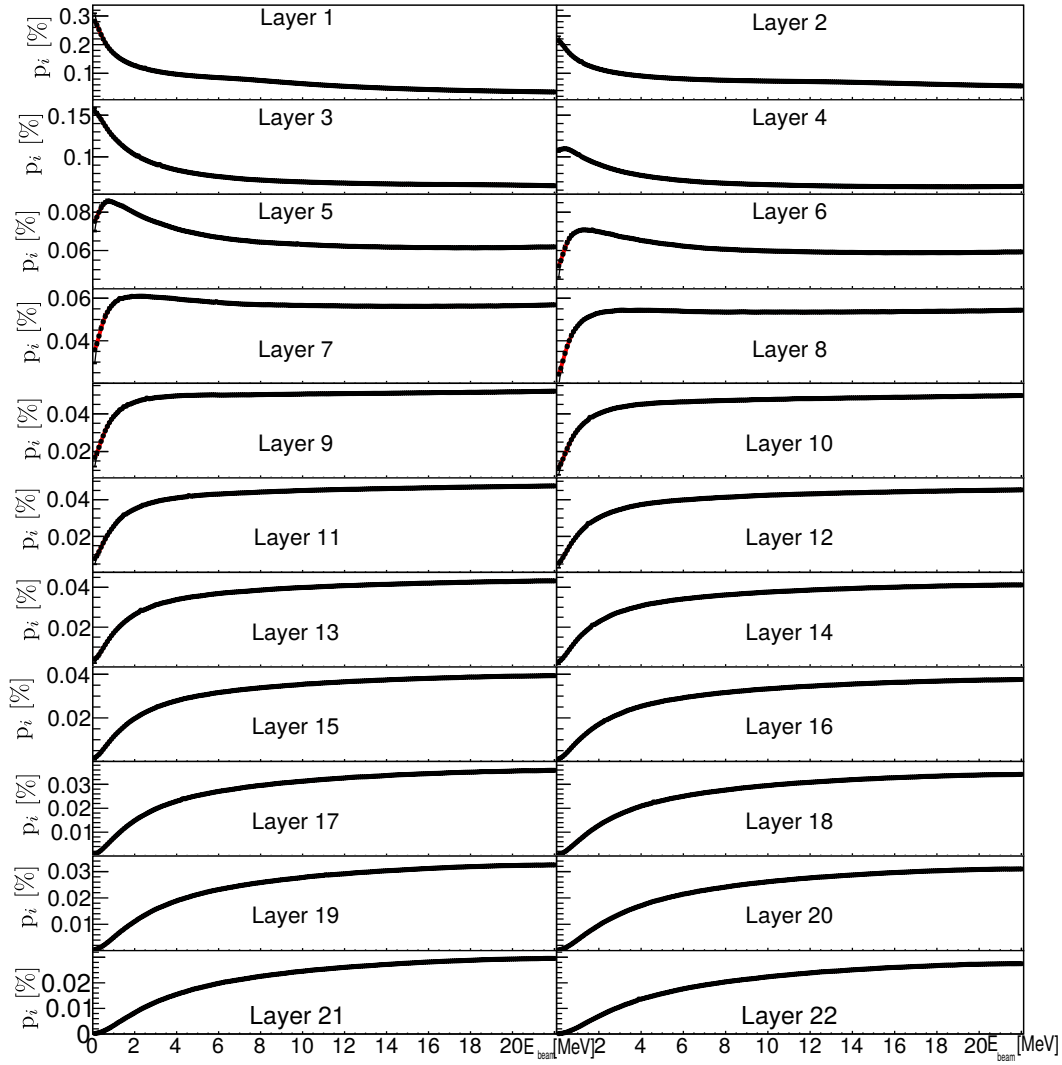

Figure 116: Fraction of the released energy in each of the 22 layers of the calorimeter as a function of the photon energy.

We parametrized as a function of the γ beam energy also $f(E_{beam})$, that is the fraction of sampled energy with respect to the total energy flow carried by the beam, defined as follows:

$$f(E_{beam}) = \frac{E_{tot}}{\sum_{j=1}^{N_\gamma} E_{\gamma,j}} = \frac{\sum_{i=1}^{22} E_i}{\sum_{j=1}^{N_\gamma} E_{\gamma,j}} \tag{21}$$

where E_i is the energy deposited in the i-th layer and $E_{\gamma,j}$ is the energy of the j-th photon in a beam composed by N_γ photons. The average values of $f(E_{beam})$ obtained from the simulation is shown with black points in Fig. 117, while the parametrized function is shown in red.

In both cases the interpolation of the points has been made using the method of Nadaraya-Watson kernel regression estimate [66], [67], which is available in the ROOT analysis framework [68].

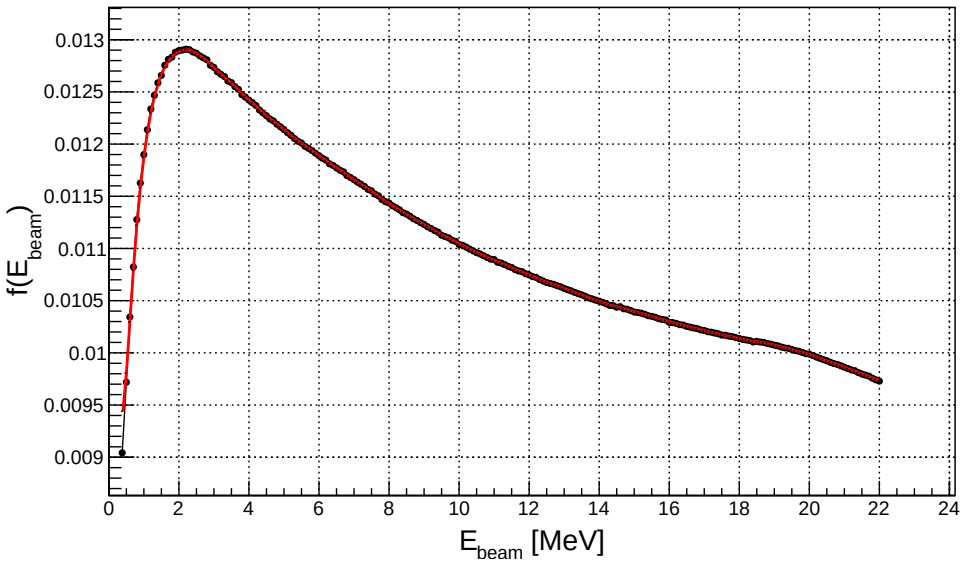

Figure 117: Fraction of energy released in the whole calorimeter with respect to the total beam energy reported in function of the photon energy.

To reconstruct the input beam average energy the measured longitudinal profile is fitted against the parametrized one (MC^{thruth}). During the fit procedure the value of the average energy is left as a free parameter and a scan on beam energies close to a starting one is carried out. The fit procedure try to minimizing the χ^2 function:

$$\chi^2 = \sum_{i=1}^{22} \frac{(p_i(E_{beam}) - p_i^{MC^{thruth}}(E_{beam}))^2}{\sigma_i^2} \tag{22}$$

using the IMPROVE algorithm of Minuit [69]. In this equation p_i is the fraction of measured energy in the i-th layer defined in Eq.20, $p_i^{MC^{thruth}}$ is the expected fraction of energy released in the i-th layer for a beam of given energy (E_{beam}) and σ_i is the standard deviation of $p_{E,i}$.

To optimize the fit procedure we estimate a starting value for E_{beam}, using the barycenter of the deposited energies calculated as follow:

$$b(E_{beam}) = \frac{\sum_{i=1}^{22} i \cdot E_i}{\sum_{i=1}^{22} E_i} \tag{23}$$

where E_i is the measured energy by the i-th layer and the dependence of the barycentre on the beam energy (E_{beam}) is explicit. The obtained barycentre is compared to the ones calculated for the MC^{thruth} samples searching for the simulated E_{beam} that produces the closest barycentre value. The so found E_{beam} value is used as initial guess for the fit procedure.

The fit procedure consists in minimizing the χ^2 function (defined in Eq.22) and corresponds to find the value of the beam energy (E_{beam}) that minimizes the differences between the measured profile and the one expected from the MC parametrization. Using this fit procedure we estimate the beam energy E_{beam} and the associated error δE_{beam}.

Once the beam energy E_{beam} is known, in the hypotesis of a monochromatic beam (beam bandwith $\leq 0.5\%$, Tab.1), the number of photons in a pulse, N_γ, can be determined from the total energy E_{tot} (see Eq.21) measured in the calorimeter:

$$E_{tot} = N_\gamma \cdot E_{beam} \cdot f(E_{beam}) \tag{24}$$

$$N_\gamma = \frac{\sum_{i=1}^{22} E_i}{f(E_{beam}) \cdot E_{beam}} \tag{25}$$

where E_i is the measured energy in the i-th layer and $f(E_{beam})$ is the fraction of the total energy released in the calorimeter. The value used for $f(E_{beam})$ in Eq.25 are the ones obtained from the parametrization curves shown in red on Fig. 117. The error on the determination of N_γ was calculated using the errors propagation on Eq.25. Taking into account the dependence on E_{beam} of the f factor and neglecting the correlation between f and E_{beam}, we obtain for δN_γ the following expression:

$$\delta N_\gamma = N_\gamma \cdot \left(\left[1 + \frac{E_{beam}}{f(E_{beam})} \cdot \left(\frac{\delta f(E_{beam})}{\delta E_{beam}} \right) \right]^2 \cdot \left(\frac{\delta E_{beam}}{E_{beam}} \right)^2 + \left(\frac{\Delta f(E_{beam})}{f(E_{beam})} \right)^2 \right). \tag{26}$$

From the Eq.26 can be noticed that the error in the determination of N_γ is essentially composed by two types of contributions. The first is the contribution due to the uncertainty on the determination of E_{beam}, that propagates in the information related to $f(E_{beam})$ and the second term is due to statistical fluctuations associated with the fraction of energy detected by the calorimeter.

To test the reconstruction energy procedure, we simulated the GCAL response to an independently generated MC sample named "MC^{DATA}". We simulated 1000 different beam pulses of 10^5 photons in the energy range

between 1 MeV and 20 MeV, in steps of 0.5 MeV. We used a larger energy range to obtain the energy profile parametrization (0.5 - 22 MeV) in order to correctly parametrize also the events that populate the tails of the energy reconstructed spectrum.

An example of the energy reconstruction procedure performed on a simulated beam of 3 MeV is shown in Fig. 118. In the top graph is shown the fraction of deposited energy in each layer ($p_{E,i}$) and with a red line the obtained fit function. In the bottom plot are reported the χ^2 values obtained from the energies scan from which we obtained a minimum for $E_{beam} = 3.00 \pm 0.03$ MeV.

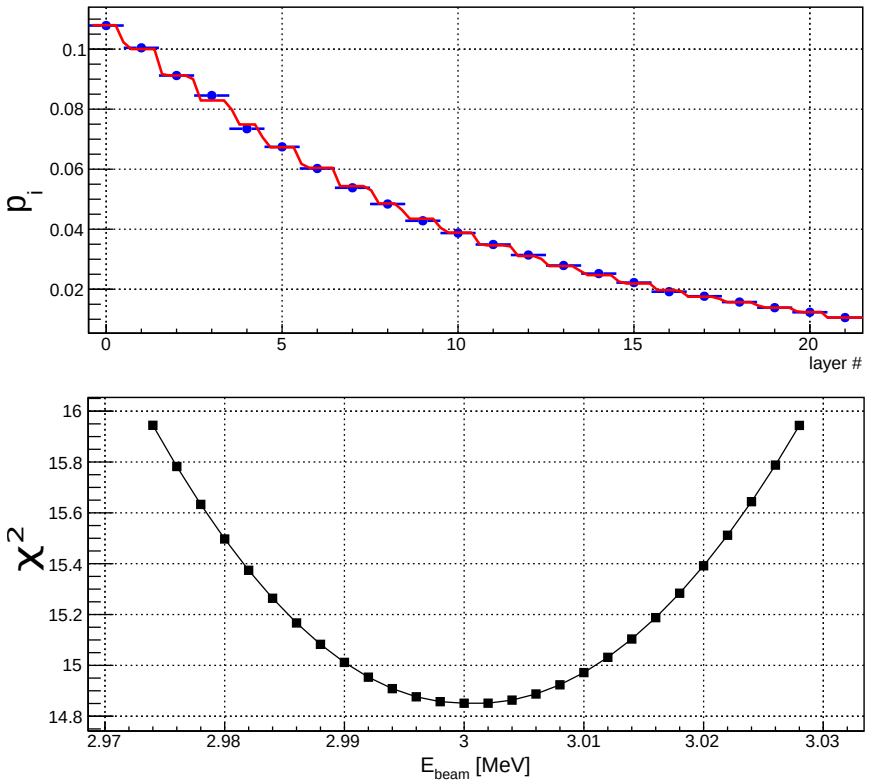

Figure 118: Example of the energy reconstruction procedure. The signal fractions of the energy deposited in each calorimeter plane, provided by MC^{DATA} sample for a nominal 3 MeV beam energy, and shown as blue dots on the top plot, are fitted against the expected profile. The lower plot shows the fit χ^2 scan.

Performing the fit procedure on all these "MC^{DATA}" pulses we evaluate the performances of the GCAL on the reconstruction of the average energy and intensity of the beam at different energies.

As an example are shown in Fig. 119 the distributions of the values of E_{beam} and N_γ obtained from the fit procedure for a beam of 4 MeV, the superimposed red lines represent the gaussian fit to the distributions which provides the reconstructed beam energy value (the fit mean) and associated error (the fit σ).

The expected resolution on the beam energy ($R_{E_{beam}}$) and on the beam intensity (R_{N_γ}) together with the offset between true and reconstructed en-

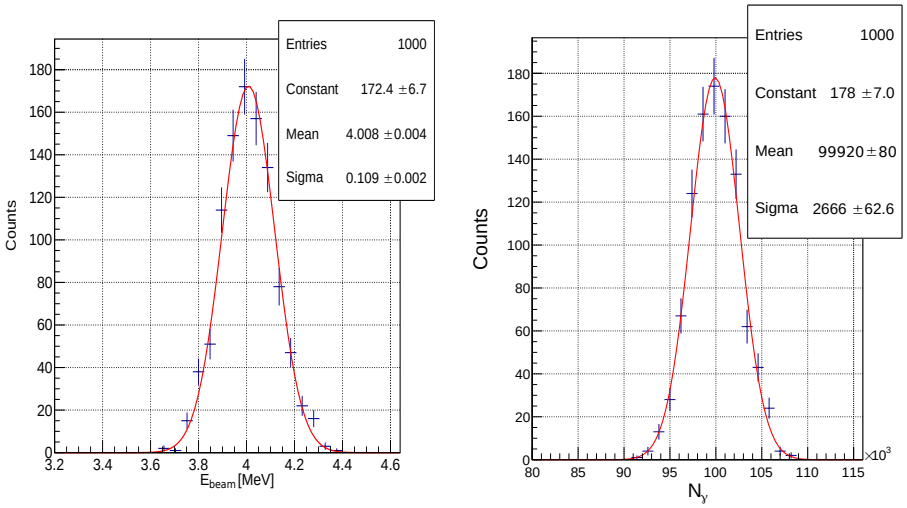

Figure 119: This figure shows the distribution of the reconstructed energy and intensity of 1000 simulated samples of 10^5 γ with 4 MeV energy.

ergy and intensity values, $B_{E_{\mathrm{beam}}}$ and B_{N_γ} are calculated using the following equation:

$$R_{\mathrm{E_{beam}(N_\gamma)}} = \frac{\sigma_{E_{\mathrm{beam}}(N_\gamma)}}{\mathrm{E^{rec}_{beam}}(N^{\mathrm{rec}}_\gamma)} \tag{27}$$

$$B_{\mathrm{E_{beam}(N_\gamma)}} = \frac{\mathrm{E^{rec}_{beam}}(N^{\mathrm{rec}}_\gamma) - \mathrm{E^{true}_{beam}}(\mathrm{N}^{\mathrm{true}}_\gamma)}{\mathrm{E^{true}_{beam}}(N^{\mathrm{true}}_\gamma)} \tag{28}$$

where $\mathrm{E^{true}_{beam}}(N^{\mathrm{true}}_\gamma)$ are the simulated energy and intensity values and $\sigma_{E_{\mathrm{beam}}(N_\gamma)}$ and $\mathrm{E^{rec}_{beam}}(N^{\mathrm{rec}}_\gamma)$ are the sigma and mean values obtained from the fit of the MC^{DATA} sample.

The results in terms of achievable statistical resolution is shown on Fig. 120, while the offset performances are presented on Fig. 121 for the statistics of 10^5 beam γ, corresponding to one ELI-NP pulse. In the plots the resolutions are shown as a function of the beam energy. The displayed errors are calculated from Eq.27 and 28 using the fit errors on $\sigma_{E_{\mathrm{beam}}(N_\gamma)}$ and $\mathrm{E^{rec}_{beam}}(\mathrm{N}^{\mathrm{rec}}_\gamma)$; therefore only statistical errors due to the fluctuations of the longitudinal profile are taken into account in these plots. As it can be seen from the figure the best possible statistical accuracy for a measurement with a single pulse is a few percent. We note that this uncertainty becomes lower than 0.1% after collecting data corresponding to few seconds of beam operation with its nominal parameters.

Due to the correlation between the beam energy and the intensity we expected a similar resolutions on this two values. Indeed, N_γ is calculated using the value of $\mathrm{E_{beam}}$ obtained from the fit, therefore its error is mainly due to the error on $\mathrm{E_{beam}}$ estimation. The fact that for energy lower than about 2.5 MeV the error on N_γ is higher than the error on $\mathrm{E_{beam}}$ and vice versa for higher energy, its related to the dependency of $\mathrm{f(E}_{beam})$ from the energy (see Fig. 117). Indeed this dependency increase or decrease the error on N_γ due to the presence of the therms $\delta\mathrm{f(E_{beam})}/\delta\mathrm{E_{beam}}$ in its calculation (see Eq.26)).

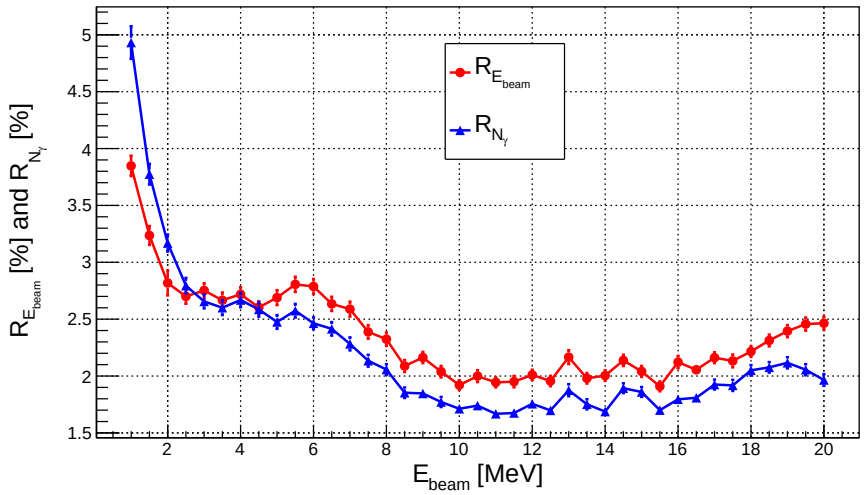

Figure 120: Expected resolution on beam energy (red dots) and on beam intensity (blue triangles), for a pulse of 10^5 photons, as a function of the beam energy.

We observe for energies lower than 4 MeV that the reconstructed energy value is systematically higher than the value used to generate the MC sample. The origin of this bias is unknown and amounts to 0.8% at 1 MeV going down to 0 at 4 MeV. Due to the anticorrelation between N_γ and E_{beam}, that can be notice from the Eq.25, and to the fact that N_γ is calculated using the value of E_{beam} obtained from the fit, if E_{beam} is overestimated than N_γ is underestimated and viceversa. This can be observed clearly in Fig.121 for E_{beam} lower than 4 MeV.

For these reasons we plan to do a final *in-situ* calibration, with the help of the NRSS. The resulting corrections are expected to constrain this systematic bias on the energy scale.

The measurement is expected to be limited by systematic uncertainties, notably related to response calibration. The study of the effects of this systematic uncertainties in the determination of the energy and intensity is presented in the next section Sec.6.2.6. Another source of uncertainty is related to the reliability of the predicted profiles, as a function of energy, which in turn depends on MC simulations. Though the processes can be simulated in great detail, comparison of different models implemented in Geant4 lead to difference up to 0.5% in the energy determination [18].

6.2.4 Transverse energy distribution

Although the knowledge about the transverse distribution of the energy release is not strictly needed for the beam energy and intensity measurement it depends on the beam energy and can be exploited to tune the MC. This dependency can be observer on Fig. 122 and Fig. 123, that show the x-y maps of the energy released in the 22 layers of the calorimeter by one pulse of 10^5 γ of a beam of 1 and 20 MeV, respectively. In the figure are clearly

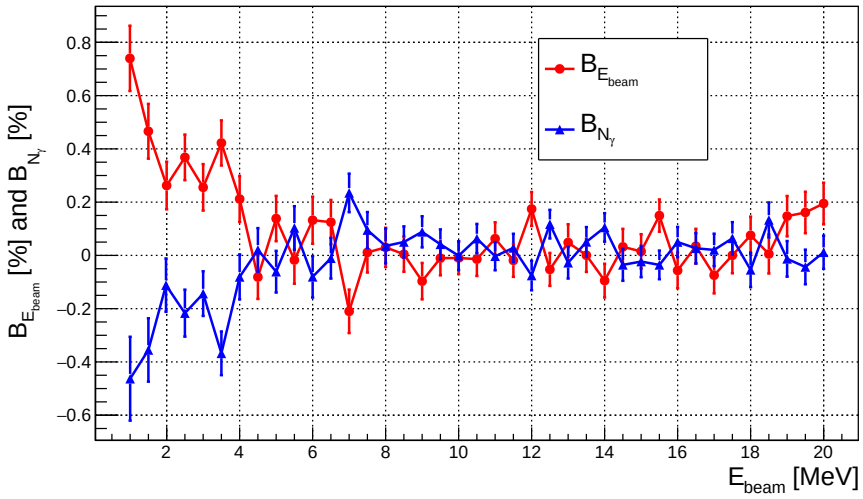

Figure 121: Expected offset on beam energy (red dots) and on beam intensity (blue triangles), for a pulse of 10^5 photons, as a function of the beam energy.

visible the dead area, the spacing between the active pads of the detectors and also the alternating placement along x and y directions. The radius of the showers increases with increasing beam energy, although, mostly of the energy is released on the central silicon pad.

To obtain a rough estimation of the transverse energy distribution inside the detector, the first two layer of the calorimeter will be read-out independently. In particular only for this two layers will be acquired an independent output signal for the 5 central sensors and 1 output signal obtained summing the 7 silicon sensors, while for the remaining layers only the sum signal will be digitised. The information on the average energy deposited on the two outer sensors will be obtained by subtracting from the total sum the energy deposited in the central region. The expected transverse energy profile obtained with this procedure is shown in Fig. 124 for one pulse at nominal intensity and for different beam energies. The energy is shown as a function of the silicon pad number. Discrepancies in these patterns will provide informations on a possible displacement of the beam or the presence of beam halo. In addition the comparison between the profile shown on Fig. 124 and the measured ones will allow to test the predictivity of the Monte Carlo simulations.

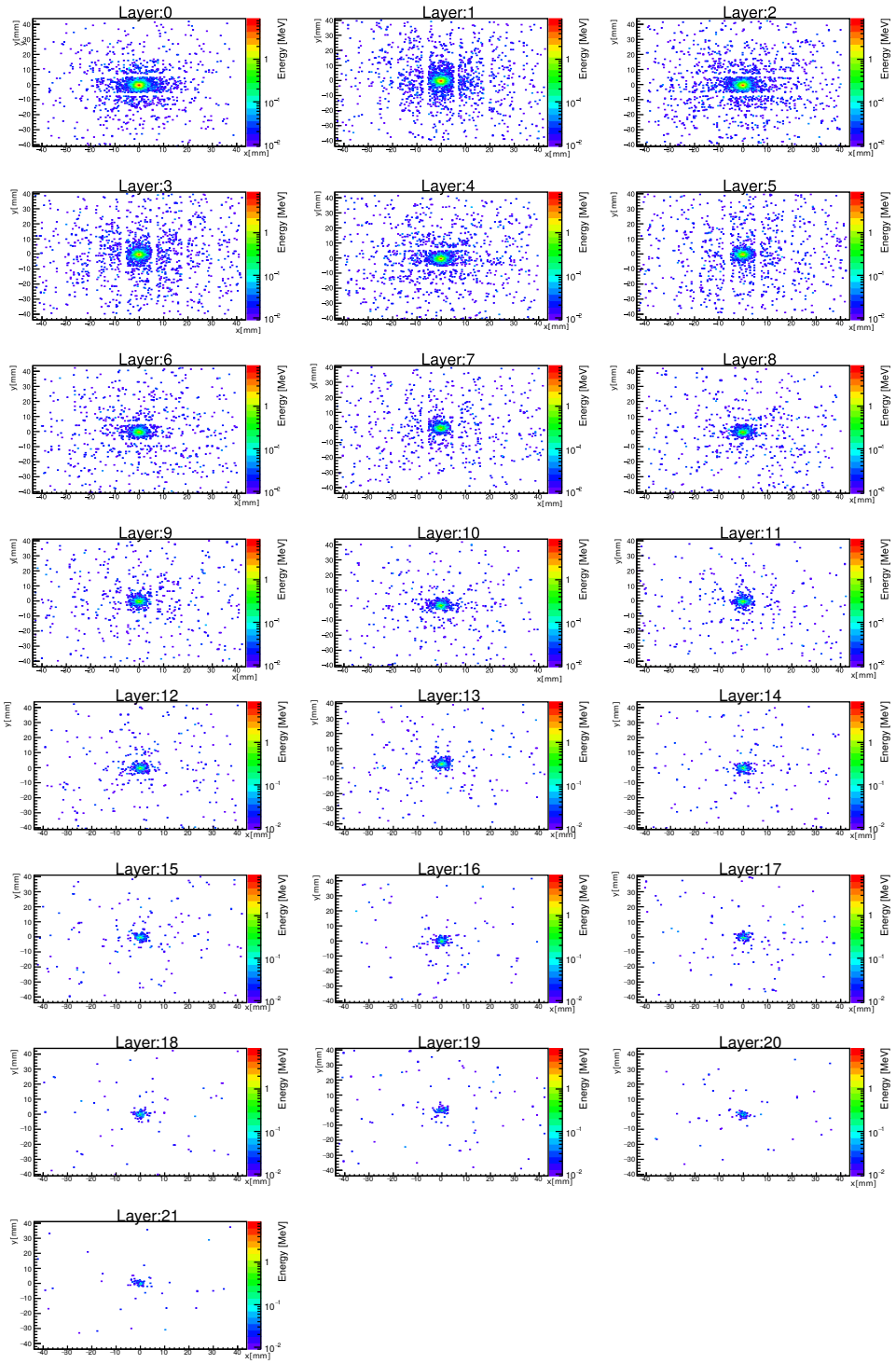

Figure 122: X-Y maps of the energy deposition in the 22 layers of the calorimeter for one pulse of a gamma beam with energy of 1 MeV and nominal intensity.

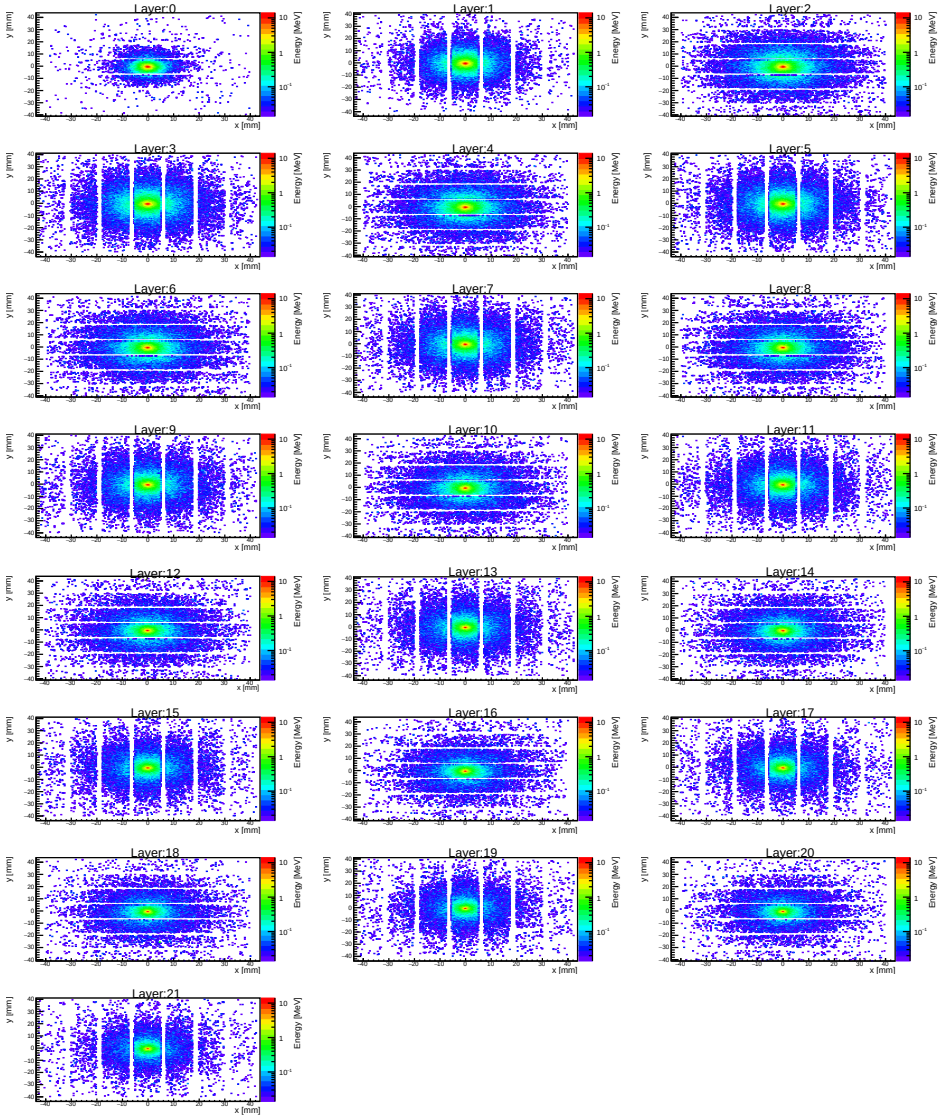

Figure 123: X-Y maps of the energy deposition in the 22 layers of the calorimeter for a gamma beam with energy of 20 MeV and nominal intensity.

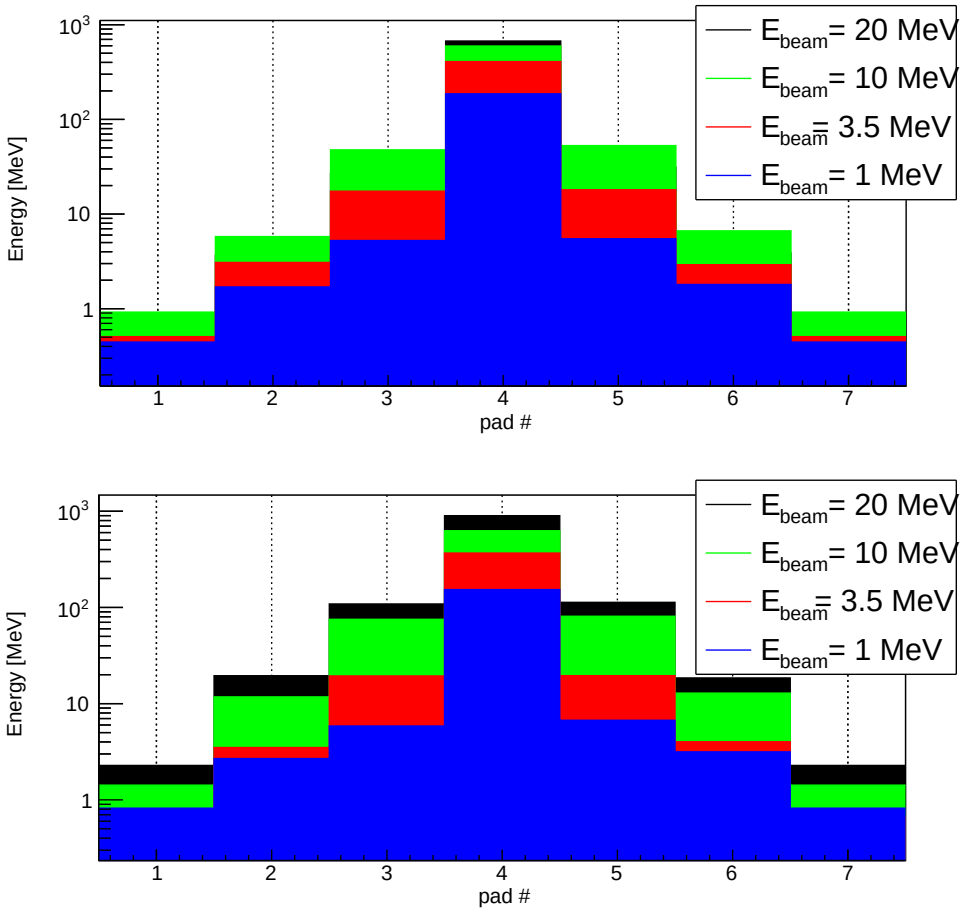

Figure 124: Expected transverse energy profile in the first (top) and second (bottom) calorimeter layers.

6.2.5 Background study:

A study of the effect of the background particles on the calorimeter performance has been done using the MC sample described in Sec.2.2. In Fig.125 are shown the tracks of 10 background events for a beam of 10 MeV entering GCAL.

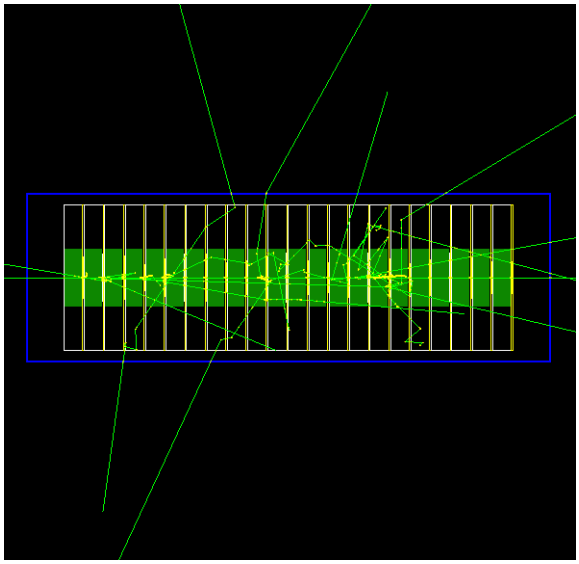

Figure 125: Example of 10 background events entering GCAL relative to a γ beam of 10 MeV.

To illustrate the characteristics of the background radiation we use the MC background sample generated with a statistics corresponding to a macropulse and an energy of 3 MeV. Fig.126 shows the X-Y distribution of the impinging background. The circles drawn in the figure representing the γ beam-pipe that has a radius of 20 mm and a thickness of 3 mm.

As already presented on Sec.2.2, the background particle, intrinsically generated by mechanism inside the collimator, can be distinguished in two different types: randomly distributed component entering the detector from all directions ("external" component), due to γ scattering on the concrete walls of the room and beam-line components, and another one due to particles scattered by the collimators which travel inside the beam-pipe ("beam-like" component). In Fig.127 are shown the correlations between the energy of the background particle and its distance from the beam axis. A solid black line is plotted at a distance of 20 mm, the pipe radius, to clarify which particles arrive from inside or outside the beam pipe. From the figure it can be seen that most of the "beam-like" events have the same energy of the beam (3 MeV), while the "external" component has a lower energy, smaller than 0.5 MeV.

The correlations between the energy and the imping time on the scoring box is presented on Fig.128. The arriving time of the beam particle is at about 55 ns, and can be seen that the background arriving in time with the beam has also the same energy, while the "external" component arrives later up to 150 ns after the beam pulse. Summarizing the "beam-like" particles,

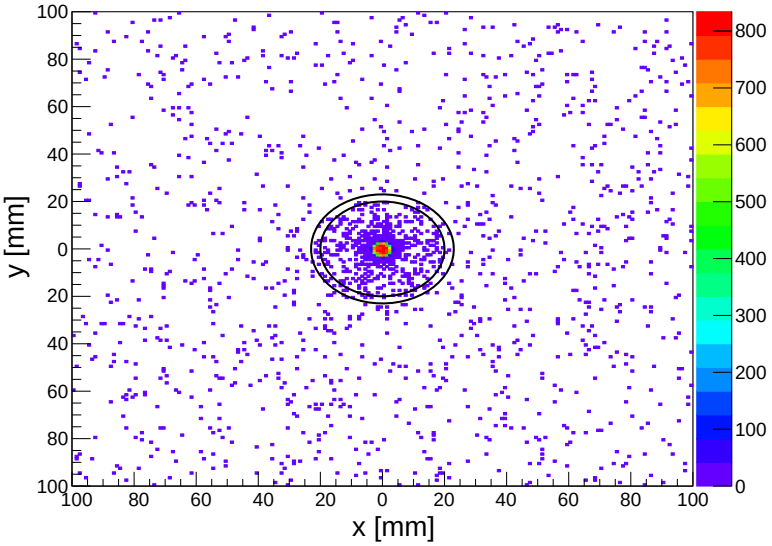

Figure 126: X-Y distribution of the background particles imping on the front side of a scoring box surrounding the calorimeter for a beam macro-pulse of energy E_{beam} = 3MeV. The two drawn circles represent the γ beam-pipe.

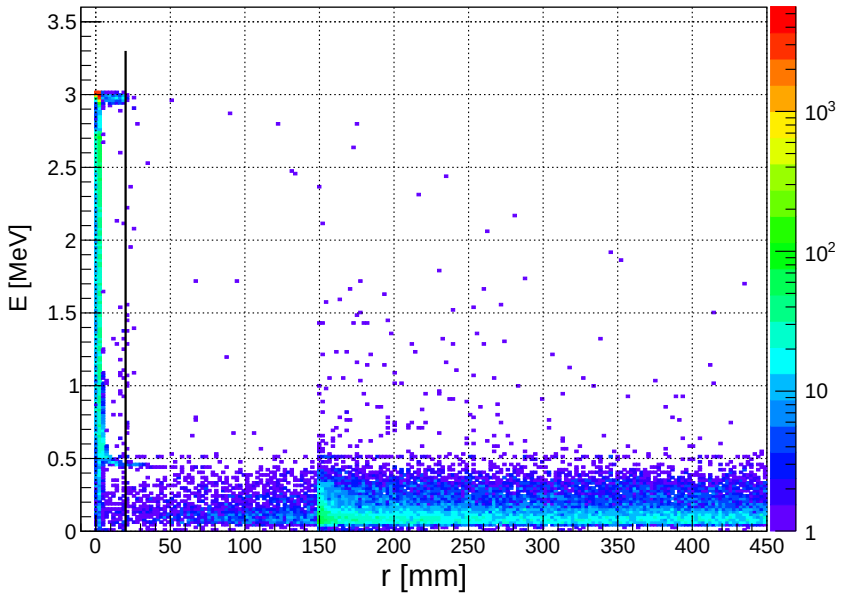

Figure 127: Correlation between the energy of the background particle and its distance from the beam axis obtained for a beam of 3 MeV. The solid black-line represent the beam-pipe position.

that are the main component of the background, have the same direction of the beam, a similar energy and arrive at the same time.

We study also which type of particles compose the background radiation at different beam energies. On Tab.15 are reported the number of the different kind of background particles expected in a pulse. The background is essentially composed by photons, electron and positron for the low-energy

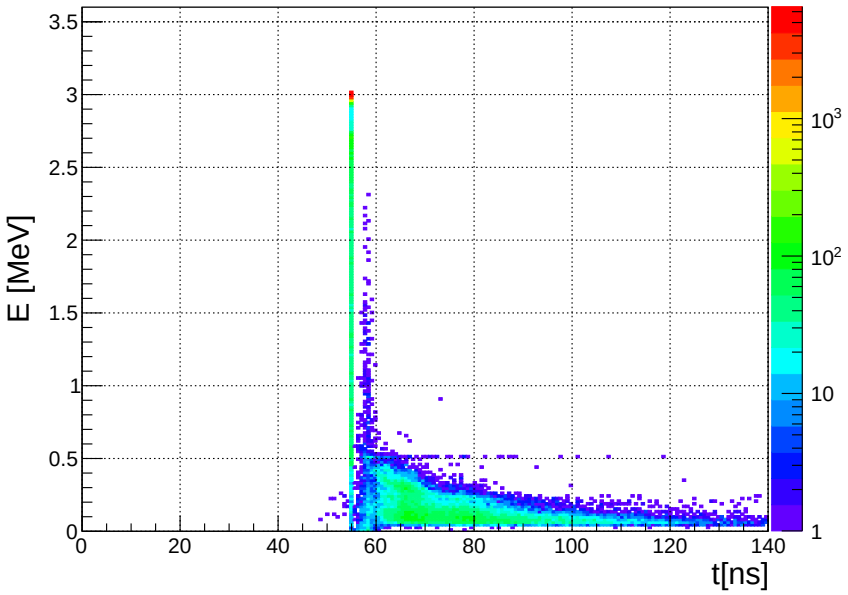

Figure 128: Correlation between the energy of the background particle and its arriving time obtained for a beam of 3 MeV.

line, while for the high-energy one also neutrons are produced due to nuclear photodisintegration. As can be seen from the table, these numbers of particles are a small fraction of the 10^5 γ that enter the calorimeter during a pulse.

$\mathbf{E}_{beam}$ [MeV]	γ	e^-	e^+	n
2	1932 ± 8	237 ± 3	1.8 ± 0.2	-
3	1504 ± 7	150 ± 2	2.5 ± 0.3	-
19.5	4908 ± 12	139 ± 2	39.3 ± 1.1	500 ± 4

Table 15: Numbers of background particles entering a scoring box surrounding the calorimeter for different beam energies.

To study a possible effect of this background on the performances of the calorimeter we evaluate the energy deposited from this radiation inside the detector. Fig. 129 reports the energy released in the different layers for 10 macro-pulses of 3 MeV γ (top graph) and of 10 MeV γ (bottom). As it can be seen the background effects are negligible given that the energy released is four order of magnitude smaller than the one released by the beam. We can therefore neglect this background contribution.

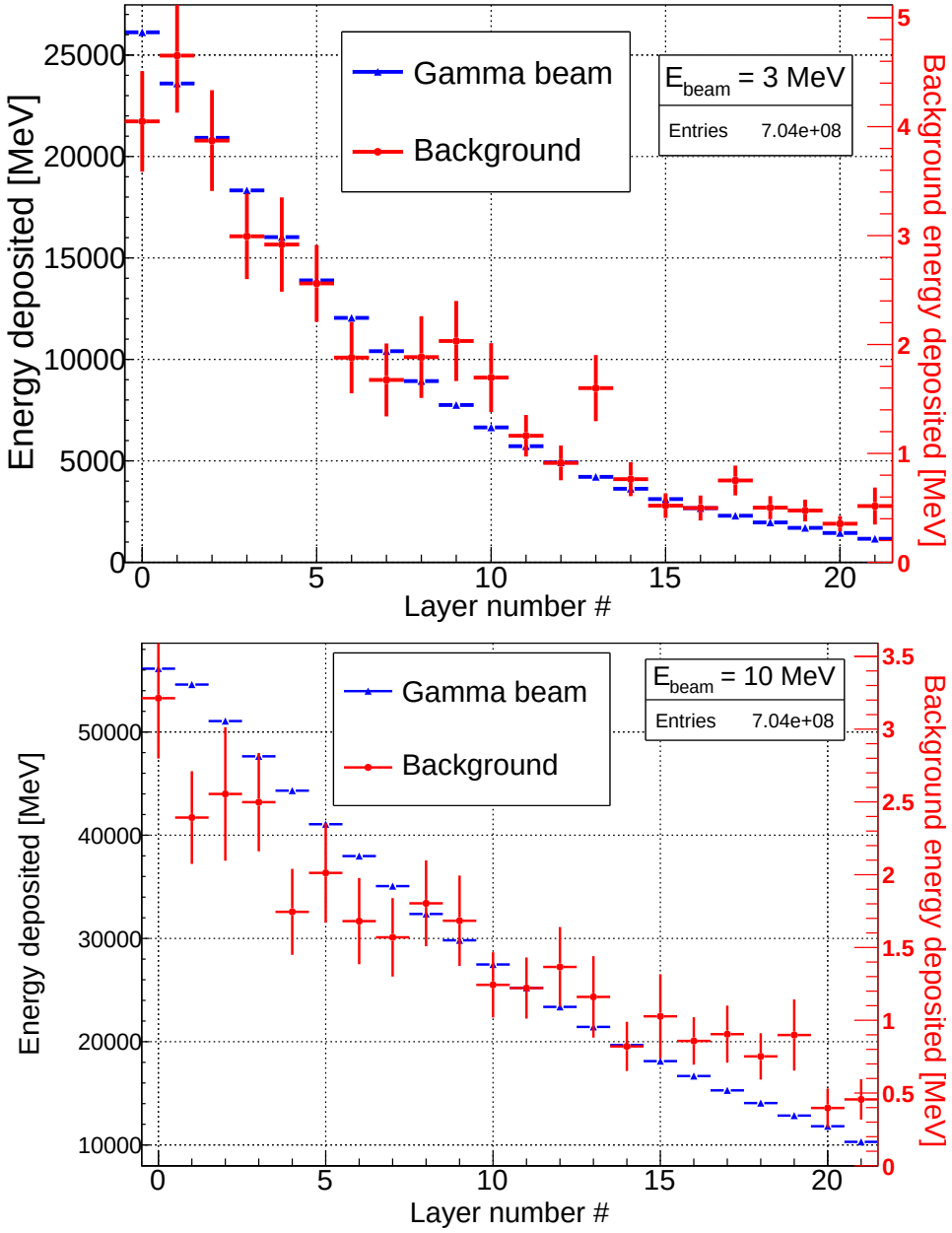

Figure 129: Comparison between the longitudinal profile distribution of energy deposited by the gamma beam and by the background particles. On the top graph are presented the results obtained with a gamma beam of 3 MeV and in the bottom graph those of 10 MeV. In this graphs are used two different scales for the y-axis: the left one, which is referred to the gamma beam and the right one, related to background.

6.2.6 Sistematic uncertainties studies

Only the statistical error have been considered in the results presented in the previous section. Here will be reported the studies done to assess the main sources of systematic uncertainty in the determination of the energy and intensity. Due to limitations in disk space and CPU we restricted the studies to a sample corresponding to a single beam pulse (10^5 gamma).

From monochromatic to realistic beam simulation

The simulation presented in the previous paragraph were obtained using a monochromatic and point-like beam. As described in Sec.2.2 a realistic simulation of the beam characteristics including the energy bandwidth has been realized and will be used here for this assessment. Starting from the interaction point between the electron and the laser beam, the photons were followed through the ELI-NP collimation system down to the detectors. The resulting beam energy is not monochromatic but distributed according to a characteristic spectrum. High statistic simulations of the realistic beam are available, at the moment, only for three different energies: 1, 3 and 10 MeV. In Fig.130 are displayed the corresponding beam energy distributions.

As it can be seen the beam shows an asymmetric distribution peaked around the nominal energy value, in addition it shows a spatial distribution rather than being point-like. The beam divergence is greater for low energy photons, as can be seen from Fig.131, where the beam distribution along the two axes (X,Y) before entering the calorimeter is shown for different energies.

This spatial distribution can be observed also in the energy deposition inside the calorimeter. In Fig. 132 are represented side by side, as an example, the XY distributions of the energy deposited on the second calorimeter layer for γ beam with energies of 1, 3 and 10 MeV for the monochromatic and realistic beam cases.

The greater beam divergence for low energy photons, can be observed more in detail comparing the radial energy distribution. This is done on Fig. 133 where the energy released in different layers are reported as a function of the distance from the beam axis. The top plots displays the results obtained with 1 MeV photons, the middle ones with 3 MeV photons and the bottom with 10 MeV γ. The red continuous lines show the energy distribution obtained with a default beam and the blue dashed lines the one obtained with a realistic beam. The black lines drawn on the graphs correspond to the limit of the active area of the silicon central pad. It is possible to see that for 1 MeV photons the maximum of energy release, in the realistic case, is well displaced from the 0 of beam axis, while as energy increases it tends to become centered on the zero.

However, even in the low energy realistic case, the one which shows the greatest difference between the two cases, the energy deposition is concentrated within the central pad, so we expect that the energy loss in the dead area between two pads does not increase in this case. This can be observed in Fig.134, where are compared the fraction of energy deposit in

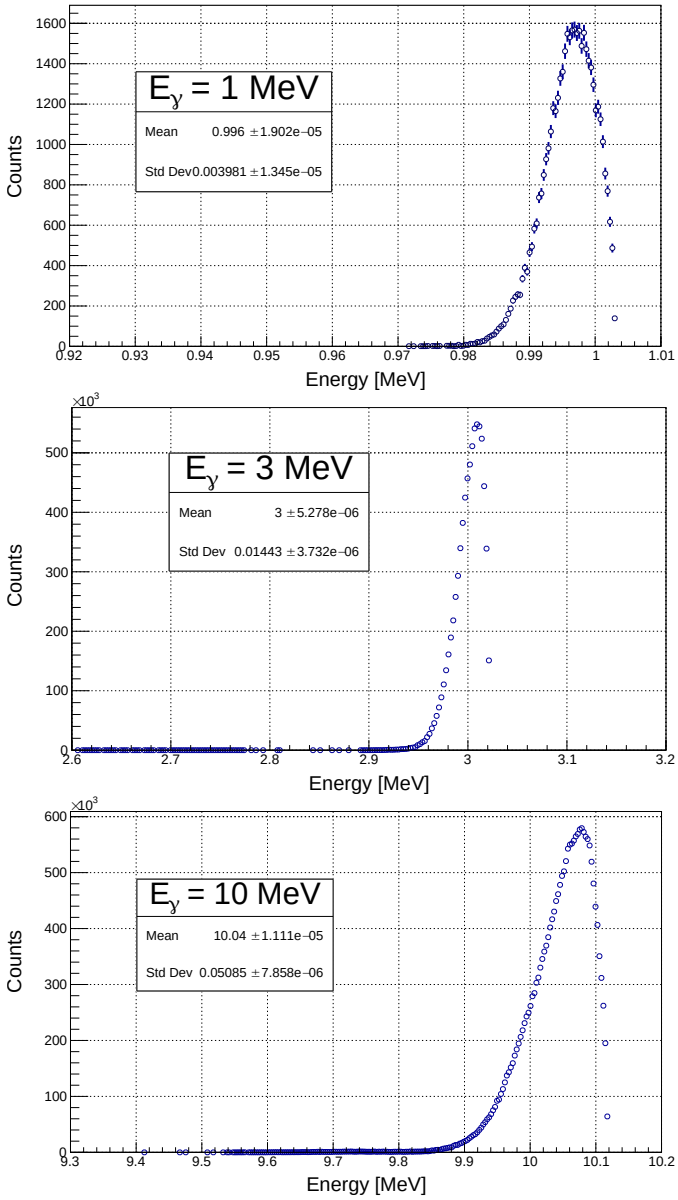

Figure 130: In the graph are shown the simulated beam energy distributions for a nominal value of 1 (top), 3 (center) and 10 (bottom) MeV, respectively.

the dead area reported as function layer number for a realistic beam (blue triangles) and for the default case (red dots). We notice that the obtained ratio is almost the same in the two cases, indeed we do not have a variation in the energy loss related to the realistic beam divergence.

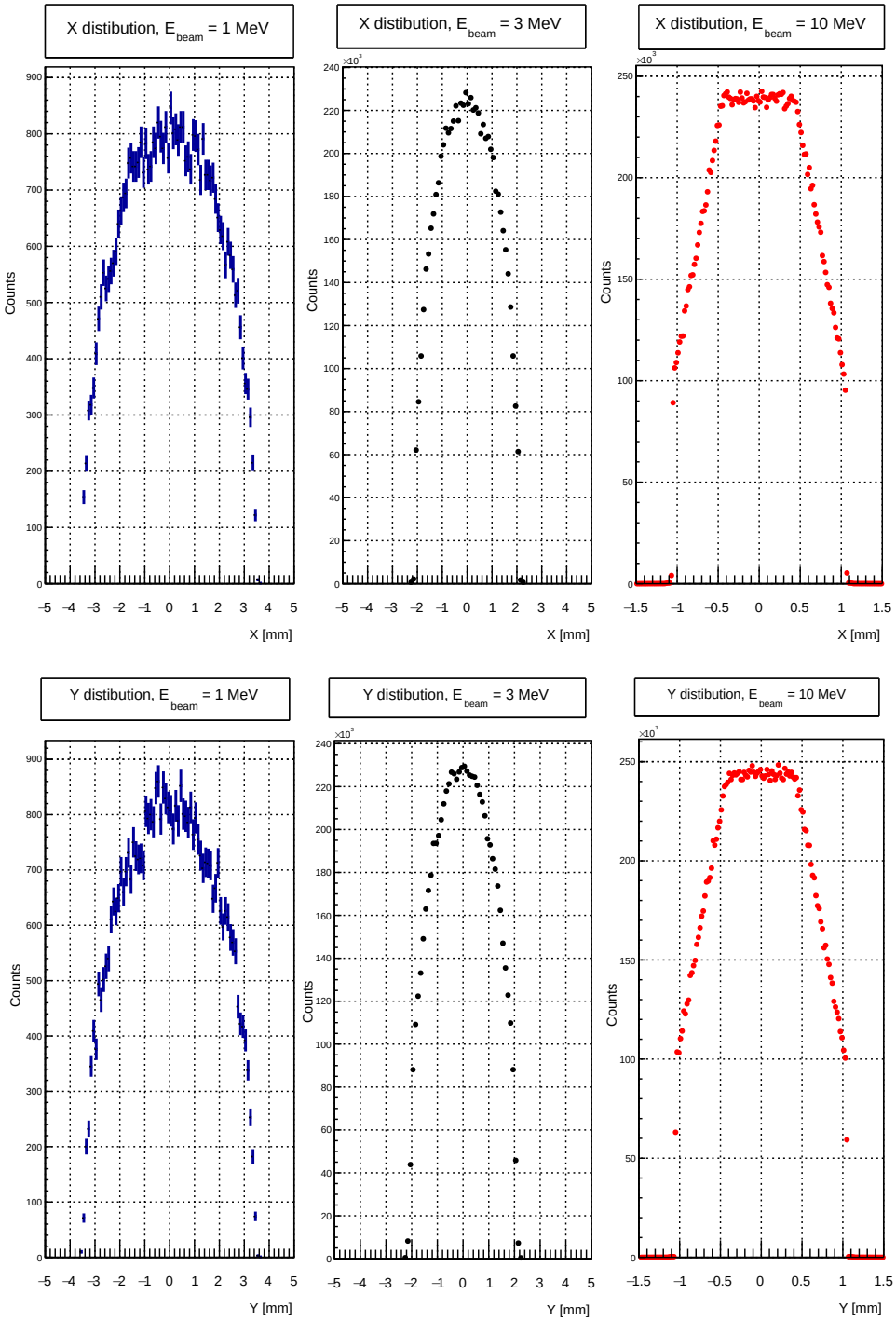

Figure 131: Distribution along the X (top) and the Y (bottom) axis of the beam photons impinging on the calorimeter. On the left are shown the results obtained for a gamma beam with nominal energy of 1 MeV, on the centre of 3 MeV and on the right of 10 MeV.

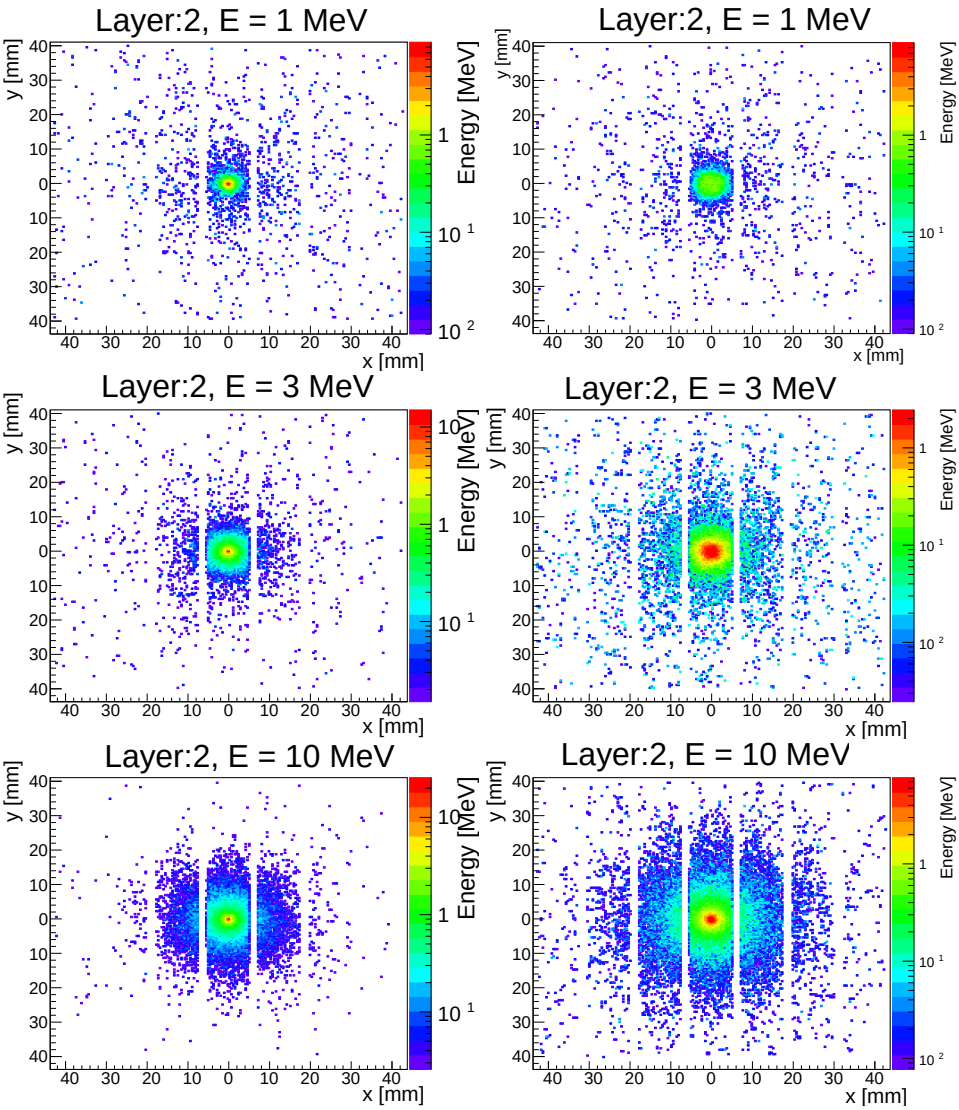

Figure 132: Bidimensional maps of the energy deposition in the second layer of the calorimeter for a gamma beam with nominal energy of 1, 3 and 10 MeV. On the left is depicted the case of monochromatic and point-like beam, on the right the realistic one.

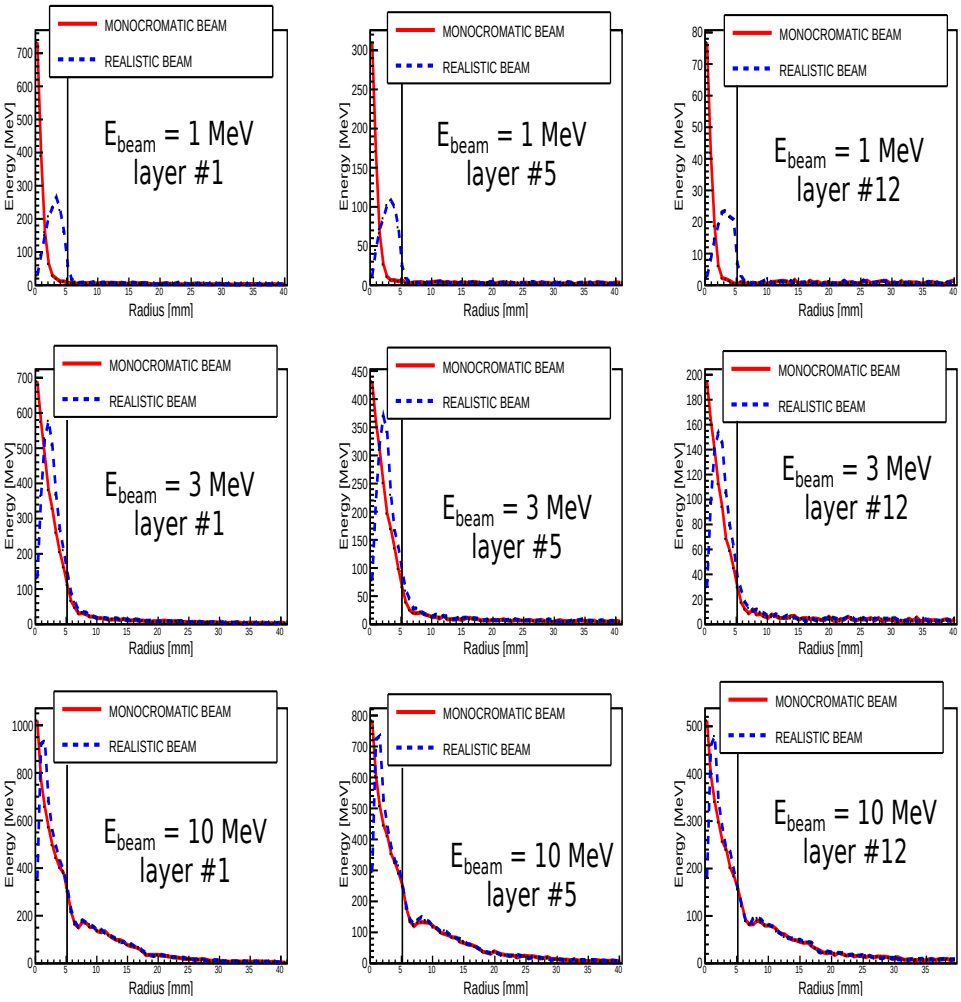

Figure 133: Transverse distribution of the energy released in three different layers (1, 5 and 12) for photons of 1 MeV (top), 3 MeV (center), 10 MeV (bottom). The red continuous lines refer to the default monochromatic beam and the dashed blue lines to the realistic one. The vertical black lines mark the limit of the active area of the silicon central pad.

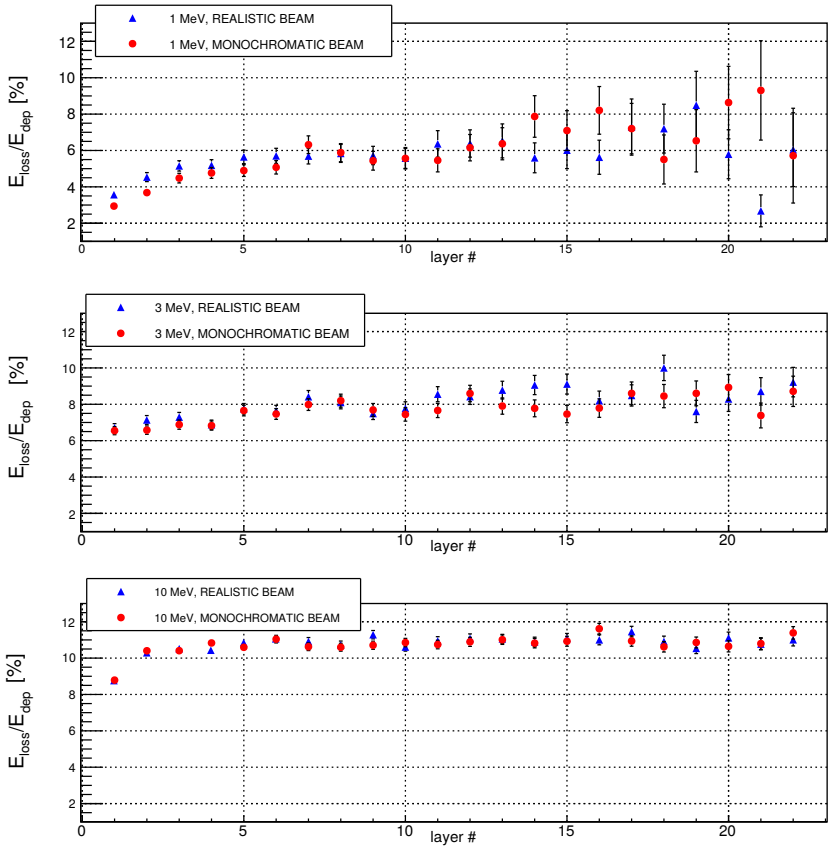

Figure 134: Comparison of the ratio of the energy loss (E_{loss}) and the deposited energy (E_{dep}) in the 22 detector layers for different γ beam energies (1 MeV on the top, 3 MeV on the centre and 10 MeV on the bottom) for the default simulation with a monochromatic beam (red dots) and for the realistic one (blue triangles).

A set of 1000 MC samples each composed by 10^5 γ of the three available energies of the "realistic beam" have been generated and the reconstruction procedure has been implemented. Fig. 135 displays a comparison of the longitudinal profile obtained with the default monochromatic case and with this sample used for systematic studies showing the ratio between the two profiles. From the figure it can be seen that the obtained ratio is not exactly constant in all the layers, meaning that there are tiny differences in the shape of the two profiles.

Using this new set of MC samples we evaluated the possible systematic effects on the calorimeter performance. In Fig.136 are shown the energy and intensity resolution obtained for the default monochromatic case (red dots) and with this realistic sample (blue triangles). From the figure can be noticed that the obtained resolution is not changed with respect to the default case, this is related to the fact that the width of the beam energy distribution (see Fig.130) is small compared to the GCAL resolution relative to a beam pulse.

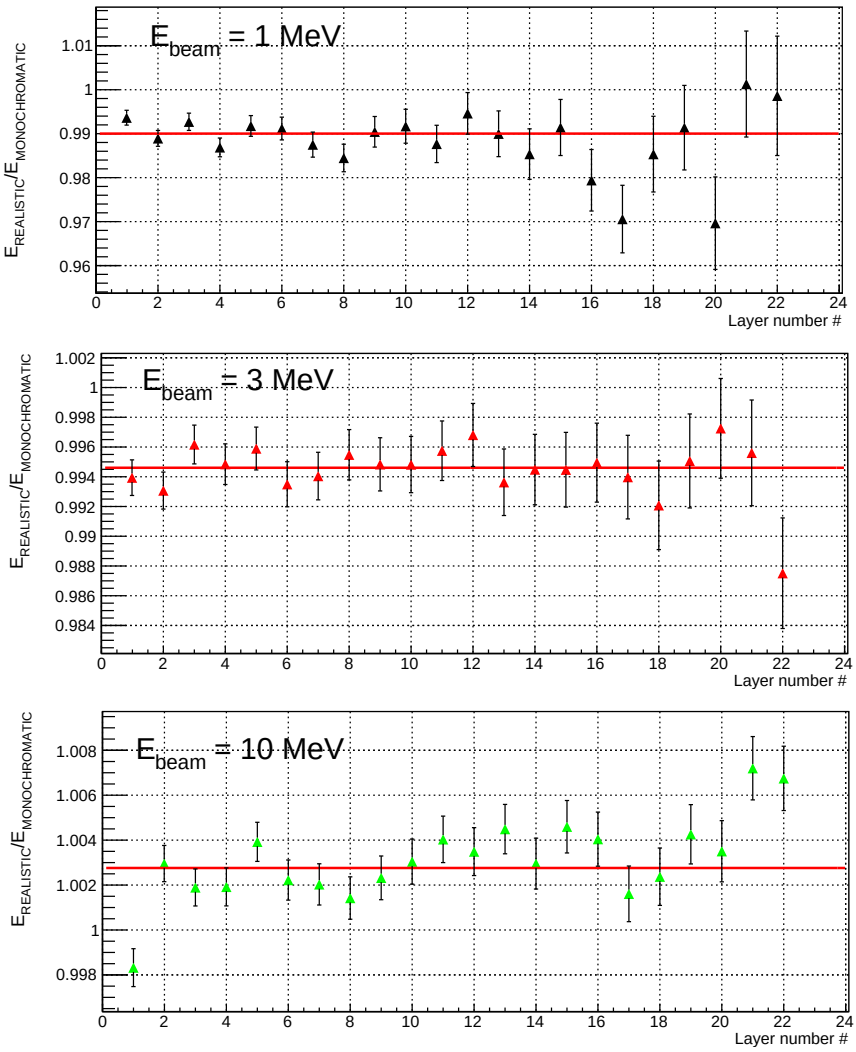

Figure 135: Ratio between the expected longitudinal profile of the energy deposition in the calorimeter obtained in the realistic case and in the default monochromatic case. The plotted red-line represents the average values of the fractions measured in the different layers.

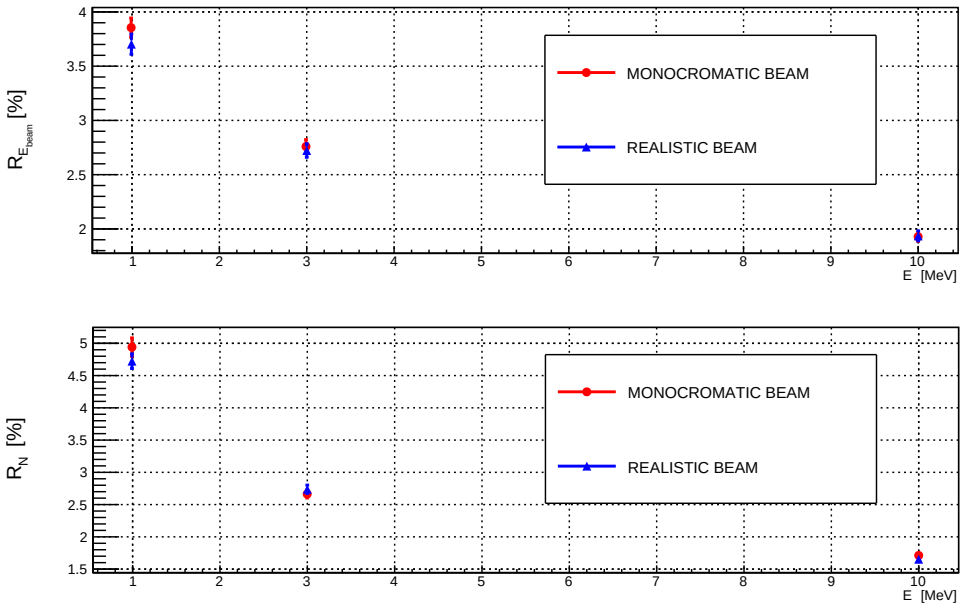

Figure 136: In the figure the resolution on E_{beam} (top) and N_γ (bottom) obtained with sample using a realistic energy distribution are shown with blue triangles, the monochromatic case is plotted with red dots.

The calorimeter is designed to reconstruct the average beam energy and intensity. Using as input an asymmetric energy distribution we expect to observe an additional offset (see Sec.6.2.3), in particular a shift towards different values of the reconstructed energy corresponding to the difference between the peak value and the average. This effect is shown on the top of Fig.137. The least affected value is the one corresponding to a 3 MeV beam due to the fact that in this case the peak and the average value of the distribution coincide, anyway also the observed shifts for 1 and 10 MeV beam are coherent with the average values of the energy distributions (shown on Fig.130).

The asymmetry on the low-energy side of the distribution in the energy spectrum will correspond to a lower total energy deposited inside the calorimeter. This change will not affect the beam energy determination, that depends only on the fraction of energy released in each layer ($p_i(E_{beam})$ see Eq.20), but will change the estimation of the beam intensity that is directly related to the total energy released in the calorimeter E_{tot}, as can be seen from Eq.25. Indeed, this lower total energy deposition will manifest itself as if less photons were detected producing an underestimation of the reconstructed beam intensity. This can be observed in Fig.137, the effect ranges from a 0.6% down to 0.1% at the higher energy.

To mitigate these additional systematic offsets, we plan to use the energy spectrum measured by the CSPEC and generate a new MC^{truth} sample to produce profile parametrization (and $f(E_{beam})$ fractions) which correctly accounts for the beam not being monochromatic.

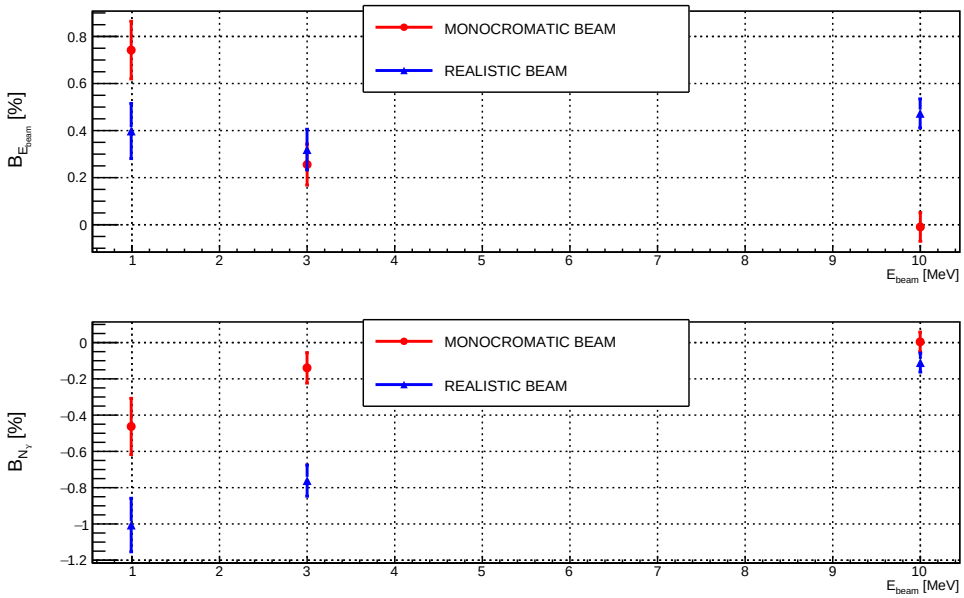

Figure 137: In the figure the offset on E_{beam} (top) and N_γ (bottom) obtained with the sample using the realistic energy distribution are shown with blue triangles while the monochromatic case is plotted with red dots.

Effects of energy and intensity jitter

According to the technical specifications of the GBS we expect a jitter on the values of the energy and intensity from pulse to pulse (see Tab.1). The jitter on the energy is expected to be lower than 0.2% and that on the number of photons lower than 3%.

To evaluate the effect of the energy jitter on the low-energy line calorimeter performances we simulated a new MC sample of 1000 beam pulses each composed by 10^5 photons. The photons inside each pulse have the same energy, but this energy changes randomly for different pulses according to a gaussian distribution centered on E_{beam} and with $\sigma = E_{beam} \cdot 0.002$.

In Fig.138 are shown the results of this study. The obtained resolutions (top) and the offset (bottom) are displayed for the two beam cases. From the figure we observe an overlap of the results indicating that this effect is negligible when compared to the resolution achievable for one pulse.

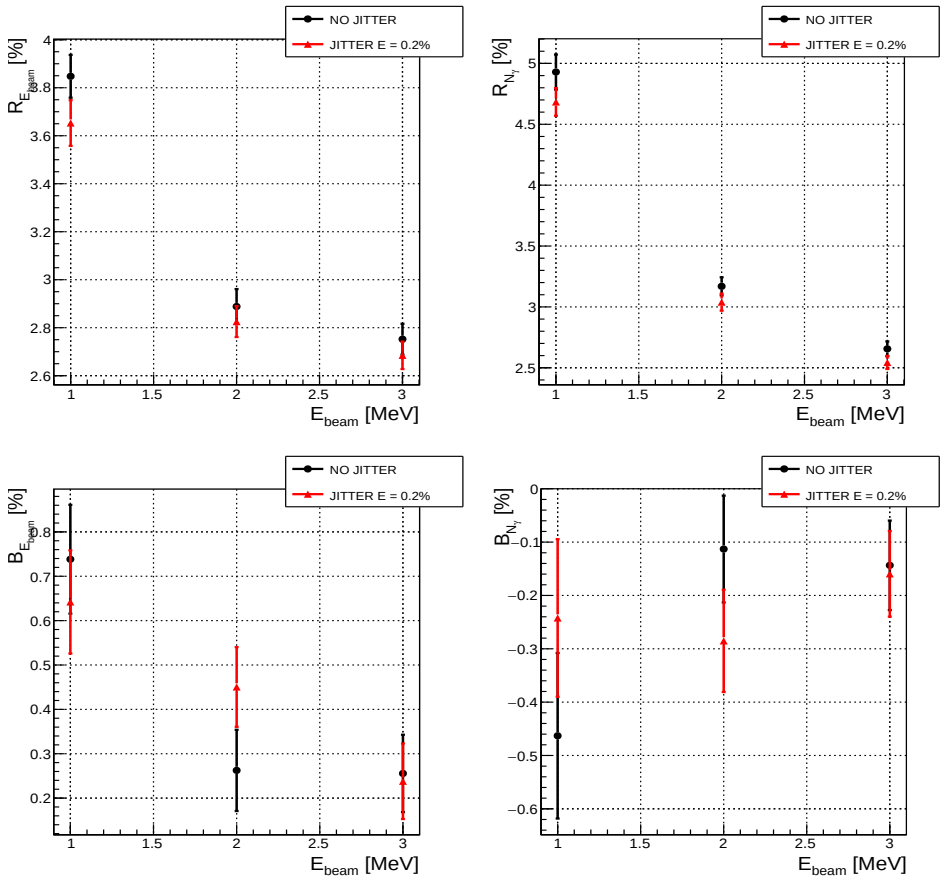

Figure 138: Comparison between the obtained resolution (top) and bias (bottom) in the default monochromatic case (red triangles) and simulating an energy beam jitter of 0.2%. On the right are shown the results related to the reconstruction of E_{beam} and on the left to the calculation of N_γ.

The presence of a jitter on the number of photons composing the gamma beam pulses, has been studied. The fit algorithm, presented on Sec.6.2.3, has been tested on the default MC^{DATA} sample; however, instead of analyzing all the 10^5 generated γ per pulse, the number of events has been randomly extracted according to a gaussian distribution centered on 10^5 and with a standard deviation of 3%.

The results of this study are presented on Fig.139. The top plots report the obtained resolutions and the bottom ones the calculated offsets. We can see from the figure that this systematic effect has no impact on the energy evaluation but affects the determination of the beam intensity. This is expected and provides a cross-check of the proper functioning of the reconstruction procedure that give a measurement of E_{beam} that does not depend on the beam intensity.

The worsening of the intensity resolution performances are related to the non negligible amounts of the expected jitter on N_γ. The total obtained resolution is approximately the sum in quadrature between the default resolution and the beam jitter. These results refer to what is obtainable with the statistics of 1 pulse at nominal intensity. The effect of the jitter will become negligible analyzing larger data samples with statistics corresponding to few seconds of data taking. No effect is expect on a possible energy/intensity bias due to the "symmetric" nature of this jitter and actually none is observed (Fig.139 bottom).

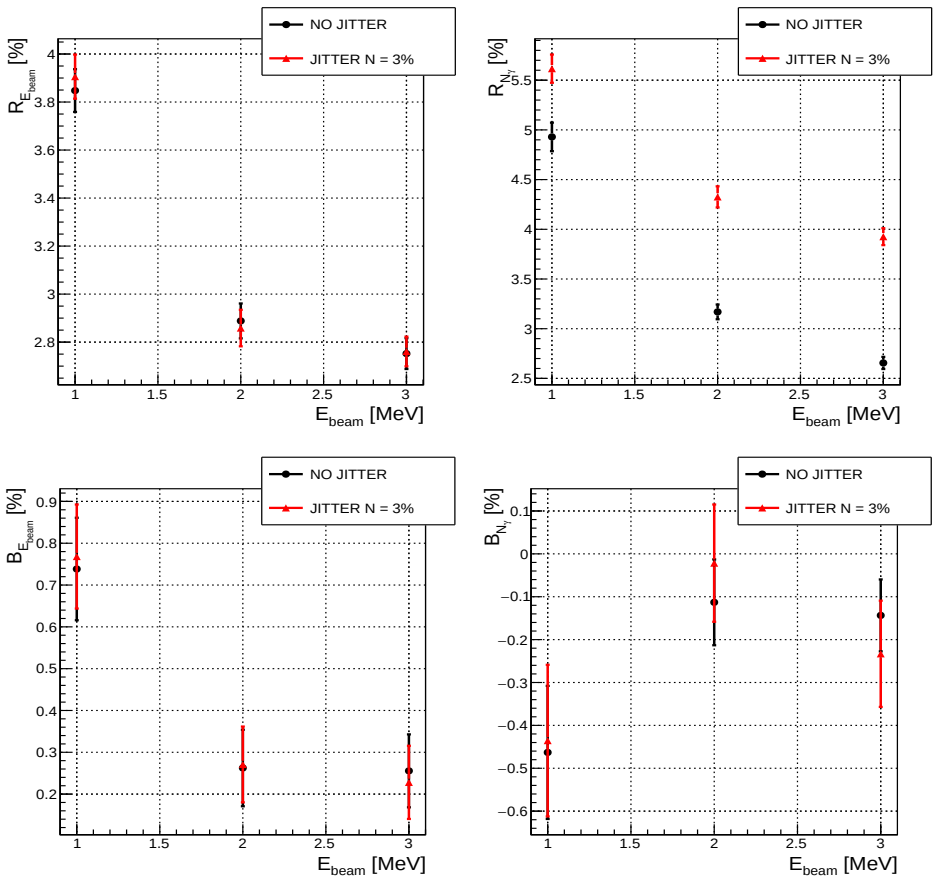

Figure 139: Comparison between the obtained resolution (top) and bias (bottom) in the default monochromatic case (red triangles) and simulating a jitter of 3% on the number of photons per pulse. On the right are shown the results on the reconstruction of E_{beam} and on the left of N_γ.

Effects of detector miscalibration

The measured longitudinal beam profile can be distorted by an incorrect intercalibration of the different detector layers, or by small differences in the detector response or in the electronic gain.

The gain of the calorimeter silicon strip pads was measured at the LABEC [70] facility in Firenze using a 3 MeV proton beam [71]. The gain distribution is shown in Fig. 140. As it can be seen from the figure, these factors are randomly distributed according to a gaussian function with a standard deviation of about 1 %. We investigate the possible systematic contributions due to the effects of miscalibrations between different silicon pads with the help of a toy MC.

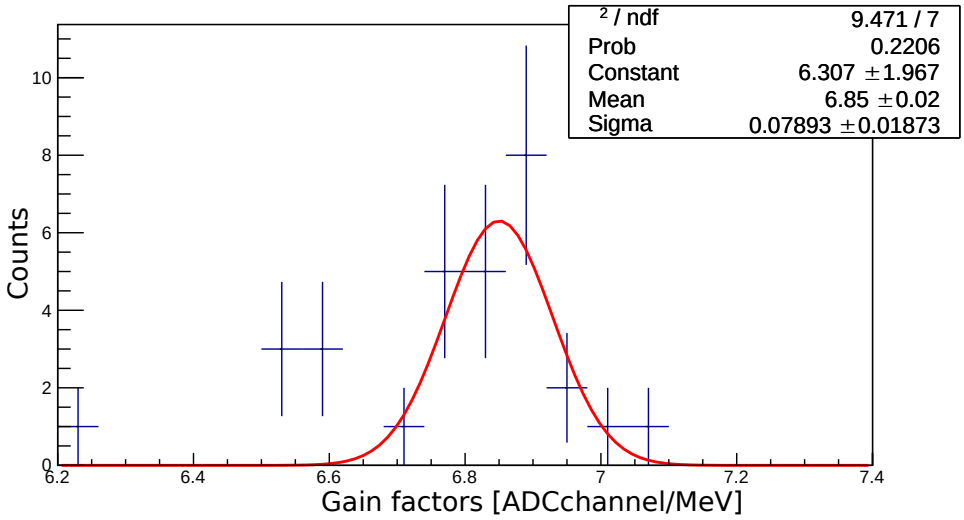

Figure 140: Distribution of the measured gain factor for the silicon pad tested with protons at LABEC facility.

After normalizing the distribution, for every board we extract a possible configuration of 7 gain factors, one for each sensor. We use this set of numbers g_i^j, where the index i refers to the pad number and the index j to the chosen configuration, to rescale the energy released in each layer, E_{rec}^j, as follows:

$$E_{rec}^j = \sum_{i=1}^{7} E_i \cdot g_i^j \tag{29}$$

where E_i is the energy released in the i-th pad

A new longitudinal profile of energy released inside the calorimeter relative to the j-th configuration of gain is then obtained using E_{rec}^j. We apply the fit procedure to these new profiles calculated for the standard MC^{DATA} sample of 1000 pulses. With this procedure we reconstruct the values of energy and intensity corresponding to this particular configuration of gain factors. We reiterated the procedure by extracting hundreds of possible gain configuration and for every configurations we re-run the reconstruction procedure.

We found that the presence of this miscalibration effect introduces a systematic shift of the values of the beam energy and intensity, without affecting their resolutions. Indeed we obtained resolution values that are compatible with the default ones and errors lower than the statistical ones.

The additional offset values obtained with the toy MC for the different configurations are distributed gaussianly and are displayed for a γ beam of 2 MeV in Fig.141. We use the standard deviation of these distributions to assess this systematic contribution, in Tab.16 the values obtained for different beam energies are reported.

$\mathbf{E}_{beam}$ [MeV]	$\sigma_{B_{E_{beam}}}$ [%]	$\sigma_{B_{N_\gamma}}$ [%]
1	0.52 ± 0.04	0.79 ± 0.06
2	0.54 ± 0.04	0.70 ± 0.05
3	0.60 ± 0.05	0.70 ± 0.05

Table 16: Systematic errors on the energy and intensity offset (Eq.28) obtained for different beam energies.

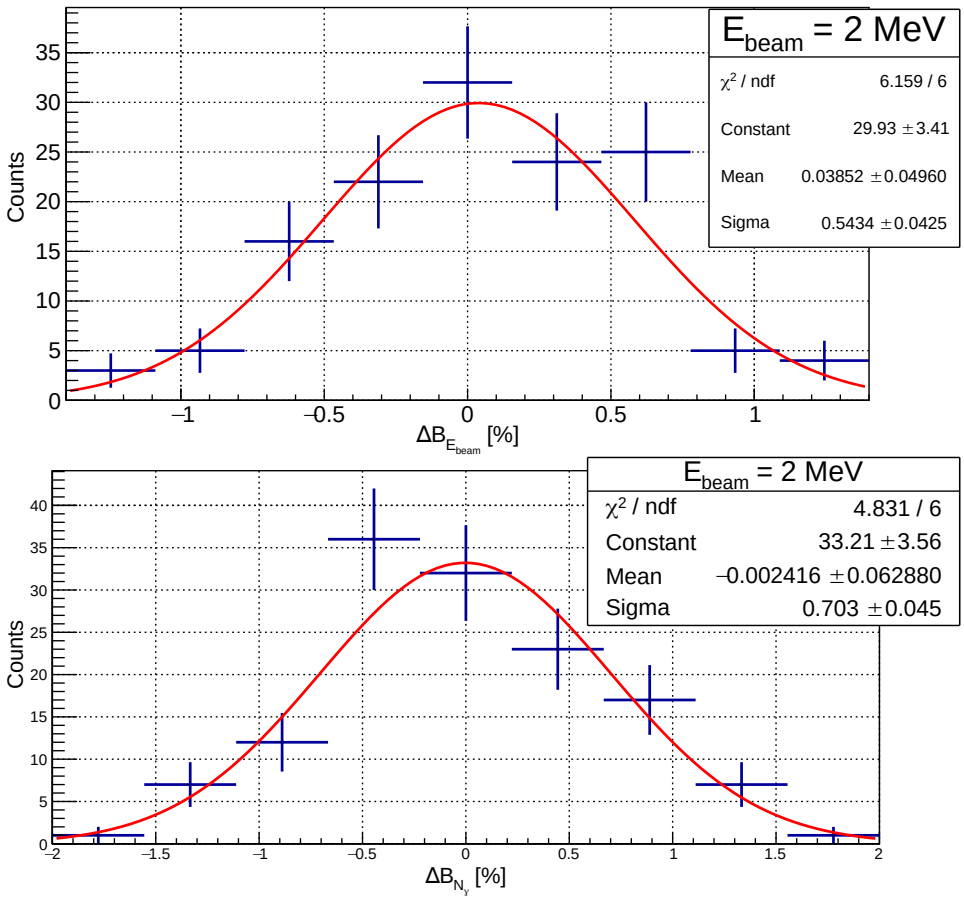

Figure 141: The graphs show the distribution of the bias (as defined in Eq.28) contribution in the reconstruction of E_γ (top) and N_γ (bottom) due to the presence of miscalibration factor in the response of different sensors. The plots are relative to a gamma beam of 2 MeV.

CONCLUSION

The activities described in this work concern the development and the characterization of a Compton Spectrometer (CSPEC) and a Gamma Calorimeter (GCAL). These detectors are part of the ELI-NP Gamma Beam Characterization System and are devoted to the measurement of the ELI-NP γ beam energy distribution and intensity.

The first detector described is the CSPEC, that is expected to reconstruct the γ beam energy spectrum with a precision of about the 0.1% on the reconstruction of the beam peak energy and width. The resolution on the beam energy measurement critically depends on the accuracy of the electron energy determination, which is correlated to the HPGe energy resolution and to the energy loss in the materials preceding the HPGe active volume. We verified the excellent energy resolution and linearity of the HPGe exposing the detector to different radioactive γ sources and obtaining a resolution of 0.156% at 1332 keV. In addition, the accuracy of the HPGe MC simulations, in particular of the parameters related to the dead layers preceding the HPGe crystal, has been verified using electrons of definite energy emitted by a ^{207}Bi source. The measured peak positions are in agreement with the simulated ones with a precision better than 1 keV confirming the correctness of the simulation geometry. The MC simulation describe well also the width of the peaks, for which we measured values that differ less than 0.4 keV from the expected ones. Concerning the CSPEC photon detector we implemented a signal shape identification method that use the ratio between the two light components of the BaF_2 detector to discriminate between signals produced by γ and those due to α particles (the intrinsic radioactivity of the crystal) or to those due to thermal noise. We also characterized the crystals response in terms of linearity and energy resolution using different γ sources. In addition we verified that the BaF_2 crystals intrinsic radioactivity can be used to monitor changes in the energy calibration of the detector.

The second detector subject of this thesis is the GCAL, a calorimeter providing a fast combined measurement of the beam average energy and intensity by absorbing the gamma pulses in a longitudinally segmented calorimeter. In this thesis we tested the detector time response, that is a critical issue due to the fact that the calorimeter has to be able to resolve the 16 ns separated pulses of the ELI-NP beam. This test, performed with an infrared laser, has shown that the silicon sensors equipped with a fast custom electronics are able to disentangle pulses with the same time structure of the beam, with an accuracy at the level of per mill. Using the laser we checked the functionality of each sensor composing the calorimeter. We verify the signal dependence from the γ impact point and that there are no anomalies on detector response, scanning the sensors horizontally and vertically. The last part of the activity has regarded the optimization of the calorimeter MC simulation. Starting from a simplified simulation used in the early

stage of the project were there was no geometry details, new simulations were made considering a thorough description of the microstrip detectors (dead area, aluminum strip and backplane metallization) and including the presence of the aluminum supporting structures and of the acquisition board. The performances of the GCAL have been evaluated executing the energy reconstruction procedure on these new MC samples and indicate a statistical accuracy on the average beam energy and on the number of photons, better than few per mill after collecting data for a few seconds of beam operation. We have checked that the effect of the background particles is negligible given that the energy released from these particles is four order of magnitude smaller than the one released by the γ beam. The effects of some of the main sources of systematic uncertainties in the determination of the beam energy and intensity of the low-energy calorimeter have been investigated. We have studied the variations produced by having a γ beam with a characteristic energy spectrum and spatial distribution or with a random jitter on the beam energy (or intensity) rather than a monochromatic point-like beam and finally the effects related to incorrect inter-calibration of the different detector layers. The energy and intensity beam jitters do not deteriorate the GCAL performance and with a realistic beam, we obtained a reconstructed energy that is the average energy of the beam rather than the peak value in agreement with the calorimeter working principle. Due to the asymmetry on the low-energy side of the energy spectrum, the offset in the total energy deposited translates into an underestimation of the beam intensity. This effects can be accounted for by correctly simulating the beam energy distribution when producing the energy profiles. The main systematic effect turns out to be the miscalibration of the silicon pads that introduces a systematic shift on the values of the beam energy and intensity that amounts to about 0.5% for the energy and 0.7% for the intensity.

A ASYMMETRIC PEAK FUNCTIONS

This appendix summaries the equation of the main functions used in the texts

A.1 BUKIN FUNCTION

The Bukin function is given by:

$$f(x; x_B, \sigma_B, \xi, \rho, N) = \mathrm{N} \exp\left[\frac{\xi\sqrt{\xi^2+1}(x-x_1)\sqrt{2ln(2)})}{\sigma_B(\sqrt{\xi^2+1}-\xi)^2 ln(\sqrt{\xi^2+1})+\xi} + \rho\left(\frac{x-x_i}{x_B-x_i}\right)^2 - ln2\right], \tag{30}$$

where $\mathrm{x}_{1,2}$, ρ and x_i are defined as:

$$x_{1,2} = x_B + \sigma_B\sqrt{2ln2}\left(\frac{\xi}{\sqrt{\xi+1}} \mp 1\right), \tag{31}$$

$$\rho = \rho_1,\ x_i = x_1 \quad \text{for } x < x_1 \tag{32}$$

$$\rho = \rho_2,\ x_i = x_2 \quad \text{for } x \geq x_2. \tag{33}$$

The parameters x_B and σ_B are the peak position and the width, and ξ is an asymmetry parameter.

A.2 CRYSTAL BALL FUNCTION

The Crystal Ball function is given by:

$$f(x; \alpha, n, x_C, \sigma_C) = N \cdot \begin{cases} \exp(-\frac{(x-x_C)^2}{2\sigma_C^2}), & \text{for } \frac{x-x_C}{\sigma_C} > -\alpha \\ A \cdot (B - \frac{x-x_C}{\sigma_C})^{-n}, & \text{for } \frac{x-x_C}{\sigma_C} \leq -\alpha \end{cases} \tag{34}$$

where

$$A = \left(\frac{n}{|\alpha|}\right)^n \cdot \exp -\frac{|\alpha|^2}{2}, \tag{35}$$

$$B = \frac{n}{|\alpha|} - |\alpha|\,, \tag{36}$$

$$N = \frac{1}{\sigma_C(C+D)}, \tag{37}$$

$$C = \frac{n}{|\alpha|} \cdot \frac{1}{n-1} \cdot \exp\left(-\frac{|\alpha|^2}{2}\right), \tag{38}$$

$$D = \sqrt{\frac{\pi}{2}}\left(1 + \operatorname{erf}\left(\frac{|\alpha|}{\sqrt{2}}\right)\right). \tag{39}$$

The parameters x_C and σ_C are the peak position and the width and N is a normalization factor.

BIBLIOGRAPHY

[1] ELI, "Home page & eli project." https://eli-laser.eu/.

[2] M. Aléonard et al., *WHITEBOOK ELI-Extreme Light Infrastructure; Science and Technology with Ultra-Intense Lasers*. 01 2011. https://doi.org/10.13140/2.1.1227.0889.

[3] "Physics nobel prize web site." https://www.nobelprize.org/prizes/lists/all-nobel-prizes-in-physics/.

[4] D. Strickland and G. Mourou, "Compression of amplified chirped optical pulses," *Optics Communications*, vol. 56, no. 3, pp. 219 – 221, 1985. https://doi.org/10.1016/0030-4018(85)90120-8.

[5] N.V. Zamfir et al., "Extreme light infrastructure: Nuclear physics," *Proc SPIE*, vol. 8080, 05 2011.

[6] Ur, C. A. and Balabanski et al., "New Frontiers in Nuclear Physics Research at ELI-NP," *54th Cracow School of Theoretical Physics: QCD meets experiment: Zakopane, Poland, June 12-20, 2014*, vol. B46, no. 3, p. 743, 2015. http://www.eli-np.ro/scientific-papers/NEW%20FRONTIERS%20IN%20NUCLEAR%20PHYSICS%20RESEARCH.pdf.

[7] P. Cardarelli, *Devices and techniques for the characterization of inverse Compton sources*. PhD thesis, Universitá degli Studi di Ferrara, 2010-2012.

[8] O. Adriani et al., "Technical design report eurogammas proposal for the eli-np gamma beam system," *arXiv:1407.3669*, 2014. https://www.researchgate.net/publication/263930417_Technical_Design_Report_EuroGammaS_proposal_for_the_ELI-NP_Gamma_beam_System.

[9] Gales, S et al., "New frontiers in nuclear physics with high-power lasers and brilliant monochromatic gamma beams," *Physica Scripta*, vol. 91, 09 2016.

[10] P. Cardarelli et al., "Monte carlo simulation of a collimation system for low-energy beamline of eli-np gamma beam system," *Nucl. Instr. and Meth. in Phys. Res. B*, vol. 355, pp. 237 – 240, 2015. https://doi.org/10.1016/j.nimb.2015.02.057.

[11] G. Paternó et al., "A collimation system for eli-np gamma beam system - design and simulation of performance," *Nucl. Instr. and Meth. in Phys. Res. B*, vol. 402, pp. 349 – 353, 2017. https://doi.org/10.1016/j.nimb.2017.03.057.

[12] Wormser, *The White Book of ELI Nuclear Physics Bucharest-Magurele, Romania*. 12 2010.

[13] C.A. Ur et al, "Nuclear resonance fluorescence experiments at eli-np," *Romanian Reports in Physics*, vol. 68, pp. S483–S538, 01 2016.

[14] Suliman, "Gamma beam industrial applications at eli-np," *International Journal of Modern Physics: Conference Series*, vol. 44, p. 1660216, 01 2016.

[15] Balabanski, D.L et al., "Photofission experiments at eli-np," *Romanian Reports in Physics*, vol. 68, pp. S621–S698, 01 2016.

[16] Camera, "Gamma above the neutron threshold experiments at eli-np," *Romanian Reports in Physics*, vol. 68, pp. S539–S619, 01 2016.

[17] Tesileanu, "Charged particle detection at eli-np," *Romanian Reports in Physics*, vol. 68, pp. 699–734, 01 2016.

[18] M.Gambaccini et al., "D081- gamma beam characterisation design report," 03 2015.

[19] S.Agostinelli et al., "Geant4a simulation toolkit," *Nuclear Instruments and Methods in Physics Research Section A.*, vol. 203, pp. 250–303.

[20] J.Allison et al., "Geant4 developments and applications," *IEEE Transactions on Nuclear Science.*, vol. 1, pp. 270–278.

[21] Bacci,A. et al., "Electron linac design to drive bright compton backscattering gamma-ray sources," *Journal of Applied Physics*, vol. 113, no. 19, p. 194508, 2013.

[22] K. Yokoya, *User Manual of CAIN, version 2.40.*

[23] M.G. Pellegriti et al., "Eurogammas gamma characterisation system for eli-np-gbs: The nuclear resonance scattering technique," *Nucl. Instr. and Meth. in Phys. Res. A*, 11 2016.

[24] M.G. Pellegriti et al., "The nuclear resonance scattering calibration technique for the eurogammas gamma characterisation system at eli-np-gbs," *Journal of Instrumentation*, vol. 12, no. 03, p. C03058, 2017. https://doi.org/10.1088/1748-0221/12/03/C03058.

[25] NNDC, "Nudat 2.7." http://www.nndc.bnl.gov/nudat2/.

[26] P. Cardarelli et al., "A gamma beam profile imager for eli-np gamma beam system," *Nucl. Instr. and Meth. in Phys. Res. A*, vol. 893, pp. 109 – 116, 2018. http://www.sciencedirect.com/science/article/pii/S0168900218303565.

[27] F. Salvat, "Penelope-2008 : A code system for monte carlo simulation of electron and photon transport," *Workshop Proceedings Barcelona , Spain 30 June-3 July 2008*, 2009.

[28] S.Straulino et al., "The silicon microstrip detectors of the pamela experiment:simulation and test results," *Nucl. Instr. and Meth. in Phys. Res. A*, vol. 518, pp. 158–160, February 2004.

[29] S. Straulino, *Simulation of Silicon Microstrip Detectors for a Cosmic Ray Experiment*. PhD thesis, Universitá degli Studi di Bologna, 15 Marzo 2003.

[30] IDEAS, "The va1." http://www.ideas.no.

[31] S.Straulino et al., "The pamela silicon tracker," *6th International Conference on Large Scale Applications and Radiation Hardness of Semiconductor Detectors*, vol. 530, pp. 168–172, 2004.

[32] https://www.mirion.com/.

[33] http://www.canberra.com/products/detectors/cryostats-coolers-cryopulse.asp.

[34] SCIONIX. https://scionix.nl/.

[35] https://www.hamamatsu.com/resources/pdf/etd/H12700_TPMH1348E.pdf.

[36] K.Wisshak, "The karlsruhe 4π barium fluoride detector," *Nucl. Instr. and Meth. in Phys. Res. A*, vol. 3, p. 292, 1990.

[37] R.R.Kinsey, et al., "The nudat/pcnudat program for nuclear data," *9 th International Symposium of Capture-Gamma_ray Spectroscopy and Related Topics*. https://www.ld-didactic.de/software/524221en/Content/Appendix/Ra226Series.htm.

[38] *Technical Information Manual: MOD.V1495, GENERAL PURPOSE VME BOARD*. http://www.caen.it/csite/CaenProd.jsp?idmod=484&parent=11.

[39] *User Manual UM2606: DT5780 Dual Digital MCA*. http://www.caen.it/csite/CaenProd.jsp?parent=64&idmod=756#.

[40] *User Manual UM4279*. http://www.caen.it/csite/CaenProd.jsp?parent=11&idmod=661.

[41] *Technical Information Manual: MOD. V812 series 16 CH. CONSTANT FRACTION DISCRIMINATORS*. http://www.caen.it/csite/CaenProd.jsp?parent=20&idmod=792.

[42] *Fast-Timing Discriminator Introduction*. https://www.ortec-online.com/-/media/ametekortec/other/fast-timing-discriminator-introduction.pdf?la=en.

[43] Berger et al., "Xcom: Photon cross section database." http://physics.nist.gov/xcom.

[44] Valentin T. Jordanov and Glenn F. Knoll, "Digital synthesis of pulse shapes in real time for high resolution radiation spectroscopy," *Nucl. Instr. and Meth. in Phys. Res. A*, vol. 345, no. 2, pp. 337 – 345, 1994. http://www.sciencedirect.com/science/article/pii/0168900294910111.

[45] *User Manual UM3182: MC2Analyzer User Manual.* http://www.caen.it/csite/CaenProd.jsp?parent=64&idmod=756#.

[46] Knoll, Glenn F, *Radiation detection and measurement; 4th ed.* New York, NY: Wiley, 2010. http://cds.cern.ch/record/1300754.

[47] "Experiment 6, beta spectroscopy." https://www.ortec-online.com/-/media/ametekortec/third%20edition%20experiments/beta-spectroscopy.pdf?la=en.

[48] *A1536 AG536 Family Power Supply Boards.* http://www.caen.it/csite/CaenProd.jsp?parent=20&idmod=792.

[49] CAEN, *A251x Series 50W LV Boards User Manual.* http://www.caen.it/csite/CaenProd.jsp?idmod=874&parent=20.

[50] E. Dafni, "A note on the application of baf_2 scintillators to γ-ray and charged particle detection," *Nucl. Instr and Meth*, vol. A254, pp. 54–60.

[51] E. De Filippo, "A study of light quenching in baf_2 crystals for heavy ions at intermediate energies," *Nucl. Instr. and Meth. in Phys. Res. A*, vol. 342, pp. 527–533.

[52] Borrello L et al., "Sensor design for the cms silicon strip tracker," *CERN CMS NOTE*, 08 2003.

[53] T. Bergauer, "Process quality control of silicon strip detectors for the cms tracker," Master's thesis, Vienna university of technology, August 2004.

[54] D.H. Habing, "The use of laser to simulate radiation-induced transient in semiconductors and circuits.," *IEEE TRANSACTIONS ON NUCLEAR SCIENCE NS-12*, vol. 6.

[55] PicoQuant. https://www.picoquant.com/products/category/picosecond-pulsed-driver/pdl-800-b-picosecond-pulsed-diode-laser-driver.

[56] DeltaOHM, *HD 9216 instruction manual.* http://www.deltaohm.com/ver2012/download/hd9216_M_uk.pdf.

[57] CAEN, *A7030-AG7030 3kV/ 1mA (1.5W) HV Boards.* http://www.caen.it/csite/CaenProd.jsp?parent=20&idmod=944.

[58] TEKTRONIX. https://www.tek.com/signal-generator/afg3000-function-generator/afg3252.

[59] Geant4 Collaboration, "Physics list guide." http://geant4-userdoc.web.cern.ch/geant4-userdoc/UsersGuides/PhysicsListGuide/html/physicslistguide.html.

[60] Geant4 Low Energy Electromagnetic Physics Working Group, "Low energy electromagnetic physics working group." https://new-geant4-dev.web.cern.ch/node/1615.

[61] Apostolakis, "GEANT4 low-energy electromagnetic models for electrons and photons," Aug 1999. http://cds.cern.ch/record/397049.

[62] J. Sempau et al., "Experimental benchmarks of the monte carlo code penelope," *Nucl. Instr. and Meth. in Phys. Res. B*, vol. 207, no. 2, pp. 107 – 123, 2003. https://doi.org/10.1016/S0168-583X(03)00453-1.

[63] F. Salvat et al., "Penelope - a code system for monte carlo simulation of electron and photon transport.," *Workshop Proceedings Issy-les-Moulineaux, France; AEN-NEA, 5-7 November 2001.*

[64] J. Apostolakis et al., "Geometry and physics of the geant4 toolkit for high and medium energy applications.," *Radiation Physics and Chemistry*, 2009. https://doi.org/10.1016/j.radphyschem.2009.04.026,doi:10.1016/j.radphyschem.2009.04.026.

[65] HAMAMATSU, "Detector technical drawing, private communication."

[66] E. A. Nadaraya, "On estimating regression," *Theory of Probability and its Applications*, vol. **9**, 1964.

[67] G. S. Watson, "Smooth regression analysis," *Sankhyā: The Indian Journal of Statistics, Series A 26*, 1964.

[68] C. collaboration, "Root home page." https://root.cern.ch/.

[69] F.James and M.ROOS, "Minuit a system for function minimization and analysis of the parameter errorsand correlations," *Computer Physics Communications*, 1975.

[70] F.A. Mirto, L. Carraresi,, "The pulsed beam facility at the tandetron accelerator in florence.," *Nucl. Instr. and Meth. in Phys. B.*, vol. 266.

[71] M. Veltri et al., "A γ calorimeter for the monitoring of the eli-np beam," *Nucl. Instr. and Meth. in Phys. Res. A*, 2018.